Lyle, M., Wilson, P.A., Janecek, T.R., et al., 2002
Proceedings of the Ocean Drilling Program, Initial Reports Volume 199

11. Site 1218[1]

Shipboard Scientific Party[2]

BACKGROUND AND OBJECTIVES

Site 1218 (8°53.378′N, 135°22.00′W; 4828 meters below sea level [mbsl]; Fig. **F1**) is the sole site to be drilled on the 40-Ma transect during Leg 199 and will be used to investigate paleoceanographic processes in the equatorial Paleogene Pacific Ocean during the inferred transition of Earth's climate from the early Paleogene "greenhouse" into the late Paleogene "icehouse." Site 1218 is situated on a basement swell ~3° north of the Clipperton Fracture Zone in the central tropical Pacific Ocean. The age of basement at Site 1218 was poorly constrained prior to Leg 199 because the crust formed near the Eocene magnetic equator so that little magnetic anomaly data are available between the Clipperton and Clarion Fracture Zones (Cande et al., 1989). Thus, prior to Leg 199, our estimate for basement age at Site 1218 (~40 Ma) was based on previous drilling and assumed spreading rates. Nevertheless, at the outset of Leg 199 drilling, the availability of sediment descriptions from Deep Sea Drilling Project (DSDP) Sites 161, 574, and 575 meant that the Cenozoic history of sedimentation in the region of Site 1218 was better constrained than in the regions of Sites 1215, 1216, and 1217. Based on data from these rotary-cored holes, shallow-penetration piston cores taken near Site 1218 (taken on the site survey EW9709-7PC), and seismic profiling (Fig. **F2**), we expected the sedimentary sequence at Site 1218 to comprise a relatively thick (25 to 35 m thick) section of clays overlying radiolarian and nannofossil oozes to chalks of early Miocene–late Eocene age with little to no chert (estimated total depth ~250–280 meters below seafloor [mbsf]).

Site 1218 was chosen because it is anticipated to have been located on the equator at 40 Ma (at ~0°N, 107°W) based upon a fixed hotspot model (Gripp and Gordon, 1990, for 0- to 5-Ma Pacific hotspot rotation pole; Engebretson et al., 1985, for older poles) and because our interpretation of seismic data suggested that this site afforded the best possibil-

F1. Site location map, p. 40.

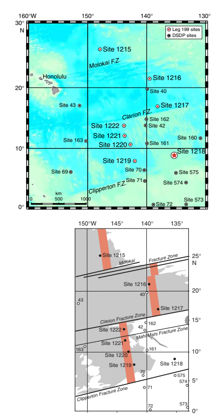

F2. Seismic reflection profile, p. 41.

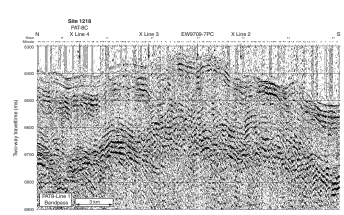

[1]Examples of how to reference the whole or part of this volume.
[2]Shipboard Scientific Party addresses.

Ms 199IR-111

ity of penetrating Eocene/Oligocene (E/O) boundary sediments within the depth range of the Ocean Drilling Program's (ODP's) advanced piston corer (APC) system (~180 mbsf in these sediments).

The paleoceanographic and paleoclimatic objectives of drilling the sedimentary sequence anticipated at Site 1218 are as follows: (1) to help define the shift in the Intertropical Convergence Zone through the Paleogene by following the change in eolian dust composition and flux (red clays) through time; (2) to help constrain changes in the calcite compensation depth (CCD) from the late Eocene to the early Oligocene; (3) to obtain a complete Oligocene section of tropical-assemblage carbonate and siliceous microfossils with good magnetostratigraphic control; and (4) to sample the E/O boundary, late Oligocene, and Oligocene/Miocene (O/M) boundary, three of the most climatologically interesting intervals of Cenozoic time. Recovery of deep-sea sediments from above the CCD across the E/O boundary time interval during Leg 199 is a particularly high priority because complete E/O boundary sections for this time interval are not available from the Pacific Ocean.

SUMMARY

Site 1218 (8°53.38′N, 135°22.00′W) is the only Leg 199 drill site on the 40-Ma transect and is situated at a water depth of 4826 m. It was chosen for drilling in order to investigate paleoceanographic processes in the equatorial Paleogene Pacific Ocean during the inferred transition of Earth's climate from the early Paleogene greenhouse into the late Paleogene icehouse state. Site 1218 is situated on a basement swell ~3° north of the Clipperton Fracture Zone in the central tropical Pacific at a water depth of 4826 m. Pacific plate motion carried Site 1218 across the equator at ~40 Ma based upon a fixed hotspot model (Gripp and Gordon, 1990, for the 0- to 5-Ma Pacific hotspot rotation pole; Engebretson et al., 1985, for older poles). Based upon the same model, the site remained within 2° of the equator from the time crust was formed until 27 Ma. Therefore, sediments recovered from Site 1218 should record near-equatorial oceanographic conditions from the middle Eocene until the early Oligocene. The precise age of basement at the site was poorly constrained prior to Leg 199 because little magnetic anomaly data are available between the Clipperton and Clarion Fracture Zones (Cande et al., 1989).

At Site 1218, we recovered a complete sediment section to within 15 m of basaltic basement. A continuous spliced section (from 0 to 263 mbsf) was developed using the three drilled holes (~41–42 Ma; nannofossil biostratigraphic Subzone CP14a). The sediments immediately overlying basalt are from near the CP14a/CP13 boundary (42 Ma), which indicates that basement at Site 1218 is slightly older than originally expected. A full suite of downhole logs were obtained to the base of the Hole 1218A, and the data are of excellent quality.

The sediment column at Site 1218 is made up of four sedimentary units. At the top of the sedimentary column is 52 m of yellowish brown radiolarian clay with occasional barren intervals and intervals with nannofossils. The age of this unit is Pleistocene–middle Miocene. Below this unit are nannofossil oozes and chalks of early Miocene–Oligocene age from 52 to 217 mbsf. The basal boundary is abrupt. The upper Eocene and upper middle Eocene sediments (217–250 mbsf) are composed of radiolarites and nannofossil chalk with occasional chert beds.

In contrast to other sites, the cherty sections at Site 1218 were completely recovered by extended core barrel (XCB) coring, undoubtedly because they were interbedded with chalks rather than ooze. The base of the sediment column is middle Eocene chalk (250–274 mbsf). The lower 7 m of the chalk is dolomitized with up to 20% dolomite in the coarse fraction. Basalt was recovered at the base of the drilled section.

Planktonic foraminifers are sporadically present through the lower Miocene, Oligocene, and middle Eocene sediments at Site 1218 with generally less consistent presence than other calcitic groups such as benthic foraminifers and calcareous nannofossils. Samples show at least some dissolution of planktonic foraminifers with preferential preservation of thick-walled, large specimens, in many cases. Middle Oligocene sediments (Zones P21 and P20) were generally the best preserved and most species-rich sediments for planktonic foraminifers at Site 1218. Benthic foraminifers are present in core catchers throughout the cored interval except in the Neogene radiolarian clays and the upper Eocene interval. Calcareous nannofossils, in contrast, are present at varying concentrations and states of preservation from uppermost middle Miocene Zone NN8 (37mbsf) to the base of the sediment section. Radiolarians were found in all recovered cores.

Pore water chemical profiles at Site 1218 are subtle. Sulfate concentrations are near seawater values throughout the section, indicating the lack of significant organic matter diagenesis, whereas trends in Ca and Mg reflect modest basement alteration. Bulk-sediment concentrations (measured every 1.5 m) outline the major lithologic units. Only Ca and Sr concentrations are high in the lower Oligocene–Miocene nannofossil oozes, and all other elements tend to be higher in the clays and radiolarite sediments. Biogenic enrichment of Ba can be detected through Ba/Ti ratios. High Mg concentrations can be found in the basal dolomitized chalk.

Natural remanent magnetization (NRM) intensity of the sediments at Site 1218 is relatively strong, and magnetic overprint from drilling can be mostly removed by alternating-field (AF) demagnetization. An excellent record of magnetic reversals was made for the entire APC-cored sediment section (0–210 meters composite depth [mcd]) to Chron C12r of the early Oligocene. In addition, magnetic inclinations were determined on discrete samples after more thorough demagnetization. Middle and early Miocene samples have an average inclination of 5.2° (range = +2.2° to +8.4°), whereas the Oligocene samples have an average inclination of 3.8° (α_{95} = 6.2), which is indistinguishable from the paleoequator.

Highlights

Composite Section

Recovered sediments at Site 1218 have high-amplitude multisensor track (MST) data sets such that it was possible to direct drilling in real time in Holes 1218B and 1218C to construct a complete composite sediment section to a depth of ~263 mbsf (~287 mcd). This section will help to define and calibrate Cenozoic biostratigraphic zonation, to develop an astronomically tuned Cenozoic timescale, and to generate high-resolution paleoceanographic and paleoclimatic records of the Paleogene–Neogene transition.

Oligocene–Miocene Transition

The short range of nannofossil species *Sphenolithus delphix* provides a reliable marker close to the O/M boundary between Subchrons C6Cn.3n and C6Cn.2n (Raffi, 1999), and on this basis, the O/M boundary in Site 1218 occurs at ~98 mbsf. The first occurrence of the planktonic foraminifer *Paragloborotalia kugleri* (the marker for the O/M boundary) and first occurrence of the radiolarian *Cyrtocapsella tetrapera* also occur at this depth.

Calcareous benthic foraminifer assemblages indicate lowermost bathyal and upper abyssal paleodepths at Site 1218. Examination of test walls under transmitted light indicates that most of the benthic foraminifers at this site have suffered little or no postburial diagenetic alternation. Average sedimentation rates across the Oligocene–Miocene transition (~1–2 cm/k.y.) are relatively high for a deep-ocean Pacific setting.

Eocene–Oligocene Transition

The E/O boundary at Site 1218 is characterized by a major lithologic change involving a two-step downcore shift from pale nannofossil chalk to dark radiolarite. This transition from carbonate-rich to carbonate-poor sediments is also evident as a two-step decrease in gamma ray attenuation (GRA) bulk density and a decrease in magnetic susceptibility (MS) values in MST data. Based upon biostratigraphic information, this transition occurs across or just above the Eocene–Oligocene transition.

The extinction of the calcareous nannofossil *Discoaster saipanensis* is estimated to have occurred ~0.3 m.y prior to the E/O boundary event sensu stricto (extinction of the planktonic foraminifer genus *Hantkenina*), and the last representative of the Paleogene rosette-shaped discoasters, *Discoaster barbadiensis,* disappeared ~0.2 m.y. before *D. saipanensis*. *D. barbadiensis* and *D. saipanensis* are constrained to have disappeared over narrow (~20–30 cm) intervals in Site 1218 sediments, shortly below the major change in lithology. These findings reveal that the entire two-step change in lithology occurred within Zone NP21 (CP16c) above the extinction of the last Eocene discoasters. Based on a linear sedimentation rate (LSR), the estimated position of the E/O boundary is at 243.3 mcd, whereas the midpoint of the initial change in carbonate composition is at 242.0 mcd. The midpoint of the second, final step in carbonate composition is at 240.0 mcd. The boundary-condition change of the ocean-climate system that caused the first step of this drastic deepening of the CCD and accompanying change in sedimentation in the tropical Pacific Ocean occurred near the middle of Oi-1 (33.5–33.1 Ma) (Zachos et al., 2001) on the common timescale used (Cande and Kent, 1995). The abrupt change in the lithologies across the Eocene–Oligocene transition is a reflection of the rapid deepening of the CCD (van Andel et al., 1975) in the Oligocene. Site 1218 demonstrates that the change in CCD occurred during the earliest Oligocene in two steps: as a rapid increase in calcium carbonate ($CaCO_3$) over 10–~20 k.y. followed by a pause of ~100–200 k.y. and then another rapid increase in $CaCO_3$ over 10–~20 k.y. The CCD was shallower than ~3600 mbsl in the latest Eocene radiolarite interval based on the paleodepth of Site 1218.

Middle and Late Eocene Radiolarites

From Site 1218, it is clear that radiolarian-rich sediments are characteristic of the late and late–middle Eocene Pacific Ocean, even near the equator. Nannofossils occasionally are dominant sediment components, showing that the CCD deepened beyond the paleodepth of Site 1218 at times within the late and middle Eocene. The presence of radiolarians and occasional intervals of nannofossils and the relative absence of diatoms (except in specific intervals near the E/O boundary) is more typical of Neogene plankton assemblages found at the fringes of the equatorial high-productivity zone than in the near-equatorial position that Site 1218 probably occupied during the middle and late Eocene.

Middle Eocene Basal Sediments

The basal nannofossil chalks of Site 1218 abruptly become radiolarites upcore at ~40 Ma (base of nannofossil Subzone CP14b; Core 199-1218C-21X). The transition from chalks to radiolarites occurs over only 1.5 m when the site was at a paleodepth of 3000–3100 m. The middle Eocene rise in CCD at 40 Ma is almost as abrupt as the drop in CCD at the E/O boundary.

Finally, the basal 7 m of nannofossil chalk that overlies basement is, like its Site 1215 and 1217 counterparts, dolomitized, which is an intriguing discovery given its proximity to what is generally considered to be a kinetically more favorable geochemical sink for Mg (alteration minerals in the upper oceanic crust).

OPERATIONS

Transit to Site 1218 (PAT-8C)

The 497-nmi voyage to proposed Site PAT-8C was accomplished in 47.0 hr at an average speed of 10.6 kt. At 0030 hr on 14 November, 2001, the vessel slowed to 5 kt, and a short 3.5-kHz survey was made from north to south across the site. Upon conclusion of the 45-min survey, the vessel came about and returned to site as the thrusters were lowered and the dynamic positioning system (DPS) was activated. The Global Positioning System receiver interface to the DPS was employed, and the vessel was over the coordinates of the new location by 0115 hr. A beacon was deployed at 0241 hr. The corrected precision depth recorder (PDR) depth was 4848.0 meters below rig floor (mbrf).

Hole 1218A

After the drill string was deployed to a depth of 4811 mbrf, the driller then lowered the bit until the heave compensator appeared to activate, suggesting contact with a firm sea bottom at a bit depth of ~4840 mbrf. Hole 1218A was spudded with the APC at 1000 hr on 14 November. The seafloor depth indicated by the recovery of the initial core was 4837.3 mbrf, 10.7 m shallower than the PDR depth.

Hole 1218A was deepened to 188.7 mbsf (base of Core 20H) before it became necessary to switch to XCB operations to accomplish the deeper objectives of the hole. Cores 3H–20H were oriented. All 20 piston cores fully stroked, but the core barrels for Cores 19H and 20H could not be pulled free with 80,000 lb of overpull; thus, both were drilled over to release them from the sediment. The average recovery for the APC section was 102.8% (Table T1).

Ten XCB cores were taken over the interval from 188.7 to 276.8 mbsf (Cores 21X–30X). A small sample of basalt was obtained in the last core, confirming basement contact. XCB coring deepened the hole 88.1 m and recovered 72.4 m (82.2% recovery). The total recovery of Hole 1218A was 266.4 m, which represents 96.3% of the cored interval (Table T1).

T1. Coring summary, p. 87.

Downhole Logging Operations (Hole 1218A)

To prepare Hole 1218A for logging, the drill string was pulled up to 78 mbsf and then lowered back to 277 mbsf. The hole was then displaced with 110 bbl of 8.9-lb/gal sepiolite mud, and the bit was placed at the logging depth of 85 mbsf. Logging rig-up operations began at 1130 hr on 16 November and, after some minor technical problems, were completed by 1645 hr. The triple combination (triple combo) tool was then run to the bottom of the hole (276.8 mbsf), and logging began at 2210 hr on 16 November.

Two passes were made with the triple combo tool in Schlumberger mode and a third pass in "Lamont mode" for multisensor gamma ray tool (MGT) data acquisition. Two passes were also made with the Formation MicroScanner-sonic velocity (FMS-sonic) tool string. At the end of the second FMS-sonic pass, the drill pipe was gradually withdrawn to a depth of 65 mbsf, providing an extra 20 m of logged formation. In total, five logging runs were made with no bridges encountered, and the bottom of the hole was reached on all attempts (see **"Downhole Measurements,"** p. 32, for details of the downhole logging operations and tool strings). After logging operations, the bit was pulled free of the seafloor at 1917 hr on 17 November, and the vessel was offset 20 m north of Hole 1218A.

Hole 1218B

In order to obtain a good stratigraphic overlap with cores from the first hole, the spud-in position for Hole 1218B was 3 m shallower than that for Hole 1218A. Hole 1218B was spudded with the APC at 2050 hr on 17 November. Eighteen piston cores were obtained over the interval from 0 to 165.40 mbsf with orientation beginning at Core 3H. The average APC recovery was 102.1%. Heat flow measurements were obtained at 32.4 mbsf (Core 4H), 60.9 mbsf (Core 7H), 89.4 mbsf (Core 10H), and 108.4 mbsf (Core 12H). Following APC operations, 11 XCB cores were collected over the interval from 165.40 to 263.50 mbsf, with an average recovery of 92.2%. Core 25X was drilled only 5 m instead of the usual 9.6 m in order to maintain a good stratigraphic overlap with cores from Hole 1218A. The total recovery of the hole was 259.25 m, representing 98.4% of the cored interval.

Hole 1218C

Once the bit cleared the seafloor at 1654 hr on 19 November, the vessel was moved another 20 m north, and Hole 1218C was spudded at 1735 hr. The coring objective for the third hole was to fill the gaps in the compiled stratigraphic record of the first two holes. The hole was washed ahead to 55 mbsf and then piston cored to 163.5 mbsf. The average recovery from the 11 piston cores was 103.4%. All the cores were oriented. It was necessary to drill from 140.5 to 144.5 mbsf to maintain the required overlap with cores from Holes 1218A and 1218B. Heat flow measurements were made at 83.5 mbsf (Core 3H), 102.5 mbsf (Core 5H), and 121.5 mbsf (Core 7H).

After APC coring operations ceased, the hole was deepened with 10 XCB cores to a total depth of 256.8 mbsf (Table T1). The interval from 220.0 to 223.0 mbsf was drilled to maintain stratigraphic overlap with the cores from Holes 1218A and 1218B. XCB operations resulted in 90.3 m cored with 99.7% recovery. The total for the hole was 194.8 m cored and 198.05 m recovered (101.7%).

After drilling operations ceased, drilling equipment was secured, and the beacon was successfully recovered. The transit to the next site began at 1300 hr on 21 November.

LITHOSTRATIGRAPHY

Drilling of the three holes at Site 1218 recovered a 274-m section of pelagic sediment (Fig. F3). The four sedimentary units are differentiated by sedimentary composition. Fifty-two meters of early Miocene and younger pelagic and radiolarian clay overlies 165 m of nannofossil ooze and chalk, 33 m of radiolarite, and 24 m of nannofossil chalk. A fifth unit consists of seafloor basalt and was sampled only in Hole 1218A. The basement was not reached in Hole 1218B. Hole 1218C was washed down to 55.0 mbsf, and drilling was terminated at 256.8 mbsf.

F3. Lithologic summary, p. 42.

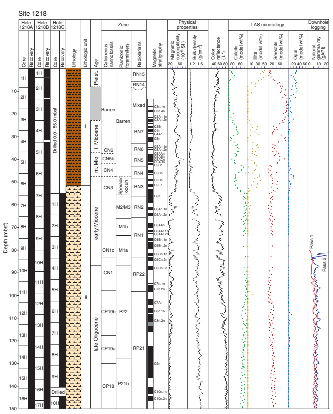

Unit I

Intervals: Section 199-1218A-1H-1, 0 cm, through 6H-4, 140 cm; and Section 199-1218B-1H-1, 0 cm, through 6H-CC, 12 cm
Depths: 0–52.1 mbsf (Hole 1218A) and 0–51.0 mbsf (Hole 1218B)
Age: Holocene to early Miocene
Lithology: radiolarian clay, clay with radiolarians, and clay with zeolites

The sediment of Unit I alternates between light yellowish brown (10YR 6/4) radiolarian clay and dark yellowish brown (10YR 4/4) clay with radiolarians. At 15.8 mbsf (Hole 1218A), there is a 56-cm-thick interval of dark grayish brown (10YR 4/2) to very dark grayish brown (10YR 3/2) clay with zeolites. Clay with zeolites is found at 17.7 mbsf and gradually changes to clay with radiolarians downcore. In Hole 1218B, smear slide estimates show diatoms comprise the main siliceous component from 0 to 10.8 mbsf. Distinct 40- to 60-cm-thick yellowish brown to brown (10YR 4/3 to 10YR 5/4) nannofossil ooze layers with various amounts of clay and radiolarians are present through the interval from 35.7 to 46.3 mbsf in Hole 1218A and from 34.3 to 44.1 mbsf in Hole 1218B.

All lithologies exhibit slight to moderate mottling. Lithologic contacts are obscured by mottles. In interval 199-1218B-3H-2, 94–97 cm, a 3-cm-diameter manganese nodule was recovered (Fig. F4).

F4. Unit I manganese nodule, p. 44.

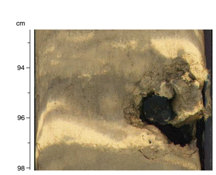

Unit II

Intervals: 199-1218A-6H-4, 140 cm, through 24X-2, 70 cm; 199-1218B-6H-CC, 12 cm, through 24X-2, 35 cm; and 199-1218C-1H-1, 0 cm, through 17X-6, 90 cm

Depths: 52.1–216.9 mbsf (Hole 1218A); 51.0–215.6 mbsf (Hole 1218B); and 55.0–218.5 mbsf (Hole 1218C)
Age: early Miocene to early Oligocene
Lithology: nannofossil ooze, clayey radiolarian nannofossil ooze, and chalk

The upper part of Unit II consists of nannofossil ooze, with clay content varying from 5% to 20% (Hole 1218A: 52.1–84.7 mbsf; Hole 1218B: 51.0–80.0 mbsf; and Hole 1218C: 55.0–84.2 mbsf). The sediment color alternates from pale brown (10YR 7/3) to yellowish brown (10YR 5/3) and brown (10YR 4/3). The lowermost part of this unit is a pale brown (10YR 8/2) to white (10YR 8/1) nannofossil ooze grading downcore to a nannofossil chalk with minor amounts of radiolarians (Hole 1218A: 84.2–216.9 mbsf; Hole 1218B: 80.0–215.55 mbsf; and Hole 1218C: 84.2–218.5 mbsf). In Hole 1218B, several centimeter-scale nannofossil chalk layers are present within the light nannofossil ooze at 122.9 and 124.8 mbsf and at 147.5 mbsf in Hole 1218C.

Diatom content increases in the lower 15 m of Unit II, with intervals containing up to 50% diatoms (e.g., intervals 199-1218A-23X-1, 0 cm, to 24X-CC, 35 cm; 199-1218B-22X-4, 0 cm, to 22X-CC, 6 cm; and 199-1218C-17X-5, 2 cm, to 17X-6, 90 cm). A stepwise shift to the darker radiolarite of Unit III is seen in Sections 199-1218C-17X-5 and 17X-6. Interval 199-1218C-17X-5, 2 cm, through 17X-6, 90 cm, contains brown (10YR 5/3) nannofossil chalk with clay, diatoms, and radiolarians. Mottles are common to abundant throughout Unit II, often obscuring lithologic contacts. Rice-shaped carbonate crystals without square-tipped terminations, 15–20 µm long, are occasionally observed in the dominant lithology (~5%) and burrow infills. Although similar in appearance to aragonite needles (Rothwell, 1989), X-ray diffraction analysis shows only calcite mineralogy. Manganese oxides are common in black (10YR 2/1) burrows. All lithologic contacts are gradational.

Small millimeter- to centimeter-sized medium gray (N5) pumice fragments are sporadically present throughout Holes 1218A, 1218B, and 1218C (e.g., intervals 199-1218A-17H-7, 84 cm; 199-1218B-22X-3, 70–71 cm; and 199-1218C-1H-3, 5–7 cm). Black (N1) centimeter-sized chert fragments and nodules are occasionally found throughout the unit. A 50-µm spherical, glassy green mineral was found in a sieved core catcher sample from Core 199-1218A-23X and was inferred to be a microtectite.

The nannofossil chalk and underlying units are biscuited (commonly 5–50 cm in size) by XCB coring. The biscuits are surrounded by a slurry matrix.

Unit III

Intervals: 199-1218A-24X-2, 70 cm, through 27X-CC, 11 cm; 199-1218B-24X-2, 35 cm, through 28X-1, 150 cm; and 199-1218C-17X-6, 90 cm, through 21X-4, 48 cm
Depths: 216.9–250.2 mbsf (Hole 1218A); 215.6–249.0 mbsf (Hole 1218B); and 218.5–252.2 mbsf (Hole 1218C)
Age: earliest Oligocene to middle Eocene
Lithology: radiolarite and nannofossil chalk

Unit III is characterized by a sequence of interlayered radiolarite and nannofossil chalk, each containing various amounts of clay (up to 30%). The color alternates between very dark brown (10YR 2/2) and brown

(10YR 4/3). In Holes 1218A, 1218B, and 1218C, several 7- to 12-cm-thick, 6- to 27-cm-thick, and 6- to 10-cm-thick, respectively, very dark brown to black (10YR 2/2 to 10YR 2/1) intact chert layers were recovered in the intervals 199-1218A-25X-1, 49 cm, to 27X-1, 41 cm (225.2–244.3 mbsf), 199-1218B-25X-1, 12 cm, to 25X-1, 141 cm (223.4–224.7 mbsf), and 199-1218C-18X-3, 90 cm, to 20X-2, 120 cm (227–244.9 mbsf). For details, see Table T2 and Figure F5. These layers are present in the very dark brown (10YR 2/2) radiolarian intervals. Mottling in the lithified chert layers is common.

T2. Intervals of intact chert layers recovered, p. 90.

Gray (10YR 6/1) siliceous horizons, probably porcellanite, are present in interval 199-1218B-26X-7, 27–82 cm (237.1–237.6 mbsf). In interval 199-1218A-24X-4, 0 cm, to 24X-CC, 10- to 40-cm-thick layers of dark grayish brown (10YR 4/2) diatomite are present within dark brown (10YR 3/3) radiolarite (Sections 199-1218B-24X-2 through 24X-CC).

F5. Unit III chert layer, p. 45.

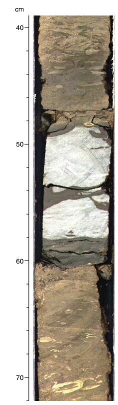

The entire unit contains abundant mottles. *Zoophycos* and *Chondrites* burrows are common through this unit. Small fractures with centimeter-scale offset are present in Core 199-1218B-24X.

Sediments from this unit are strongly biscuited (10–20 cm in size) by XCB coring. A slurry matrix surrounds the biscuits.

Unit IV

Intervals: 199-1217A-27X-CC, 11 cm, through 30X-CC, 27 cm; 199-1218B-28X-1, 150 cm, through 29X-CC, 37 cm; 199-1218C-21X-4, 48 cm, through 21X-CC, 17 cm
Depths: 250.2–274.3 mbsf (Hole 1218A); 249.0 mbsf to base of hole (Hole 1218B); and 252.2 mbsf to base of hole (Hole 1218C)
Age: middle Eocene
Lithology: nannofossil chalk and nannofossil chalk with dolomite

Unit IV is differentiated into two subunits on the basis of mineralogical and sedimentary composition. Subunit IVB was not recovered in Holes 1218B and 1218C.

Subunit IVA

Intervals: 199-1218A-27X-CC, 11 cm, through 29X-3, 134 cm; 199-1218B-28X-1, 150 cm, through 29X-CC, 37 cm; and 199-1218C-21X-4, 48 cm, through 21X-CC, 17 cm
Depths: 250.2–267.4 mbsf (Hole 1218A); 249.0 mbsf to base of hole (Hole 1218B); and 252.2 mbsf to base of hole (Hole 1218C)
Age: middle Eocene
Lithology: nannofossil chalk

Subunit IVA consists of a nannofossil chalk containing 10%–30% clay and 5%–15% diatoms. Color varies from very pale brown (10YR 8/2) to white (10YR 8/1). Layers of fragmented, very dark brown (10YR 2/2) chert are present within intervals 199-1218A-29X-2, 117 cm, to 29X-CC, 20 cm (265.8–268.7 mbsf) and 199-1218B-29X-1, 96 cm, to 29X-3, 102 cm (258.2–261.2 mbsf). Strong mottling is present throughout Subunit IVA.

Subunit IVB

Interval: 199-1218A-29X-3, 134 cm, through 30X-CC, 27 cm
Depth: 267.4–274.3 mbsf (Hole 1218A)

Age: middle Eocene
Lithology: nannofossil chalk with dolomite

Subunit IVB is composed of nannofossil chalk with dolomite and various amounts of clay (up to 15%) and radiolarians (up to 20%). Sediment varies between dark yellowish brown and light yellowish brown (10YR 4/6 and 10YR 6/4). The color change between Subunits IVA and IVB is gradational. Chert layers are present in interval 199-1218A-29X-4, 20 cm, to 29X-CC, 20 cm (267.8–268.7 mbsf). Bedding shows inclinations up to 45°. Centimeter-scale faults are observed throughout this unit (Fig. F6). The dolomite content increases to 20% in the coarser sediment near the base of Section 199-1218A-30X-CC. Dolomite crystals, commonly as large as 100 µm, are authigenic and euhedral. Smear slide analysis indicates that dolomite is principally replacing discoasters and coccoliths. Sediments of Subunit IVB contain abundant mottles.

F6. Subunit IVB fault, p. 46.

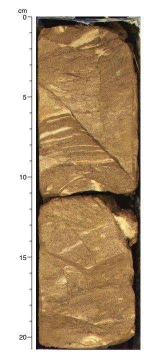

Unit V

Interval: 199-1218A-30X-CC, 27 cm, through 30X-CC, 31 cm
Depth: 274.3–274.34 mbsf (Hole 1218A)
Age: middle Eocene
Lithology: basalt

At the bottom of Hole 1218A, a centimeter-sized piece of weathered basalt was recovered. The fragment is fine-grained phaneritic and has a glassy rind. We terminated coring before reaching basement in Holes 1218B and 1218C.

Discussion/Summary

The middle Eocene basalt is overlain by 274 m of pelagic sediments at Site 1218. The middle Eocene pelagic unit is represented by carbonate-rich sediments with radiolarians. The middle–late Eocene is dominated by a dark radiolarite, reflecting the paleoequatorial productivity zone of the Pacific Ocean. The E/O boundary interval is characterized by a major lithologic change from dark radiolarite to pale nannofossil chalk. The first interval with remarkable radiolarian content in the nannofossil-dominated lithology above the radiolarite emphasizes a stepwise shift to the pale-colored lower Oligocene sediments. DSDP Sites 161 and 162 show similar compositional changes near the E/O boundary interval (van Andel, Heath, et al., 1973). The MST data (see "Composite Depths," p. 21) indicate a stepwise shift in the lithologies at the E/O boundary. Tektites were not found in the upper Eocene sediments in the interval proposed for the late Eocene impact. The abrupt change in the lithologies at the E/O boundary interval may reflect a rapid deepening of the CCD (van Andel et al., 1975). The lower Oligocene–lower Miocene interval is characterized by an alternating sequence of dark and pale nannofossil ooze with various amounts of clay (5%–20%). Holocene–lower Miocene sediments are dominated by pelagic clay.

BIOSTRATIGRAPHY

Pleistocene–middle Eocene strata were recovered at Site 1218 and permit the development of an integrated calcareous and siliceous biozonation (Fig. F7). All microfossil groups, with the exception of radiolar-

F7. Biostratigraphic zonation, p. 47.

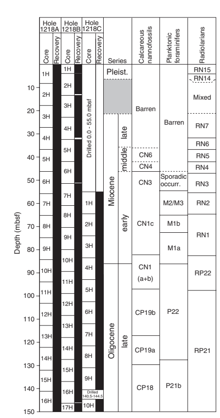

ians, have sporadic occurrences and often poor preservation in the upper Neogene sequence but become better preserved in the lower Miocene–Oligocene interval. Radiolarians are consistently present in the recovered material, but their abundance and preservation are variable in the younger parts of the Neogene. The presence of expanded, well-preserved radiolarian fauna throughout the Miocene–Eocene section will permit the detailed calibration of the tropical radiolarian zonation to magnetostratigraphy and calcareous microfossil stratigraphy. The O/M boundary is well constrained by radiolarian and foraminiferal datum events, and the presence of the nannofossil *S. delphix* provides an additional reliable marker close to the boundary. At Site 1218, we recovered a complete succession of Oligocene and upper Eocene biozones, including a record of the E/O boundary interval with a well-defined radiolarian and calcareous nannofossil biostratigraphy. Calcareous nannofossils generally suffer from some dissolution but were sufficiently well preserved to construct a detailed biozonation in the Eocene, whereas planktonic foraminifers have been completely removed from upper Eocene sediments and are only represented by dissolution-resistant taxa in the middle Eocene. Benthic foraminifers are present in most samples of lower Miocene–middle Eocene sediments and represent a cosmopolitan bathyal to abyssal fauna.

Calcareous Nannofossils

Calcareous nannofossils are present at varying concentrations and states of preservation from the uppermost middle Miocene Zone NN8 (CN6) in Core 199-1218A-4H to the basal part of the middle Eocene Zone NP16 (CP14a) in Core 30X. Nannofossils are lacking from the seafloor to Sample 199-1218A-4H-6, 50 cm, because of calcite dissolution. Below this barren interval, assemblages are consistently affected by calcite dissolution, albeit less so in the lower Miocene and Oligocene carbonate-rich assemblages than in the Eocene assemblages. Preservation is generally poor in the condensed middle Miocene sediments, except for discoasters. Depth positions and age estimates of key biostratigraphic marker events are shown in Table T3.

T3. Distribution of calcareous nannofossil datums, p. 91.

Miocene

The uppermost carbonate-bearing sediments in interval 199-1218A-4H-6, 85 cm, contain a low-diversity assemblage consisting chiefly of *Discoaster* spp., *Catinaster* spp., and *Triquetrorhabdulus rugosus,* suggesting that Site 1218 last moved below the CCD during Zone NN8 (CN6) time. *Discoaster kugleri* is present in Sample 199-1218A-4H-CC, placing this sample in Zone NN7 (CN5b), which corresponds to Sample 199-1218B-5H-2, 56 cm.

Sample 199-l218B-5H-CC held the highest occurrence of both *Cyclicargolithus floridanus* and *Coronocyclus nitescens* and the lowest occurrence of *T. rugosus*. Rare aberrant forms with *Triquetrorhabdulus* affinity are also present in Sample 199-1218B-5H-CC, presumably reflecting the evolutionary transition creating the *T. rugosus* lineage from *Orthorhabdus serratus*. This core catcher sample also contains a well-preserved discoaster assemblage lacking calcite overgrowth with abundant *Discoaster exilis* and other species belonging to the *Discoaster deflandrei, D. exilis, Discoaster variabilis* group and beautifully developed *Discoaster signus,* having a range in lower Zone NN5 (CN4) and upper NN4 (CN4–CN3 transition).

Section 199-1218B-6H-1 has a discoaster assemblage with abundant *D. deflandrei*. This marked change in proportion among discoasters indicates a position below the CN4/CN3 boundary when using Bukry's (1973) top acme *D. deflandrei* concept as boundary definition. The corresponding change in Hole 1218A is observed between Samples 199-1218A-5H-6, 15 cm, and 5H-CC. In this latter sample, only rare specimens of *Sphenolithus heteromorphus* were observed, suggesting that this core catcher sample belongs to lower Zone NN4 (CN3).

Several lower Miocene samples investigated from below Section 199-1218A-5H-CC contain common to abundant sphenoliths but no *S. heteromorphus* or *Sphenolithus belemnos*. Sediment deposits with an age range of over 7 m.y. may be contained in Cores 199-1218A-5H and 6H. Available calcareous nannofossil data cannot resolve if a hiatus is present or if condensation was a factor.

O/M Boundary Interval

Several species events are employed in the classical zonal schemes to subdivide the interval around the O/M boundary, which is recognized by the presence of *S. delphix* in the upper portion of Core 199-1218A-10H. Three other events are commonly used to subdivide the lowermost Miocene. These include the base of *Discoaster druggii* (observed in the lower part of Section 199-1218B-9H-5), the base of *Sphenolithus disbelemnos* (observed in Section 199-1218A-9H-4), and the top of *Triquetrorhabdulus carinatus* (observed in the core break between Cores 199-1218A-6H and 7H). Detailed distribution patterns of these species at the Oligocene–Miocene transition are shown in Figure F8. *S. disbelemnos* provides a distinct biostratigraphic signal just above the O/M boundary, in contrast to the basal part of the range of *D. druggii,* which is characterized by discontinuous occurrences of few to rare specimens. *Triquetrorhabdulus milowii* is observed in a short interval immediately above the range of *T. carinatus*. Two biohorizons are recognized within the upper range of *T. carinatus,* based on the pattern observed between Cores 199-1218A-7H and 9H and Cores 199-1218B-7H and 10H (Fig. F8). The interval between Sections 199-1218A-7H-5 and 9H-2 yields only discontinuous, rare specimens of *T. carinatus,* which becomes an abundant member of the assemblage in Sample 199-1218A-9H-2, 130 cm, and downhole for a long interval into the upper Oligocene.

Three species events are used to subdivide the uppermost Oligocene. These include the top of common to abundant *Cyclicargolithus abisectus* (≥10 µm) in Section 199-1218A-11H-5, the top of *Sphenolithus ciperoensis* in Section 11H-3, and the top of *Dictyococcites bisectus* in Section 13H-6. *C. abisectus* provides a distinct event, whereas *D. bisectus* and *S. ciperoensis* are rare members of the assemblages in the uppermost part of their ranges, implying that their true extinctions are difficult to determine accurately. Specimens of *C. abisectus* in Section 199-1218A-7H-CC are considered to be reworked from Oligocene strata (Fig. F8).

S. ciperoensis overlaps with abundant *C. abisectus* for a short interval in Core 199-1218A-11H, causing Subzone CN1a to disappear. A similar relationship between these two species events is observed on the Ontong Java Plateau in the western equatorial Pacific Ocean (Kroenke, Berger, Janecek, et al., 1991) and the Ceara Rise in the western equatorial Atlantic Ocean (Curry, Shackleton, Richter, et al., 1995).

Of the discussed lower Miocene–upper Oligocene calcareous nannofossil events, only three are well calibrated to an independent chronology: namely, the base of *S. disbelemnos* at 22.7 Ma, the top of *S. delphix*

F8. Distribution of calcareous nannofossil taxa, p. 49.

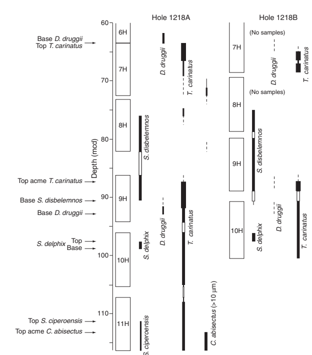

at 23.0 Ma, and the base of *S. delphix* at 23.2 Ma (Shackleton et al., 1999).

Oligocene

Oligocene assemblages are generally monotonous in composition apart from the evolution observed among the sphenoliths. Helicosphaerids are absent in Miocene and upper Oligocene sediments at Site 1218, probably because of dissolution, but are rare to few in the assemblages of the lower Oligocene and are notably represented by *Helicosphaera compacta*.

Key elements of upper lower Oligocene (NP23/CP17–18) assemblages are abundant (*C. floridanus, D. bisectus,* and *Sphenolithus moriformis*) few to common (*Coccolithus pelagicus, Coccolithus eopelagicus, Dictyococcites hesslandii* [junior synonym: *Dictyococcites scrippsae*], and *D. deflandrei),* and few to rare (*Sphenolithus predistentus, Sphenolithus celsus, Reticulofenestra gartneri, Discoaster tanii,* and *H. compacta*).

The NP23/NP22 (CP17/CP16c) boundary is distinct in Section 199-1218A-22X-2, occurring over a 77-cm-long interval. Core 199-1218A-22X also contains unusually large specimens of *D. bisectus,* similar in size to the large (per definition) *Reticulofenestra umbilicus*. The NP22/NP21 (CP16c/CP16a+b) boundary is equally distinct, occurring over a 35-cm interval in the uppermost part of Section 199-1218A-23X-3.

E/O Boundary Interval

The extinction of the planktonic foraminifer genus *Hantkenina* is adopted for recognition of the E/O boundary. The nearest calcareous nannofossil event is the extinction of *D. saipanensis,* estimated to have occurred ~0.3 m.y. prior to the *Hantkenina* event and, thus, the E/O boundary. The last representative of the Paleogene rosette-shaped discoasters, *D. barbadiensis,* disappeared ~0.2 m.y. before *D. saipanensis*.

D. barbadiensis disappeared over a 30-cm interval in Section 199-1218A-24X-5, and *D. saipanensis* disappeared over a 22-cm interval in Section 24X-4, shortly below the major change in lithology. The lithology change occurs in two steps, from radiolarite below to nannofossil chalk above, observed in Cores 199-1218A-24X and 199-1218C-17X, respectively. A complete composite stratigraphic section is obtained from these cores, revealing that the entire two-step change in lithology occurs within Zone NP21 (CP16a and CP16b) above the extinction of the last Eocene discoasters. By assuming an LSR within Zone NP21 in this composite section, an age estimate of 33.3 Ma is obtained for the initial change (midpoint of transition) in lithology and an estimate of 32.9 Ma for the midpoint of the second, final step. The boundary condition change of the ocean-climate system that caused the first step of this drastic deepening of the CCD and the accompanying change in sedimentation in the tropical Pacific Ocean occurred in middle Oi-1 (33.5–33.1 Ma) (Zachos et al., 2001) on the common timescale of Cande and Kent (1995).

Rare specimens of the "cool-water marker" (Bukry, 1973), or "nontropical species" in Martini's (1971) vocabulary, *Isthmolithus recurvus* were only observed in Samples 199-1218A-24X-1, 1 cm, and 17X-CC, perhaps indicating brief episodes of cooler surface water conditions.

Eocene

The number of species preserved and the total abundance of calcareous nannofossils were strongly biased by calcite dissolution in the upper Eocene and upper middle Eocene radiolarites. Typical remaining forms included *C. pelagicus, C. eopelagicus, D. barbadiensis, D. saipanensis, D. tanii, Discoaster nodifer, D. bisectus, D. hesslandii, Ericsonia formosa, R. umbilicus, Reticulofenestra dictyoda,* and *R. gartneri*. Three middle Eocene species events were determined in the interval, which show enhanced dissolution: the top of *Chiasmolithus grandis,* the base of *D. bisectus,* and the top of *Chiasmolithus solitus*.

Sphenoliths reappeared in the better-preserved, lowermost interval of Hole 1218A and included *Sphenolithus furcatolithoides* and *Sphenolithus radians,* both becoming extinct in middle Eocene Subzone CP14a (NP16). The assemblage of large reticulofenestrids is characterized by higher abundances of morphotypes <14 µm in the lowermost sample of the sequence (Sample 199-1218A-30X-CC). The species *R. umbilicus* (≥14 µm) is still present in that sample, albeit as a rare member of the nannofossil assemblage. The uppermost occurrence of *Nannotetrina* spp. is also observed in Section 199-1218A-30X-CC, indicating that this section was formed during Zone NP16 close to the CP14a/CP13 boundary.

Planktonic Foraminifers

Planktonic foraminifers are present sporadically through the lower Miocene, Oligocene, and middle Eocene at Site 1218 with generally less consistent occurrence than other calcitic groups such as benthic foraminifers and calcareous nannofossils. Most samples show at least some dissolution of planktonic foraminifers, with preferential preservation of thick-walled, large specimens in many cases. Middle Oligocene sediments (Zones P21 and P20) are generally the best preserved and most species rich, whereas the Pleistocene–middle Miocene and lower Oligocene could not be zoned at all owing to the absence of dissolution-susceptible marker species (Table T4). Planktonic foraminifers were completely absent in samples within the upper Eocene. The distribution of middle Eocene species is given in Table T5. Well-defined datum levels for planktonic foraminifers are presented in Table T6.

Planktonic foraminifers can be used to delineate a condensed sequence of lower Miocene Zones M1a–M3 in Holes 1218A and 1218B (Fig. F7). Core catchers from Hole 1218A contain planktonic foraminifers in Sample 199-1218A-5H-CC (46.35 mbsf) that include an undifferentiated Miocene assemblage of *Paragloborotalia mayeri, Paragloborotalia continuosa,* and *Paragloborotalia siakensis*. The top of Zone M3 is located in Sample 199-1218A-6H-7, 39-41 cm, which contains the highest occurrence of *Catapsydrax dissimilis ciperoensis*. The M2/M3 boundary could not be differentiated at Site 1218 owing to the absence of *Globigerinatella insueta*. Zone M2/M3 assemblages are present as deep as Section 199-1218A-7H-CC and are characterized by dissolution-resistant species such as *Globoquadrina praedehiscens, Globoquadrina venezuelana, P. mayeri,* and *Globorotaloides suteri*. The highest occurrence of *Paragloborotalia kugleri* is in Sample 199-1218A-8H-2, 110–114 cm (67.8 mbsf), and defines the top of Subzone M1b. Subzone M1a is present between Sections 199-1218A-8H-6, 60–62 cm, and 10H-1, 130–132 cm, as recognized, respectively, by the disappearance of *Globoquadrina dehiscens* and the first appearance of *P. kugleri*. The corresponding interval in Hole 1218B is indicated by the last downhole occurrence of *G. dehiscens*

T4. Distribution of Miocene–upper Eocene planktonic foraminifers, p. 92.

T5. Distribution of middle Eocene planktonic foraminifers, p. 96.

T6. Planktonic foraminifer datum levels, p. 97.

in Sample 199-1218B-9H-4, 63–65 cm. The base of Subzone M1a, and, therefore, the M/O boundary, is placed between Samples 199-1218A-10H-1, 130–132 cm, and 10H-2, 74–75 cm (86.15 ± 0.30 mbsf).

Catapsydrax dissimilis displays two distinctive morphologies in the Oligocene–lowermost Miocene section at Hole 1218A. One form closely resembles the holotype of this species; it possesses 3.5 large inflated chambers and a thin, straplike bulla over the aperture. The other form is similar to the holotype specimen of *C. dissimilis ciperoensis,* named by Blow and Banner (1962), and specimens figured as *C. dissimilis* by Kennett and Srinivasan (1983). Specimens we refer to *C. dissimilis ciperoensis* have four slightly compressed chambers and an aperture completely covered by a flattened bulla that forms two slitlike secondary apertures. Our studies suggest that *C. dissimilis* (sensu stricto) ranges only to the top of Subzone M1a at Site 1218, whereas *C. dissimilis ciperoensis* is the form that ranges to the top Zone M3 and defines the M3/M4 zonal boundary.

A number of long-ranging Miocene species have first occurrences in the basal Miocene sequence at Site 1218, although several characteristic species of the Oligocene range into the lower Miocene. *Dentoglobigerina altispira, P. continuosa, G. praedehiscens,* and *Globoquadrina biniaensis* have first occurrences within Zone M1 in Hole 1218A. Species typical of the Oligocene, such as *Globoquadrina sellii, Paragloborotalia pseudokugleri, Globoquadrina tripartita,* and *Subbotina gortani,* were all found in the lower Miocene at this site. The Miocene ranges of *G. sellii, G. tripartita,* and *S. gortani* are unusual and when coupled with the occurrence of these taxa in the Oligocene of Site 1218 suggest reworking from Oligocene strata.

Assemblages of Zone P22 are present between Sections 199-1218A-10H-2 and14H-4 (86.9–127.01 mbsf). Preservation is mostly very poor in this interval, with only dissolution-resistant species present in Cores 199-1218A-10H, 11H, and 13H. Characteristic species include *Globoquadrina tapuriensis, G. tripartita, G. suteri,* and, in the lower part, *Paragloborotalia opima nana.*

Subzone P21b is recognized by the highest occurrence of *Paragloborotalia opima opima* in Sample 199-1218A-14H-5, 32–37 cm (128.52 mbsf), and the first common occurrence of *Chiloguembelina cubensis* in Sample 16H-7, 39–44 cm (150.59 mbsf). This interval includes the best-preserved planktonic foraminifer assemblages in the whole of Site 1218. The zone marker, *P. opima opima,* is present continuously and is frequently the most abundant species. Therefore, the top of Subzone P21b is very well delineated. In contrast, *C. cubensis* is very rare in Hole 1218A and may not be useful as a datum level. Subzone P21b includes *G. tapuriensis* (including specimens with an inflated, subspherical final chamber), *G. tripartita, G. praedehiscens, G. praeturritilina, Subbotina euapertura, Catapsydrax dissimilis, Tenutiella clemincea,* and *Tenutellinata angustiumbilicata* in the >150-mm size fraction. Also present at low abundance levels is *Globoquadrina prasaepis,* a relatively large four-chambered taxon that is similar to *S. euapertura* but differs from it by having a more compressed final chamber and a more restricted, lower aperture. Large and typical forms of *G. venezuelana,* which are consistently present throughout the lower Miocene and upper Oligocene, disappear below Core 199-1218A-15H from this site. It is of note that a number of the forms referred to *C. dissimilus ciperoensis* are extraordinarily large and inflated for the taxon.

The assemblages from Samples 199-1218A-16H-CC to 18H-4, 98–103 cm, are assigned to the P20/P21 zonal range. This interval is delineated at its base by the downhole first occurrence of *Turborotalia ampliapertura* in Sample 199-1218A-18H-4, 98–103 cm. The assemblages are less well preserved than in Subzone P21b and only occasionally contain *G. tapuriensis* and *G. tripartita*. The last downhole occurrence of five-chambered low trochospiral species, including *P. mayeri,* is present in Sample 199-1218A-17H-CC. *Globigerina angulisuturalis* was not found in the samples from Site 1218, and therefore, we are unable to differentiate Zone P20 from Subzone P21a.

Planktonic foraminiferal assemblages become increasingly dissolved and impoverished from Sample 199-1218A-19H, 98–103, through 23X-CC, coincident with the shift from the nannofossil ooze to chalk at the base of lithostratigraphic Unit II. Based on the occurrence of *Turborotalia ampliapertura* and a lack of characteristic Eocene forms, we assign this interval to the P18/P19 zonal range. The assemblages from this interval are composed of dissolution-resistant species, with *Catapsydrax dissimilis, G. suteri, Paragloborotalia nana, G. tripartita,* and *Tenutellinata angustiumbilicata* occurring most consistently. *Catapsydrax unicavus* is also present in Samples 199-1218A-18H-5, 98–100 cm, to 20H-2, 102–104 cm, but disappears below this. *S. euapertura,* which ranges from the top of Core 199-1218A-15H, has its last common downhole occurrence in Sample 199-1218A-19H-4, 100–105 cm. *Subbotina angioporoides* and *S. utilisindex* are also present in the middle part of Core 199-1218A-20H. We do not find *Pseudohastigerina micra,* the marker species for the base of the Oliogocene, in any of the samples from Site 1218 and are, therefore, unable to identify the lower boundary of Zone P19. Dissolution may be responsible for the absence of most foraminifers other than heavily encrusted species from the <150-µm fraction below Core 199-1218A-20H. Samples 199-1218A-22X-2, 28–32 cm; 22X-1, 40–45 cm; and 23X-CC contain a species that is very similar to, but slightly smaller than, *P. opima opima* (to which it has been referred) and not as small as co-existing *P. opima nana*. This is an unusually low occurrence for *P. opima opima* and suggests contamination of younger material downhole. However, the small size of these specimens indicates that they may represent an in situ but, as yet, unidentified species that is closely related to *P. opima opima* s.s.

The E/O boundary interval, which occurs in Core 199-1218A-24X and the subjacent core (25X) contains well-preserved benthic foraminifers but is barren of planktonic foraminifer species. Thus, we were unable to identify the end Eocene event, as denoted by the last occurrence of *Hantkenina* (Coccioni et al., 1988). The bottom four cores of Hole 1218A (199-1218A-26X through 29X) contain sparse and moderately well-preserved dissolution-resistant planktonic foraminifers of middle Eocene age. The assemblages are composed mainly of parasubbotinids, paragloborotalids, and the broken, yet distinctive, elongate chambers of various species of the genus *Clavigerinella*. Species include small and compact *Parasubbotina griffinae, Paragloborotalia nana,* a form comparable to "*H.*" cf. *bolivariana* (Toumarkine and Luterbacher, 1985; fig. 27, p. 126), *Clavigerinella jarvisi, C. eocanica, C. colombiana, C. akersi, Catapsydrax unicavus,* and *Muricoglobigerina senni*. Species of the genera *Morozovella* and *Globigerinatheka* are not present, which makes precise dating of these assemblages problematic. The occasional occurrence of *Acarinina bullbrooki, A. rohri, A.* cf. *collactea,* and *A. punctocarinata* indicate a middle Eocene age (probably equivalent to Zones P11 and P12) and a minimum age of 40.5 Ma (last occurrence datum of *A. bullbrooki*). Also present in these assemblages is a heavily calcified three-chambered form, here referred to as *Parasubbotina* cf. *linaperta*. As the name suggests, this species resembles *Subbotina linaperta* in general morphology but has a more prominent apertual lip and a wall texture that is more closely comparable to that of *Parasubbotina* or *Paragloborotalia.*

Similar assemblages containing unusually large numbers of parasubbotinids and clavigerinellids, commonly occurring with radiolarian-rich sediments, have been found at ODP Sites 959 and 960 (Ivory Coast), Kane 9-C piston core (Endeavour Seamount), and onshore sections in Ecuador, Peru, Colombia, and California. This restricted distribution pattern suggests that their presence may be linked to conditions of high productivity due to upwelling during the Eocene. The occurrence of *Clavigerinella* and *Parasubbotina* at Site 1218, which is believed to have been located within the equatorial productivity belt during the middle Eocene, further supports this view.

Benthic Foraminifers

Benthic foraminifers are present throughout the cored interval at Site 1218 (Table T7), except for core catcher Samples 199-1218A-24X-CC through 27X-CC and 1H-CC through 4H-CC, which are barren of benthic foraminifers. The assemblages examined are predominantly composed of well-preserved and diverse calcareous forms, and agglutinated foraminifers are rare and poorly preserved (Fig. F9).

T7. Distribution of benthic foraminifers, p. 98.

F9. Wall texture in benthic foraminifers, p. 50.

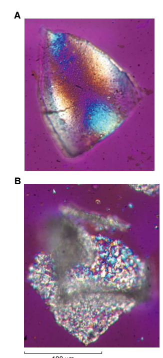

Benthic foraminifers such as *Siphonodosaria abyssorum, Oridorsalis umbonatus, Pullenia subcarinata,* and various forms of dentalinids/nodosarids are consistently present in all samples. These species are long ranging (Eocene–Holocene) and of little stratigraphic use. Species of the genera *Globocassidulina, Gyroidinoides,* and *Cibicidoides* are also common in most samples at this site. Species of the genus *Cibicidoides,* such as *C. havanensis, C. grimsdalei,* and *C. praemundulus,* also have long stratigraphic ranges and are present from the middle Eocene to the middle Miocene. They are indicators of lower bathyal and abyssal palaeoenvironments but are also commonly reported from abyssal paleodepths (van Morkhoven et al., 1986). These assemblages indicate lowermost bathyal and upper abyssal paleodepths at this site during the middle Miocene and Oligocene.

Nuttallides umbonifer is present but rare in middle Miocene–Oligocene sediments between Samples 199-1218A-16H-CC and 23X-CC and is sporadically present between 5H-CC and 15H-CC. This species is tolerant of low food supply and is adapted to waters that are undersaturated with respect to calcite (Nomura, 1995). *O. umbonatus* is present in all the samples where foraminifers are present. *C. praemundulus* is sporadically present between Samples 199-1218A-10H-CC and 30X-CC. *O. umbonatus* is considered to be adapted to sediments with low organic carbon (C_{org})content. *Cibicidoides mundulus,* which is the descendant of *C. praemundulus,* is also common in areas of low productivity or low C_{org} content (Nomura, 1995). This information suggests that little organic material was received at the seafloor in this deepwater setting. *Globocassidulina* spp. are very common in Sections 199-1218A-9H-CC to 12H-CC. Some of these taxa are similar to *Globocassidulina subglobosa,* which is sometimes reported as preferring environments with high C_{org} content. However, there are taxonomic problems associated with the identification of this species, so we do not utilize these taxa to interpret the depositional environment. In contrast, *Epistominella exigua* indicates the influence of high productivity at other times. This species, which is long ranging in most deep-sea sites, is restricted to Sections 199-1218A-8H-CC and 9H-CC.

Samples 199-1218A-24X-CC through 27X-CC contain very poorly preserved foraminiferal assemblages that are characterized by large specimens of *C. grimsdalei, C. eocaenus, Siphionodosaria abyssorum,* and *O. umbonatus*.

Nuttallides truempyi, which is commonly found in Samples 199-1218A-28X-CC and 29X-CC, is present in association with *Cibicidoides eocaenus, C. grimsdalei, C. praemundulus,* and *Anomalinoides spissiformis*. *N. truempyi* commonly disappears at the end of the middle Eocene (Berggren and Miller, 1989; Nomura, 1995); thus, Samples 199-1218A-28X-CC and 29X-CC can be assigned to the middle Eocene. The assemblage composition indicates lower bathyal to abyssal paleodepths.

In order to evaluate the preservation of foraminiferal test walls more thoroughly than is possible under reflected light, optical textures of a number of species were examined under transmitted light: *O. umbonatus* in Samples 199-1218A-10H-CC, 17H-CC, 22H-CC, and 28H-CC; *Globocassidulina* sp., *Gyrodinoides* sp., and *P. subcarinata* in Sample 199-1218A-10H-CC; and *Fursenkoina* sp., *Fissurina* sp., and *N. truempyi* in Sample 199-1218A-28X-CC. *Fissurina* sp. and *N. truempyi* show a well-defined radial texture (Fig. **F9A**) that indicates the original crystalline structure is preserved. Other species, which have a granular texture, also retain an original crystalline structure (Fig. **F9B**). These observations indicate that most of the benthic foraminifers at this site have suffered little or no postburial diagenetic alternation. The exceptions to this are Samples 199-1218A-24X-CC through 27X-CC and 29X-CC through 30X-CC, in which benthic foraminifers show signs of dissolution.

Radiolarians

Radiolarians were found in all recovered material. The stratigraphic distribution of radiolarian datums is shown in Table **T8.** The fauna in Samples 199-1218A-1H-1, 45–47 cm, to 1H-3, 46–48 cm, consists of moderately well preserved and relatively rare Pleistocene radiolarians belonging to Zone RN15. Sample 199-1218A-1H, 45–47 cm, contains a similar fauna belonging to Zone RN14. Sections 199-1218A-1H-5 through 2H-7 contain a mixed assemblage of sparse and poorly preserved Eocene–Miocene radiolarians, for which we were unable to assign an age. These mixed assemblages may be the result of slumping or unusual current activity. Sample 199-1218A-2H-CC is tentatively assigned to Zone RN10.

T8. Distribution of radiolarian datum levels, p. 100.

The quality and quantity of the radiolarian fauna improves somewhat in Sample 199-1218A-3H-4, 46–48 cm (Zone RN7), is variable throughout the late Miocene and late middle Miocene assemblages found in Cores 199-1218A-4H and 5H, and is generally common to abundant and well preserved in the rest of the downhole material. The boundary between Zones RN7 and RN6 lies between Samples 199-1218A-4H-3, 45–47 cm, and 4H-5, 45–47 cm. The latter sample contains an abundance of monospecific, D-shaped sagittal rings. The boundary between Zones RN6 and RN5 lies between Sample 199-1218A-4H, 45–47 cm, and Section 4H-CC, based on the absence of *Diartus petterssoni* in the latter sample. The boundary between Zones RN5 and RN4 lies between Samples 199-1218A-5H-4, 45-47 cm, and 5H-5, 45–47 cm. The first occurrence of *Calocyclotta costata* in Sample 199-1218A-6H-1, 45–47 cm, places the RN4/RN3 boundary between Samples 199-1218A-6H-

1, 45–47 cm, and 6H-2, 45–47 cm, whereas the first occurrence of *Stichocorys wolffii* places the RN3/RN2 zonal boundary between Samples 199-1218A-6H-7, 45–47 cm, and 6H-CC. The earliest Neogene zone (RN1) is found in Sample 199-1218A-7H-7, 46–48 cm, and continues through 9H-5, 74–75 cm.

The O/M boundary is approximated here by the range of calcareous nannofossil *S. delphix* between Subchrons C6Cn.3n and C6Cn.2n (Raffi, 1999) and the first occurrence of the planktonic foraminifer *P. kugleri* at the same level and lies within the upper part of radiolarian Zone RP22. This latest Paleogene radiolarian zone is found between Samples 199-1218A-9H-6, 74–75 cm, and 11H-3, 44–46 cm, and is marked by the presence of *Lychnocanoma elongata* and the absence of *Cyrtocapsella tetrapera*. For radiolarian biostratigraphy, the first occurrence of *C. tetrapera* serves as a good approximation to the O/M boundary (Sanfilippo and Nigrini, 1995).

Below Sample 199-1218A-11H-3, 44–46 cm, there is an expanded Oligocene comprised of only two zones (RP21 and RP20). The boundary between these zones, which is defined by the evolutionary transition from *Tristylospyris triceros* to *Dorcadospyris ateuchus,* is between Samples 199-1218A-18H-6, 46–48 cm, and 18H-CC. The section between 199-1218A-19H-CC and 23X-CC is also rich in diatoms.

The top of the next older radiolarian zone (RP19) is thought to approximate the E/O boundary and is present in Hole 1218A between Samples 199-1218A-23X-CC and 24X-1, 45–47 cm. The upper limit of this zone was further constrained using material from Hole 1218C and was found to lie between Section 199-1218A-23X-CC (238.58 mcd) and Sample 199-1218C-17X-4, 56–58 cm (238.96 mcd). The lithologic change from nannofossil chalk to radiolarite is placed at 241.98 mcd. Zone RP19 extends to Section 199-1218A-24X-CC. Upper Eocene Zone RP18 is represented in only one sample (199-1218A-25X-1, 24–26 cm). The rest of the hole is of middle Eocene age with Zone RP17 extending from Sample 199-1218A-25X-2, 82–24 cm, through 6X-1, 46–48 cm; Zone RP16 from 26X-2, 45–47 cm, through 27X-1, 45–47 cm; and Zone RP15 from 27X-2, 45–47 cm, through 28X-4, 46–48 cm, at least. Sections 199-1218A-28X-CC through 29X-3, 49–51 cm, belong to either Zone RP15 or RP14. Trace occurrences of radiolarians in the rest of Cores 199-1218A-29X and 30X contain no age diagnostic species.

A limited number of samples were taken from Holes 1218B and 1218C in order to further constrain some first and last occurrences of species and zonal boundaries (Table **T8**).

PALEOMAGNETISM

A total of 49 cores from Holes 1218A, 1218B, and 1218C were measured with the shipboard pass-through cryogenic magnetometer. The NRM was measured at 5-cm intervals in each core section, followed by three to four steps of AF demagnetization up to a maximum peak field of 20 mT. XCB cores were not measured because they are made up of short "biscuits," typically <7 cm long, and the information obtained from a given core would not contribute any interpretable directional data. On the other hand, individual biscuits can be measured and oriented using the direction of the modern-day field overprint. This procedure seemed to work for Core 199-1218A-24X. In addition to core measurements, ~100 discrete samples were taken from Hole 1218A cores to carry out more detailed progressive demagnetization. Only a few core sections from Site 1218 were in poor condition, mostly because of drilling disturbance, and, therefore, were not used for paleomagnetic study.

NRM magnetization intensities were in the order of 10^{-2} to 10^{-1} A/m and decreased to ~10^{-3} to 10^{-2} A/m after partial AF demagnetization (Fig. **F10**). These values, typical of the sediments found during this leg, are well above the magnetometer's noise level even in the most weakly magnetized carbonate units. A large group of NRM inclinations showed steep downward directions (~70°), which are indicative of a drilling-induced overprint. This overprint was mostly removed with AF demagnetization, typically disappearing at 10 to 15 mT. Some magnetic directions did not reach a stable point between 5 and 20 mT, suggesting that the characteristic remanent magnetization (ChRM) has not been fully isolated.

F10. Magnetization intensities after AF demagnetization, p. 51.

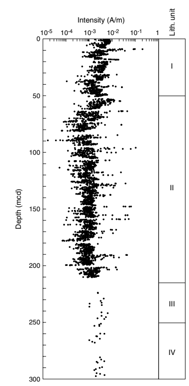

Orientation

The Tensor tool was used to orient Hole 1218A APC cores starting with Core 199-1218A-3H. The Tensor tool provided a good first-order orientation for most of the cores. Although pass-through measurements were not done on XCB cores, some discrete samples were taken from individual biscuits in Cores 199-1218A-22X through 30X because the E/O boundary was thought to occur within Cores 199-1218A-23X to 24X. To orient the samples taken from XCB cores, we assume that a soft magnetic component directed toward present-day magnetic north is still recognizable in the samples and is only partially masked by the drilling-induced overprint. This component of the magnetization vector can possibly be recognized after a detailed demagnetization. We applied this procedure on all measured samples from XCB cores with various degrees of success. Also, a few APC cores produced abnormal directions after correction for the Tensor tool data (e.g., east-west–trending declinations). In these cases, we also used the overprint direction to help determine the orientation of the cores. In all cases, results were cross-checked among Holes 1218A, 1218B, and 1218C to produce consistent results.

Discrete Sample Analysis

About 100 oriented discrete samples (8-cm^3 plastic cubes) were collected from Hole 1218A, and 55 of them were AF demagnetized. These samples were used to determine the stability of the remanent magnetization and compute a more faithful ChRM direction. We divided the samples into two sets based on their age (Fig. **F11**). The average Fisher mean inclination for the Miocene set of samples is 10.4° (with the 95% confidence interval α_{95} = 12°), corresponding to a paleolatitude of 5.2°N (error margin = 2.2°/8.4°), whereas the Oligocene set has an average inclination of 3.8° (α_{95} = 6.2°), which indicates a paleolatitude indistinguishable from the paleoequator. Although the confidence cones of the two means overlap, the increase in inclination from the Oligocene to the Miocene is consistent with the expected plate motion. The overall mean inclination for the discrete samples (6°; α_{95} = 5.9°) is significantly shallower than the mean inclination (11.7°) obtained from blanket demagnetization in the best sections of the archive halves. Apparently, either the ChRM of the archive halves is not fully isolated or the sediment's magnetization is disturbed near core edges by the coring

F11. Age-based ChRM directions of discrete samples, p. 52.

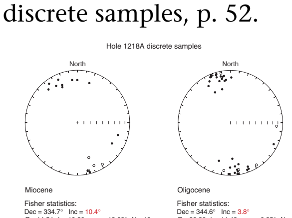

procedure. Both these hypotheses can be addressed by shore-based studies.

Magnetic Polarity Stratigraphy

Except for a very few sections that had to be discarded because of excessive drilling disturbance, Site 1218 provided an excellent record of geomagnetic reversals, which are readily interpreted as magnetozones (Table T9). Overall, the composite magnetic stratigraphy of the oriented cores from Site 1218 spans the interval from the Pleistocene (Chron 1n) to the early Oligocene (Chron 12r; 33.5 Ma). The upper 18 m of Hole 1218A was interpreted by using changes in declination after inspecting the orientation of the soft-component overprint (Fig. F12A). ChRM inclinations are very shallow as expected in these latitudes, and a few cores that were given a reversal test gave a particularly good set of ChRMs, which suggests that they represent a relatively clean record of the geomagnetic field directions. The magnetostratigraphy of Site 1218, shown in Figure F12, results from a composite of the virtual geomagnetic pole latitudes of Holes 1218A, 1218B, and 1218C that were spliced using MST data (see **"Composite Depths,"** p. 21). The polarity reversals from Holes 1218A, 1218B, and 1218C match remarkably well with a few exceptions. In Core 199-1218C-6H, from 108 to 115 mcd (Fig. F12C), Subchron C7n.2n is shorter than that in Holes 1218A and 1218B, and Chron C7An is shifted upcore, suggesting a hiatus in sedimentation or uncertainty in the composite-depth column. We also notice that in Core 199-1218C-6H, from 123 to 126 mcd (Fig. F12C), the magnetic polarity does not agree with that of Holes 1218A and 1218B. As before, possible explanations include partial magnetic cleaning of the samples, uncertainty in the composite-depth column and possible compression of the core relative to other cores (see **"Composite Depths,"** p. 21). It is worthwhile to point out that the directions used for the magnetostratigraphy are based on blanket demagnetization only, and consequently, it is possible that secondary components have not been completely eliminated. The short normal-polarity interval in Hole 1218C at ~175 mcd is attributable to machine error probably caused by a flux-jump during the last demagnetization step. The 20-mT demagnetization step was repeated in Section 199-1218C-11H-2 and updated in the Janus database.

In the magnetostratigraphy working upsection, we identify Chron C12 (early Oligocene) only in Hole 1218A at ~201 to 203.7 mcd. The three records from Holes 1218A, 1218B, and 1218C start overlapping in Chron 11n, which displays both Subchrons C11n.1n and C11n.2n. All subsequent geomagnetic reversals up to the mid-Pliocene (Chron C2Ar) have been successfully identified. The magnetic stratigraphy of Site 1218 is, therefore, virtually complete and offers a highly detailed history of geomagnetic reversals during the last 30 m.y.

T9. Composite depths of geomagnetic reversals, p. 101.

F12. Composite magnetic stratigraphy, p. 53.

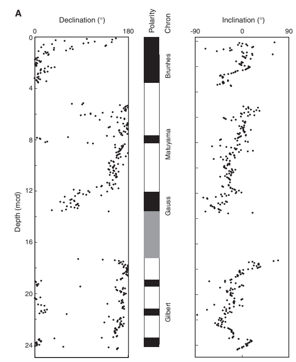

COMPOSITE DEPTHS

In contrast to other Leg 199 sites, the recovered sediment was only mildly affected by drilling disturbances. Under these circumstances and in the presence of high signal-to-noise ratio data sets, it was possible to direct drilling in Holes 1218B and 1218C in real time to complete the construction of the composite sediment section. MST and color reflectance data collected from cores from Holes 1218A, 1218B, and 1218C were used to construct a continuous sequence down to ~263 mbsf (~287 mcd). Hole 1218A was extended to basement at ~274 mbsf, but the two lowermost cores (Cores 199-1218A-29X and 30X) could not be bridged with data from Hole 1218B or Hole 1218C. Disturbed intervals, as determined by visual inspection of split cores, are listed in Table **T10.** Data from these intervals were removed prior to further correlation work. Table **T11** lists the offsets that were applied to cores from each hole to create a composite depth record. This allowed the construction of a spliced record designed for sampling purposes as listed in Table **T12.**

T10. Core disturbance intervals, p. 102.

T11. Composite depth offsets, p. 103.

T12. Splice tie points, p. 104.

On cores from Hole 1218A, MS, *P*-wave velocity, and color reflectance data were collected at 2-cm intervals and GRA bulk density at 4-cm intervals down to Core 199-1218A-22X, below which GRA bulk density data were acquired at 2-cm intervals. GRA bulk density data showed a strong and characteristic signal. Because of time constraints, it was desirable to obtain GRA bulk density data at a higher resolution (2-cm intervals) at the expense of *P*-wave velocity measurements. In addition, the *P*-wave whole-core logger does not operate properly in XCB-cored intervals because the core does not make full contact with the core liner. For these reasons, *P*-wave velocity data were not collected below Core 199-1218A-22X and then only from selected intervals from Holes 1218B and 1218C. GRA bulk density data were collected at 2-cm intervals throughout Holes 1218B and 1218C. Readings from the natural gamma ray (NGR) instrument showed only background radiation levels below ~5 mbsf. This component from the MST assemblage was only run on Hole 1218A cores. Color reflectance data were collected at 2-cm intervals on all cores.

The interval from the seafloor to ~55 mbsf was cored only in Holes 1218A and 1218B. However, a 3- to 4-m coring offset between the two holes provided complete coverage of gaps between cores. This upper section consists of clay (see **"Lithostratigraphy,"** p. 7) and has a very characteristic MS signal, whereas the GRA density data are rather featureless. The MS data allow a very clear correlation between holes in this upper interval as illustrated in Figure **F14.** The stratigraphic correlation in deeper intervals is supported by a strong signal in the GRA bulk density data that arises from varying proportions of $CaCO_3$, silica, and clay end-members. GRA bulk density (Fig. **F13**) and MS (Fig. **F14**) data made the interhole correlation straightforward down to a depth of ~155 mbsf (~174 mcd), above which there is only very little stretching or squeezing observed between features that can be seen in more than one hole. An exception to this general situation is evident in Core 199-1218C-6H where, alignment of this core with equivalent sections in the other holes suggests that the core is compressed. This core disturbance is supported by the apparent misalignment of paleomagnetic reversal datums between the holes over this interval (see **"Paleomagnetism,"** p. 19). The disappearance and reappearance of two biostratigraphic datums (see **"Biostratigraphy,"** p. 10) across Cores 199-1218A-7H and 8H indicates an additional interval with lithological disturbance that is not apparent from the MST data.

F13. GRA bulk density data vs. composite depth, p. 56.

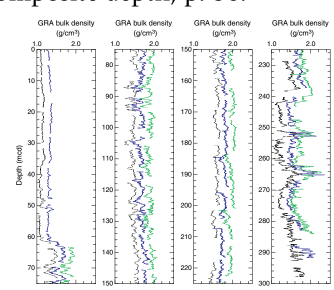

F14. Magnetic susceptibility data plotted vs. composite depth, p. 57.

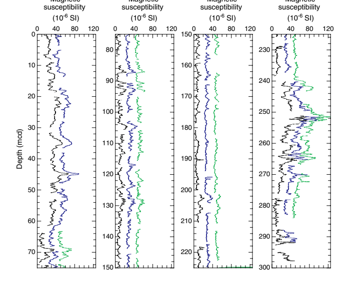

Below Core 199-1218B-21X (~220 mcd), cores from Holes 1218A and 1218B did not overlap sufficiently to cover gaps between cores. Thus, coring of Hole 1218C was designed to cover the missing intervals as well as provide additional material for high-resolution studies. The coring effort in Hole 1218C was successful at covering gaps between cores in Holes 1218A and 1218B to a depth of ~262 mbsf (287 mcd). In contrast to the overlying interval, the XCB-cored lower part of Site 1218 (below 210 mcd) shows medium to strong differential stretching and squeezing between features that are clearly recognizable in different holes. Thus, it is not always possible to align all apparently correlative features in one hole with those in other holes in the basal interval of the site.

Following construction of the composite depth section for Site 1218, a single spliced record was assembled for the aligned cores down to 263 mbsf (~287 mcd) by using cores from Holes 1218A as the "backbone" and patching across core gaps primarily with cores from Hole 1218B (Table T12). Intervals having significant disturbance or distortion (see Table T10) were avoided. The Site 1218 splice can be used as a sampling guide to recover a single sedimentary sequence between 0 and 287 mcd, although it is advisable to overlap a few decimeters from different holes when sampling in order to accommodate anticipated ongoing development of the depth scale. Stretching and compression of sedimentary features in aligned cores indicates distortion of the cored sequence. Because much of the distortion occurs within individual cores on depth scales of <9 m, it was not possible to align every feature in the MST and color reflectance records. However, at crossover points along the splice (Table T12) care was taken to align highly identifiable features from cores in each hole.

F15. Spliced records of GRA bulk density and MS, p. 58.

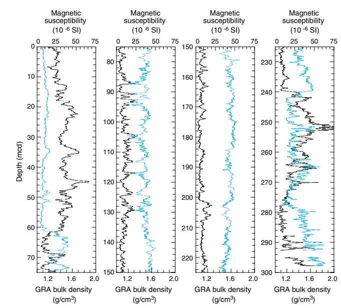

Intervals that are dominated by varying $CaCO_3$ content show a clear cyclical signal as well as an anticorrelation between MS and GRA bulk density. The lithology-dependent correlation or anticorrelation of MS and GRA bulk density measurements is illustrated in Figure F15. Of particular interest is the transition from carbonate-poor to carbonate-rich sediments, evident as a two-step increase in GRA bulk density and decrease in MS values from 243 to 239 mcd. Based upon biostratigraphic information (see **"Biostratigraphy,"** p. 10), this transition occurs across or just above the Eocene–Oligocene transition. In Figure F16, the spliced records of MS, GRA bulk density, and the color reflectance at Site 1218 show that this transition was preceded by an interval with large variations in MS and bulk density that correspond to five closely spaced thin chert layers between 253 and 251 mcd (the top of Cores 199-1218A-25X and 199-1218B-25X and the middle of Core 199-1218C-18X) (see **"Lithostratigraphy,"** p. 7).

F16. Spliced records of GRA bulk density, magnetic susceptibility, and color reflectance parameter, p. 59.

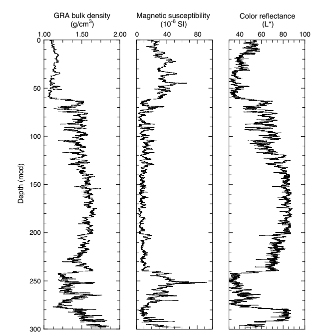

Overall, the composite depth record from Site 1218 is expanded in length compared to the mbsf depth scale by ~11%. However, in detail, the expansion of the composite depth record relative to the mbsf depth measurement varies with depth as illustrated by Figure F17. Down to a depth of ~120 mbsf in Core 199-1218A-13H (~135 mcd), the relative expansion is ~14%, whereas the cores below generally only require an adjustment of ~9% with respect to their mbsf depth. This decrease in core expansion, which coincides with a change of character in the MS and GRA bulk density records, reflects a lithologic change to a stiffer, more chalklike nannofossil ooze.

F17. Offsets applied to each core vs. depth, p. 60.

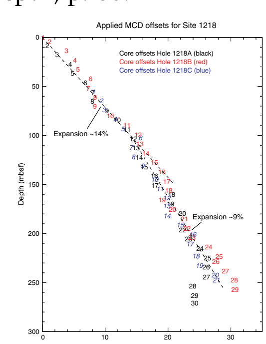

SEDIMENTATION AND ACCUMULATION RATES

Average LSRs at Site 1218 are based on all the principal biostratigraphies plus a good set of paleomagnetic reversals defined in Holes 1218A, 1218B, and 1218C (Tables T13, T14). Only radiolarians are present in the uppermost part of the section. From the lower middle Miocene through the lower Oligocene, all three fossil groups were use-

T13. Paleomagnetic events, p. 105.

T14. Nannofossil, foraminifer, and radiolarian events, p. 106.

ful in establishing age control. In most of the Eocene, both radiolarians and nannofossils were present (Fig. **F18**).

Lithologic Unit I (see **"Lithostratigraphy,"** p. 7) contains two well-constrained radiolarian datums in Core 199-1218A-1H. This is in marked contrast to piston core EW9709-7P (~15 m long) taken during the site survey cruise and located only a few miles from Site 1218. Most of the sediment contained in this piston core is a nonfossiliferous pelagic "red" clay, but the bottom 3 m contains a middle Miocene radiolarian fauna, and a few nannofossils are preserved in the lower 1–2 m. However, the EW9709-7P piston-cored sequence can be correlated to the upper 67 m of the Site 1218 composite section using the MST GRA density records (Fig. **F19**). This comparison shows that core EW9709-7P has a sedimentation rate of ~0.87 m/m.y. through most of its length, a rate that is about four times lower than sediments accumulating in lithologic Unit I at Site 1218.

The paleomagnetic reversal data, based primarily on declination data in oriented APC cores (see **"Paleomagnetism,"** p. 19) (Fig. **F12**), show a suite of over 70 reversal boundaries that can be used for detailed sedimentation rate determinations from ~20 to 200 mcd (Table **T13**). These data seem to indicate an interval of extremely rapid deposition, bounded by short intervals of slow deposition at ~6.6 Ma and 28 mcd (Core 199-1218A-3H). The report on radiolarians (see **"Biostratigraphy,"** p. 10) notes that Cores 199-1218A-2H and 3H contain poorly preserved specimens representing a great variety of Neogene and Paleogene ages. In combination with the paleomagnetic data, this observation suggests that sediments in Cores 2H and 3H represent a rapid depositional event, perhaps associated with a slump (Fig. **F18**).

The LSRs noted in Figure **F18** are based on radiolarian events down to the top of reliable magnetic data at ~20 mcd. Below that point to ~200 mcd, the sedimentation rates are derived from linear fits to the paleomagnetic data. From the base of the Oligocene near 200 mcd to the bottom of the drilled section, sedimentation rates are based on nannofossil events. Average sedimentation rates are 3–4 m/m.y. through most of the Neogene, with the exception of the slumped interval. Average sedimentation rates reach a maximum of >18 m/m.y. during the middle part of the Oligocene. Rates in the Eocene appear to be more variable, ranging from >4 to ~11 m/m.y. The rates are generally higher in the higher carbonate intervals.

LSR values may be combined with the dry bulk density (DBD) data from porosity measurements on individual samples, averaged over the intervals reported (see **"Physical Properties,"** p. 27) (Table **T19**) to determine the bulk mass accumulation rates (MARs) of the sediments (Table **T15**). Sediment with an LSR of 1.0 cm/k.y. and a DBD of 1.0 g/cm^3 will have an MAR value of 1.0 g/cm^2/k.y. The observed values are rarely this high, so we report the data in milligrams per square centimeter per thousand years (mg/cm^2/k.y.).

At Site 1218, which has a more extensive paleomagnetic and biostratigraphic datum record than other Leg 199 sites, we have determined MAR values at each horizon where there is a value for DBD (see **"Physical Properties,"** p. 27) (Table **T19**). This permits a quantification of the bulk-sediment MARs for the entire 42-Ma record (Fig. **F20**). Flux values are low in lithologic Unit I, generally <150 mg/cm^2/k.y. Lithologic Unit II, dominated by calcareous material, accumulated at 700–2000 mg/cm^2/k.y., with the maximum flux rates in the very light brown to white nannofossil ooze of early Oligocene age. Lithologic Unit III, dominated by radiolarian ooze and radiolarite, has much lower MARs

F18. LSRs and chronostratigraphic markers, p. 61.

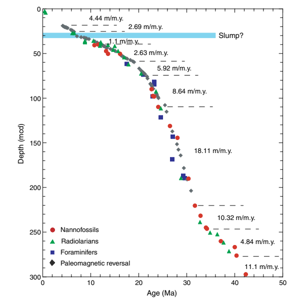

F19. GRA bulk density records, p. 62.

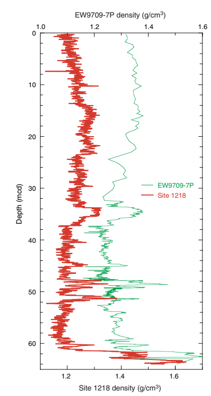

T15. Depths, ages, rates, and fluxes of sediments, p. 107.

F20. MARs of sediments, p. 63.

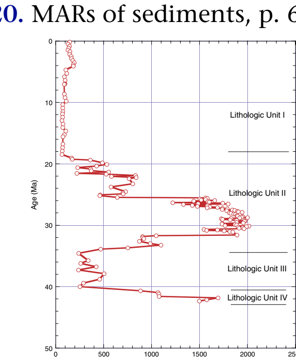

of ~300 mg/cm²/k.y. The basal chalk of Unit IV accumulates at rates similar to the carbonates of Unit II.

GEOCHEMISTRY

Interstitial Water Geochemistry

We collected interstitial waters from 14 samples from Hole 1218A at depths ranging from 5.95 to 273.65 mbsf (Table T16; Fig. F21). Chemical gradients in the interstitial waters from Site 1218 reflect the dissolution of biogenic opal, the limited amount of organic matter diagenesis, and possibly the diffusive influence of reactions in the underlying basalt.

T16. Interstitial water data, p. 110.

F21. Interstitial water data, p. 64.

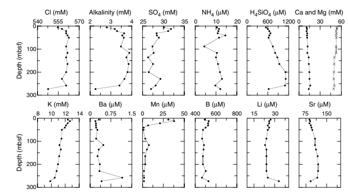

Chlorinity, as measured by titration, increases with depth from values of ~555 mM at 5.95 mbsf to values of ~560 mM at 22.15 mbsf and remains nearly constant until 200.35 mbsf. Chlorinity generally decreases between 200.35 and 273.65 mbsf to a minimum value of ~548 mM. Sodium concentrations, as determined by charge balance (on average 1% lower than those measured by ion chromatograph), increase from ~476 to ~487 mM between 5.95 and 22.15 mbsf and then generally decrease to values of ~468 mM at 273.65 mbsf. Salinity, as measured by a handheld refractometer, does not vary much downhole; most interstitial waters were measured as 35.0.

Alkalinity variations of the pore waters follow those of chlorinity. Alkalinity increases downhole from 2.8 mM at 5.95 mbsf to 3.9 mM at 164.65 mbsf. Alkalinity decreases downhole between 164.65 and 273.65 mbsf to values of ~2.26 mM. pH generally decreases downhole from 7.27 at 5.95 mbsf to 7.15 at 88.65 mbsf, remains relatively low until 229.15 mbsf, and then increases to 7.32 at 273.65 mbsf. Dissolved silica concentrations increase with depth, from values of ~548 µM at 5.95 mbsf to values of ~1116 µM at 229.15 mbsf, followed by an abrupt decrease to 626 µM at 273.65 mbsf. The increase in interstitial water silica concentration with depth probably reflects the dissolution of biogenic silica and subsequent diffusion.

Interstitial water sulfate concentrations remain at or above seawater concentration (28 mM) throughout most of the hole, which indicates that the amount of labile organic matter available for oxidation is low. The lowest sulfate values (26.3 mM), which are lower than at any of the previous sites (Sites 1215–1217), are reached at ~136.15 mbsf. Ammonium is present at extremely low levels (<13 µM) at Site 1218 interstitial pore waters, which is consistent with high sulfate values.

Dissolved manganese concentrations found at Site 1218 decrease from ~30 to ~1.5 µM between 5.95 and 41.15 mbsf. Manganese concentrations remain low (<10 µM) from 41.15 mbsf to basement. Lithium concentrations in the interstitial waters decrease from seawater values (~27 µM) to ~24 µM between 5.95 and 88.65 mbsf and remain constant downhole until increasing to a maximum of ~33 µM near basement (273.65 mbsf). Strontium concentrations in the interstitial waters at Site 1218 increase from ~88 to 119 µM between 5.95 and 229.15 mbsf and subsequently decrease to ~92 µM at 273.65 mbsf.

Calcium concentrations in the pore waters at Site 1218 are similar to seawater concentrations (~10 mM) from the top of the hole to ~165 mbsf. Between ~200 and 260 mbsf, Ca values increase to an average of 15 mM, then decrease to 13 mM at 273 mbsf. Magnesium concentrations decrease with depth and are lower than seawater values from 5.95

to 273.65 mbsf. The trends of slightly decreasing magnesium and slightly increasing calcium with depth are the first observed during Leg 199 and may reflect alteration of basalt and subsequent diffusion. Nevertheless, pore water gradients in magnesium and calcium are modest. Potassium concentrations decrease in a near-linear fashion downhole from values of ~12 mM at 5.95 mbsf to values of ~10 mM at 273.65 mbsf. Dissolved barium concentrations are low (~<1 µM) throughout the sediment column from Site 1218. Boron concentrations range from 466 to 531 µM.

In summary, the pore water profiles at Site 1218 are influenced by the dissolution of biogenic silica, the lack of organic matter diagenesis, and possibly the alteration of underlying basalt and subsequent diffusion.

Solid-Phase Geochemistry

At Site 1218, we collected bulk-sediment samples adjacent to the intervals sampled for physical properties (see **"Physical Properties,"** p. 27), resulting in a sampling resolution of approximately one per section from 0.74 to 273.75 mbsf at Hole 1218A (Table **T17;** Fig. **F22**). We measured silicon (Si), aluminum (Al), titanium (Ti), iron (Fe), manganese (Mn), calcium (Ca), magnesium (Mg), phosphorus (P), strontium (Sr), and barium (Ba) concentrations in the sediment by inductively coupled plasma–atomic emission spectroscopy (ICP-AES). Bulk-sediment geochemistry primarily reflects the changing lithology of the sediments downhole from red clay (Unit I) to nannofossil ooze and chalk (Unit II) to radiolarian ooze (Unit III) to nannofossil chalk with dolomite (Unit IV) (Fig. **F22**).

T17. Bulk-sediment data, p. 111.

F22. Bulk-sediment data, p. 65.

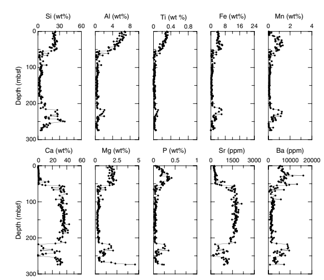

Silicon varies between 1 and 30 wt% at Site 1218, which primarily reflects sediment lithology. Silicon concentrations are ~20 wt% in Unit I, 1–3 wt% in Unit II, and ~30 wt% in Unit III. Silicon concentrations decrease through Unit IV, reaching ~4 wt% near basement.

Aluminum and titanium concentrations are highest in the clay and siliceous sediments (Units I and III) and lowest in the carbonate sediments (Units II and IV). Aluminum concentrations decrease downhole from ~7 to ~0.5 wt% between 0.74 and 213.23 mbsf and then increase to almost 2 wt% at 218.03 mbsf. Farther downhole, aluminum concentrations decrease to 0.61 wt% at 274.23 mbsf. Titanium content decreases from ~0.3 to 0.2 wt% within Unit I, is very low (<0.10 wt%) throughout the carbonate sediments (Units II and IV), and is ~1.1 wt% in Unit III.

Al/Ti ratios vary between 12.5 and 34.0 in the silica-rich units (I and III). Si/Ti and Ba/Ti ratios are higher in Unit III than in Unit I, possibly reflecting the increased biogenic component of the silicon of Unit III relative to Unit I.

Iron and manganese contents show similar trends to aluminum and titanium, with maximum values in Units I and III and values near 1 wt% in Unit III (Fig. **F22**). Iron varies between 3 and 6 wt% in Units I and III and between 0.18 and 1.15 wt% in Units II and IV. Manganese concentrations are ~0.2 wt% in Unit II and reach ~1.5 wt% within Units I and III.

Calcium and strontium concentrations are highest in the carbonate-rich lithologies. Calcium concentrations vary between 0.38 wt% at 0.74 mbsf (Unit I) and 43 wt% at 162.44 mbsf (Unit II). However, this value of 43 wt% is too high to be real, as a result of causes discussed in **"Geochemistry,"** p. 20, in the "Explanatory Notes" chapter. Similarly, strontium concentrations are lowest (~250 ppm) in the siliceous-rich lithologies (Units I and III) and highest (~2000 ppm) in the carbonate-rich lithologies (Units II and IV). Magnesium varies between 1.4 and 2.2 wt% in the red-clay and radiolarite units and between 0.2 and 0.5 wt% in the carbonate-rich sediments. Magnesium concentrations increase to ~5 wt% near the base of the hole (~273 mbsf), which is consistent with the presence of dolomite in Unit IV.

Phosphorus concentrations are low (generally <0.5 wt% in siliceous and clay sediments and <0.2 wt% in carbonate sediments). Barium concentrations in Site 1218 sediments are higher than at previous sites. Barium concentrations are highest in the red-clay and radiolarite sediments, varying between 4,500 and 10,000 ppm with isolated peak values in Unit I reaching 15,000 ppm. Barium concentrations are lower (between 400 and 2000 ppm) throughout the nannofossil ooze and chalk and nannofossil chalk with dolomite (Units II and IV). The Ba/Ti ratio of Unit II is intermediate between that of Units I and III (see Fig. **F19,** p. 70, in the "Leg 199 Summary" chapter).

$CaCO_3$ (in weight percent) was determined by coulometric methods for approximately three samples per core from 0.74 to 274.23 mbsf in Hole 1218A (Table **T18;** Fig. **F23**). $CaCO_3$ is low (≤1 wt%) for the clay interval (Unit 1), high (~60–90 wt%) in the nannofossil ooze and chalk (Unit II), varies widely (<1–60 wt%) in the radiolarite (Unit III), and high (up to 83 wt%) in the nannofossil chalk and dolomite (Unit IV). $CaCO_3$ values calculated from Ca ICP-AES data (in weight percent) yielded similar trends to $CaCO_3$ measured via coulometer. However, $CaCO_3$ (wt%) values calculated from ICP-AES data are overestimated at high values because of analytical problems (see **"Geochemistry,"** p. 20, in the "Explanatory Notes" chapter). C_{org} (in weight percent) determined for one sample per core is uniformly low (0–0.30 wt%) for the samples measured.

T18. $CaCO_3$ and C_{org} data, p. 114.

F23. $CaCO_3$ and Ca data, p. 66.

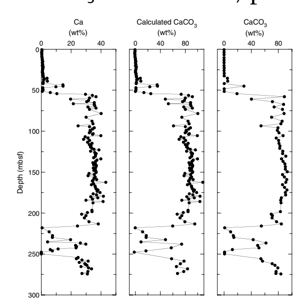

In summary, the bulk geochemistry of the sediments from Site 1218 reflects the varying lithology of the sediments between red clay, nannofossil ooze and chalk, radiolarite, and nannofossil chalk with dolomite.

PHYSICAL PROPERTIES

Physical properties at Site 1218 were measured on whole cores, split cores, and discrete samples. MST (bulk density, MS, *P*-wave velocity, and natural gamma radiation) and thermal conductivity comprised the whole-core measurements. Compressional wave velocity measurements on split cores and moisture and density (MAD) analyses on discrete core samples were made at a frequency of one per undisturbed section in Cores 199-1218A-1H through 22X and in every other section in Cores 23X through 30X. Light absorption spectroscopy (LAS) analyses were performed on the MAD samples as well as an additional one sample per section (located ~50 cm from the MAD sample). Six in situ temperature measurements were obtained using the Adara tool in Holes 1218B and 1218C.

Density and Porosity

Two methods were used to evaluate the wet bulk density at Site 1218. GRA provided an estimate from whole cores. MAD samples gave a second, independent measure of wet bulk density, along with providing

DBD, grain density, water content, and porosity from discrete samples (Table T19). The MAD and GRA bulk density measures display the same trends, but the extent of the agreement between data sets differs between APC cores and XCB cores. In APC cores, the wet bulk density is offset by values up to 0.10 g/cm³ higher than the GRA bulk density (Fig. F24). This offset is most consistent in lithologic Unit I (0–52.10 mbsf), and results from the difference between the assumed GRA coefficient used in data processing and the attenuation coefficient of the radiolarian-rich sediments. Variation in core diameter and homogenized intervals between drilling biscuits both contribute to the difference between the MAD and GRA densities in the XCB-drilled section. Crossplots of wet bulk density and DBD vs. interpolated GRA density (Fig. F25) show excellent correlation between the MAD and GRA data for sediments recovered with the APC and more variable and underestimated GRA density for XCB cores.

Wet bulk density is ~1.20 g/cm³ at the seafloor in Hole 1218A and increases to an average of 1.25 g/cm³ in a broad maximum between 14 and 31 mbsf. From 31 mbsf to the bottom of lithologic Unit I at 52.10 mbsf, wet bulk density decreases to 1.18 g/cm³. The boundary between the radiolarian clay of Unit I and the nannofossil ooze of Unit II is marked by a sharp increase in density to 1.59 g/cm³ at 57.95 mbsf. Wet bulk density is highly variable in the upper part of Unit II (52.1–112.50 mbsf in Hole 1218A), with values ranging from 1.19 to 1.64 g/cm³ and averaging 1.49 g/cm³. The variation in density follows the alternating lithology. Dark colored clayey radiolarian nannofossil ooze is less dense than the lighter colored nannofossil ooze. Between 112.50 and 187.45 mbsf in Unit II, the range in wet bulk density is narrower (1.48–1.72 g/cm³), and the average density is higher than sediments above (1.64 g/cm³). The pattern of lower-density dark colored sediments and higher-density light colored sediments continues in Unit II. A prominent bulk density minimum of 1.62 g/cm³ is present at 152.99 mbsf. From 196.76 mbsf to the base of Unit II at 216.90 mbsf, variability in bulk density increases, and the average density is lower (1.59 g/cm³). The greater abundance of diatoms, radiolarians, and clay in the radiolarite of Unit III (216.90–267.44 mbsf) is reflected by wet bulk density that is lower and more variable than the density in the lower part of Unit II. Average wet bulk density for Unit III is 1.42 g/cm³, and the range is from 1.28 to 1.66 g/cm³. Unit IV is marked by an overall increase in density with depth. Wet bulk density ranges from 1.48 to 1.61 g/cm³ in Subunit IVA (250.2–267.4 mbsf) and from 1.88 to 1.97 g/cm³ in Subunit IVB (267.4–274.3 mbsf).

Variation in grain density (ρ_s) in Hole 1218A generally matches changes in lithology. Grain density averages 2.60 g/cm³ in the uppermost 5 m in Hole 1218A. Below 5 mbsf, it decreases and becomes more variable (Fig. F24), coinciding with the LAS-indicated decrease in illite (ρ_s = 2.66 g/cm³) and increase in smectite (ρ_s = 2.2–2.6 g/cm³) in the red clays. Along with the change in clay mineralogy, the changes in the mixture of radiolarians (opal; ρ_s = 2.2 g/cm³), zeolites (ρ_s = 2.2 g/cm³), and nannofossils (calcite; ρ_s = 2.7 g/cm³) contribute to the large range in grain density (2.17–2.82 g/cm³) in Unit I. The average density for Unit I is 2.58 g/cm³. Grain density averages 2.69 g/cm³ between 52.10 and 112.50 mbsf in lithologic Unit II. Densities range from 2.59 to 2.80 g/cm³, with lower values generally associated with the darker colored, more clay-rich sediments. Between 112.50 and 187.50 mbsf, grain densities are tightly grouped about an average of 2.72 g/cm³. Within this

T19. Moisture and density measurements, p. 116.

F24. MAD measurements, p. 67.

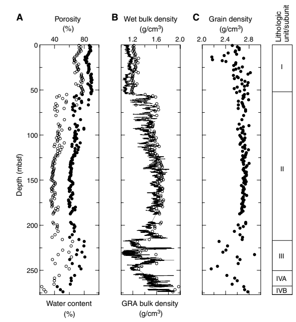

F25. Wet and dry bulk density plotted with GRA density, p. 68.

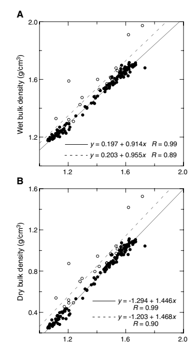

interval, there is a slight decrease in grain density from ~2.73 g/cm^3 at 150 mbsf to 2.64 g/cm^3 at 187.45 mbsf, which coincides with a decrease in the $CaCO_3$ content (see **"Geochemistry,"** p. 25). Below 187.50 mbsf, the variability of grain density in Unit II increases, but the average decreases to 2.67 g/cm^3. Unit III is characterized by highly variable grain density as a result of increasing abundances of radiolarians and diatoms. Grain density ranges from 2.15 to 2.89 g/cm^3 and averages 2.46 g/cm^3 in this unit. A peak in iron and manganese concentrations within this interval (see **"Geochemistry,"** p. 25) coincides with the high grain density. In Unit IV, grain density increases more or less continuously from 2.42 g/cm^3 at 255.62 mbsf to 2.78 g/cm^3 at 273.75, reflecting an increase in calcite and dolomite in the sediments.

Porosity and water content vary inversely with wet bulk density (Fig. **F24**). Features prominent in the bulk density profile, including the sharp change at the boundary between Units I and II, the higher variability in the upper part of Unit II and Unit III, and the prominent maxima (density minima) at 153 mbsf, are also present in the porosity profile. The highest porosity (90.7%) is present in the radiolarian clay of Unit I at 38.95 mbsf. The lowest porosity (43.7%) is present at 268.08 mbsf in the dolomitic nannofossil chalk (Subunit IVB) (see **"Subunit IVB,"** p. 9, in "Lithostratigraphy").

LAS

LAS studies were conducted on cores from Hole 1218A at a frequency of two samples per section (see **Vanden Berg and Jarrard,** this volume, for a discussion of the LAS technique). Semiquantitative mineral concentrations were calculated from the collected spectra, assuming a four-component system: calcite, opal, smectite, and illite (Table **T20**). LAS analyses do not display the major lithologic boundaries as well as at previous sites (Fig. **F26**). The light color of the clays in Units I and III may have caused an overestimation in calcite.

Lithologic Unit I shows high clay contents and a gradual increase in calcite downcore. Also, the illite–smectite transition is clearly seen in the upper 10 m of the hole. Illite concentrations between 20 and 50 mbsf are higher than expected. These higher than expected values may reflect an increase in metal oxides that darken the color of the sediment. The carbonate-rich lithologic Unit II shows an expected increase in calcite values to ~90% as well as a corresponding drop in clay content. The clay that is present is mainly smectite. The top of Unit III marks the E/O boundary with a decrease in calcite and an increase in clay. Nannofossils are still abundant in Unit III resulting in the high calcite values in this region. Unit IV is another nannofossil chalk and again contains higher calcite values (~60%).

Compressional Wave Velocity

Compressional wave velocity was measured by the *P*-wave logger (PWL) on APC whole cores from Holes 1218A, 1218B, and 1218C and by the insertion and contact probe systems on split cores from Hole 1218A (Table **T21**). For XCB cores, cube samples were cut with the dual-bladed rock saw, allowing determination of velocities in the y- and z-directions with the contact probe system. The match between the whole-core and split-core measurements is relatively good for the insertion and the contact probe systems, with only a few anomalous points (Fig. **F27**).

T20. LAS-based mineralogy, p. 118.

F26. LAS mineralogy determinations, p. 69.

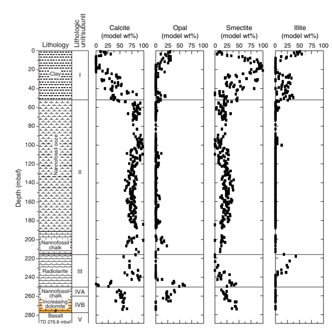

T21. Split-core velocity measurements, p. 121.

F27. Compressional wave velocity, p. 70.

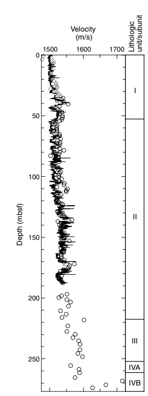

Downhole trends in velocity do not simply follow changes in lithology or bulk properties (Fig. F27). Velocity (transverse) increases with depth in Unit I from ~1500 m/s near the seafloor to 1555 m/s at 40.46 mbsf. The sharp increase in density and decrease in porosity that occurs at the boundary between Units I and II is less prominent in the velocity profile. From 51.46 mbsf, near the base of Unit I, to 54.99 mbsf, near the top of Unit II, velocity decreases from 1538 to 1512 m/s. Overall, there is a gradual increase in velocity with depth in Unit II. Small variations in velocity most likely reflect alternations in lithology. The prominent bulk density minimum and porosity maximum in Unit II at 155 mbsf is not evident in the velocity profile, and a broad velocity maximum between 170 and 180 mbsf is not reflected in the density and porosity profiles. Unit III is marked by an anomalously high velocity (1602 m/s) near the top of the unit at 218.06 mbsf. Excluding this value, the trend in Unit III is an increase in velocity from 1554 m/s at 222.94 mbsf to 1598 m/s at 248.25 mbsf. An exceptionally high velocity for Site 1218 sediments (1716 m/s) was determined for the dolomitic nannofossil chalk in Subunit IVB at 268.09 mbsf.

The lack of consistent downhole velocity trends in Hole 1218A is partly explained by the crossplot of velocity and wet bulk density (Fig. F28). The nannofossil ooze of Unit II is characterized by a general increase in velocity with increasing density. A similar trend is apparent for the nannofossil chalk of Unit IV, although the velocities are higher at the same density, most likely reflecting a difference in the sediment bulk modulus. The radiolarian clays of Unit I and the radiolarite of Unit III differ from the calcareous sediment in their relationships with bulk density. In Units I and III, there is either no relation or a weak increase in velocity with decreasing density. This pattern possibly results from the stiff sediment fabric created by the shape of radiolarians and their interlocking spines. This stiffness produces a higher shear modulus and velocities higher than expected for the high porosity of the sediment. The difference in the trends of velocity with bulk density for the calcareous and siliceous sediments explains the lack of a prominent change in velocity at the boundary between radiolarian clay of Unit I and the nannofossil ooze of Unit II.

F28. Compressional wave velocity vs. wet bulk density, p. 71.

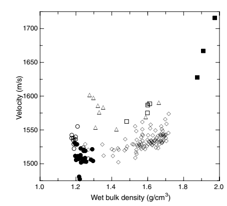

T22. Thermal conductivity, p. 123.

Velocity anisotropy was calculated from longitudinal (z-direction) and transverse (y-direction) measurements provided by the insertion probe system and the cut samples measured with the contact probe system (Table T21) to evaluate burial-induced changes in sediment fabric. The anisotropy ranges from –1.0% to 1.7% and averages 1.0% for the insertion probe system (upper 34 m of Hole 1218A). The anisotropy determined with the contact probe for sediments from 196.76 to 273.76 mbsf ranges from –0.3% to 2.6% and is marked by a clear increase in anisotropy of the sediments of Subunit IVB. The average anisotropy for the sediments below 196 mbsf is 1.0% for Unit II, 1.4% for Unit III, 0.4% for Subunit IVA, and 2% for Subunit IVB.

F29. Thermal conductivity, p. 72.

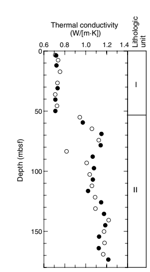

Thermal Conductivity and Temperature Measurements

Thermal conductivity was measured on the third section of Cores 199-1218A-1H through 19H and 199-1218B-1H through 19X (Table T22). The thermal conductivity shows a strong dependence on lithology (Fig. F29) and porosity (Fig. F30). The radiolarian clays of Unit I display a nearly constant conductivity, which averages 0.72 W/(m·K). Thermal conductivity increases sharply at the top of Unit II to 0.94 W/(m·K). In Unit II, conductivity increases with depth to 1.22 W/(m·K) at

F30. Thermal conductivity vs. porosity, p. 73.

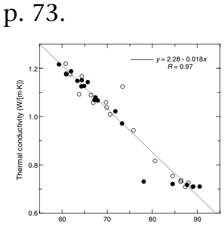

173.46 mbsf in Hole 1218A, with a pattern that roughly mimics that of porosity. The inverse relationship between thermal conductivity and porosity is well defined at Site 1218 (Fig. **F31**), with a correlation coefficient of 0.97.

F31. Heat flow calculation, p. 74.

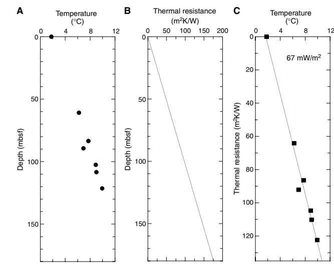

In situ temperature measurements were taken using the Adara tool with four cores in Hole 1218A and three cores in Hole 1218B. The tool did not stabilize in the borehole with Core 199-1218A-4H, and the temperature could not be calculated. Borehole temperatures range from 6.22°C at 60.90 mbsf to 9.95°C at 121.50 mbsf, with an average seafloor temperature of 1.78°C (Table **T23;** Fig. **F31**).

T23. In situ temperature, p. 124.

Heat flow at Site 1218 was determined according to the procedure of Pribnow et al. (2000). The laboratory-determined thermal conductivity was used to estimate in situ thermal conductivity (see **"Heat Flow Calculation,"** p. 28, in "Physical Properties" in the "Explanatory Notes" chapter), and a linear fit through these values was used to calculate the thermal resistance (Fig. **F31**). Because no temperature measurements were obtained from lithologic Unit I, only the conductivities from Unit II were used for the heat flow determination. Thermal resistance was estimated for the depths of the temperature measurements, and the heat flow was obtained from the inverse of the linear fit for the crossplot of temperature and thermal resistance (Fig. **F31**). The heat flow estimate at Site 1218 is 67 mW/m². This value is similar to a heat flow of 75 mW/m² at the nearest point (9°3.0′N, 133°40.0′W) in the global heat flow data set (Pollack et al., 1993).

Natural Gamma Radiation

Natural gamma radiation was measured on all whole cores at Site 1218 (Fig. **F32**). The highest NGR values are present between the seafloor and 50 mbsf, where they average 8.6 counts per second (cps) in the clay-rich lithologic Unit I. Below 50 mbsf, values drop to <1 cps in the carbonate-rich Unit II and remain at this level to a depth of 216 mbsf. A slight increase in NGR values, to an average of 0.43 cps and a maximum of 9.72 cps, marks lithologic Unit III because of an increase in clay content.

F32. NGR, p. 75.

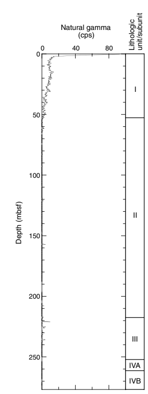

MS

Whole-core MS measurements correlate well with the major differences in lithology and to changes in bulk physical properties (Fig. **F33**). MS values in Unit I are relatively high, averaging 34 × 10^{-6} SI. The expected direct relationship between bulk density and MS is not well developed in this unit. The MS record contains significant variation that is not present in the more uniform GRA bulk density profile (Fig. **F24**), although there is a match of the general trends. A significant decrease in susceptibility marks the top of the carbonate-rich Unit II at 52 mbsf. MS values are low in Unit II, averaging 10 × 10^{-6} SI, but the variation that is present corresponds to alternations between nannofossil ooze (lower MS) and clayey nannofossil ooze (higher MS). An increase in susceptibility marks the boundary between Units II and III as the clay content increases and culminates with a maximum of 80 × 10^{-6} SI at 225 mbsf. The average susceptibility in lithologic Unit III is 31 × 10^{-6} SI. A decrease to MS values of ~10 × 10^{-6} SI corresponds to increased carbonate concentrations at the top of Unit IV. Susceptibility increases within Unit IV to 35 × 10^{-6} SI at the base of the unit.

F33. Magnetic susceptibility, p. 76.

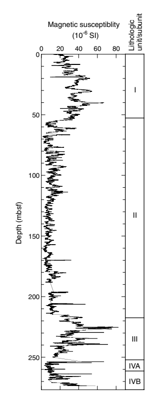

DOWNHOLE MEASUREMENTS

Logging Operations

Two logging runs (triple combo and FMS-sonic) (see Fig. **F10,** p. 55, in the "Explanatory Notes" chapter) were planned for Hole 1218A (after basement was reached at 0645 hr on 16 November) following a combination of APC (~190 mbsf) and XCB (190–280 mbsf) coring. The hole was conditioned with a wiper trip of the drill string (up to 78 mbsf and back to basement), and 2 m of fill was flushed from the bottom of the hole. The hole was displaced with 110 bbl of 8.9 lb/gal sepiolite mud, and the bit was withdrawn to 80 mbsf in preparation for logging. Tool rig-up was begun at 1130 hr and, after some technical problems, was completed by 1645 hr. The tool was run to the bottom of the hole (5118.5 mbrf), and logging began at 2210 hr on 16 November. Seasoning of the new wireline (installed during port call) limited the maximum speed to run into and out of pipe to 5000 ft/hr (~1500 m/hr), leading to an approximate doubling of the times normally expected.

The classic triple combo configuration with the Lamont-Doherty Earth Observatory high-resolution MGT on top was run first, followed by the FMS-sonic tool string (see Fig. **F10,** p. 55, in the "Explanatory Notes" chapter). Pump pressure was required to get the triple combo through the bit into open hole. Initially, this problem was thought to be the result of a mud/clay plug in the bottom-hole assembly (BHA), but upon inspection of the tool at the end of the run, a bent caliper arm was probably the cause. No serious damage was sustained by the tool. A total of five passes were made (providing ~200 m of logged section per pass) with no bridges encountered, and the bottom of the hole was reached on all passes (Fig. **F34**). A breakdown of the chronology of logging operations is provided in Table **T24,** along with details of the tools used.

The triple combo caliper log indicated good conditions for most of the hole (Fig. **F35**). After the second pass of the triple combo, control switched to the downhole measurements lab, and the tool string was again lowered to the bottom of the hole. Logging was conducted in the "Lamont mode" for high-resolution MGT data acquisition on a single pass. Upon completion of this pass, the tool string was retrieved and the FMS-sonic tool string was rigged up and run to the bottom of the hole. The dipole shear sonic imager was run in primary (compressional; *P*-wave) and secondary (shear; *S*-wave) monopole and dipole shear modes. On the first pass, a lower frequency was used, which resulted in better dipole *S*-wave measurements, and on the second pass a higher frequency was used, which resulted in better monopole *P*-wave measurements. However, because of the slowness of the formation, the *P*- and *S*-wave velocity logs are incomplete and of low quality. During both passes, there were two brief telemetry and power losses to the tool string, but this had little effect upon the log acquisition. The drill pipe was pulled upward toward completion of the second pass, providing an extra 20 m of logged formation. The tool string was then retrieved, and logging operations were completed by 1900 hr on 17 November. The weather was variable throughout the logging operation with heave typically ~2 to 2.5 m. The wireline heave compensator stroked out on only one occasion during the whole logging operation.

F34. Logging operations, p. 77.

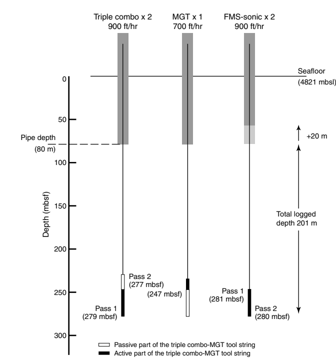

T24. Logging operations, p. 125.

F35. Caliper, acceleration, and gamma ray logs, p. 78.

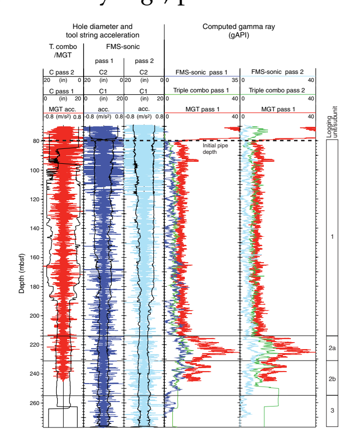

Data Quality

The hole conditions were excellent in the lower 90 m of the borehole with widths averaging 13.3 in, as recorded by the triple combo caliper (Fig. F35). Above this lower interval, the hole opens out to an average of 16.7 in for the next 55 m, before increasing to an average of 18.2 in for the remainder of the hole. A hole diameter of this magnitude may degrade the quality of the data from tools that require contact with the borehole wall (e.g., the density or porosity logs). However, there appears to be little evidence of deterioration of data quality uphole in these logs. The FMS caliper readings suggest a smaller hole (the maximum extension of the FMS calipers is only 15 in compared to 18 in for the triple combo caliper) (see Fig. F35). These observations suggest that damage sustained by the triple combo caliper arm when entering the open hole caused an overestimation in the recorded hole size. Problems were encountered during data downloading from the Lamont-Doherty Earth Observatory temperature/acceleration/pressure tool, and no data were obtained.

Tool string accelerometer data from the MGT and the FMS-sonic indicate that hole conditions and stick-slip of the tool remained at low levels until the cable head entered the BHA. The FMS recorded good data most of the way up the formation, and there is good correlation between the two passes. The sonic logs are of low quality because of the slowness of the formation. Computed gamma ray measurements from each pass show excellent correlation (Fig. F35), indicating the high quality of the data. More detailed gamma ray logs are displayed on Figure F36, with further good correlation between passes. Density and porosity logs show good repeatability, and as expected, core density and porosity values are lower than those recorded by logging. This difference between log and core data sets is assumed to result from the porosity increase in the cores caused by elastic strain recovery following unloading. Nevertheless, the correlation between data sets is good, and the log data will thus provide the baseline for depth shifting and compressing the core-derived composite-depth scale (see "Composite Depths," p. 21). The second full pass of the same tool string provided a continuous log of high quality data. As a further check on data quality, a wavelet analysis of the accelerometer data from the FMS-sonic tool string passes was undertaken. Continuous wavelet analysis provides an automatic localization of specific behavior, such as cyclic patterns or discontinuities, both in time and frequency (e.g., Torrence and Compo, 1998). In contrast to classical Fourier transform or windowed Fourier transform, which decompose the original signal on the basis of an infinite periodic function depending on a unique parameter (space frequency), the wavelet transform (WT) allows a "depth-scale" representation that depends on a scale parameter and a translation parameter. The WT analysis of the acceleration data allows the multiscale components of the tool acceleration to be deciphered (Fig. F37). The full record (80–276.8 mbsf) is characterized by acceleration/deceleration mainly over a range of <1 m. The bottom of the hole is characterized by localized stick-slip displacement over intervals of intermediate scale (~ 4–7 m) (Fig. F37B). The upper part of the hole displays a more complicated pattern with components ranging over intervals from 4 to 100 m. Whereas, the high-frequency component may be explained by incomplete heave compensation, the other components are directly linked to hole conditions. A comparison of wavelet representation and hole shape shows that the intervals where tool acceleration changes corre-

F36. Gamma ray, radioactivity, and PEF logs, p. 79.

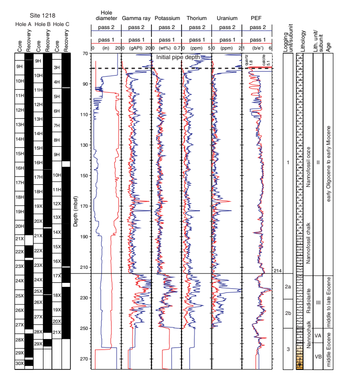

F37. Data quality, WT analysis, and caliper log, p. 80.

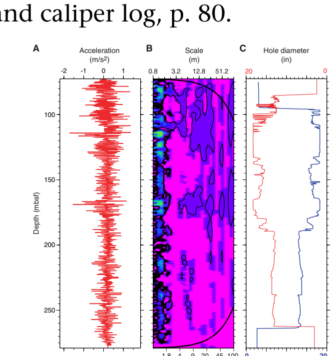

spond to changes in hole diameter (Fig. **F37**). Increases in hole diameter are connected to increases in the scale of the stick-slip intervals and vice versa.

Logging Stratigraphy

Logging units were differentiated mainly using variations in the gamma ray logs (Fig. **F36**). The static normalized FMS images confirm the logging units as do the density, porosity, and resistivity logs, but to a lesser extent (Fig. **F38**). The formation is divided into three logging units: (1) an upper unit characterized by low gamma ray counts with cyclicity at a number of depth scales, (2) a middle unit where significantly higher gamma ray counts are recorded, and (3) a lower unit characterized by a return to low gamma ray counts (this unit is defined solely on the basis of the FMS NGR tool [NGT] data). The middle logging unit is further subdivided into two subunits, based on a reduction in gamma ray counts.

Logging Unit 1: Base of Pipe, 60 mbsf to 214 mbsf

Logging Unit 1 is characterized by low total gamma ray counts (Fig. **F38**). Porosity values are initially high but drop from 129 mbsf to a minimum at ~157 mbsf and then rise again to values similar to those seen at the top of the log. An opposite trend is observed in the density data (i.e., increasing toward a plateau centered around 160 mbsf and then decreasing down to the base of the unit). The density-porosity relationship seen in the logs reflects carbonate variations downhole (see **"Physical Properties,"** p. 27, and **"Geochemistry,"** p. 25). Resistivity data remain at uniform levels throughout the unit. At higher resolution, the MGT and FMS image/microresistivity logs show cyclicity on a scale of 1–1.5 m (Fig. **F39**). The FMS image/microresistivity logs also provide a record of shorter-period cyclicity within the 1- to 1.5-m cycles. Figure **F39** shows a detailed section of this logging unit at 177 mbsf, with a plot of the microresistivity recorded by a single button on FMS pass 1, which highlights the high- and low-resistivity areas. This logging unit correlates with lithostratigraphic Unit II (nannofossil ooze) (see **"Unit II,"** p. 7, in "Lithostratigraphy").

Logging Unit 2: 214–255 mbsf

The upper boundary of logging Unit 2 is defined by a step in gamma ray values (Figs. **F35, F36**). A concomitant decrease in density, resistivity, and sonic velocity and an increase in porosity also occur at this point (Fig. **F38**). Potassium levels most consistently exemplify this change in formation properties (Fig. **F36**). The whole unit is characterized by greater amplitude variability in the gamma ray, density, porosity, and resistivity data than logging Unit 1 (Figs. **F36, F38**). The large peaks in density and resistivity at ~224.5 and 238.5 mbsf are associated with bands of chert. Figure **F40** shows a portion of both FMS passes associated with the peak around 225 mbsf. The high-resistivity chert bands are easily visible in the image, and the microresistivity log shows the record of "relative resistivity." These two peaks in density and resistivity correlate with a massive reduction in calcium and an increase in silica (see **"Solid-Phase Geochemistry,"** p. 26, in "Geochemistry"). Based on the gamma ray data (Fig. **F36**), a two-unit subdivision is made. From 214 to 231 mbsf, Subunit 2a has larger-amplitude fluctuations

F38. Log and equivalent core physical properties, p. 81.

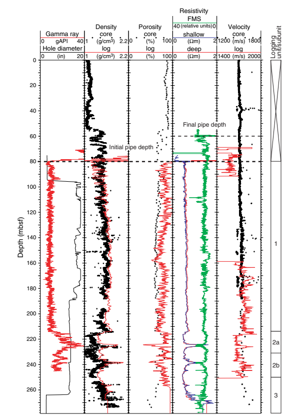

F39. FMS, geophysical, and geochemical logging data, log Unit 1, p. 82.

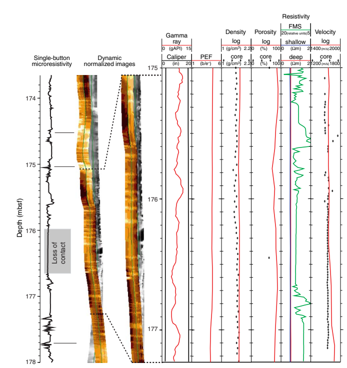

F40. Chert bands in FMS images, logging Unit 2, p. 83.

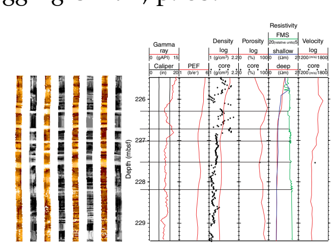

(Figs. **F36, F41**), whereas lower Subunit 2b has lower-amplitude, longer frequency variations (Fig. **F41**). The whole of logging Unit 2 correlates with lithostratigraphic Unit III (radiolarite) (see **"Unit III,"** p. 8, in "Lithostratigraphy").

Logging Unit 3: 255 mbsf to Bottom Of Logged Formation

The NGT (see Fig. **F10,** p. 55, in the "Explanatory Notes" chapter) was located just above the FMS on the second tool string and logged the formation to a depth of 270 mbsf, recording the deepest gamma ray data (Fig. **F35**). The NGT log records a decrease in the gamma ray counts at a depth of 255 mbsf, to the levels observed in logging Unit 1. Density and resistivity increase toward the bottom of the formation (Fig. **F38**). This unit is correlative with lithostratigraphic Unit IV (nannofossil chalk and dolomite) (see **"Unit IV,"** p. 9, in "Lithostratigraphy").

Discussion

Good hole conditions combined with relatively calm sea conditions led to the acquisition of excellent logging data. The main objectives of acquisition of in situ, continuous, multiparameter logging data at this site were

1. To assess the physical, chemical, and structural characteristics of the formation and to provide a baseline for depth matching the core-derived composite depth scale;
2. To perform cyclostratigraphic analysis of continuous Paleogene sequences;
3. To identify and characterize chert layers, which are usually poorly recovered in cores; and
4. To conduct a seismic integration (time-depth model and synthetic seismogram), allowing identification and dating of seismic reflectors at a regional scale.

The logging units described above correlate well with the designated lithostratigraphic units (see **"Lithostratigraphy,"** p. 7). The lower Oligocene–lower Miocene nannofossil ooze and chalk is identified as a region with consistently low NGR activity, reflecting the low clay content of these sediments. However, the high-resolution MGT gamma ray data provide a detailed record of cyclicity in sedimentation. The density in logging Unit 1 gradually increases down to 160 mbsf and then gradually decreases toward the boundary with logging Unit 2. The porosity log covaries with the density log, with the minimum porosity more sharply defined than the maximum density. These porosity/density trends have been attributed to variations in clay content (opposite to carbonate levels) with depth (see **"Lithostratigraphy,"** p. 7, **"Physical Properties,"** p. 27, and **"Geochemistry,"** p. 25). The gamma ray logs show no distinguishable shift in count levels, so if clay content is indeed the cause of the density and porosity changes, the percentage increase in clay must be below the MGT detection limits. The photoelectric factor (PEF), however, shows the same downhole trend as the density log (Fig. **F36**). The PEF is generally used as an indicator of lithology, with values toward six indicating carbonate and values toward one indicating silica. A peak in the PEF log at 224 mbsf correlates with similar peaks in density and resistivity that correspond with the first region of significant chert band-

F41. MGT data displaying shift in cycles, logging Unit 2, p. 84.

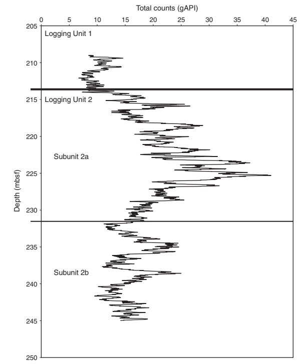

ing. Given this change in lithology (carbonate to silica), a shift toward lower values of PEF would be expected. However, the presence of iron-bearing minerals even in small quantities can also have a significant effect on the PEF (Rider, 1996). This peak in PEF is interpreted to result from the presence of iron oxides, as opposed to an enrichment of the carbonates resulting from silica migration toward the chert layers. This interpretation is corroborated by color descriptions of the sediment at this depth and by geochemical data (see **"Lithostratigraphy,"** p. 7, and **"Geochemistry,"** p. 25).

Passing downhole through the Oligocene–Eocene transition, the gamma ray counts increase significantly, indicating a higher quantity of clay in the formation. The density, porosity, and resistivity logs identify two zones where significant chert formation has occurred. The high-resolution FMS microresistivity images show that the high-resistivity, high-density/low-porosity zones are composed of multiple chert bands (e.g., Fig. **F40**). The zone between 218 and 229 mbsf is composed of two groups, an upper one comprising seven bands from 218 to 223 mbsf and a lower one comprising eight bands from 226 to 229 mbsf. The second major peak is composed of five bands between 238 and 241 mbsf. From 247 to 266 mbsf, there are a number of small groupings and single chert layers. A significant group of eight chert layers is located between 269 and 273 mbsf. In all of the locations mentioned above, the chert appears as layers. Layering width is highly variable, from detection limit up to a maximum of 15 cm at 227 mbsf. The chert layers are sinuous in the FMS images, indicating shallow dips. Below 218 mbsf, chert nodules are also observed throughout the formation, with a higher concentration in the interval 249–254 mbsf.

WT analysis was undertaken on the logging data to investigate the cyclicity in logging Unit I (Fig. **F42**). The density and porosity logs were used because they displayed cyclicity and were influenced by variable clay/carbonate content downhole. Both wavelet diagrams show a gradual increase in the depth scale of cyclicity toward a boundary around 166 mbsf, where a step change occurs to a larger depth scale in cyclicity. In order to better understand the mechanism of this shift, a cross-wavelet spectrum diagram was computed (Fig. **F42C**). The modulus diagram allows a comparison of the scale change with depth and shows a phase change occurring around 166 mbsf. The diagram shows the expected phase difference between the density and porosity logs. The scale change in cyclicity may be related to a shift in sedimentation rates during the deposition of this unit (i.e., rates ~1.5 times higher in the section above 166 mbsf).

F42. WT analyses of density and porosity logs, log Unit 1, p. 85.

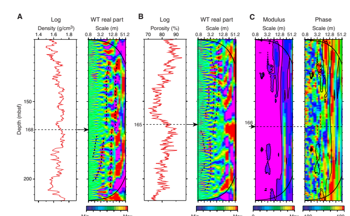

Synthetic Seismogram

The aim of creating a synthetic seismogram is to provide a means of matching up the reflections expected from the formation (measured physical properties from log and core sources) with those in the seismic data. This allows the seismic data to be interpreted in terms of the measured formation properties; for example, lithologic or chronological boundaries can be picked out as specific reflectors. If a synthetic seismogram can be generated for a number of sites, these data provide the basis for producing a regional seismic stratigraphy.

The *P*-wave labeling algorithm in the Schlumberger software had difficulty in identifying the *P*-wave of the formation from that of the drilling mud, making the velocity logs incomplete and of poor quality (Fig. **F38**). The PWL (whole core) velocity data only extend to 188 mbsf, but the *P*-wave sensor (PWS; split core) velocity data are available to 273 mbsf. Thus, the PWS velocity data were selected (the formation was assumed to be isotropic in order to obtain the longest possible data set; i.e., any axial velocity was used) and were resampled using a linear interpolation script run in GMT (Generic Mapping Tools; Wessel and Smith, 1999). The GRA density was spliced onto the top of the hostile environment litho-density tool (HLDT) density log to provide data for the entire formation. Because the core-derived densities and velocities differ from the in situ measured logging data (Mayer et al., 1985), a correction factor for the spliced density section was computed (i.e., core data were corrected to in situ values) and the raw PWS data were used. These full-depth data sets were then imported into the IESX module of the Schlumberger GeoQuest program Geoframe to calculate the synthetic seismogram. The impedance (velocity × density) was calculated, and the impedance contrast between successive layers gave the reflection coefficient series. The source wavelet (obtained by extracting the seafloor reflection from the seismic data) was convolved with the reflection coefficient series to generate the synthetic seismogram (Fig. F43).

The generated synthetic seismogram shows a good match with the seismic data. The first major reflector appears on the seismogram at 174 mbsf, which corresponds to a peak measured in the core velocities (Fig. F38). The upper chert bands appear between 218 and 229 mbsf as high-density and high-resistivity areas in the log and core data (Fig. F38). A large positive reflector is located around this depth on the seismic trace and is interpreted to represent the upper chert layers. Further analysis of the FMS data will allow the dip and dip directions of the chert layers to be determined, and these will be compared with the seismic data.

F43. Synthetic seismogram derived from velocity and density, p. 86.

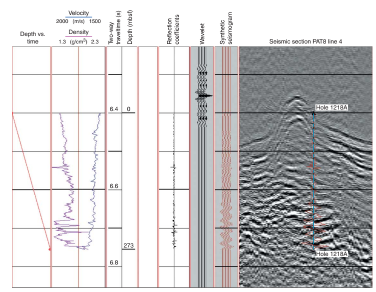

REFERENCES

Berggren, W.A., Kent, D.V., Swisher, C.C. III, and Aubry, M.-P., 1995. A revised Cenozoic geochronology and chronostratigraphy. *In* Berggren, W.A., Kent, D.V., Aubry, M.-P., and Hardenbol, J. (Eds.), *Geochronology, Time Scales and Global Stratigraphic Correlation*. Spec. Publ.—Soc. Econ. Paleontol. Mineral., 54:129–212.

Berggren, W.A., and Miller, K.G., 1989. Cenozoic bathyal and abyssal calcareous benthic foraminiferal zonations. *Micropaleontology,* 35:308–320.

Blow, W.H., and Banner, F.T., 1962. The mid-Tertiary (upper Eocene to Aquitanian) Globigerinacea. *In* Eames, F.E., Banner, F.T., Blow, W.H., and Clarke, W.J. (Eds.), *Fundamentals of Mid-Tertiary Stratigraphical Correlation:* Cambridge (Cambridge Univ. Press), 61–151.

Bukry, D., 1973. Low-latitude coccolith biostratigraphic zonation. *In* Edgar, N.T., Saunders, J.B., et al., *Init. Repts. DSDP,* 15: Washington (U.S. Govt. Printing Office), 685–703.

Cande, S.C., and Kent, D.V., 1995. Revised calibration of the geomagnetic polarity timescale for the Late Cretaceous and Cenozoic. *J. Geophys. Res.,* 100:6093–6095.

Cande, S.C., LaBrecque, J.L., Larson, R.L., Pitmann, W.C., III, Golovchenko, X., and Haxby, W.F., 1989. Magnetic lineations of the world's ocean basins. *AAPG,* 13:1.

Coccioni, R., Monaco, P., Monechi, S., Nocchi, M., and Parisi, G., 1988. Biostratigraphy of the Eocene-Oligocene boundary at Massignano (Ancona, Italy). *In* Premoli Silva, I., Coccioni, R., and Montanari, A. (Eds.), *The Eocene-Oligocene Boundary in the Marche-Umbria Basin (Italy)*. Spec. Publ., II—Int. Subcomm. Paleogr. Strat., Eocene/Oligocene Meeting, 1:59–80.

Curry, W.B., Shackleton, N.J., Richter, C., et al., 1995. *Proc. ODP, Init. Repts.,* 154: College Station, TX (Ocean Drilling Program).

Engebretson, D.C., Cox, A., and Gordon, R.G., 1985. *Relative Motions Between Oceanic and Continental Plates in the Pacific Basin*. Spec. Pap.—Geol. Soc. Am., 206.

Gripp, A.E., and Gordon, R.G., 1990. Current plate velocities relative to the hotspots incorporating the NUVEL-1 global plate motion model. *Geophys. Res. Lett.,* 17:1109–1112.

Kennett, J.P., and Srinivasan, M.S., 1983. *Neogene Planktonic Foraminifera: A Phylogenetic Atlas:* Stroudsburg, PA (Hutchinson Ross).

Kroenke, L.W., Berger, W.H., Janecek, T.R., et al., 1991. *Proc. ODP, Init. Repts.,* 130: College Station, TX (Ocean Drilling Program).

Martini, E., 1971. Standard Tertiary and Quaternary calcareous nannoplankton zonation. *In* Farinacci, A. (Ed.), *Proc. 2nd Int. Conf. Planktonic Microfossils Roma:* Rome (Ed. Tecnosci.), 2:739–785.

Mayer, L.A., Shipley, T.H., Theyer, F., Wilkens, R.H., and Winterer, E.L., 1985. Seismic modeling and paleoceanography at Deep Sea Drilling Project Site 574. *In* Mayer, L., Theyer, F., Thomas, E., et al., *Init. Repts. DSDP,* 85: Washington, (U.S. Govt. Printing Office), 947–970.

Nomura, R., 1995. Paleogene to Neogene deep-sea paleoceanography in the eastern Indian Ocean: benthic foraminifera from ODP Sites 747, 757, and 758. *Micropaleontology,* 41:251–290.

Pollack, M.N., Hurter, S.J., and Johnson, J.R., 1993. Heat flow from the earth's interior: analysis of the global data set. *Rev. Geophys.,* 31:267–280.

Pribnow, D.F.C., Kinoshita, M., and Stein, C.A., 2000. Thermal data collection and heat flow recalculations for ODP Legs 101–180. Institute for Joint Geoscientific Research, GGA, Hanover, Germany, 0120432. Available from World Wide Web: <http://www-odp.tamu.edu/publications/heatflow/>. [Cited 2001-11-22]

Raffi, I., 1999. Precision and accuracy of nannofossil biostratigraphic correlation. *Philos. Trans. R. Soc. London A,* 357:1975–1994.

Rider, M., 1996. *The Geological Interpretation of Well Logs* (2nd ed.): Caithness (Whittles Publishing).

Rothwell, R.G., 1989. *Minerals and Mineraloids in Marine Sediments: An Optical Identification Guide:* Basking, UK (Elsevier Appl. Sci. Publ.).

Sanfilippo, A., and Nigrini, C., 1995. Radiolarian stratigraphy across the Oligocene/Miocene transition. *Mar. Micropaleontology,* 24:239–285.

Shackleton, N.J., Crowhurst, S.J., Weedon, G.P., and Laskar, J., 1999. Astronomical calibration of Oligocene-Miocene time. *Philos. Trans. R. Soc. London A,* 357:1907–1929.

Torrence, C., and Compo, G.P., 1998. A practical guide to wavelet analysis. *Bull. Am. Meteorol. Soc.,* 79:61–78.

Toumarkine, M., and Luterbacher, H., 1985. Paleocene and Eocene planktonic foraminifera. *In* Bolli, H.M., Saunders, J.B., and Perch-Nielsen, K., (Eds.), *Plankton Stratigraphy:* Cambridge (Cambridge Univ. Press), 87–154.

van Morkhoven, F.P.C.M., Berggren, W.A., and Edwards, A.S., 1986. Cenozoic cosmopolitan deep-water benthic foraminifera. *Bull. Cent. Rech. Explor.—Prod. Elf-Aquitaine,* 11.

van Andel, T.H., Heath, G.R., et al., 1973. *Init. Repts. DSDP,* 16: Washington (U.S. Govt. Printing Office).

van Andel, T.H., Heath, G.R., and Moore, T.C., Jr., 1975. Cenozoic history and paleoceanography of the central equatorial Pacific Ocean: a regional synthesis of Deep Sea Drilling Project data. *Mem.—Geol. Soc. Am.,* 143.

Wessel, P., and Smith, W.H.F., 1999. The Generic Mapping Tools (GMT), version 3.2 Technical Reference and Cookbook, SOEST/NOAA.

Zachos, J.C., Pagani, M., Sloan, L., Thomas, E. and Billups, K., 2001. Trends, rhythms, and aberrations in global climate 65 Ma to present. *Science,* 292:686–693.

Figure F1. Location of Site 1218 in the Leg 199 transect. The basement age is ~42 Ma. In the lower panel, gray shading = seafloor depths >5000 mbsl, red shading = approximate position of magnetic Anomaly C25, the nominal target crust of the 40-Ma transect. FZ = fracture zone.

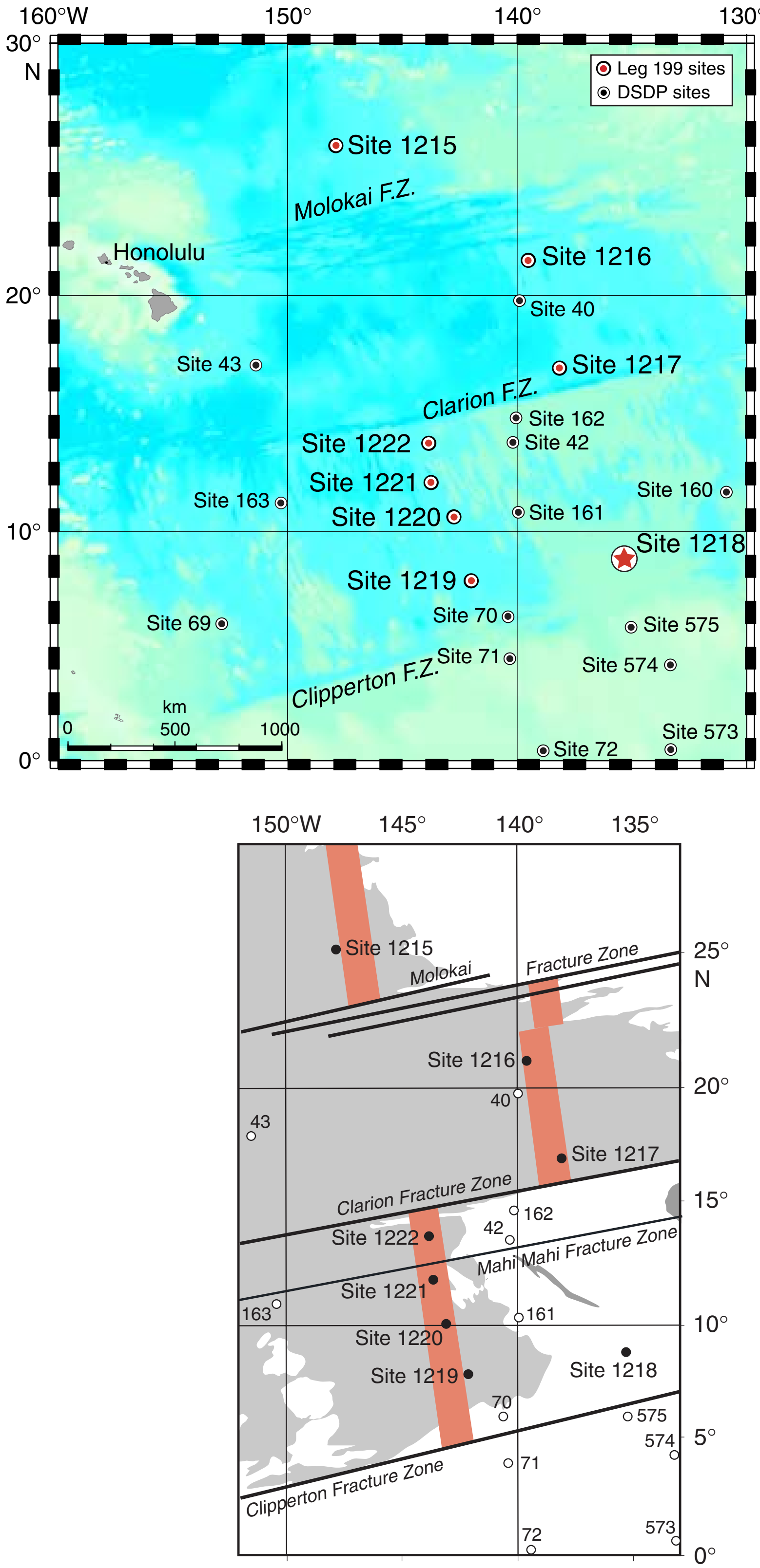

Figure F2. Seismic reflection profile through Site 1218 from the EW9709 site survey cruise of the *Ewing*. The seismic reflections can be correlated to a regional Paleogene stratigraphy (**Lyle et al.,** this volume).

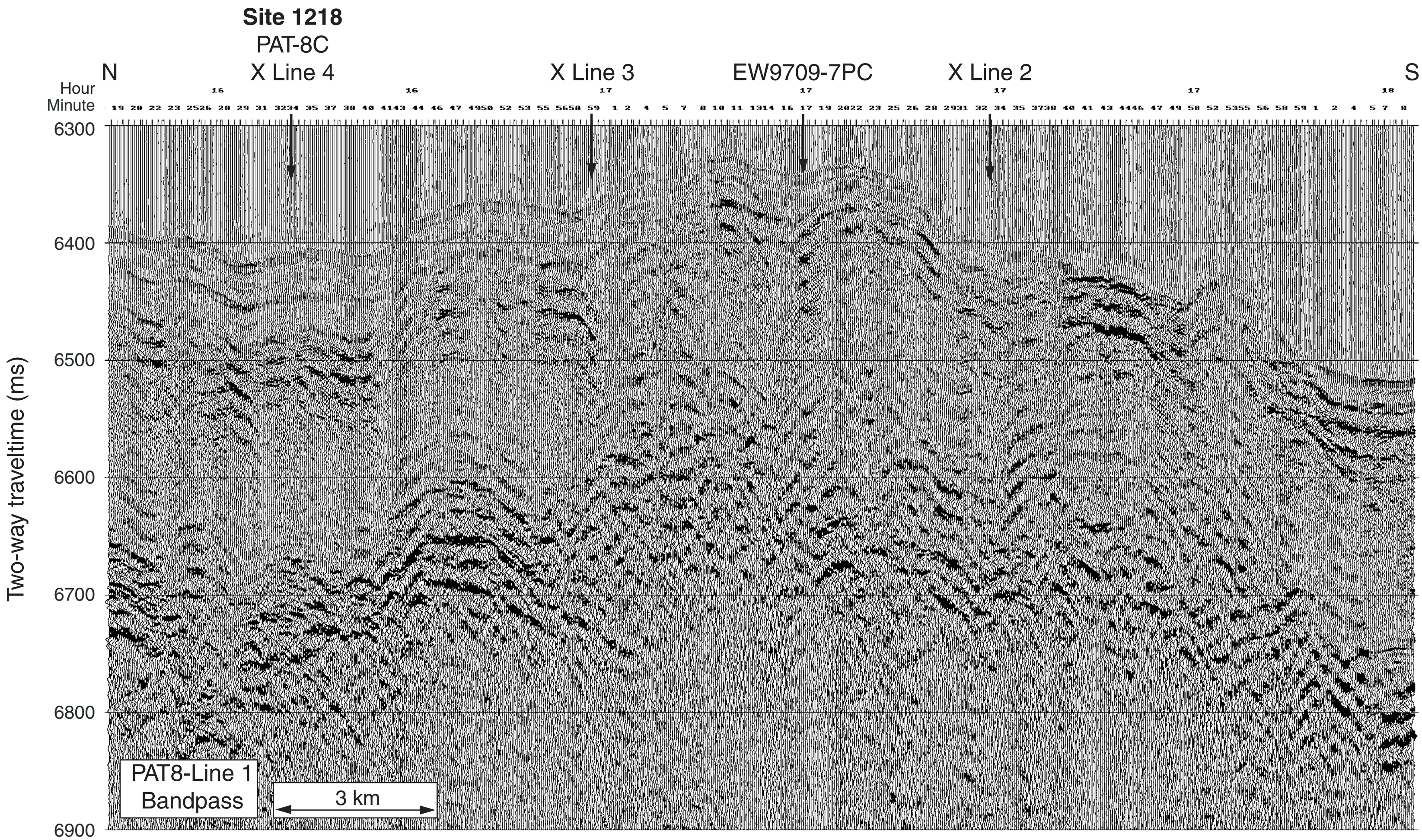

Figure F3. Lithologic summary for Site 1218. For discussion of the E/O boundary see **"E/O Boundary Interval,"** p. 13, in "Biostratigraphy." LAS = light absorption spectroscopy, gAPI = American Petroleum Institute gamma ray units, TD = total depth. (Continued on next page.)

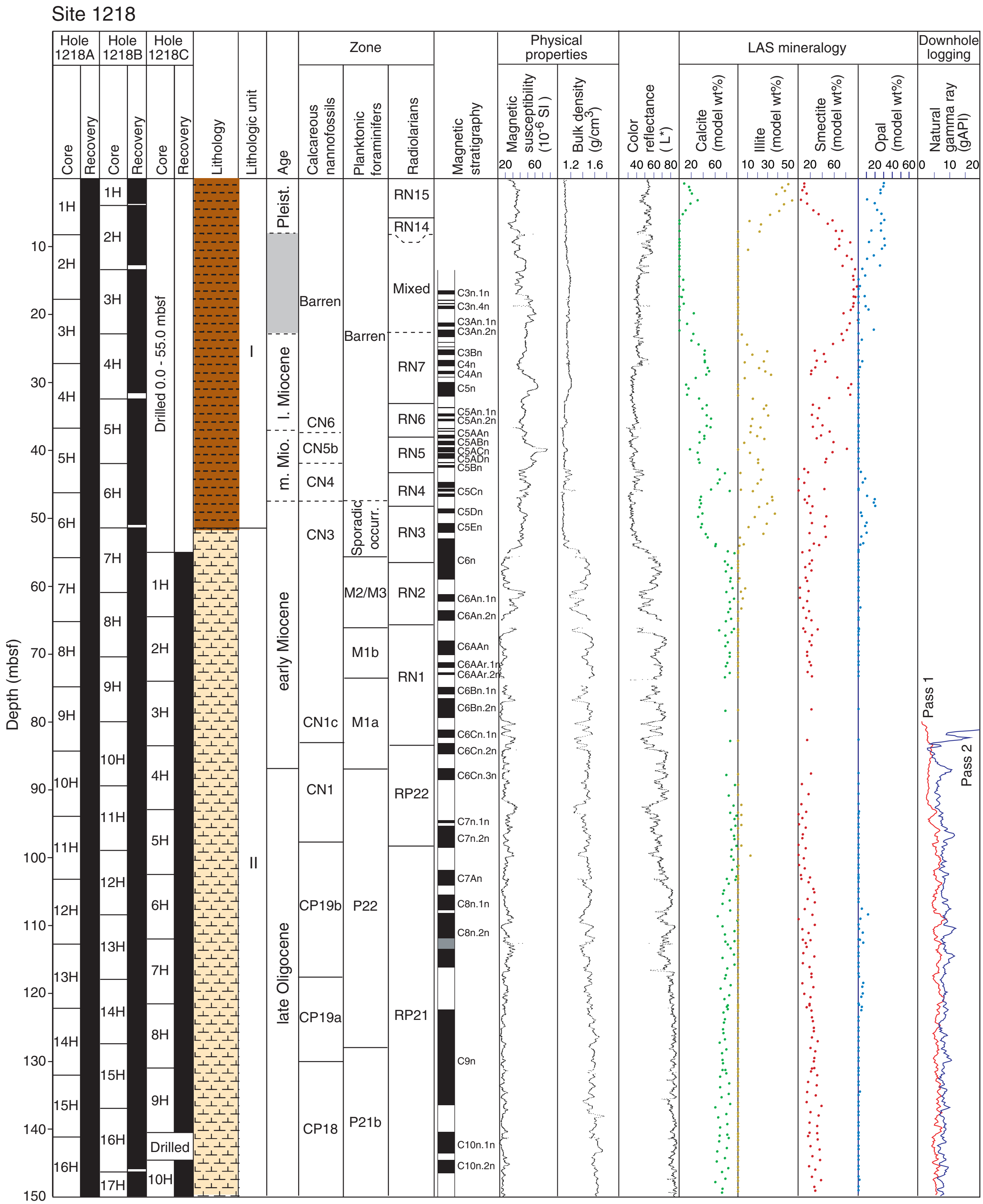

Figure F3 (continued).

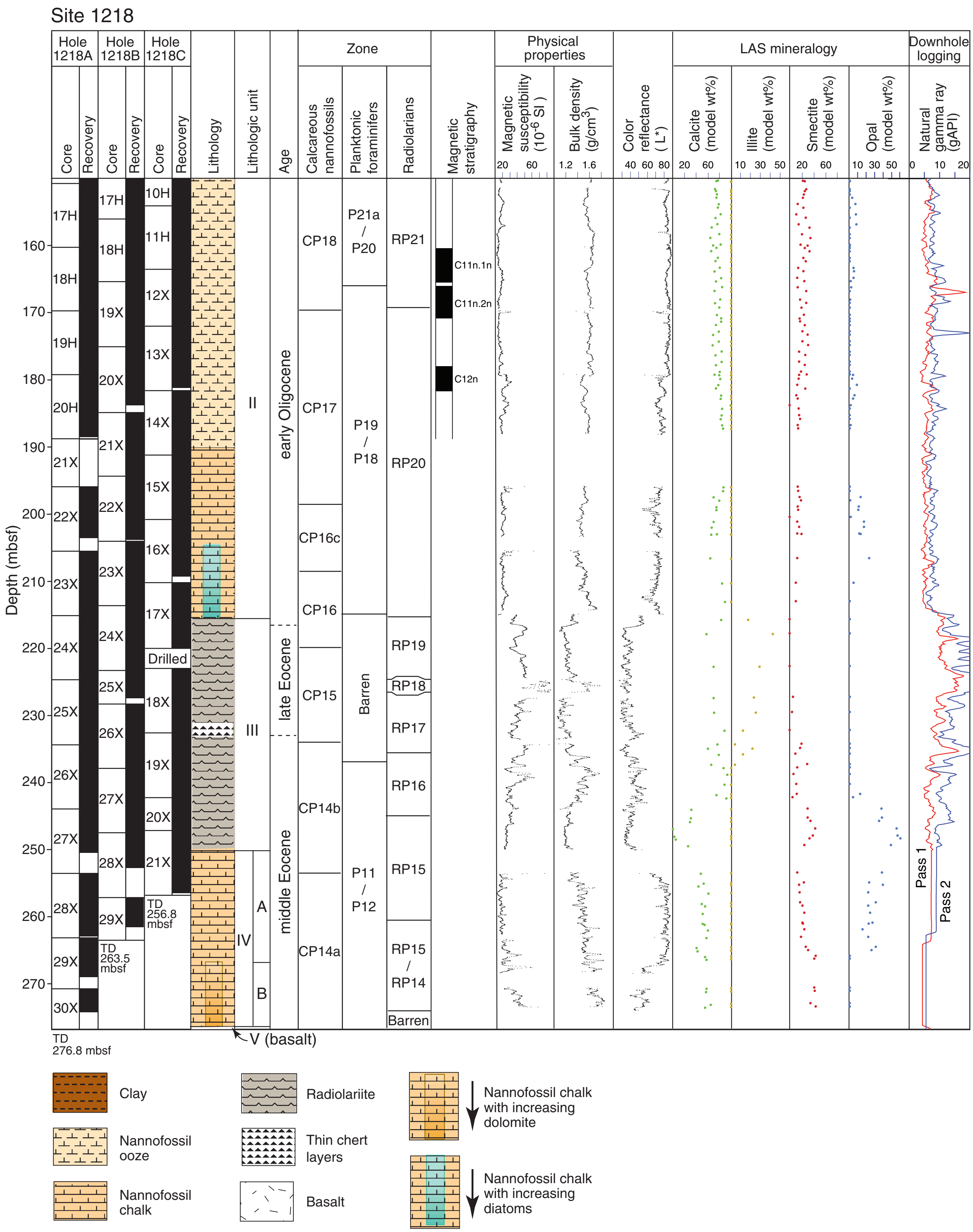

Figure F4. Close-up digital photograph of manganese nodule (at 95–97 cm) within Unit I (interval 199-1218B-3H-2, 93–98 cm).

Figure F5. Close-up digital photograph of intact chert layer (48–61 cm) within Unit III (interval 199-1218A-25X-2, 40–72 cm).

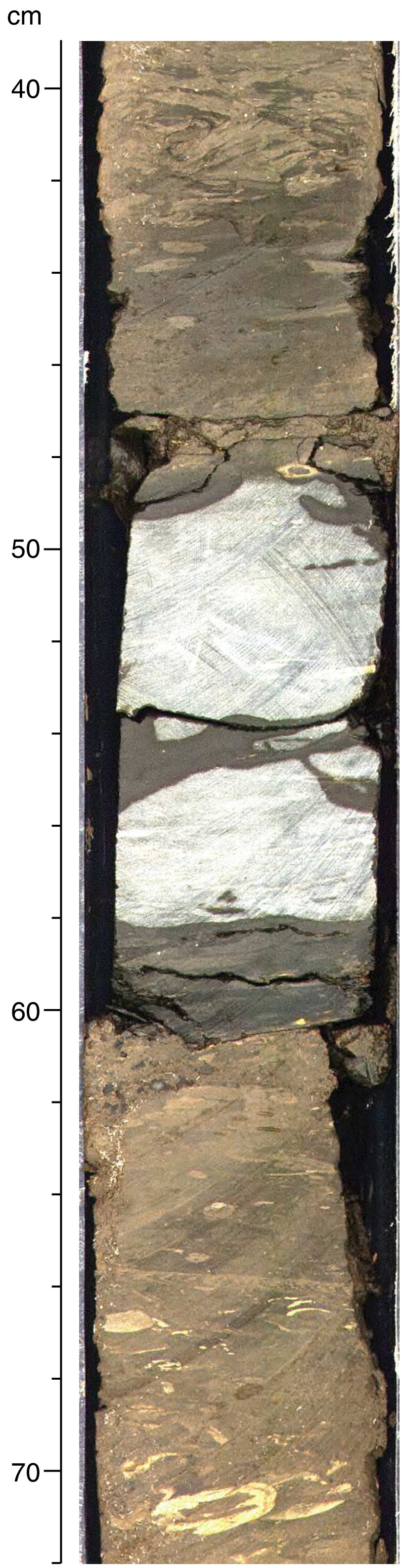

Figure F6. Close-up digital photograph of fault (at 4–11 cm) within Unit IVB (interval 199-1218A-30X-CC, 0–20 cm).

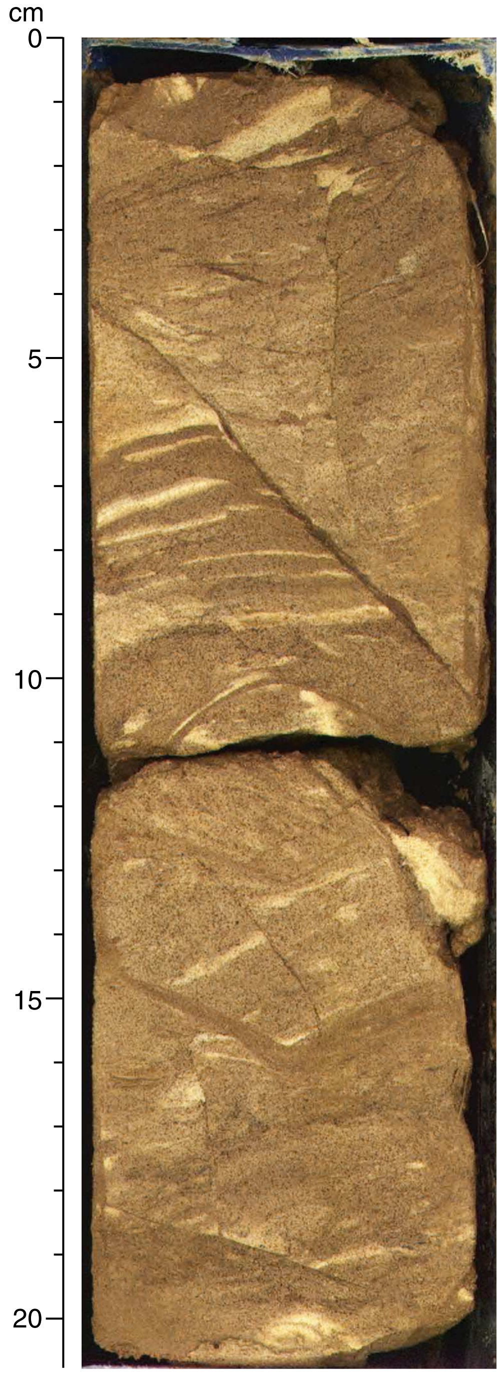

Figure F7. Biostratigraphic zonation at Site 1218. Gray shaded bar = interval for which no zonation could be assigned with confidence owing to severe reworking of radiolarian assemblages. Horizontal dashed lines = boundary can only be approximated by available biostratigraphy. Vertical dashed lines = absence of intervening zonal markers prevents further subdivision of the zonation. TD = total depth. (Continued on next page.)

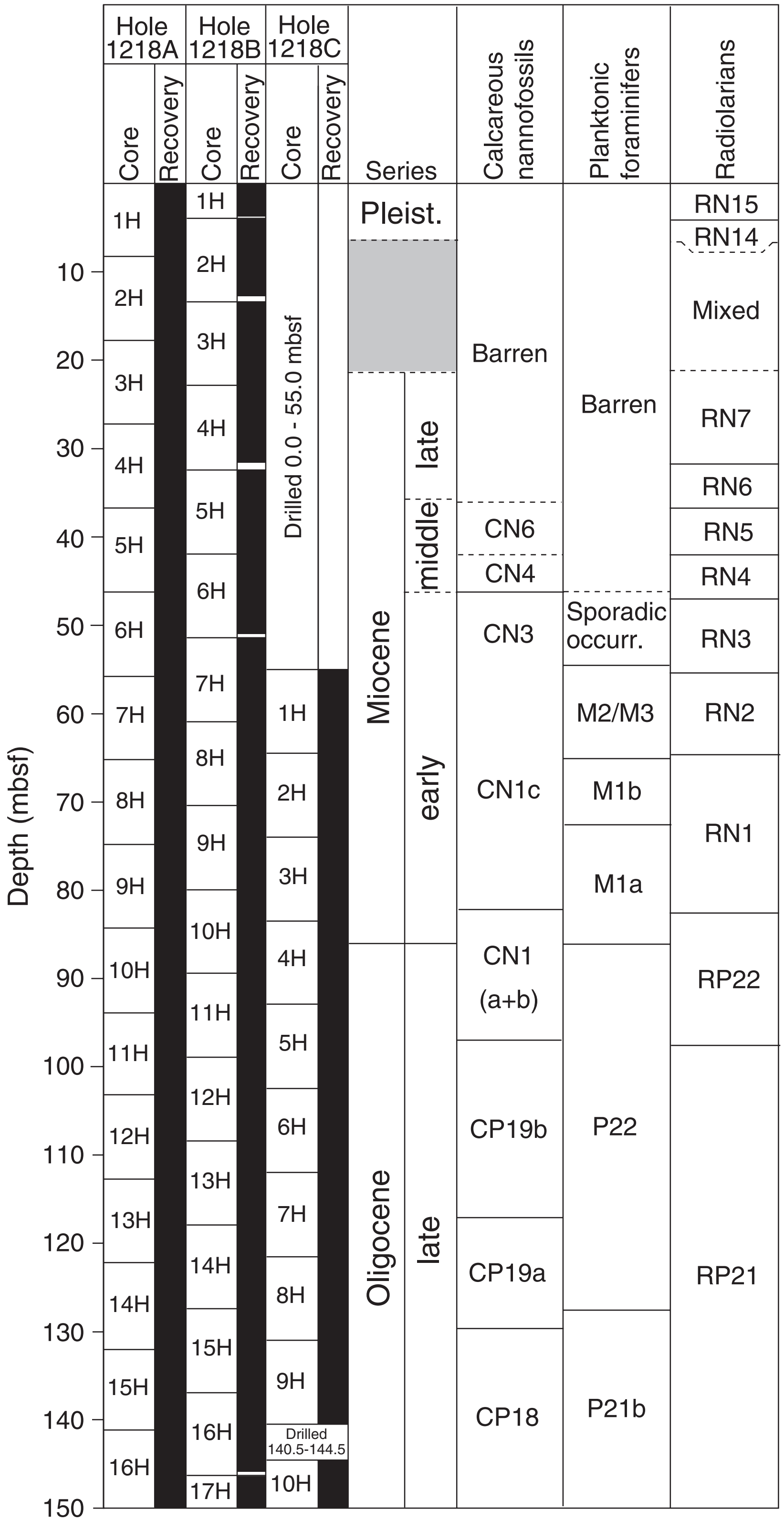

Figure F7 (continued).

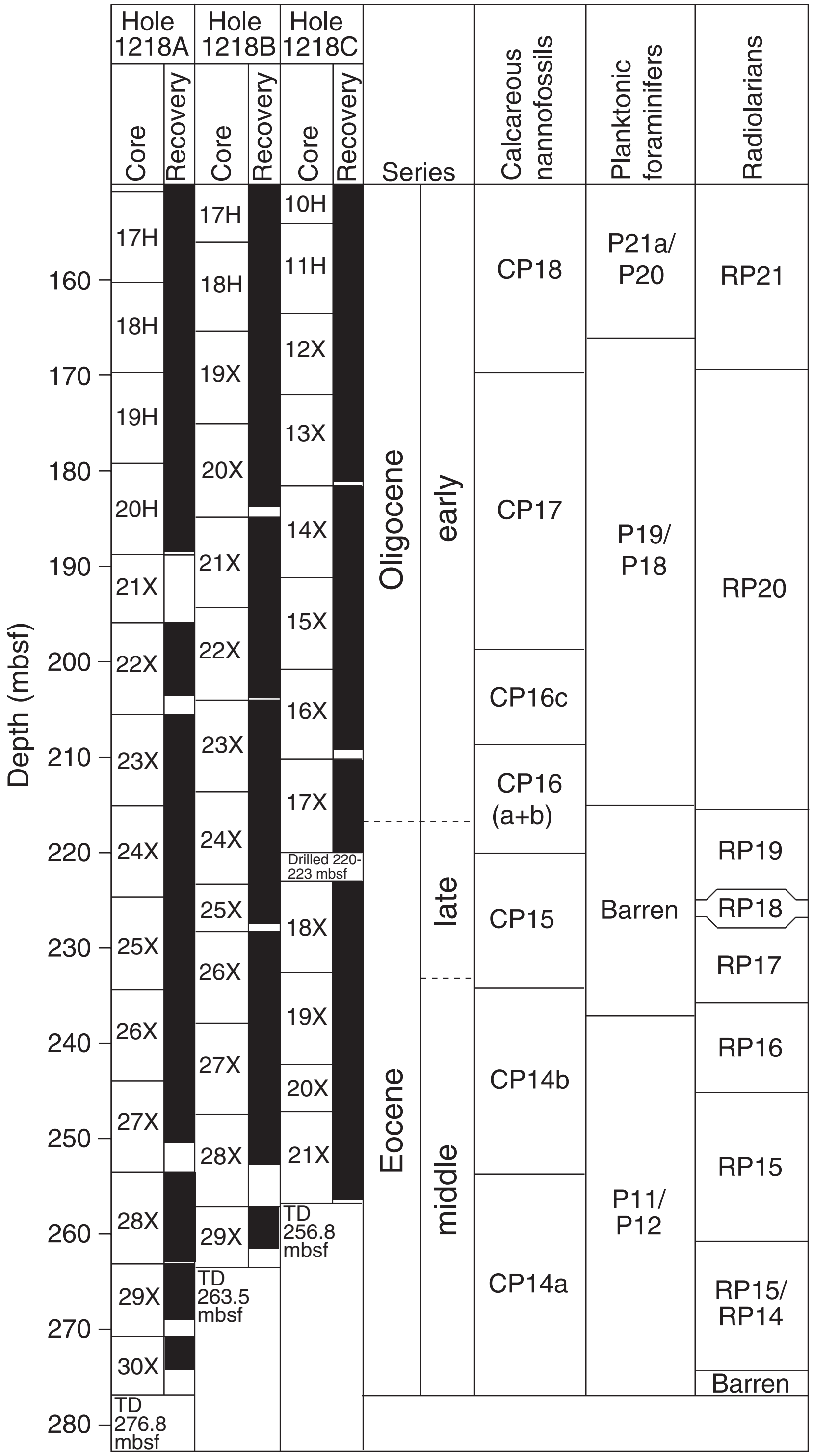

Figure F8. Distribution patterns of selected calcareous nannofossil taxa at the Oligocene–Miocene transition in Holes 1218A and 1218B.

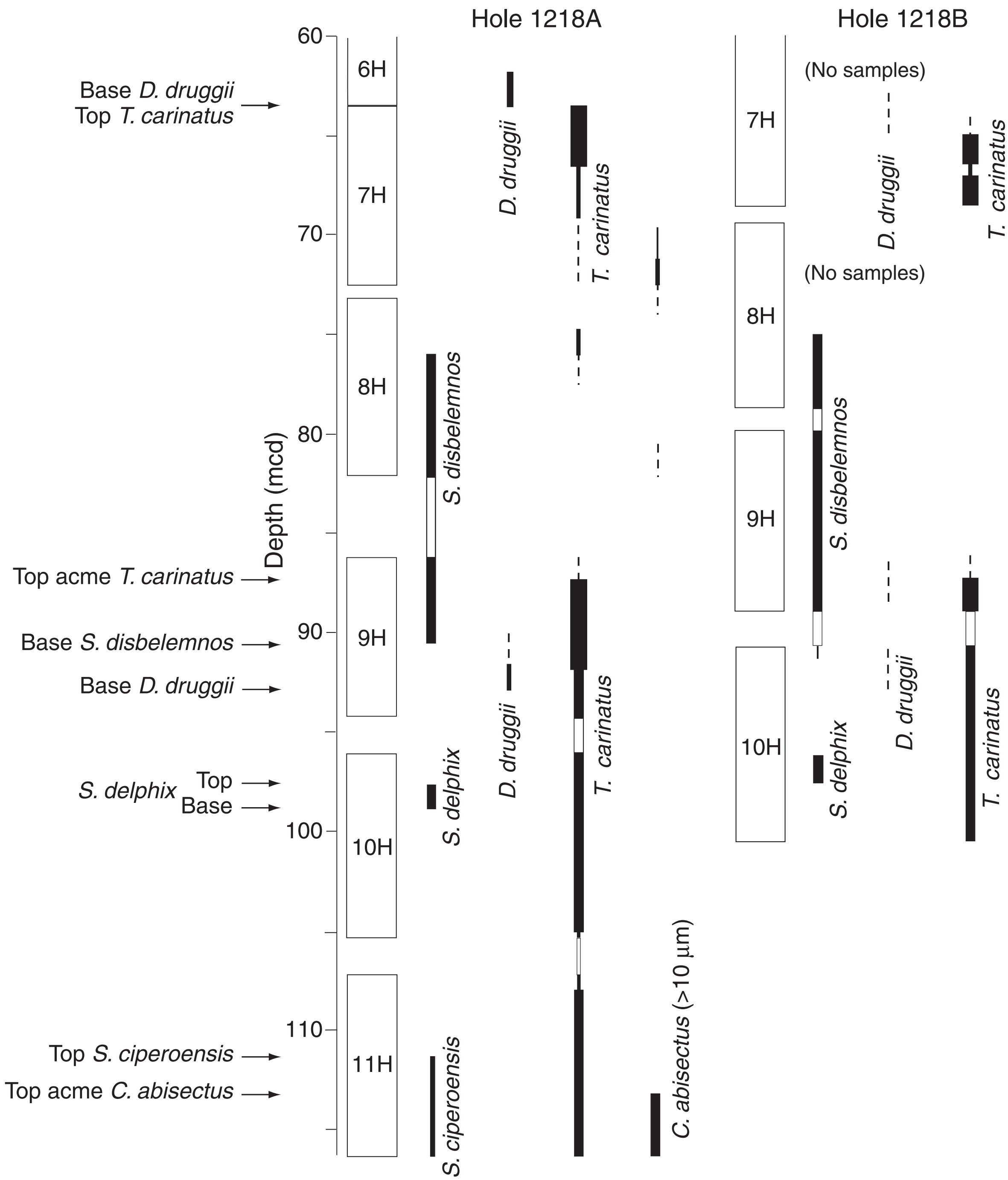

Figure F9. Photomicrographs of the wall texture in benthic foraminifers showing good preservation of the original crystalline test structure. **A.** Cross-extinction pattern of the polarized wall, indicating fragments of radial texture of *Fissurina* sp. from middle Eocene. **B.** Granular texture of *Oridorsalis umbonatus* from the early Miocene. Darker areas are due to overlap of additional broken walls.

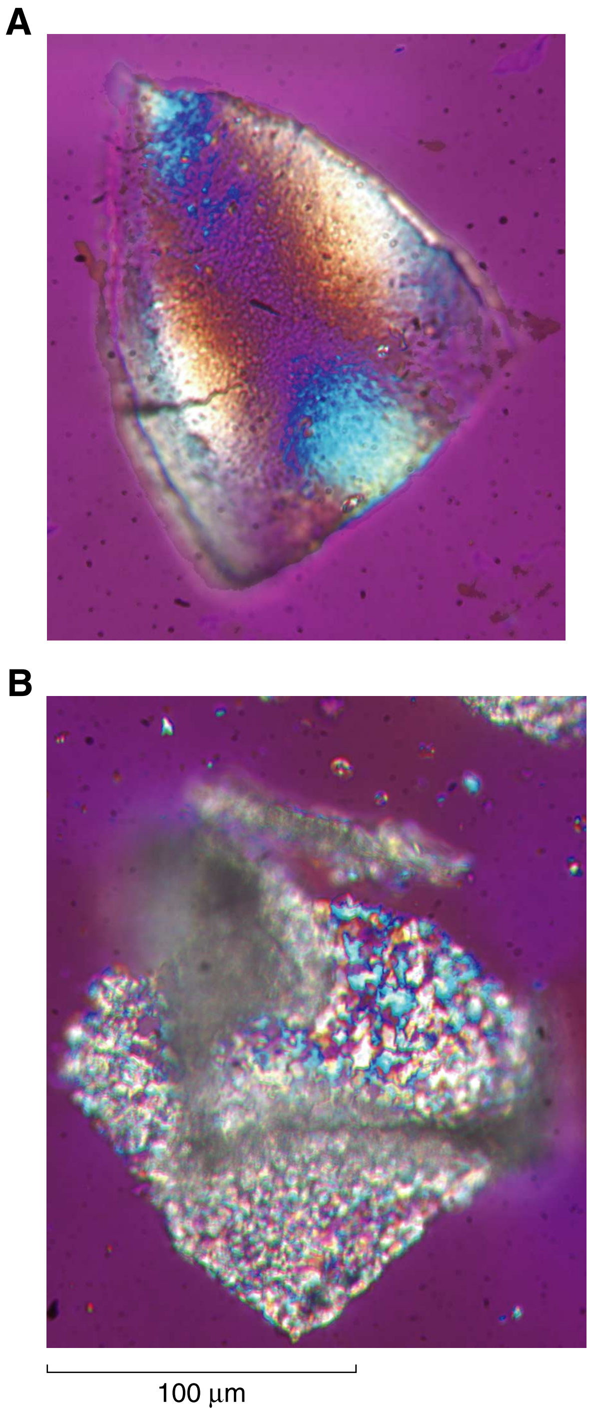

Figure F10. Archive-half magnetization intensities after AF demagnetization at a peak field of 20 mT at Hole 1218A. Lithologic units are shown on the right.

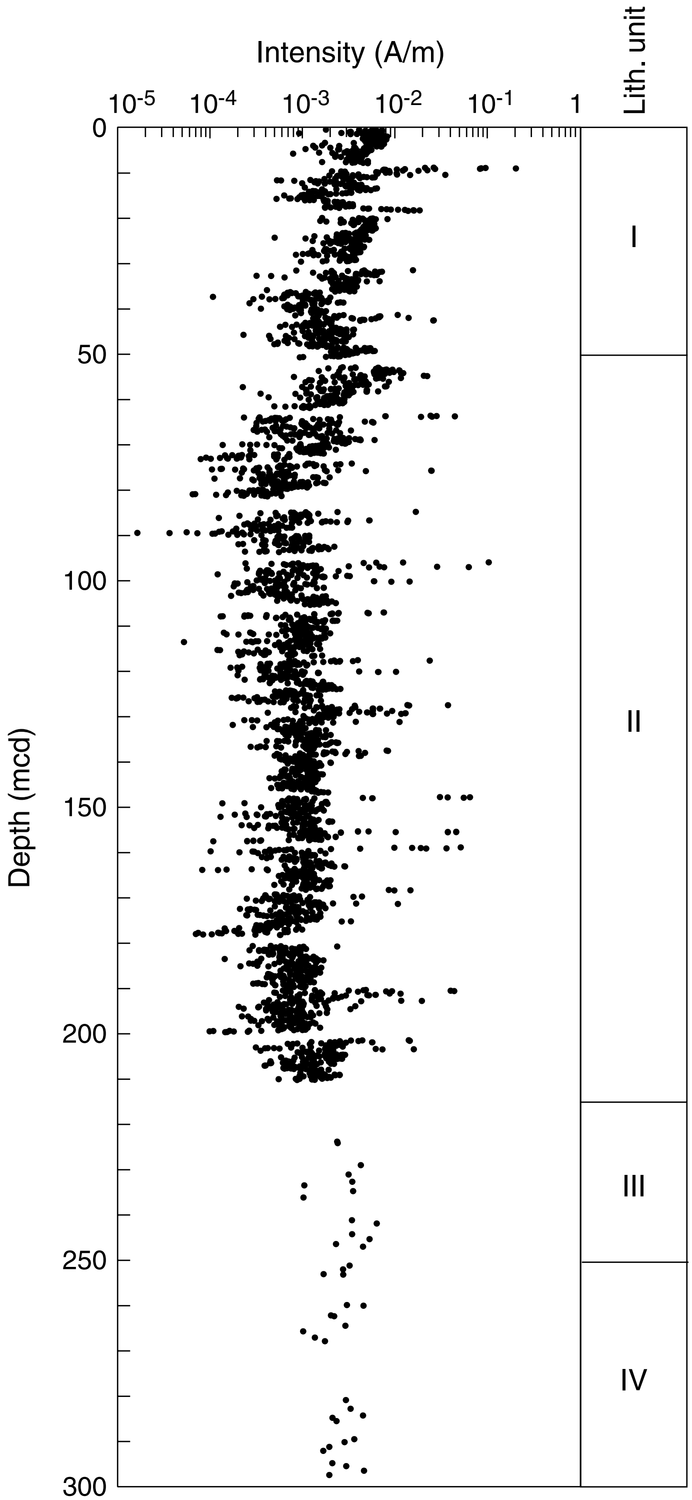

Figure F11. Equal area stereoplots of the ChRM directions calculated from discrete samples from Hole 1218A. The samples were divided into two sets according to their age (Miocene and Oligocene). Notice the coexistence of both north and south downward-pointing and shallow-magnetization directions, revealing the equatorial position of these sediments. Dec = declination, Inc = inclination, α_{95} = 95% confidence interval, k = Fisher precision parameter, R = length of vector, N = number of samples, solid circles = lower hemisphere, open circles = upper hemisphere.

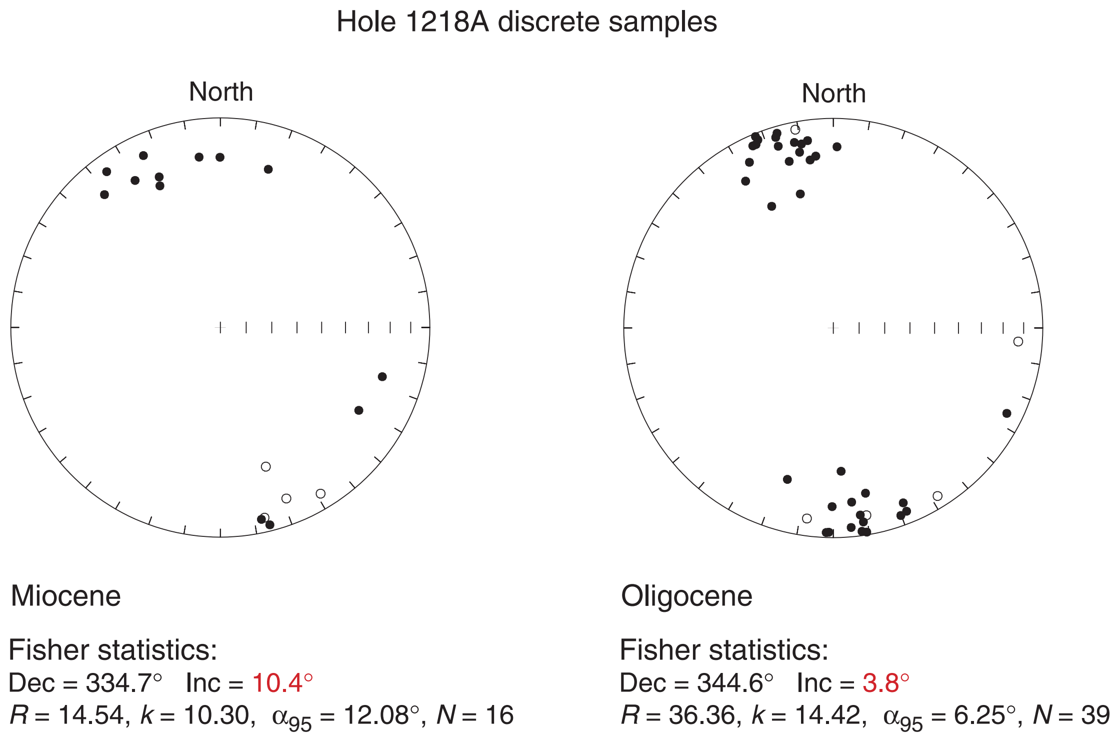

Figure F12. Composite magnetic stratigraphy at Site 1218. Virtual geomagnetic pole (VGP) latitudes were obtained after partial AF demagnetization of continuous measurements at a peak field of 20 mT. Polarity column shows interpreted zones of normal (black) and reversed (white) magnetization, and gray intervals indicate zones with an uncertain polarity interpretation. **A.** Top 24 m of Hole 1218B, including cores not oriented with the Tensor tool. (Continued on next two pages.)

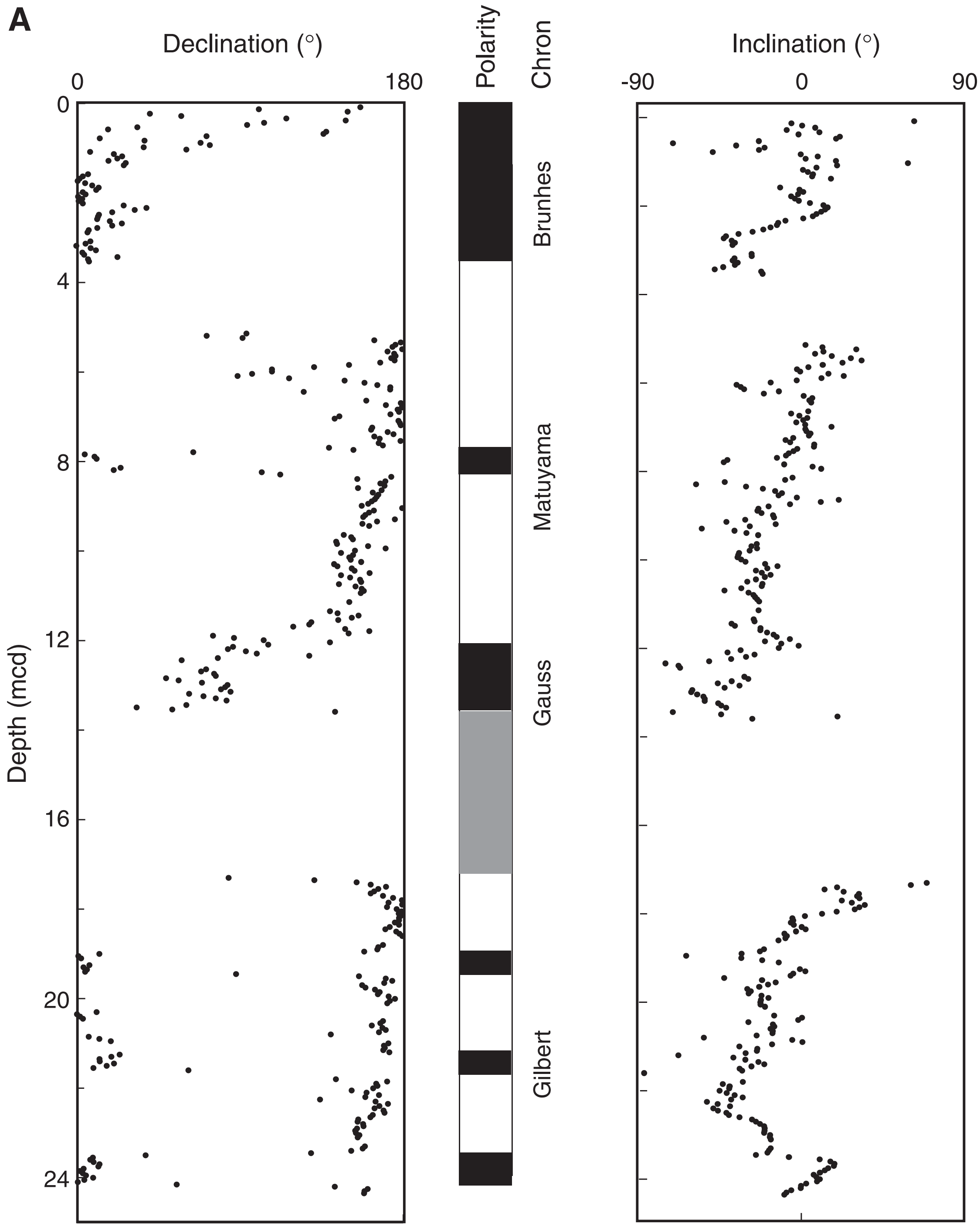

Figure F12 (continued). B. Early Miocene–Pliocene section.

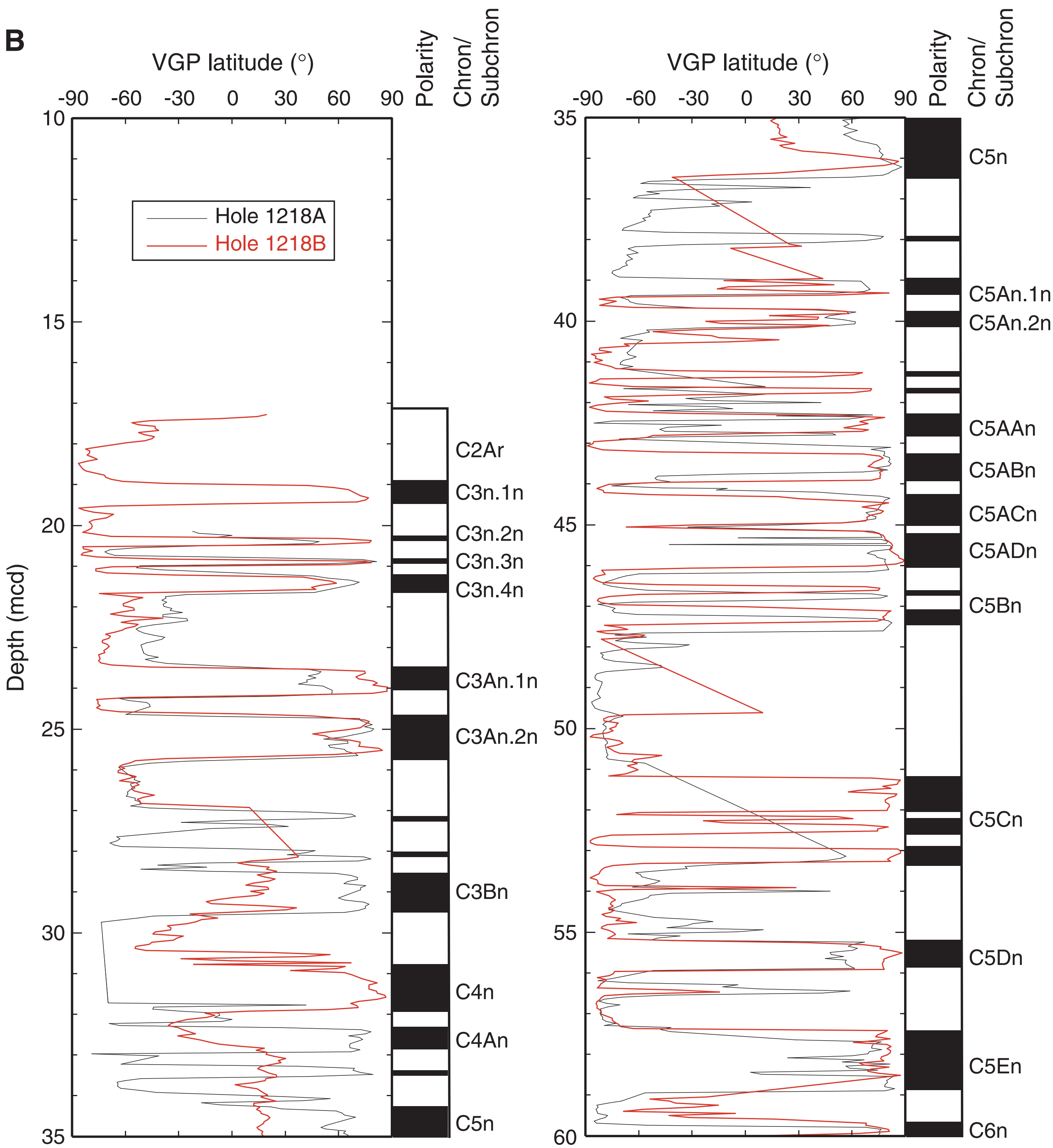

Figure F12 (continued). C. Early Oligocene–early Miocene section.

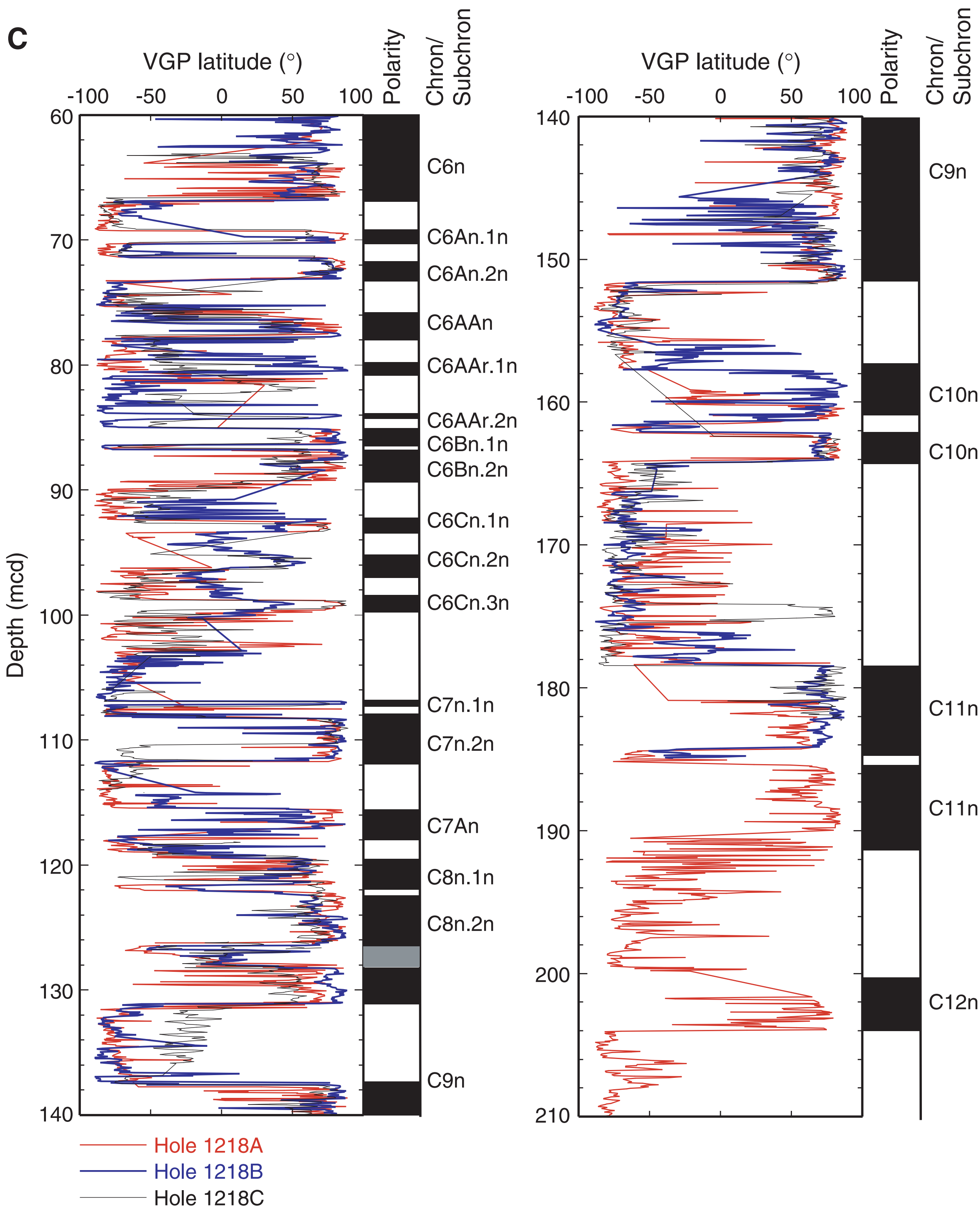

Figure F13. Gamma ray attenuation (GRA) bulk density data for Holes 1218A (left curve in each panel), 1218B (middle curve in each panel), and 1218C (right curve in each panel) plotted vs. composite depth. The data from Holes 1218B and 1218C are offset by constants for illustration purposes. All data sets are smoothed with a nine-point Gaussian filter. Intervals with obvious flow-in or drilling disturbance were removed from the data sets (see Table **T10**, p. 102).

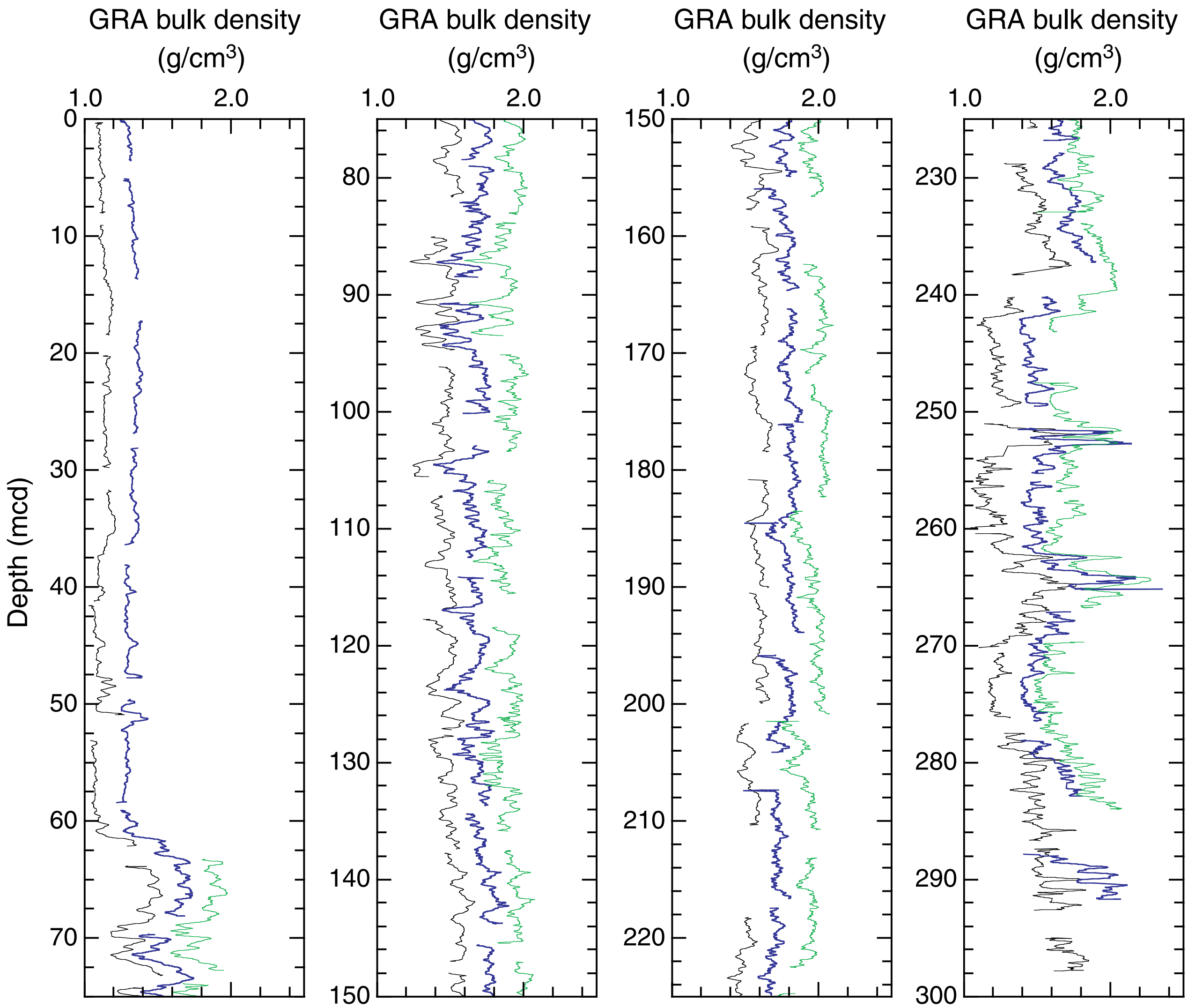

Figure F14. Magnetic susceptibility data for Holes 1218A (left curve in each panel), 1218B (middle curve in each panel), and 1218C (right curve in each panel) plotted vs. composite depth. The data from Holes 1218B and 1218C are offset by constants for illustration purposes. All data sets are smoothed with a nine-point Gaussian filter. Intervals with obvious flow-in or drilling disturbance were removed from the data sets (see Table T10, p. 102).

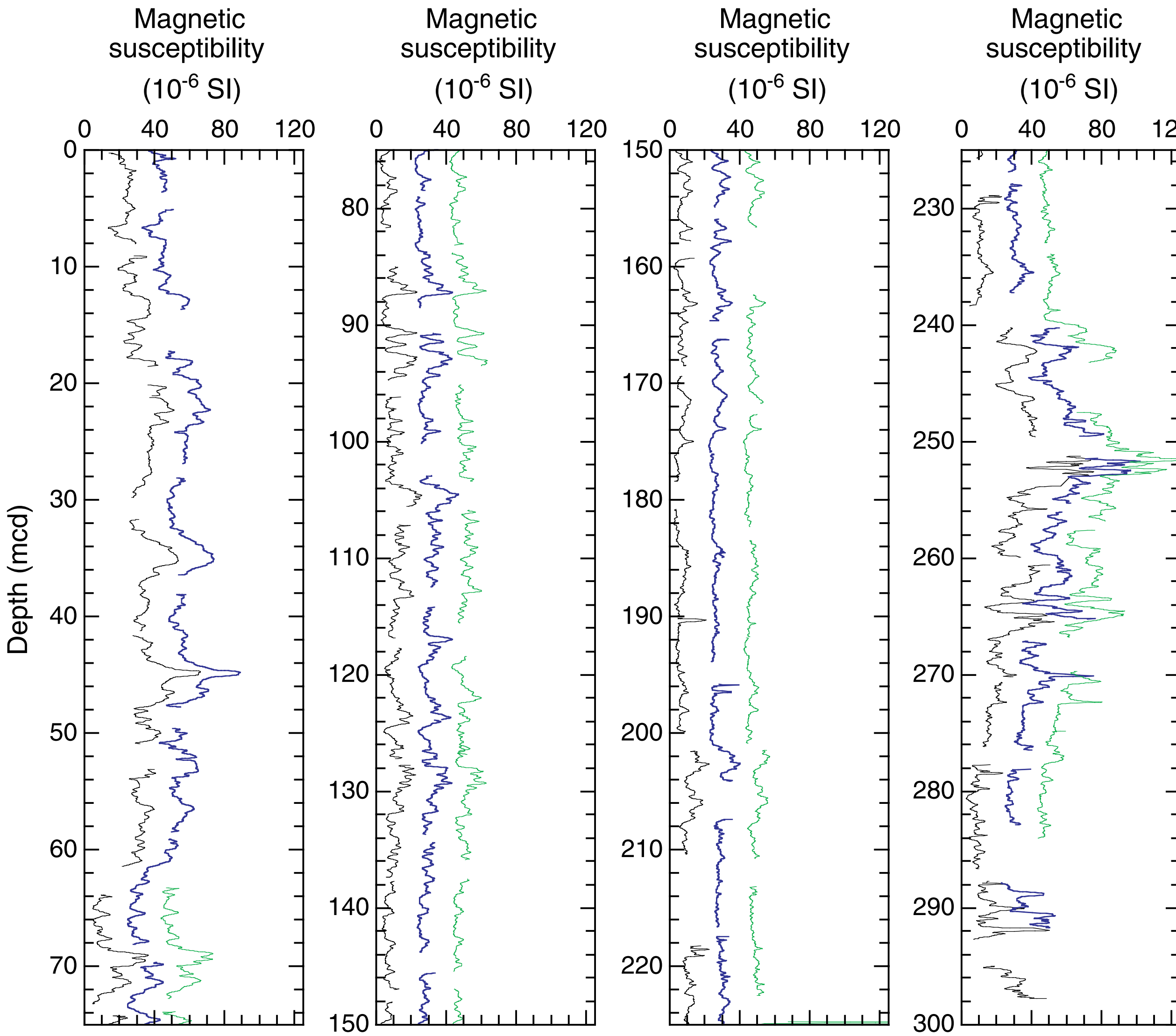

Figure F15. Spliced records of gamma ray attenuation (GRA) bulk density and magnetic susceptibility. GRA bulk density values appear either as blue or lighter lines in each panel. Note the anticorrelation between the parameters, particularly between 80 and 140 mcd. Cyclical variations in the carbonate/(clay + silica + terrigenous) ratio, with high proportions of carbonate corresponding to higher density and lower MS values, are evident throughout the record.

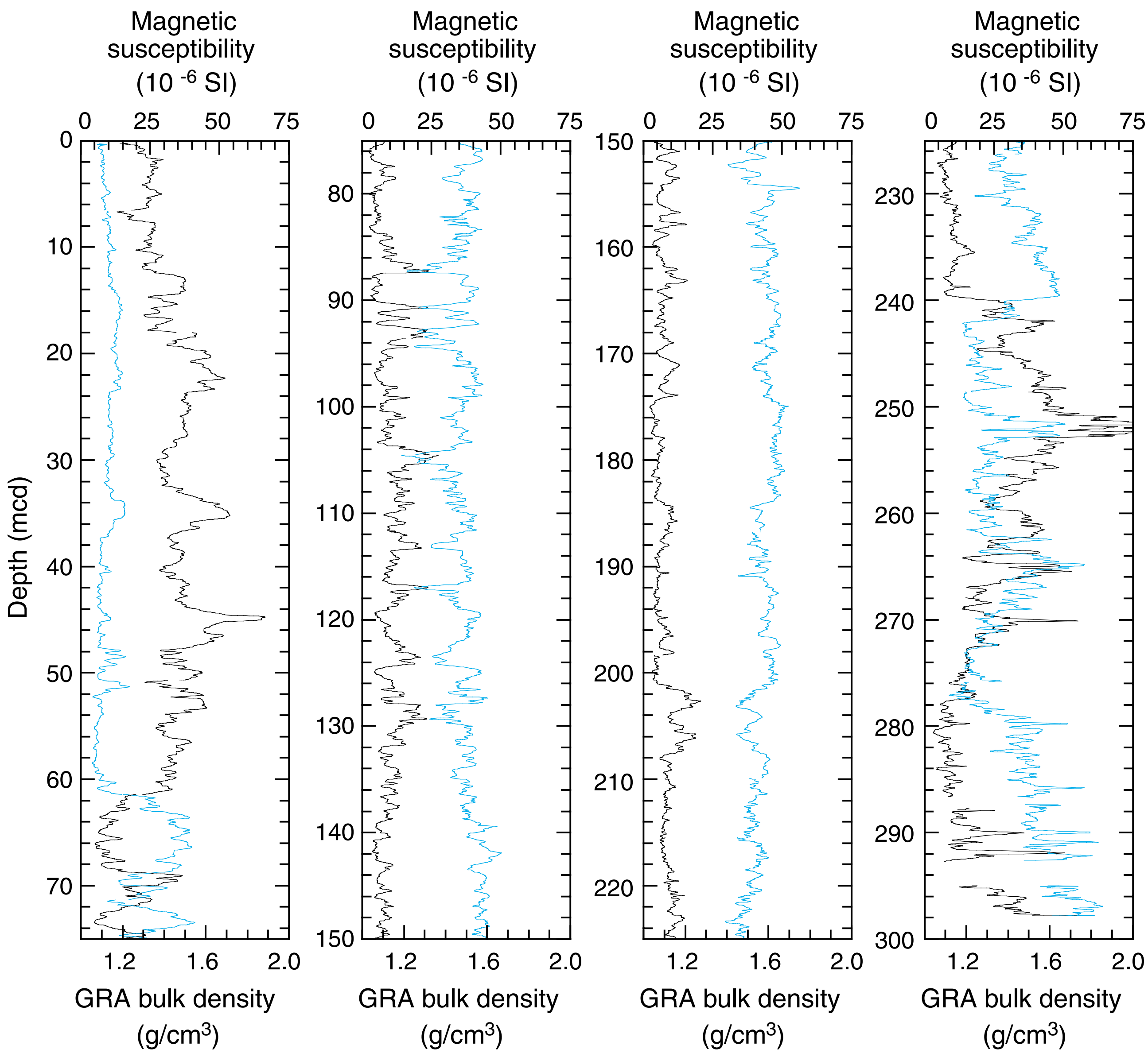

Figure F16. Spliced records of gamma ray attenuation (GRA) bulk density, magnetic susceptibility, and the color reflectance (L*) parameter shown for the entire depth of Site 1218. Lithology changes are clearly visible.

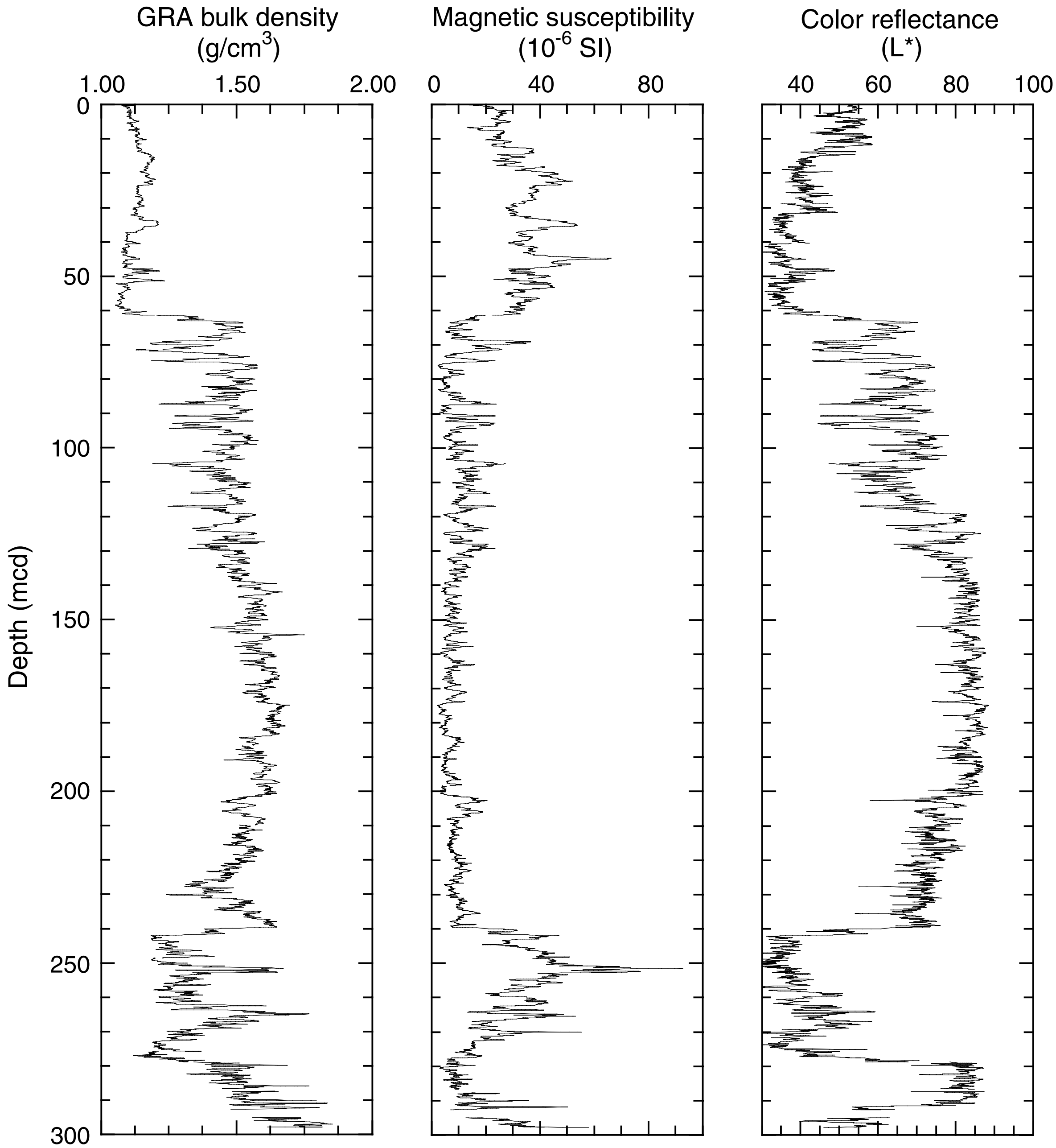

Figure F17. Offsets applied to each core vs. depth. The slope on this plot describes the relative increase in length of the composite depth record compared to the drill string–length measurement (mbsf). Below ~110 mbsf, the lithology changes to a stiffer, more chalklike nannofossil ooze consistent with a smaller expansion during the coring process. MCD = meters composite depth.

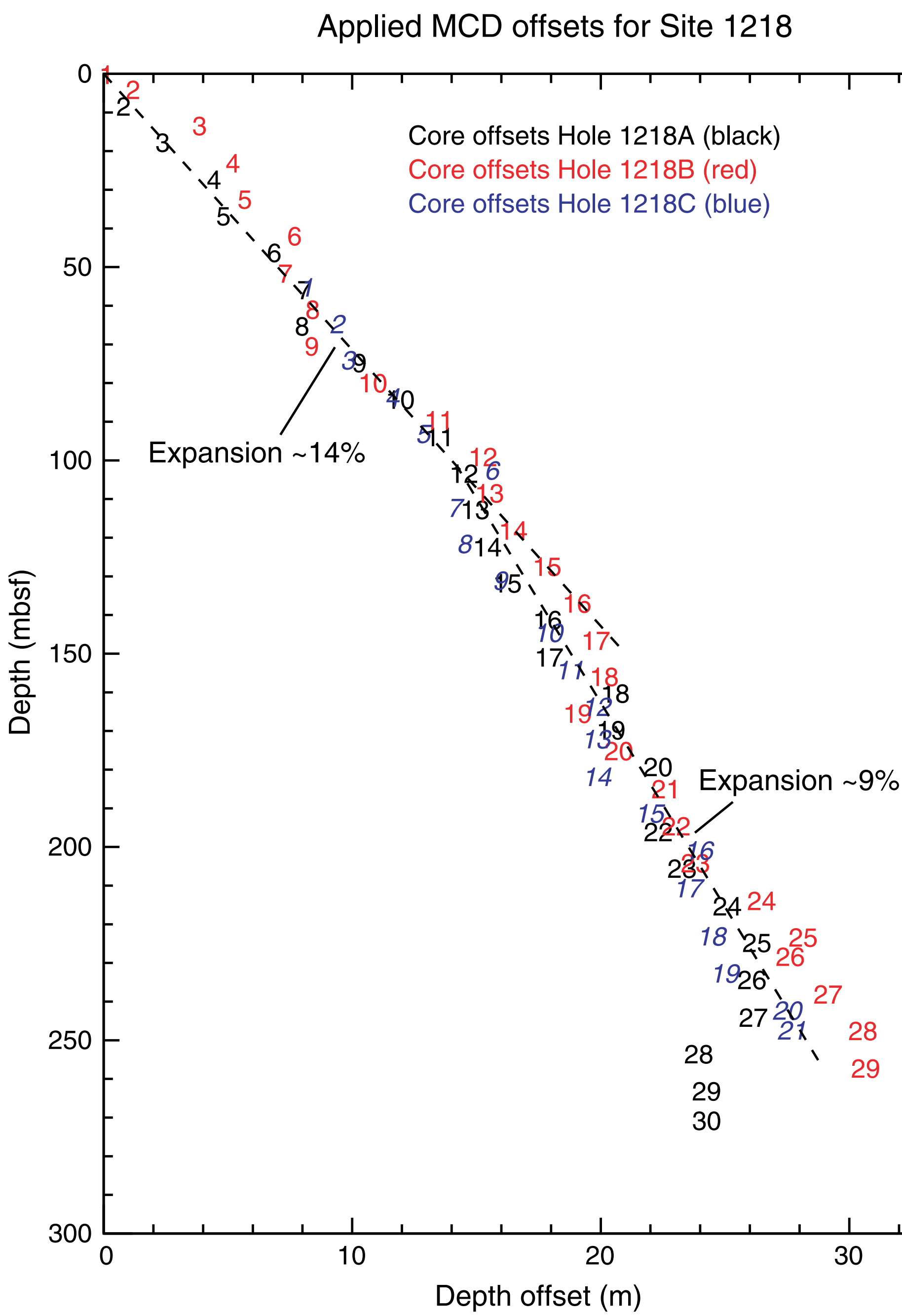

Figure F18. LSRs and chronostratigraphic markers.

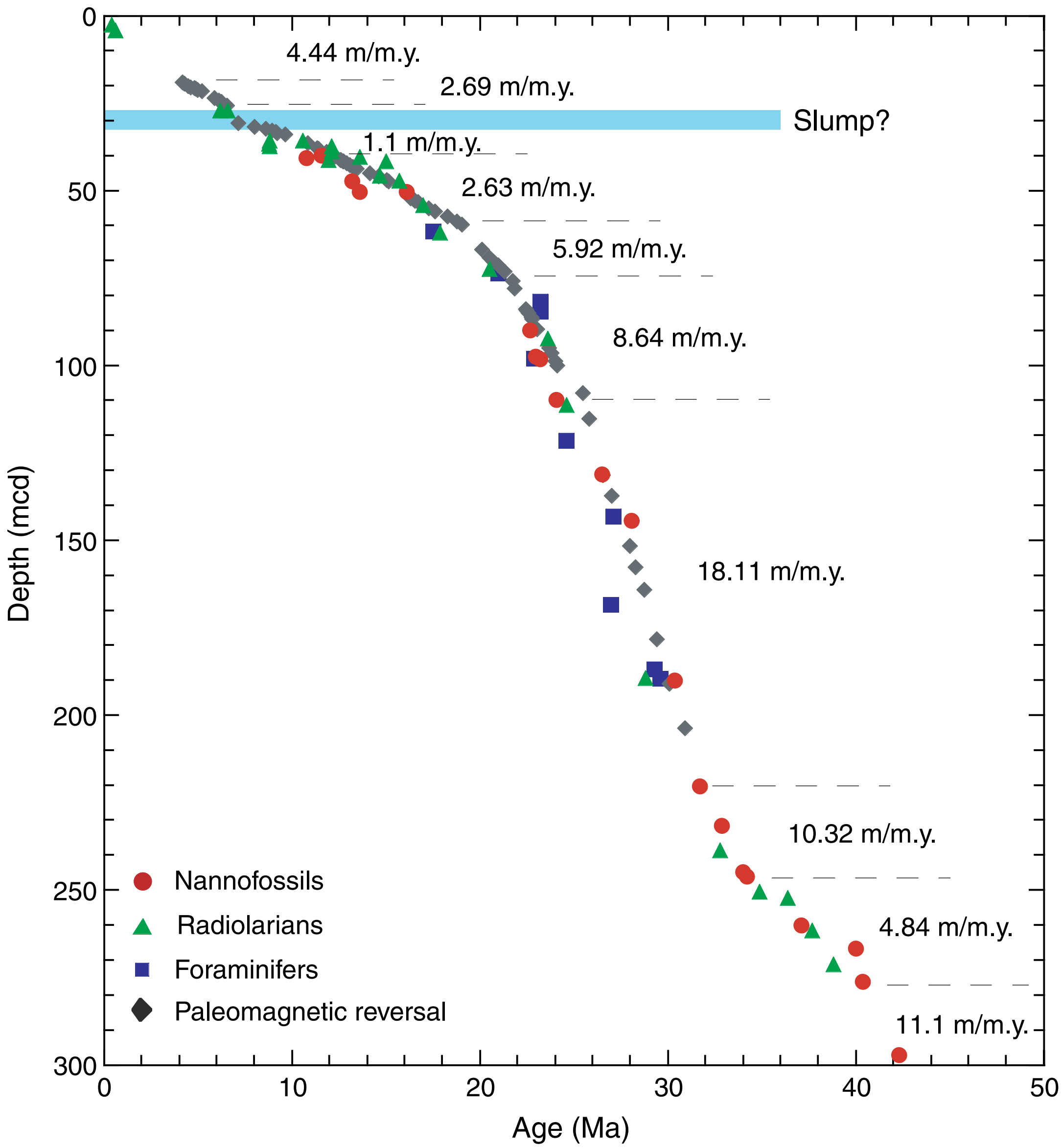

Figure F19. GRA bulk density records from site survey piston core EW9709-7P and the top 67 m of Site 1218. EW9709-7P is located at 8°47.658′N, 135°21.985′W, ~3 nmi south of Site 1218.

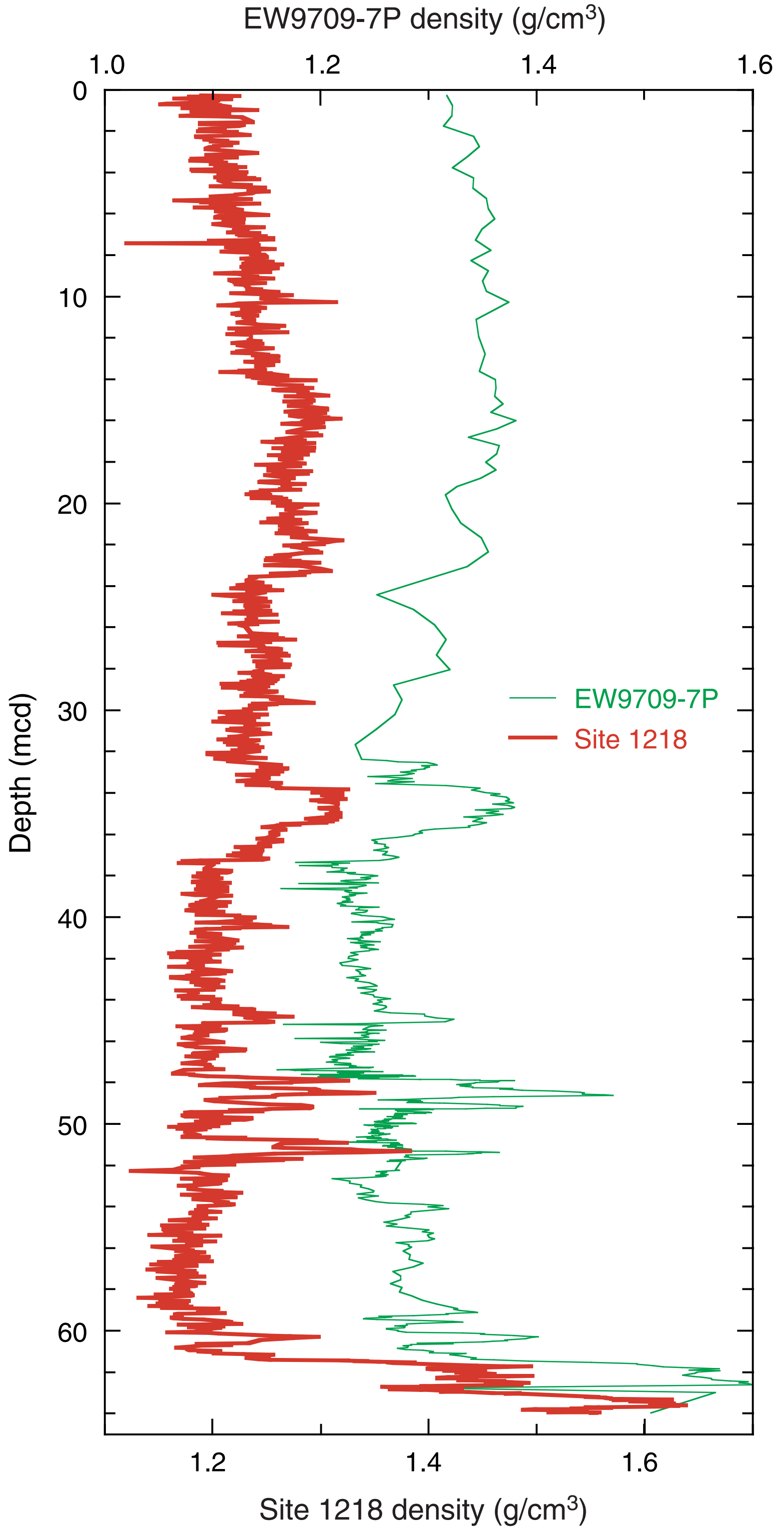

Figure F20. Mass accumulation rates (MARs) of sediments at Site 1218.

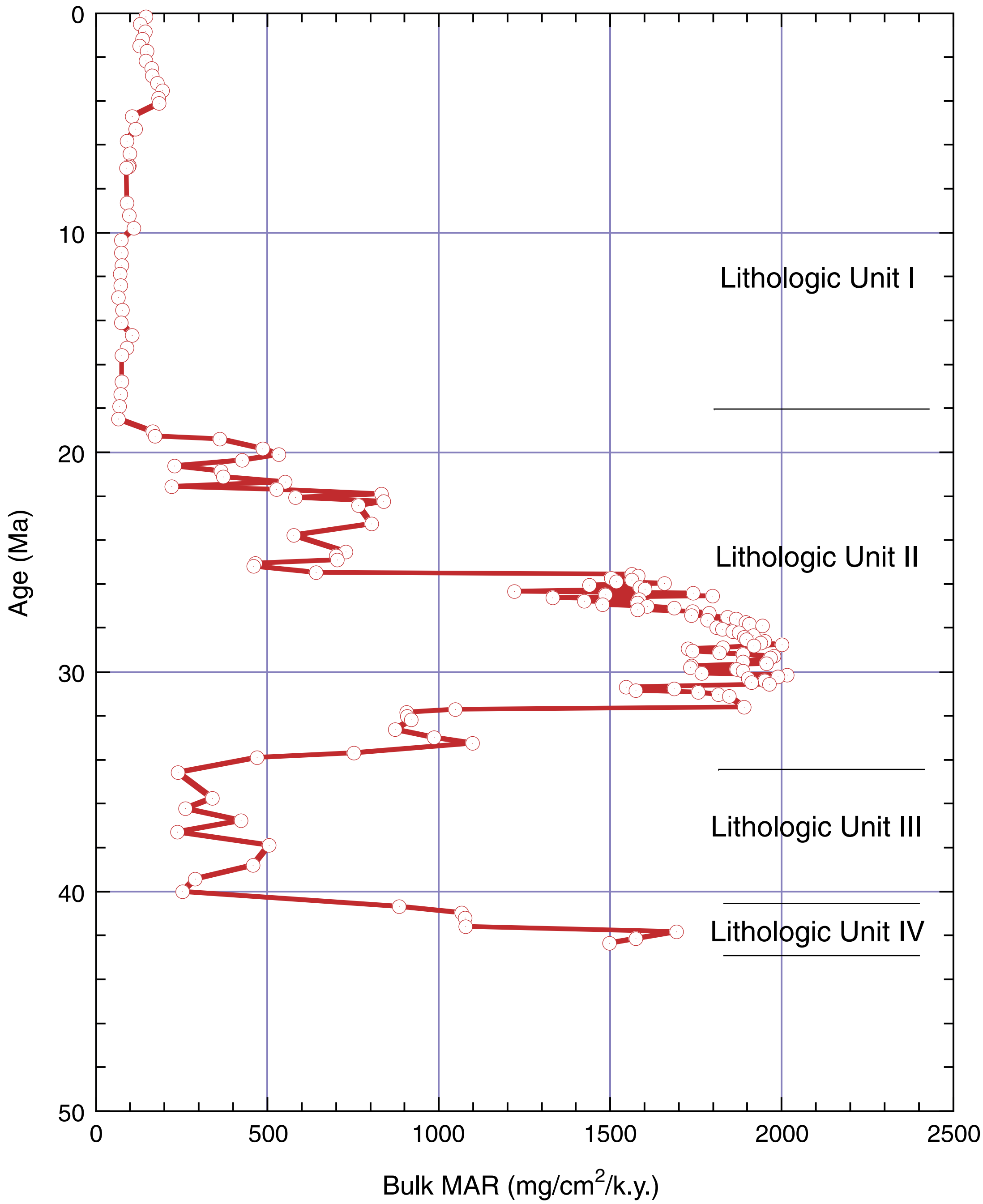

Figure F21. Interstitial water data from Site 1218. Solid circles = Ca, crosses = Mg.

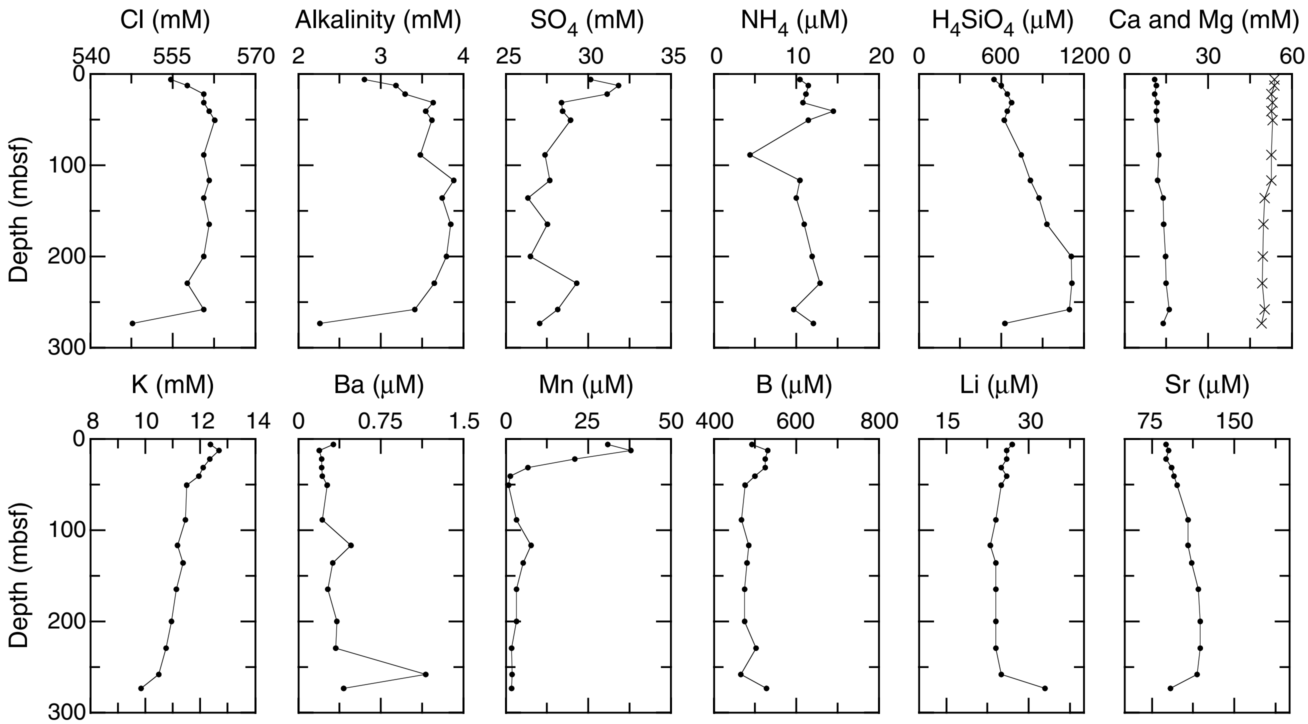

Figure F22. Bulk-sediment data from Site 1218. Ca values higher than 35.9 wt% are out of the range of the standards (see **"Geochemistry,"** p. 20, in the "Explanatory Notes" chapter).

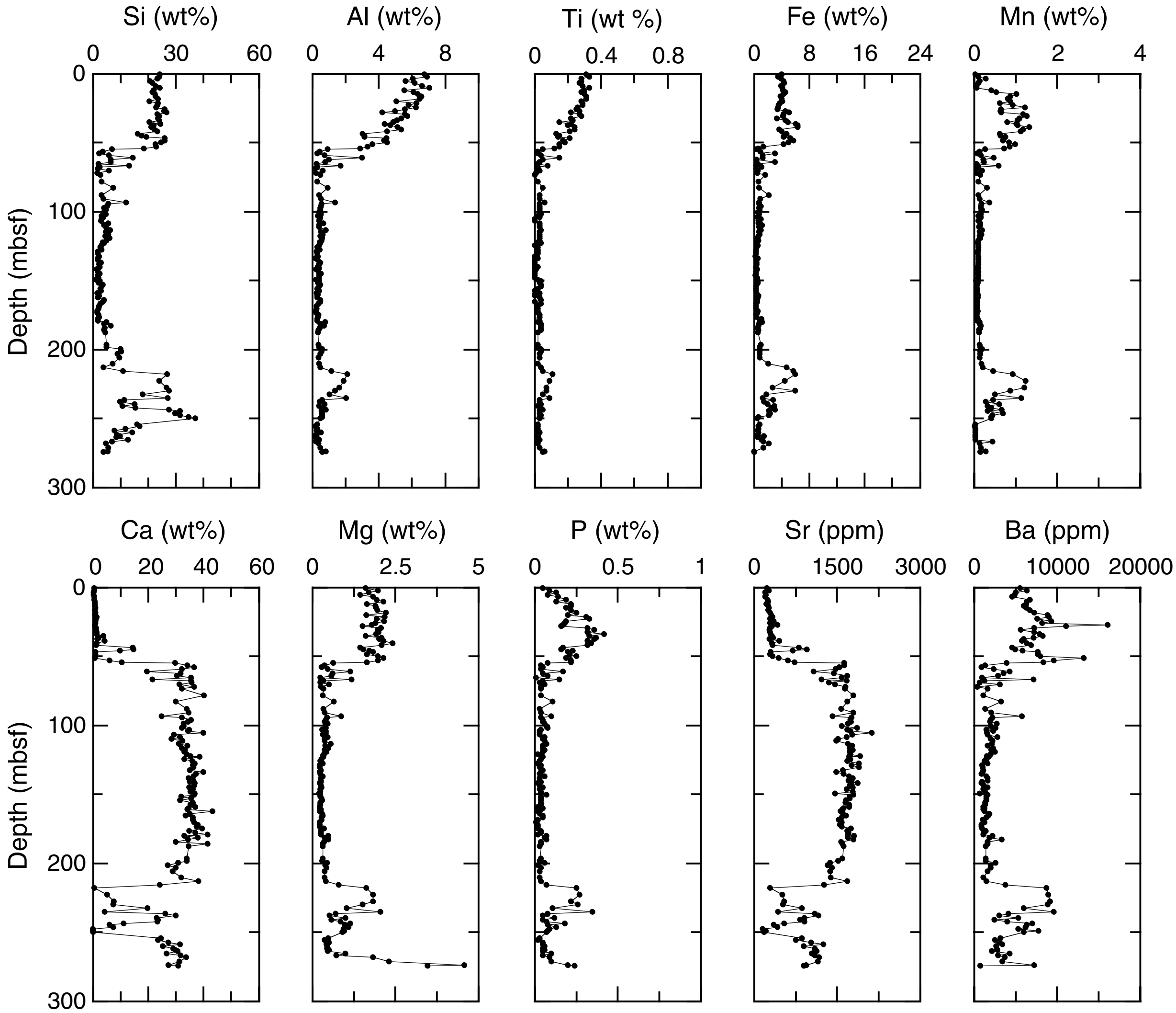

Figure F23. $CaCO_3$ and Ca data from Site 1218. $CaCO_3$ values higher than 90 wt% are calculated from Ca values out of the range of the standards (see **"Geochemistry,"** p. 20, in the "Explanatory Notes" chapter).

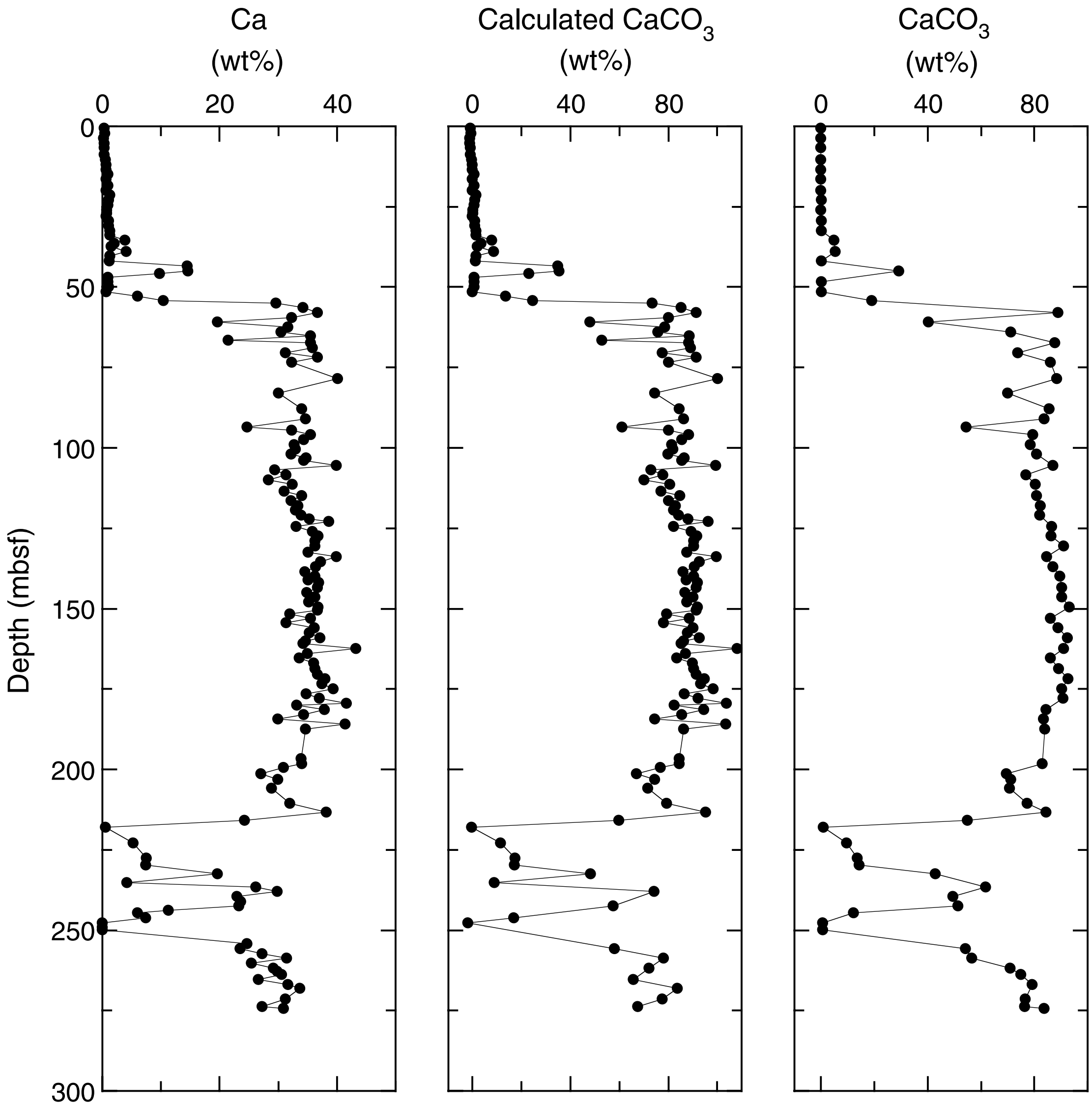

Figure F24. MAD measurements from Hole 1218A. **A.** Porosity (solid symbols) and water content (open symbols). **B.** Discrete-sample wet bulk density (open symbols) and gamma ray attenuation (GRA) bulk density (line). **C.** Grain density. Lithologic Units I–IV are noted on the right side of the figure.

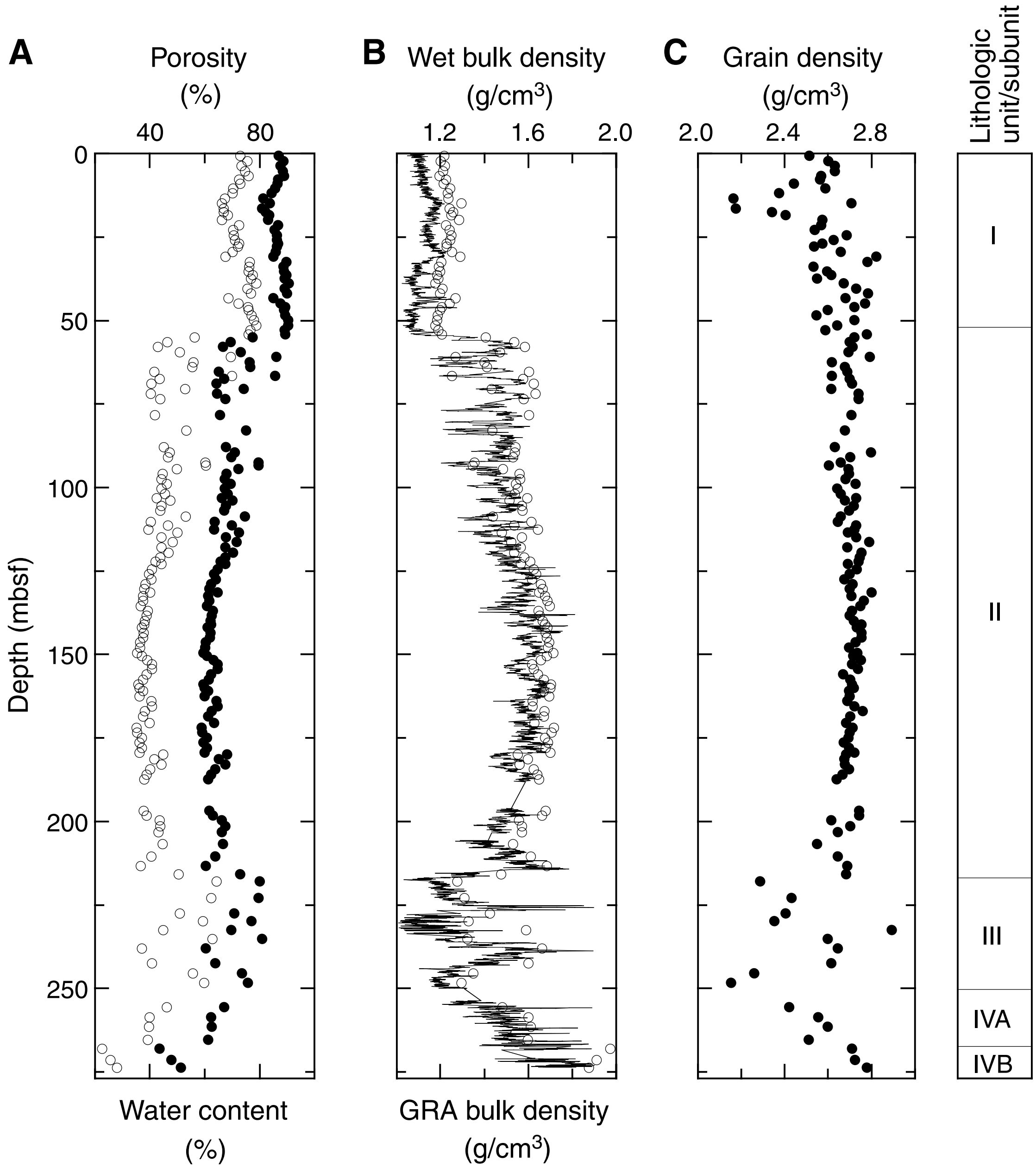

Figure F25. (**A**) Wet and (**B**) dry bulk density from discrete samples from Hole 1218A plotted with gamma ray attenuation (GRA) density interpolated with a 20-cm-wide Gaussian window. Data are from APC cores (solid symbols; solid regression line) and XCB cores (open symbols; dashed regression line).

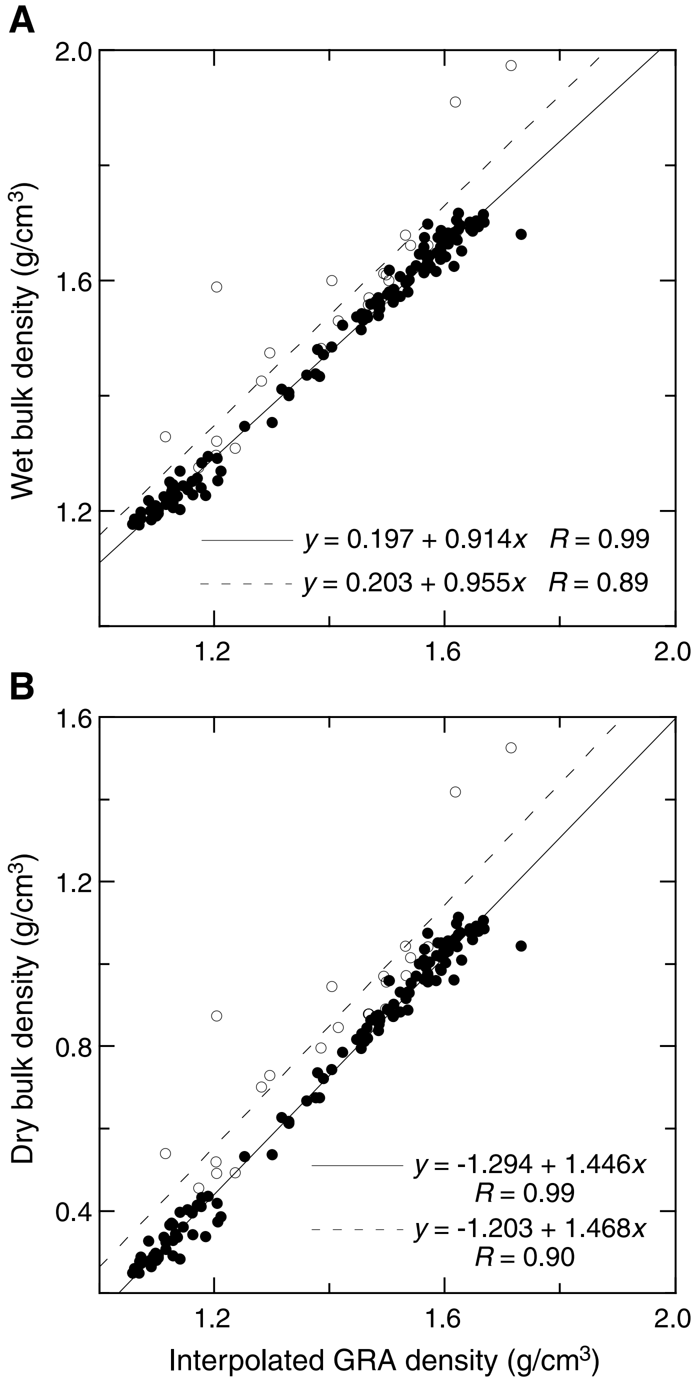

Figure F26. LAS mineralogy determinations for Hole 1218A. Lithologic Units I–IV are noted to the left of the figure. TD = total depth.

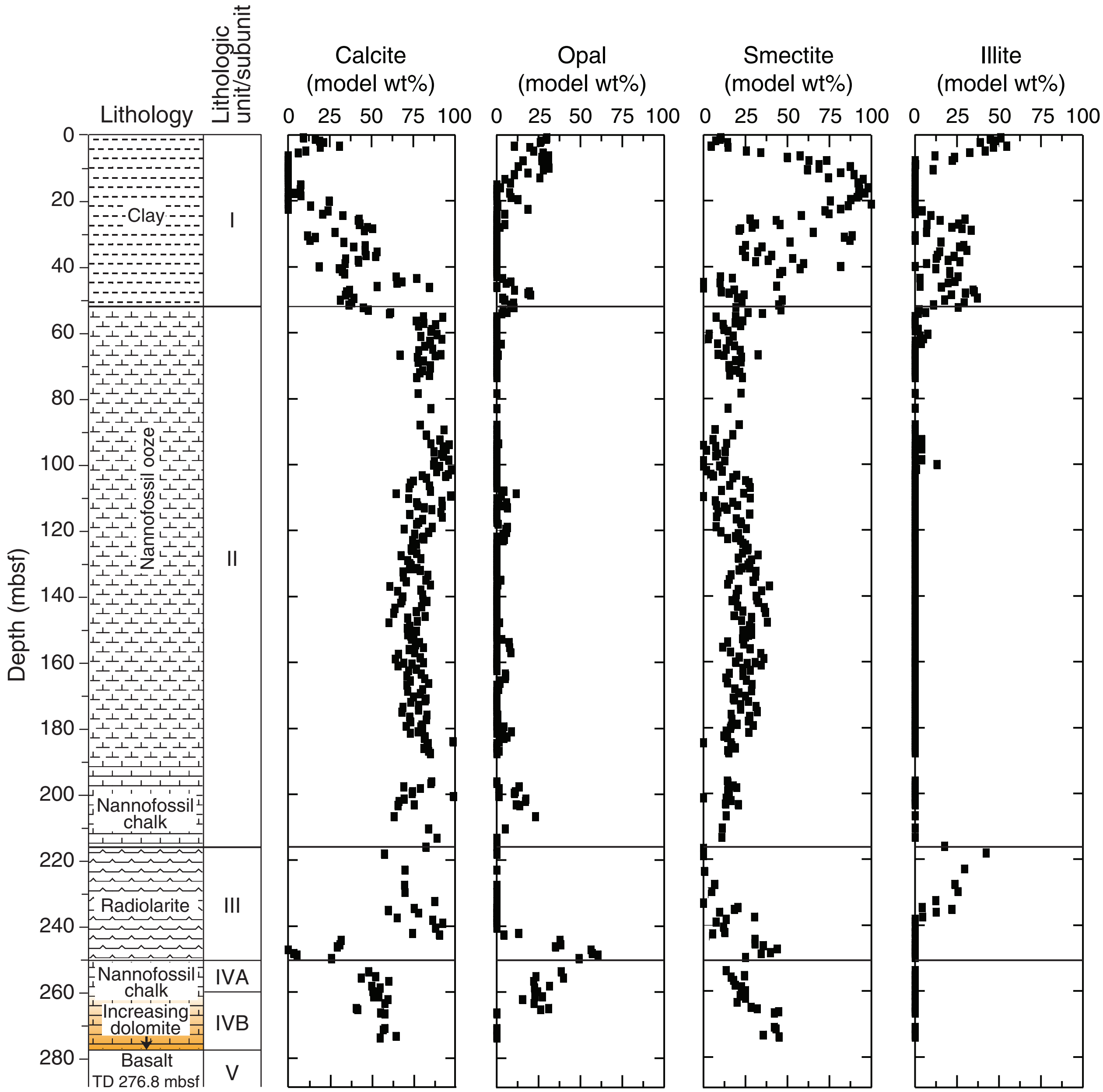

Figure F27. Compressional wave velocity from the PWL (line) and transverse velocity measurements of the insertion (diamonds) and contact probe (circles) systems for Hole 1218A. Lithologic Units I–IV are noted on the right side of the figure.

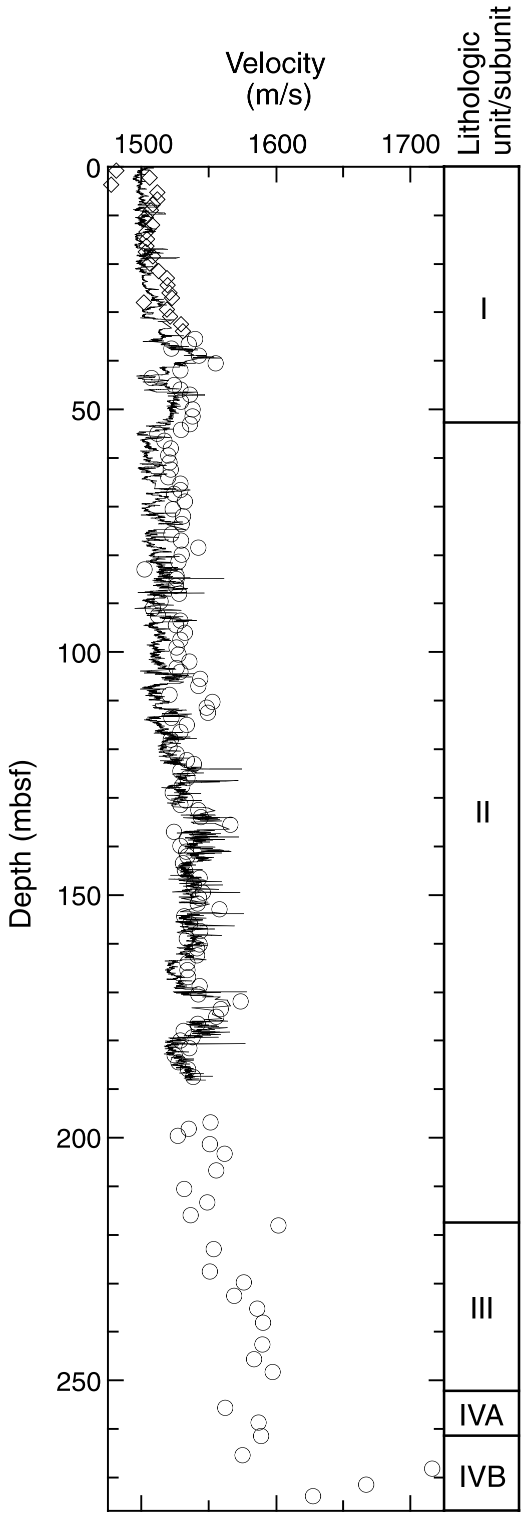

Figure F28. Compressional wave velocity (transverse) from the insertion and contact probe systems plotted with wet bulk density. Lithologic units are distinguished by symbols: Unit I insertion (solid circle), Unit I contact probe (open circle), Unit II (diamond), Unit III (triangle), Subunit IVA (open square), and Subunit IVB (solid square).

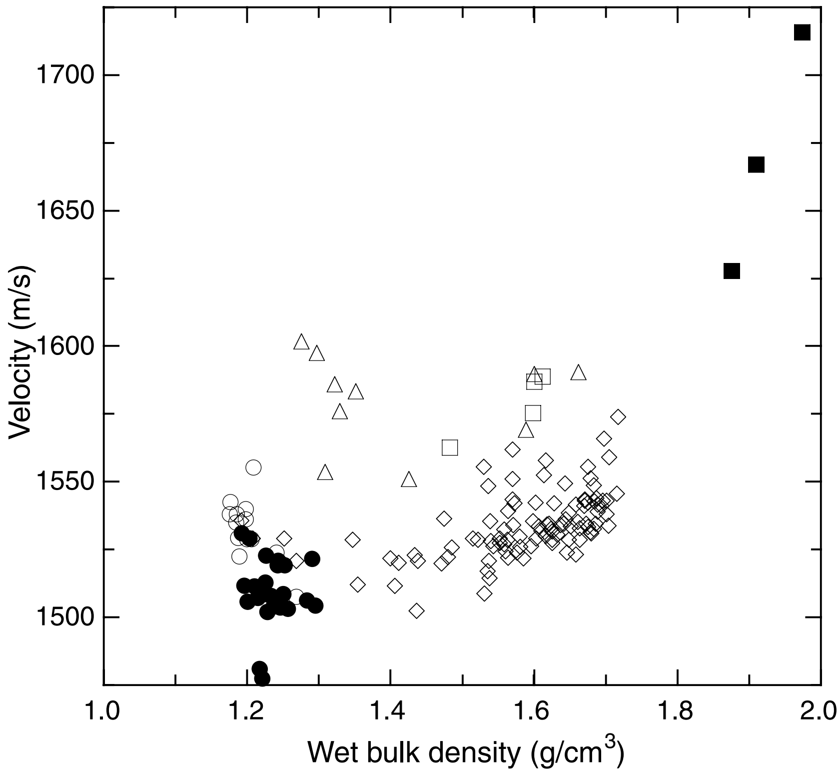

Figure F29. Thermal conductivity for the upper 180 m of Holes 1218A (solid circles) and 1218B (open circles). Lithologic Units I–IV are noted on the right side of the figure.

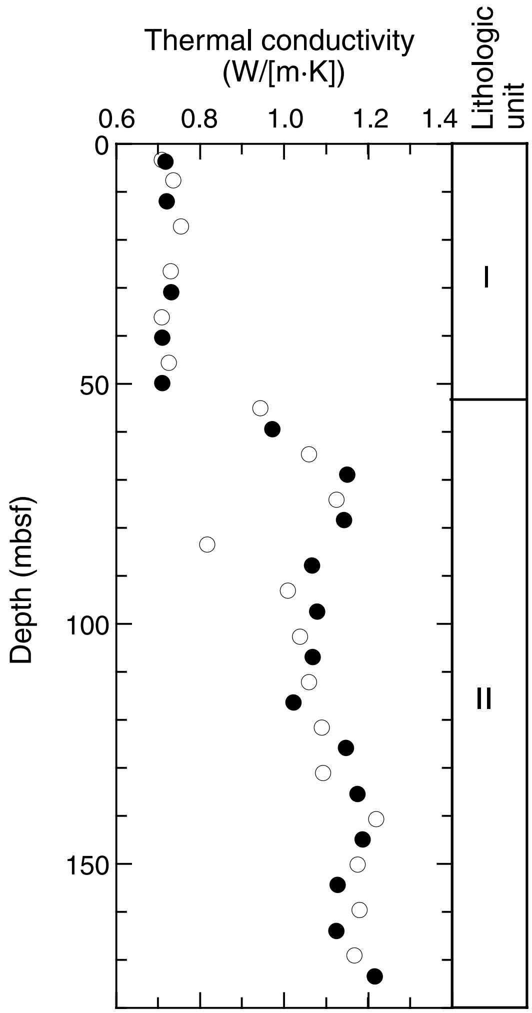

Figure F30. Thermal conductivity plotted with porosity for Holes 1218A (solid symbols) and 1218B (open symbols). Porosity values for Hole 1218B were derived from the GRA bulk density using the regression of porosity with GRA bulk density for APC recovered sediments in Hole 1218A. Porosity = 145.6 – GRA density × 52.0. R = 0.99.

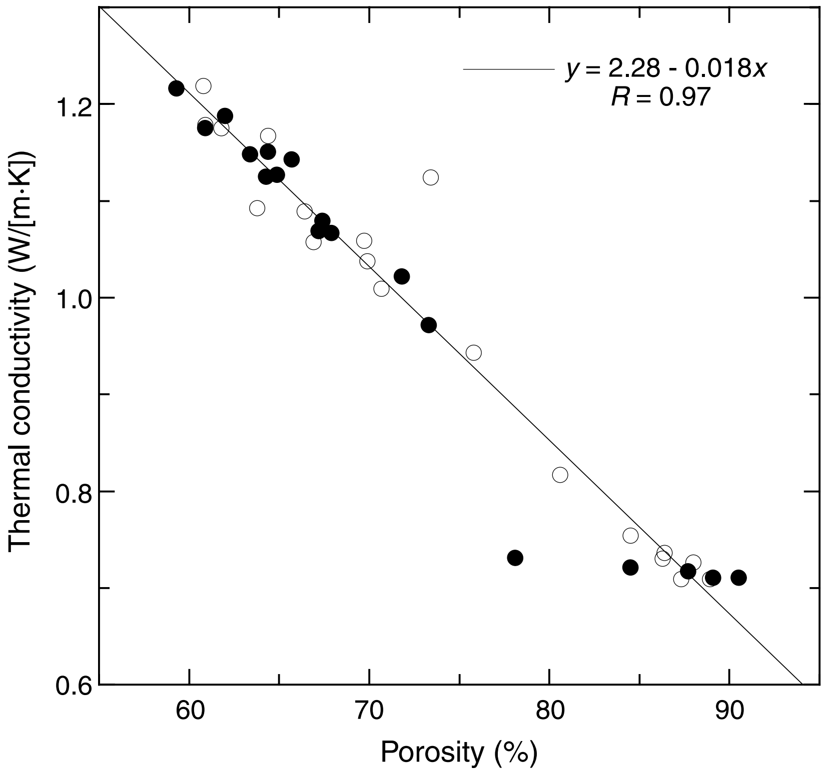

Figure F31. Heat flow calculation for Site 1218. **A.** Sediment temperatures in Holes 1218B and 1218C. **B.** Thermal resistance based on a linear increase in thermal conductivity in lithologic Unit II between 55.11 and 173.46 mbsf. **C.** Bullard plot of heat flow calculated from a linear regression of all data.

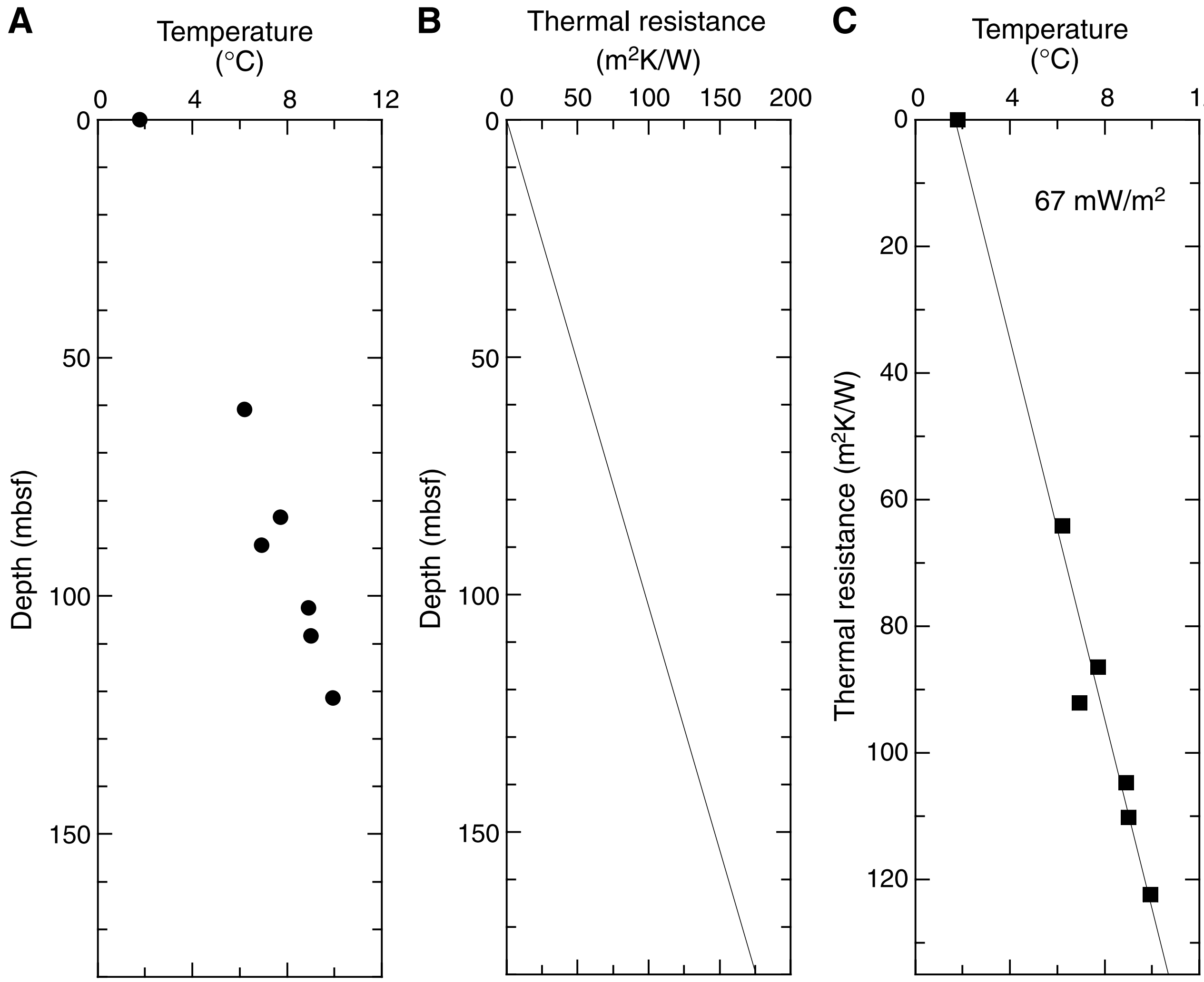

Figure F32. NGR for Hole 1218A. Most data below 60 mbsf are at or near background levels. Lithologic Units I–IV are noted on the right side of the figure. cps = counts per second.

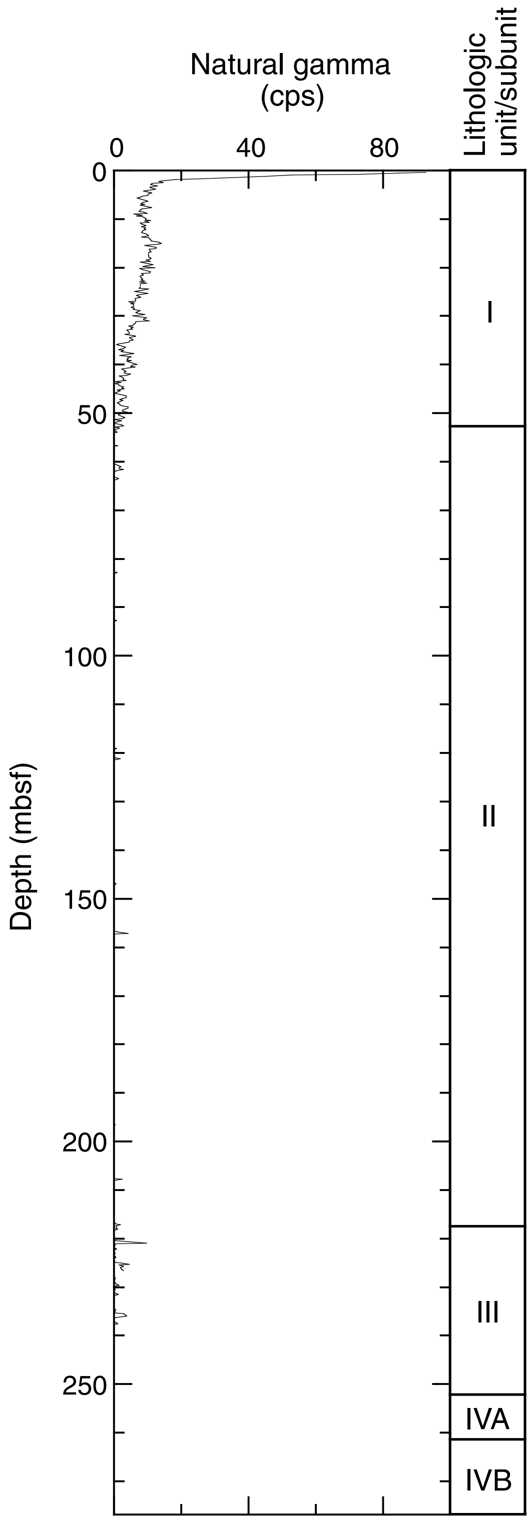

Figure F33. Magnetic susceptibility for Hole 1218A. Lithologic Units I–IV are noted on the right side of the figure.

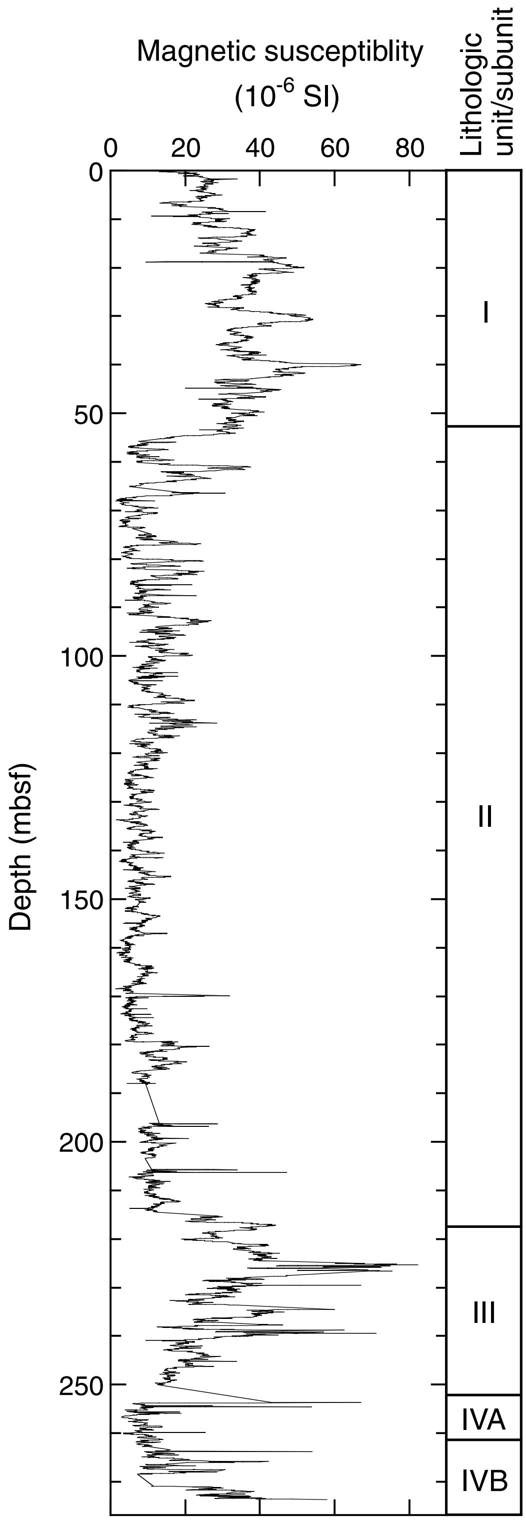

Figure F34. Summary of logging operations at Hole 1218A. Note the pulling of pipe at 20 m from the end of the second Formation MicroScanner (FMS)-sonic pass. MGT = multisensor gamma ray tool.

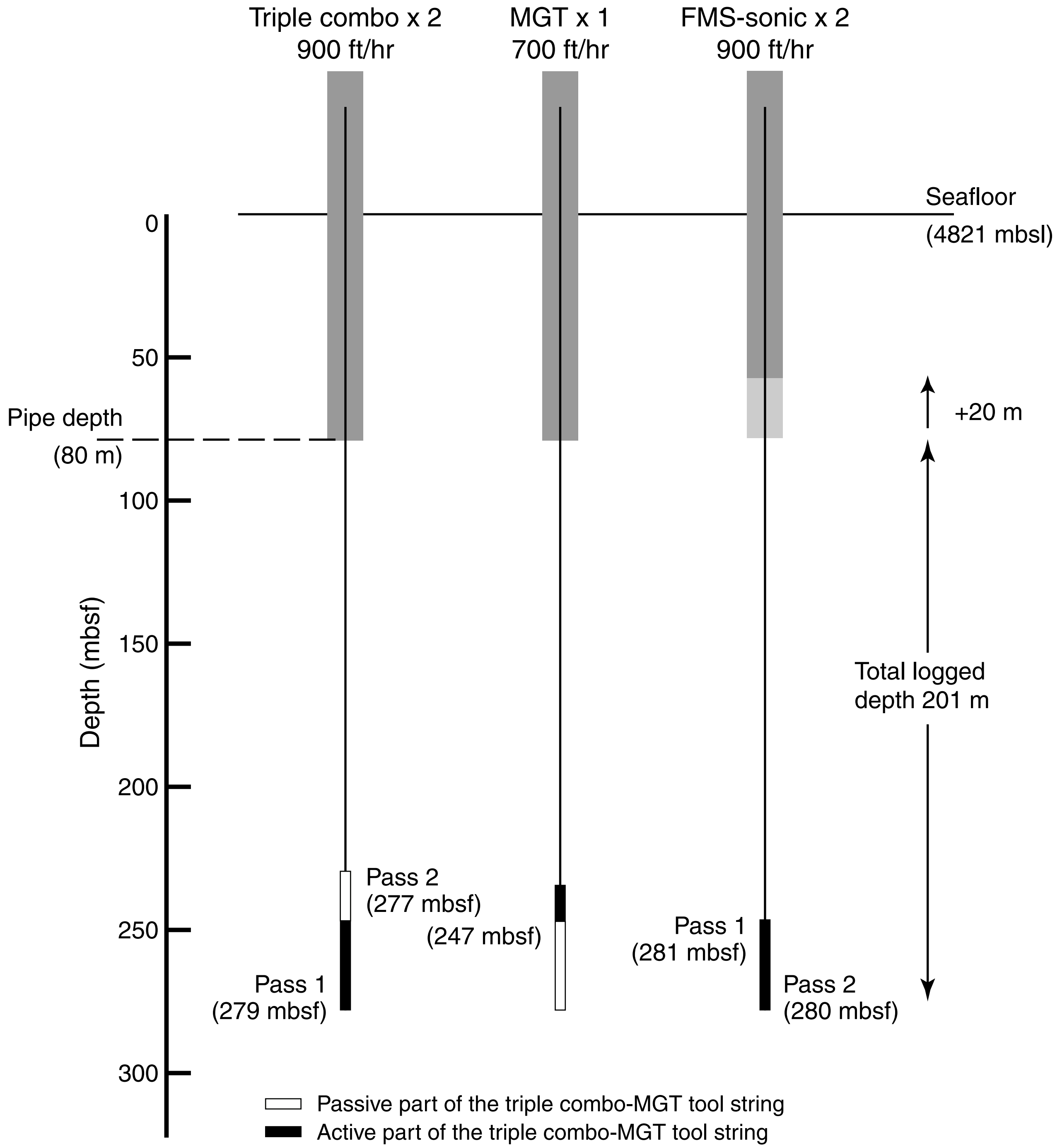

Figure F35. Caliper (C; quality control), tool acceleration (acc.; quality control), and gamma ray logs at Hole 1218A. Note the discrepancy between the triple combo and Formation MicroScanner (FMS) caliper data. T. combo = triple combo, MGT = multisensor gamma ray tool, gAPI = American Petroleum Institute gamma ray units.

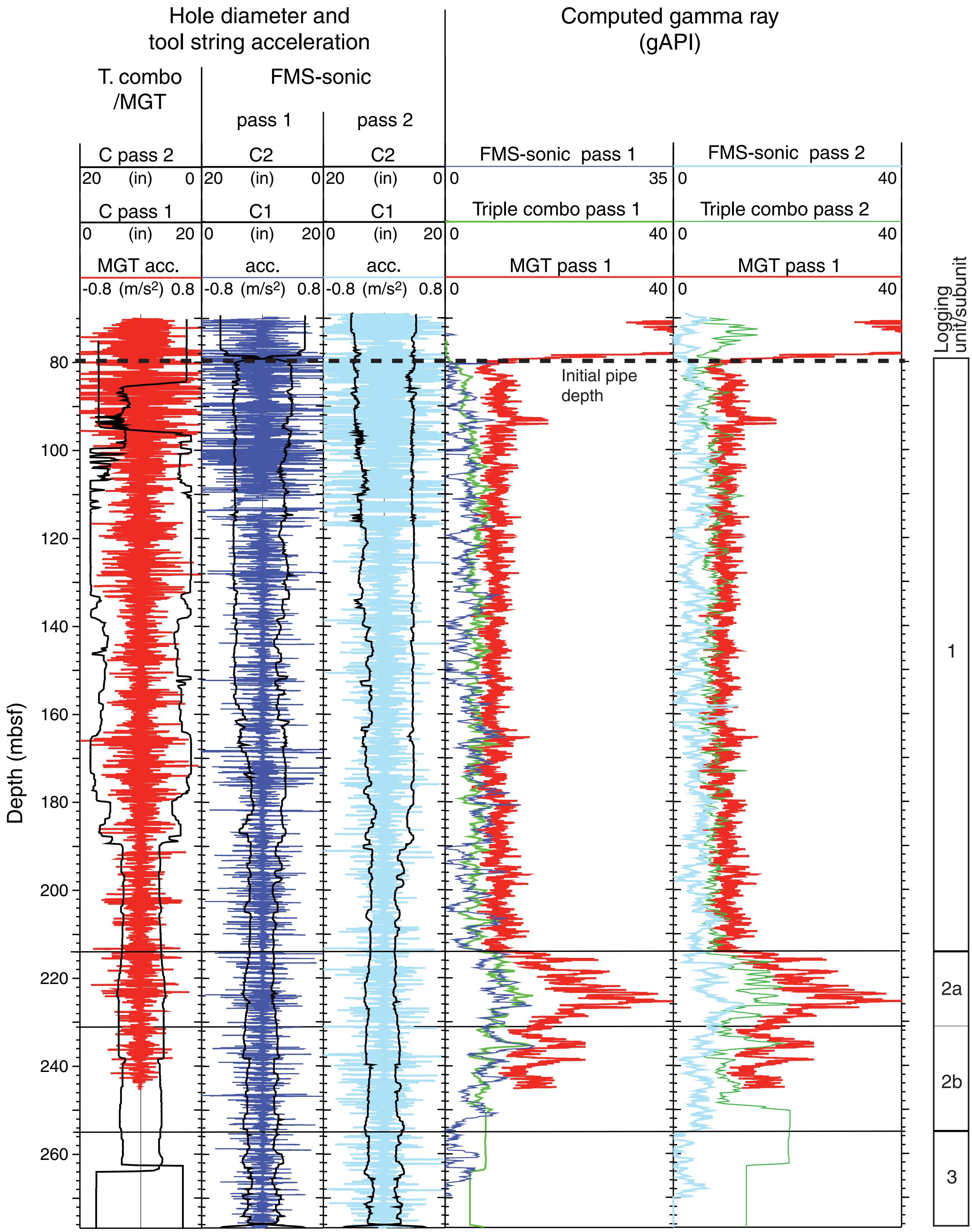

Figure F36. Core recovery, hole diameter log, hostile environment NGR sonde logs, and hostile environment litho-density tool photoelectric effect (PEF) log. gAPI = American Petroleum Institute gamma ray units, ppm = parts per million.

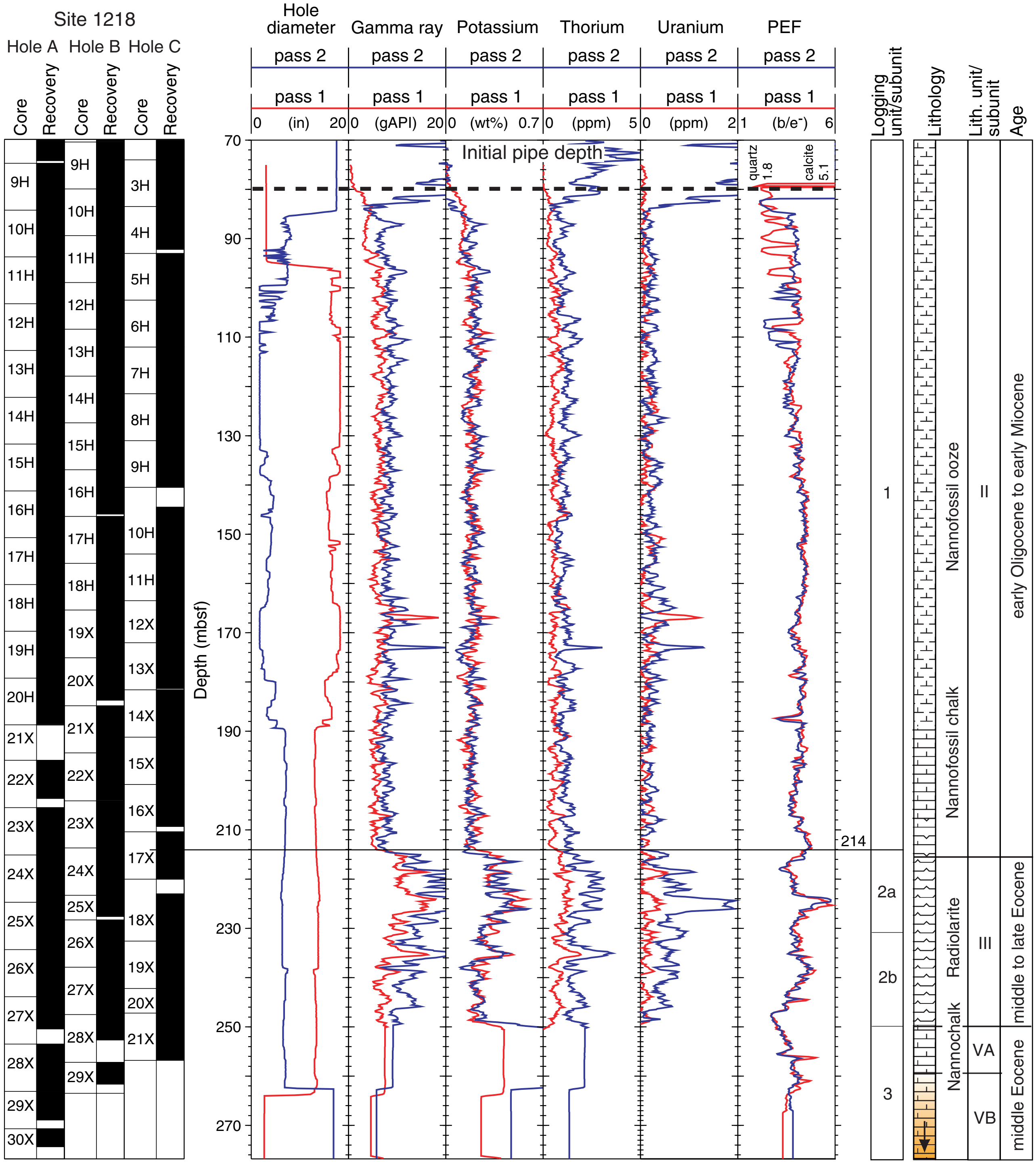

Figure F37. The data quality, in terms of stick slip of the tool (and thus quality of the depth data), is presented as acceleration. The wavelet transform analysis of these data highlights the different length scales at which the tool is being affected. The caliper log of the hole diameter indicates the hole conditions responsible for the stick slip.

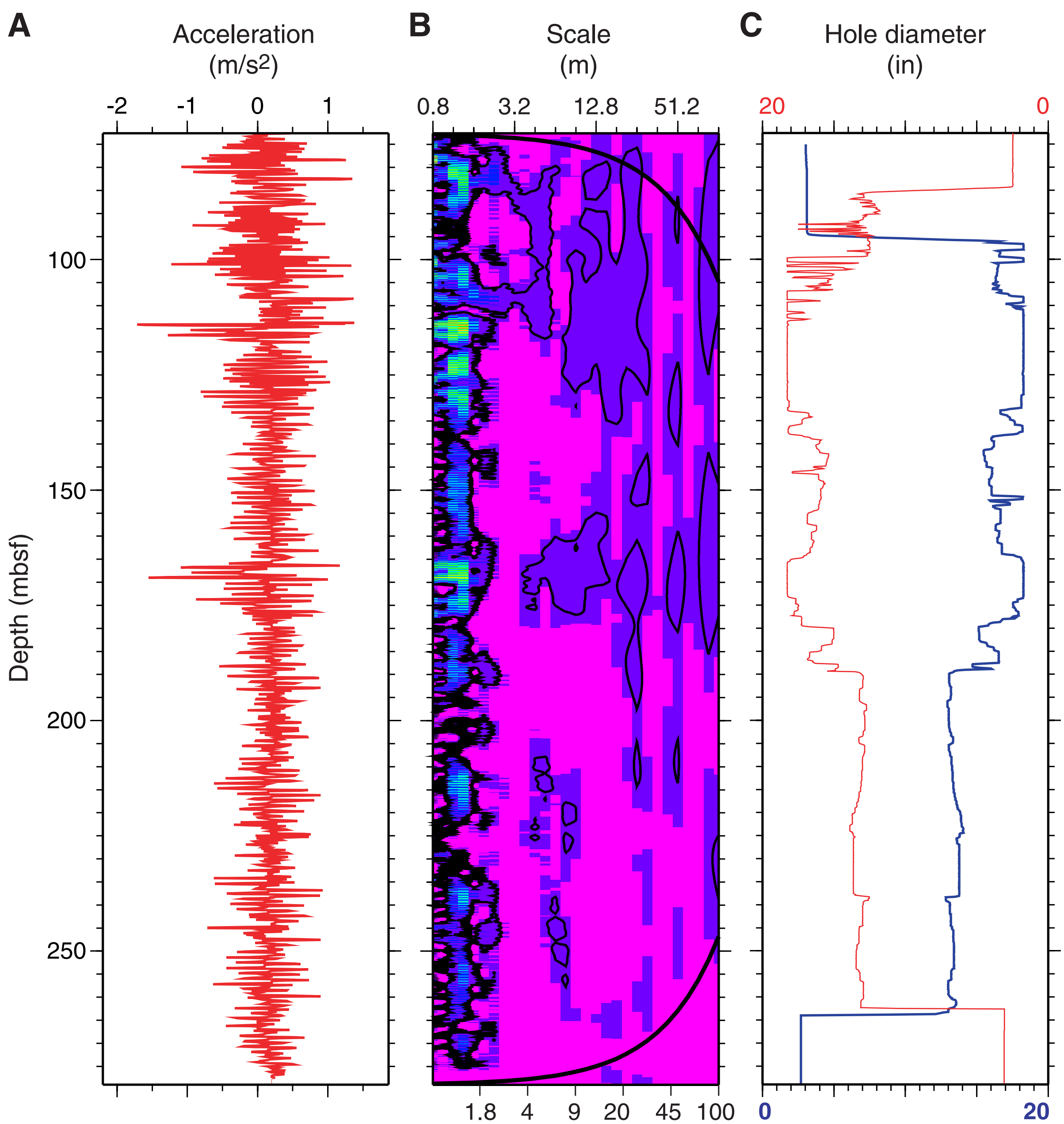

Figure F38. Geophysical logs compared with equivalent core physical properties measurements from Hole 1218A. A Formation MicroScanner (FMS) microresistivity curve is included for comparison with the triple combo resistivity logs. gAPI = American Petroleum Institute gamma ray units.

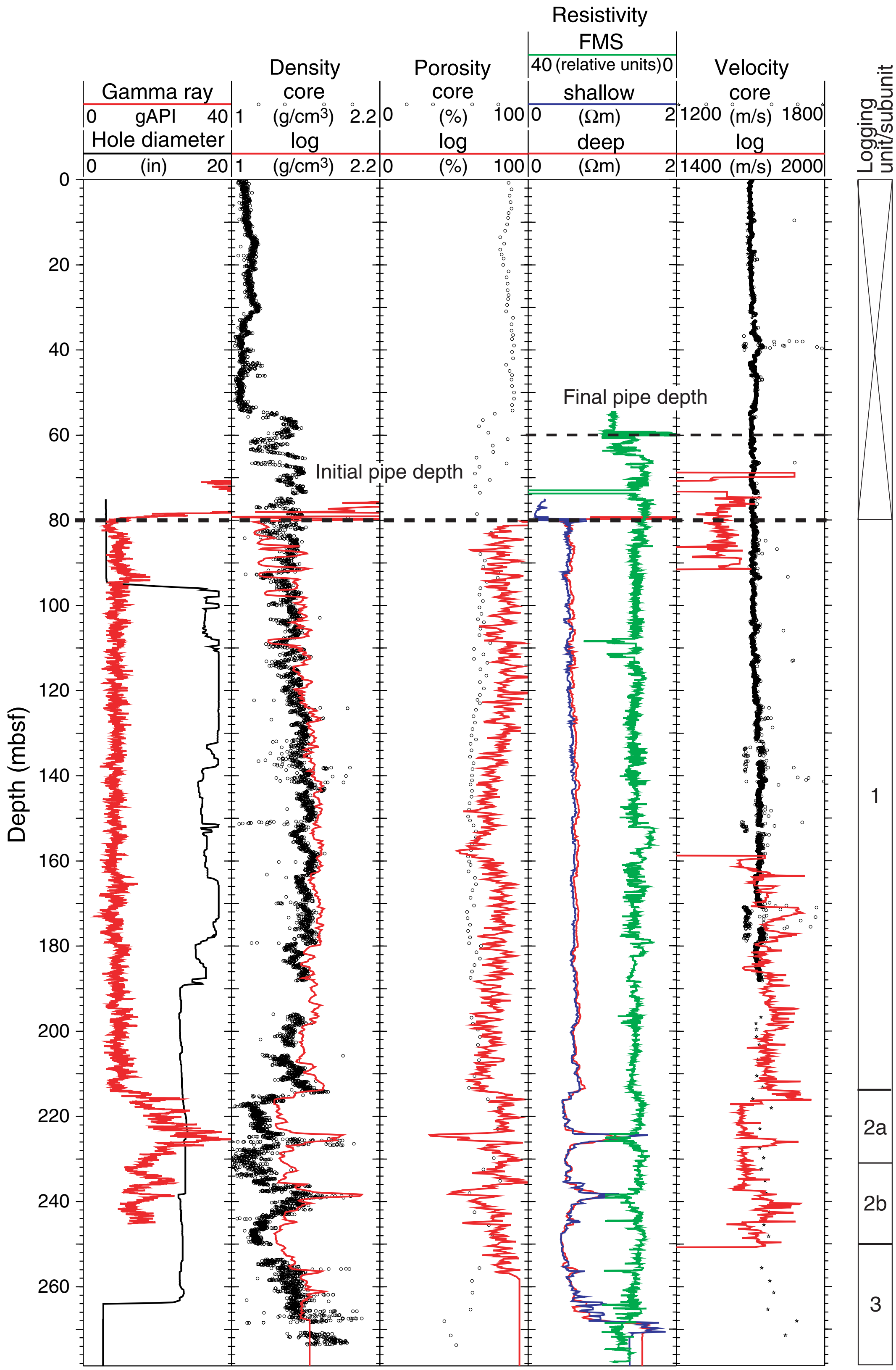

Figure F39. Formation MicroScanner (FMS) (single-button microresistivity plot and dynamic normalized image), geophysical, and geochemical log data for a section in logging Unit 1. The high-resolution gamma ray log identifies a 0.5- to 1-m cyclicity pattern, whereas the higher resolution FMS image data also identify the higher frequency cycles. PEF = photoelectric factor, gAPI = American Petroleum Institute gamma ray units.

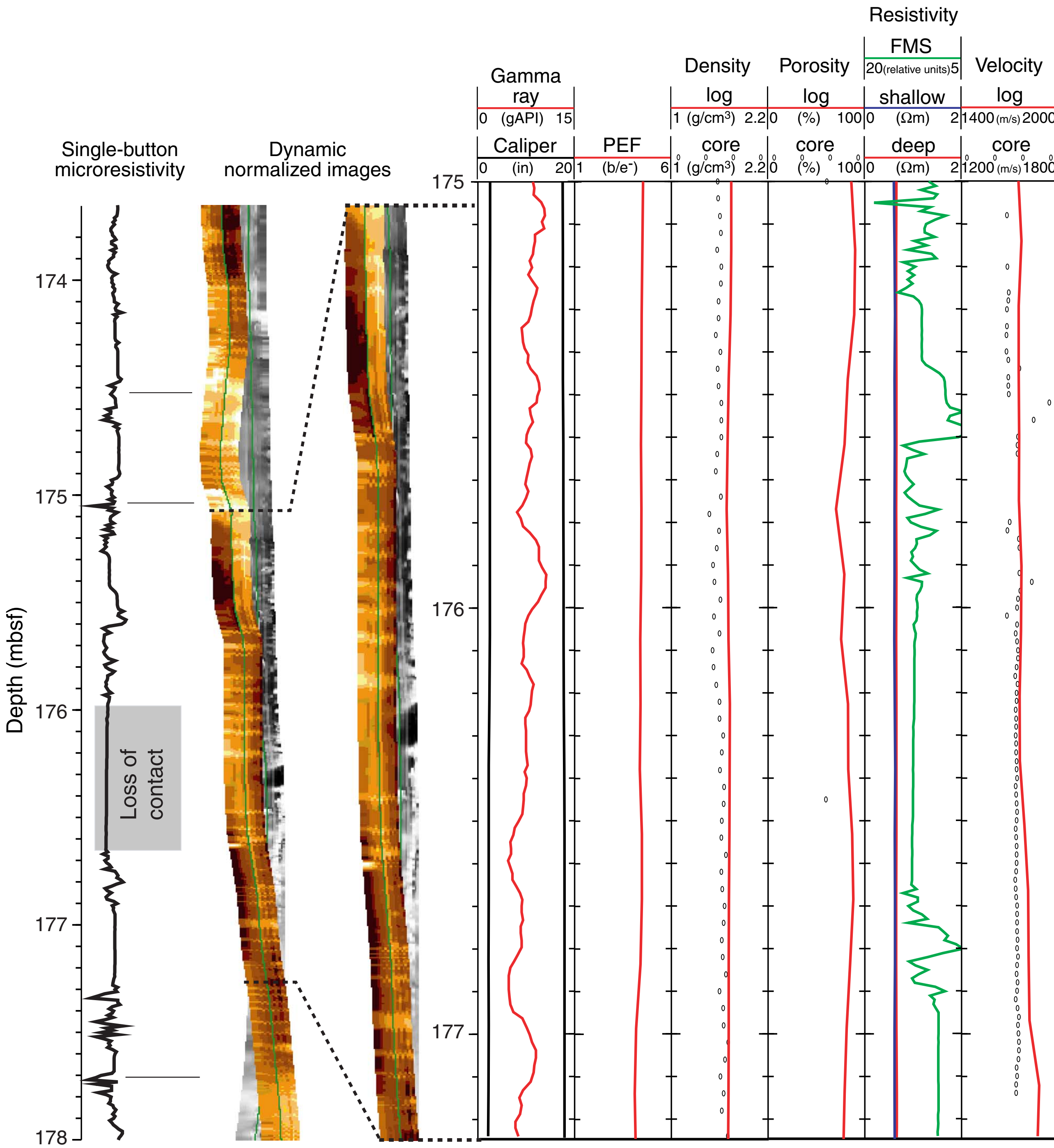

Figure F40. The chert bands in logging Unit 2, which are responsible for the resistivity and density log peaks, are easily recognizable in the Formation MicroScanner (FMS) images as the high resistivity (light) areas. A resistivity trace from an FMS button is included to show the raw data. gAPI = American Petroleum Institute gamma ray units. PEF = photoelectric effect.

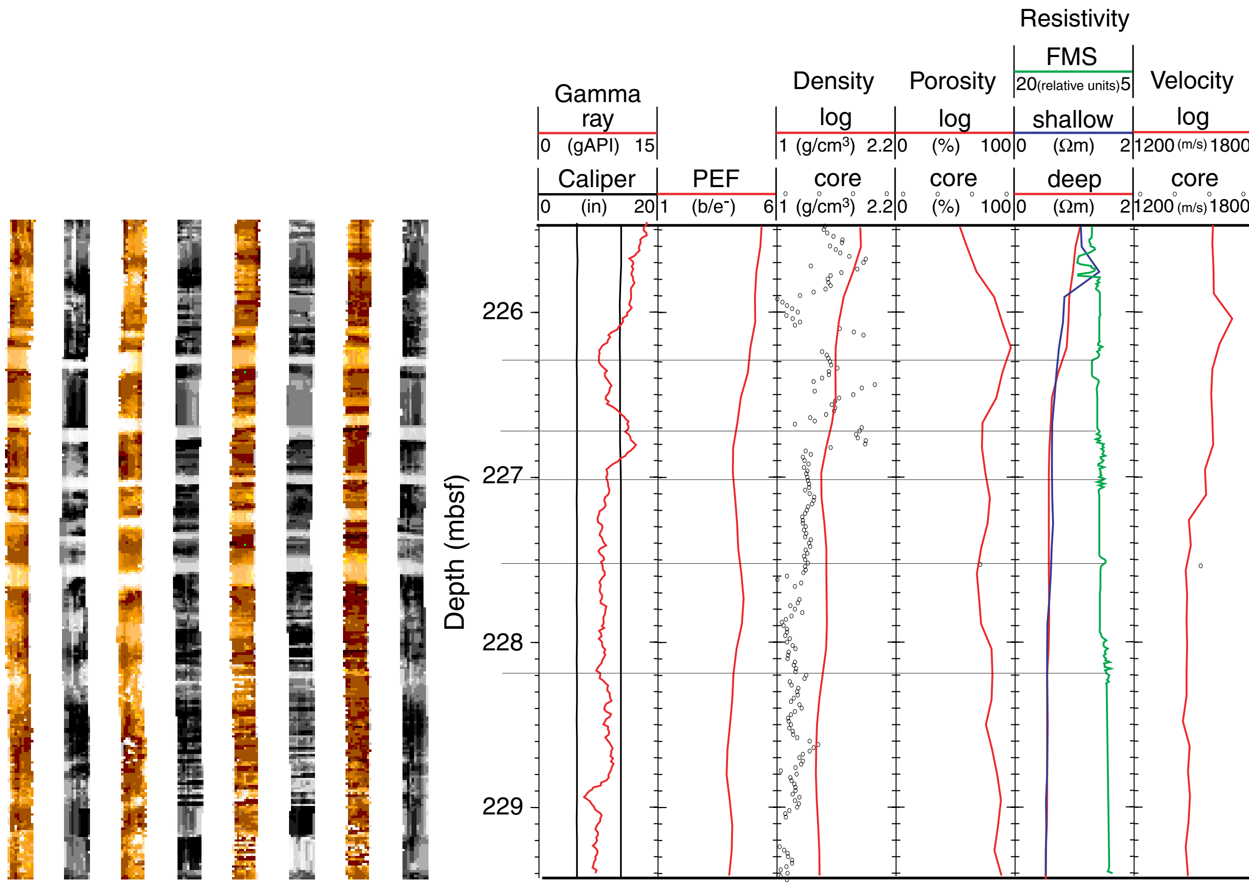

Figure F41. High-resolution data from the multisensor gamma ray tool (MGT) displaying the shift in frequency and amplitude of cycles between logging Subunits 2a and 2b. gAPI = American Petroleum Institute gamma ray units.

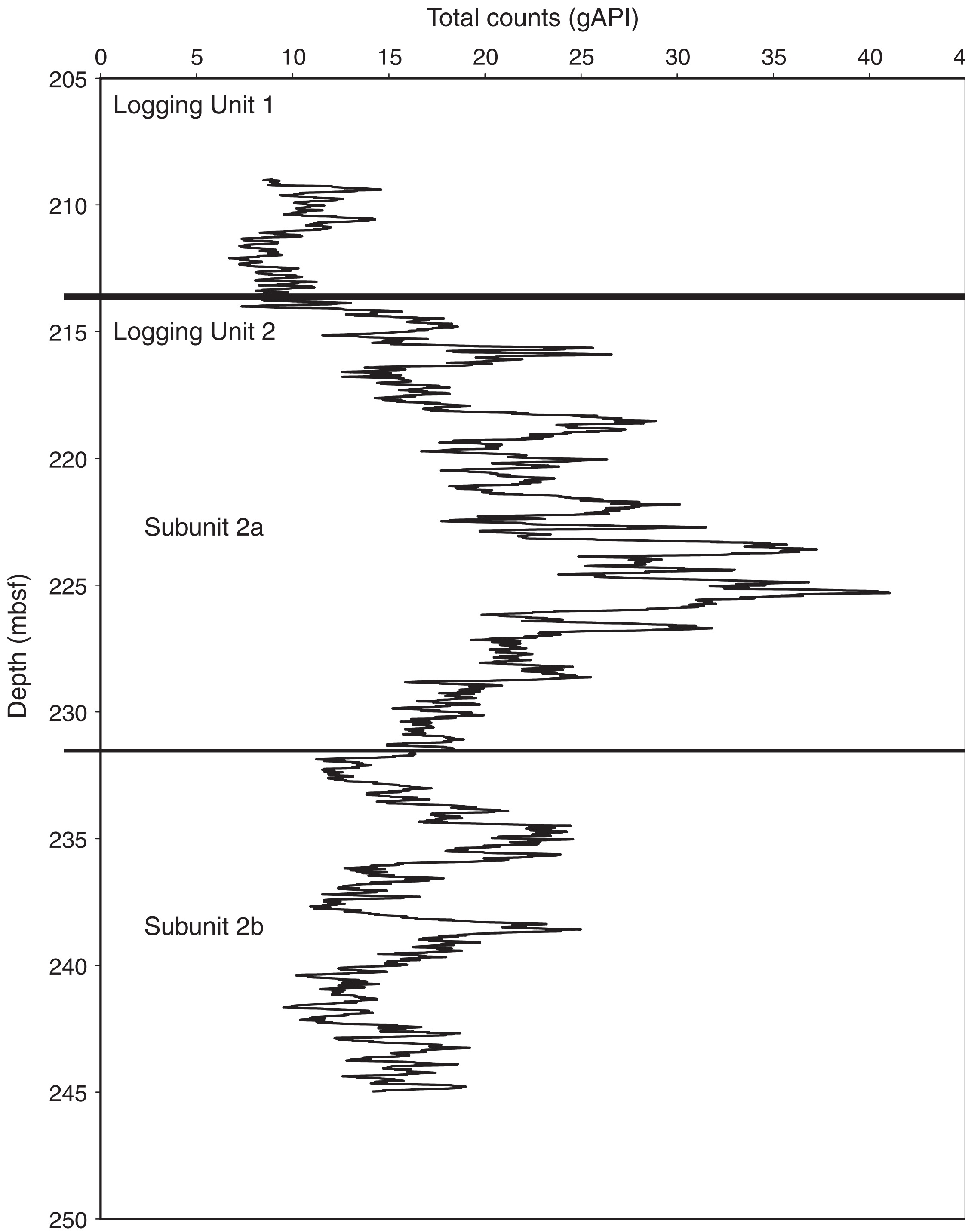

Figure F42. Preliminary wavelet transform (WT) analyses of (**A**) density and (**B**) porosity logs, logging Unit 1 (carbonate ooze). **C.** Cross-wavelet spectrum analysis. Arrows = scale change in cyclicity around 166 mbsf.

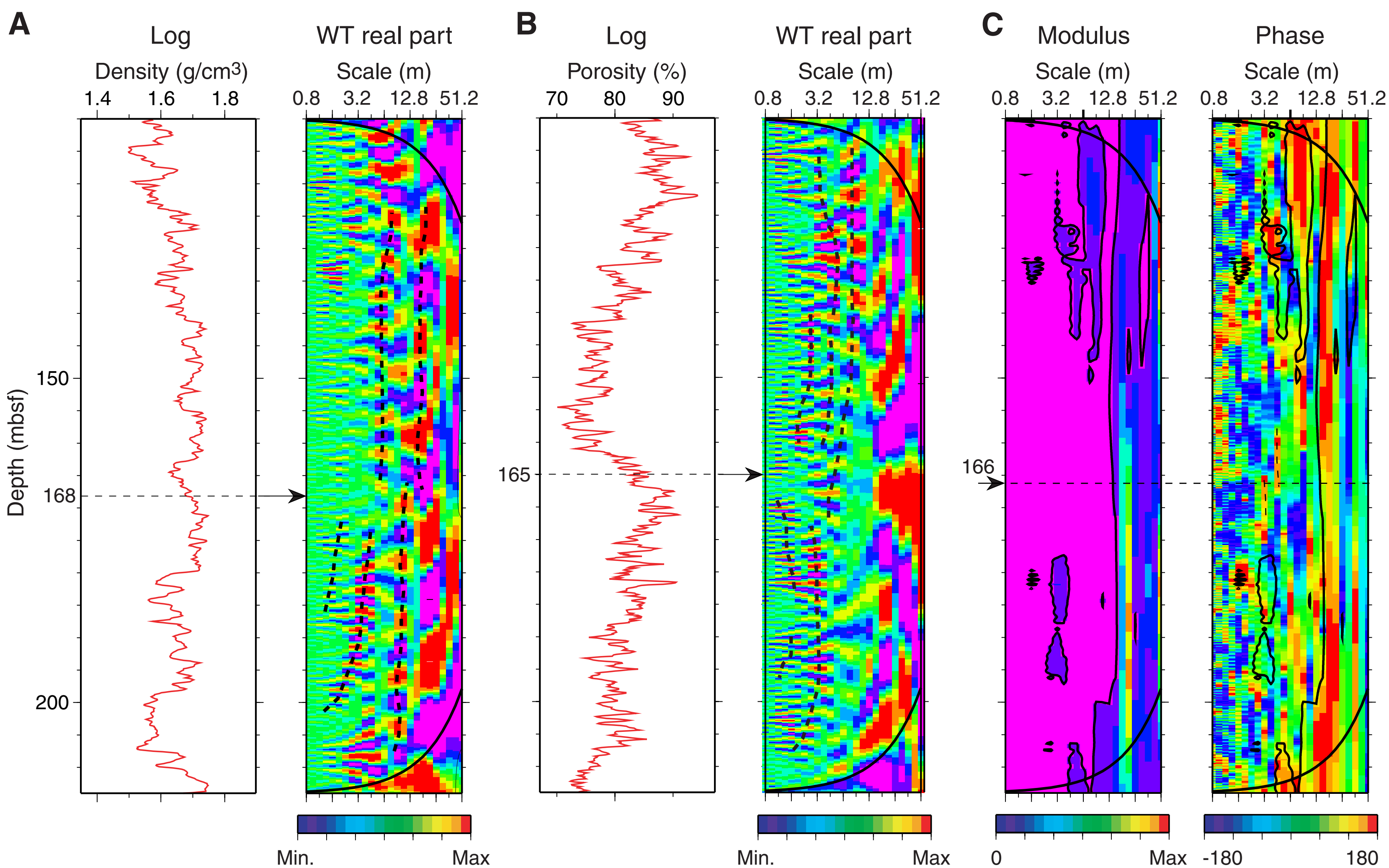

Figure F43. Synthetic seismogram derived from velocity (split core) and density (spliced log and corrected gamma ray attenuation core) data, Hole 1218A. Depth vs. time, density, velocity, and reflection coefficient curves are also shown.

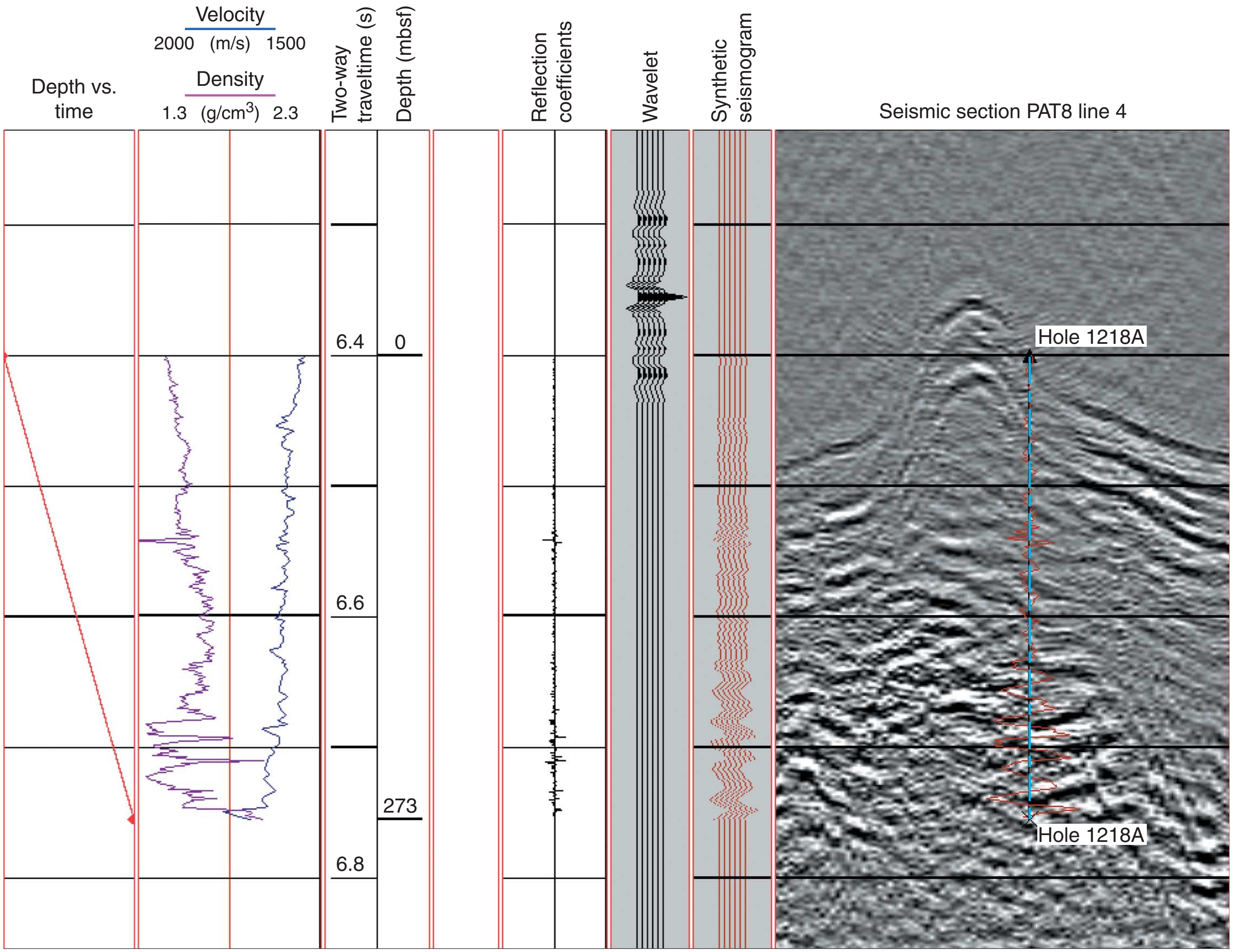

Table T1. Coring summary, Site 1218. (See table note. Continued on next two pages.)

Hole 1218A
Latitude: 8°53.3667′N
Longitude: 135°22.0002′E
Time on site (hr): 179.75 (0115 hr, 14 Nov–1300 hr, 21 Nov 2001)
Time on hole (hr): 90.00 (0115 hr, 14 Nov–1915 hr, 17 Nov 2001)
Seafloor (drill pipe measurement from rig floor, mbrf): 4837.3
Distance between rig floor and sea level (m): 11.0
Water depth (drill pipe measurement from sea level), m: 4826.3
Total depth (drill pipe measurement from rig floor, mbrf): 5114.1
Total penetration (meters below seafloor, mbsf): 276.8
Total length of cored section (m): 276.8
Total core recovered (m): 266.42
Core recovery (%): 96.3
Total number of cores: 30
Total number of drilled intervals: 0

Hole 1218B
Latitude: 8°53.3777′N
Longitude: 135°21.9995′W
Time on hole (hr): 45.65 (1915 hr, 17 Nov–1654 hr, 19 Nov 2001)
Seafloor (drill pipe measurement from rig floor, mbrf): 4838.6
Distance between rig floor and sea level (m): 11.0
Water depth (drill pipe measurement from sea level, m): 4827.6
Total depth (drill pipe measurement from rig floor, mbrf): 5102.1
Total penetration (meters below seafloor, mbsf): 263.5
Total length of cored section (m): 263.5
Total core recovered (m): 259.25
Core recovery (%): 98.4
Total number of cores: 29
Total number of drilled intervals: 0

Hole 1218C
Latitude: 8°53.3885′N
Longitude: 135°21.9997′W
Time on hole (hr): 44.1 (1654 hr, 19 Nov.–1300 hr, 21 Nov 2001)
Seafloor (drill pipe measurement from rig floor, mbrf): 4838.6
Distance between rig floor and sea level (m): 11.0
Water depth (drill pipe measurement from sea level, m): 4827.6
Total depth (drill pipe measurement from rig floor, mbrf): 5095.4
Total penetration (meters below seafloor, mbsf): 256.8
Total length of cored section (m): 194.8
Total length of drilled intervals (m): 62.0
Total core recovered (m): 198.05
Core recovery (%): 101.7
Total number of cores: 21
Total number of drilled intervals: 3

Core	Date (Nov 2001)	Local time (hr)	Depth (mbsf) Top	Depth (mbsf) Bottom	Length (m) Cored	Length (m) Recovered	Recovery (%)
199-1218A-							
1H	14	1030	0.0	8.2	8.2	8.26	100.7
2H	14	1155	8.2	17.7	9.5	9.80	103.2
3H	14	1305	17.7	27.2	9.5	10.11	106.4
4H	14	1405	27.2	36.7	9.5	9.88	104.0
5H	14	1510	36.7	46.2	9.5	9.70	102.1
6H	14	1610	46.2	55.7	9.5	9.17	96.5
7H	14	1710	55.7	65.2	9.5	10.05	105.8
8H	14	1815	65.2	74.7	9.5	8.98	94.5
9H	14	1935	74.7	84.2	9.5	10.03	105.6
10H	14	2045	84.2	93.7	9.5	9.71	102.2
11H	14	2155	93.7	103.2	9.5	10.07	106.0
12H	14	2300	103.2	112.7	9.5	9.66	101.7
13H	15	0015	112.7	122.2	9.5	10.11	106.4
14H	15	0125	122.2	131.7	9.5	9.57	100.7
15H	15	0250	131.7	141.2	9.5	10.17	107.1
16H	15	0405	141.2	150.7	9.5	9.63	101.4
17H	15	0515	150.7	160.2	9.5	10.14	106.7
18H	15	0640	160.2	169.7	9.5	9.51	100.1
19H	15	0840	169.7	179.2	9.5	10.13	106.6
20H	15	1025	179.2	188.7	9.5	9.32	98.1

Table T1 (continued).

Core	Date (Nov 2001)	Local time (hr)	Depth (mbsf) Top	Depth (mbsf) Bottom	Length (m) Cored	Length (m) Recovered	Recovery (%)
21X	15	1210	188.7	195.9	7.2	0.03	0.4
22X	15	1355	195.9	205.5	9.6	7.73	80.5
23X	15	1515	205.5	215.1	9.6	9.89	103.0
24X	15	1635	215.1	224.7	9.6	9.82	102.3
25X	15	1815	224.7	234.3	9.6	9.61	100.1
26X	15	2020	234.3	243.9	9.6	9.87	102.8
27X	15	2210	243.9	253.5	9.6	6.53	68.0
28X	16	0015	253.5	263.1	9.6	9.48	98.8
29X	16	0315	263.1	270.7	7.6	5.82	76.6
30X	16	0645	270.7	276.8	6.1	3.64	59.7
				Cored totals:	276.8	266.42	96.3
199-1218B-							
1H	17	2120	0.0	3.9	3.9	3.86	99.0
2H	17	2230	3.9	13.4	9.5	8.83	93.0
3H	17	2345	13.4	22.9	9.5	9.99	105.2
4H	18	0125	22.9	32.4	9.5	8.70	91.6
5H	18	0235	32.4	41.9	9.5	10.02	105.5
6H	18	0350	41.9	51.4	9.5	9.12	96.0
7H	18	0530	51.4	60.9	9.5	9.87	103.9
8H	18	0640	60.9	70.4	9.5	9.38	98.7
9H	18	0755	70.4	79.9	9.5	10.07	106.0
10H	18	0925	79.9	89.4	9.5	9.78	103.0
11H	18	1105	89.4	98.9	9.5	10.01	105.4
12H	18	1240	98.9	108.4	9.5	10.17	107.1
13H	18	1350	108.4	117.9	9.5	10.11	106.4
14H	18	1500	117.9	127.4	9.5	9.86	103.8
15H	18	1610	127.4	136.9	9.5	10.01	105.4
16H	18	1710	136.9	146.4	9.5	9.02	95.0
17H	18	1830	146.4	155.9	9.5	10.01	105.4
18H	18	1940	155.9	165.4	9.5	10.01	105.4
19X	18	2050	165.4	175.1	9.7	9.80	101.0
20X	18	2200	175.1	184.8	9.7	8.61	88.8
21X	18	2310	184.8	194.4	9.6	9.70	101.0
22X	19	0100	194.4	204.1	9.7	9.59	98.9
23X	19	0250	204.1	213.7	9.6	9.72	101.3
24X	19	0450	213.7	223.3	9.6	9.76	101.7
25X	19	0740	223.3	228.3	5.0	4.30	86.0
26X	19	0945	228.3	237.9	9.6	9.59	99.9
27X	19	1130	237.9	247.5	9.6	9.75	101.6
28X	19	1315	247.5	257.2	9.7	5.17	53.3
29X	19	1535	257.2	263.5	6.3	4.44	70.5
				Cored totals:	263.5	259.25	98.4
199-1218C-							
			*****Drilled from 0.0 to 55.0 mbsf*****				
1H	19	2015	55.0	64.5	9.5	9.96	104.8
2H	19	2125	64.5	74.0	9.5	9.53	100.3
3H	19	2255	74.0	83.5	9.5	10.16	107.0
4H	20	0005	83.5	93.0	9.5	8.68	91.4
5H	20	0145	93.0	102.5	9.5	10.13	106.6
6H	20	0250	102.5	112.0	9.5	9.74	102.5
7H	20	0430	112.0	121.5	9.5	10.21	107.5
8H	20	0545	121.5	131.0	9.5	9.77	102.8
9H	20	0650	131.0	140.5	9.5	10.08	106.1
			*****Drilled from 140.0 to 145.0 mbsf*****				
10H	20	0815	144.5	154.0	9.5	9.76	102.7
11H	20	0925	154.0	163.5	9.5	9.99	105.2
12X	20	1045	163.5	172.0	8.5	8.73	102.7
13X	20	1200	172.0	181.6	9.6	9.33	97.2
14X	20	1330	181.6	191.2	9.6	9.58	99.8
15X	20	1450	191.2	200.8	9.6	9.79	102.0
16X	20	1610	200.8	210.4	9.6	8.54	89.0
17X	20	1735	210.4	220.0	9.6	9.72	101.3
			*****Drilled from 220.0 to 223.0 mbsf*****				
18X	20	2115	223.0	232.6	9.6	9.74	101.5
19X	20	2315	232.6	242.2	9.6	9.60	100.0
20X	21	0125	242.2	247.2	5.0	5.53	110.6
21X	21	0315	247.2	256.8	9.6	9.48	98.8

Table T1 (continued).

Core	Date (Nov 2001)	Local time (hr)	Depth (mbsf)		Length (m)		Recovery (%)
			Top	Bottom	Cored	Recovered	
				Cored totals:	194.8	198.05	101.7
				Drilled total:	62.0		
				Total:	256.8		

Note: The expanded coring summary table is available in ASCII (see the **"Supplementary Material"** contents list).

Table T2. Intervals of intact chert layers recovered, Site 1218.

Core, section, interval (cm)	Depth (mbsf)	
	Top	Bottom
199-1218A-		
25X-1, 49–61	225.19	225.31
25X-1, 94–106	225.64	225.76
25X-1, 139–146	226.09	226.16
25X-2, 22–32	226.42	226.52
25X-2, 48–61	226.68	226.81
27X-1, 20–29	244.10	244.19
27X-1, 34–41	244.24	244.31
199-1218B-		
25X-1, 12–32	223.42	223.62
25X-1, 37–55	223.67	223.85
25X-1, 104–110	224.34	224.40
25X-1, 114–122	224.44	224.52
25X-1, 129–141	224.59	224.71
199-1218C-		
18X-3, 90–100	226.97	227.07
18X-3, 141 to 18X-4, 4	227.48	227.61
18X-4, 29–35	227.86	227.92
18X-4, 60–70	228.17	228.27
18X-4, 75–85	228.32	228.42
19X-5, 137–146	239.97	240.06
20X-1, 127–147	243.47	243.67
20X-2, 119–120	244.89	244.90

Table T3. Calcareous nannofossil datums, Site 1218.

Core, section, interval (cm) Top	Bottom	Marker species	Age (Ma)	Depth (mbsf) Midpoint	±	Depth (mcd) Midpoint	±
199-1218A-	199-1218A-						
4H-7, 50	4H-CC	B *Catinaster coalitus*	10.8	36.78	0.08	41.20	0.08
5H-7, 15	5H-CC	T *Sphenolithus heteromorphus*	13.6	46.01	0.16	50.81	0.16
5H-7, 15	5H-CC	T *Discoaster deflandrei* acme	16.2	46.01	0.16	50.81	0.16
6H-CC	7H-1, 120	T *Triquetrorhabdulus carinatus*	?	56.11	0.79	63.56	1.40
9H-2, 80	9H-2, 130	T *Triquetrorhabdulus carinatus* acme	?	77.25	0.25	87.51	0.25
9H-4, 80	9H-4, 130	B *Sphenolithus disbelemnos*	23.5	80.25	0.25	90.51	0.25
9H-5, 130	9H-6, 20	B *Discoaster druggii*	?	82.20	0.20	92.46	0.16
10H-1, 140	10H-2, 10	T *Sphenolithus delphix*	23.7	85.70	0.10	97.60	0.09
10H-2, 70	10H-3, 30	B *Sphenolithus delphix*	24.4	86.95	0.55	98.85	0.54
11H-2, 130	11H-3, 130	T *Sphenolithus ciperoensis*	24.7	97.25	0.75	110.65	0.71
11H-4, 130	11H-5, 38	T *Cyclicargolithus abisectus* acme	?	99.79	0.29	113.19	0.25
13H-3, 75	13H-4, 45	T *Sphenolithus distentus*	26.5	117.05	0.60	131.96	0.56
14H-5, 80	14H-6, 80	B *Sphenolithus ciperoensis*	28.1	129.75	0.75	145.17	0.75
18H-CC	19H-1, 120	B *Sphenolithus distentus*	30.4	170.22	0.68	190.69	0.59
22X-2, 70	22X-2, 147	T *Reticulofenestra umbilicus* ≥14 µm	31.7	198.49	0.39	220.79	0.38
23X-2, 148	23X-3, 35	T *Ericsonia formosa*	32.9	208.67	0.19	231.91	0.16
24X-4, 78	24X-4, 90	T *Discoaster saipanensis*	34.0	220.04	0.06	245.12	0.06
24X-5, 56	24X-5, 85	T *Discoaster barbadiensis*	34.2	221.41	0.15	246.49	0.15
25X-7, 70	25X-CC	T *Chiasmolithus grandis*	37.1	234.11	0.21	260.38	0.07
26X-5, 60	26X-6, 125	B *Dictyococcites bisectus*	38.5	241.98	1.08	268.05	0.32
27X-CC	28X-1, 50	T *Chiasmolithus solitus*	40.4	252.06	1.95	277.09	0.85
30X-2, 90	30X-3, 2	T *Nannotetrina* spp.	42.3	273.41	0.31	297.64	0.31
199-1218B-	199-1218B-						
5H-2, 56	5H-2, 88	B *Discoaster kugleri*	11.9	34.62	0.16	40.28	0.16
5H-7, 45	5H-CC	T *Cyclicargolithus floridanus*	13.2	42.04	0.19	47.70	0.19
13H-6, 80	13H-6, 148	T *Dictyococcites bisectus*	?	117.04	0.34	132.53	0.34

Notes: B = bottom, T = top. ? = uncalibrated datum. This table is also available in **ASCII.** [N1]

Table T4. Distribution of Miocene–upper Eocene planktonic foraminifers, Holes 1218A and 1218B. (**See table notes.** Continued on next three pages.)

Core, section, interval (cm)	Depth (mbsf)	Zone/ Subzone	Preservation	Group abundance	*Catapsydrax dissimilis ciperoensis*	*Catapsydrax dissimilis*	*Catapsydrax unicavus*	*Chiloguembelina cubensis*	*Dentoglobigerina yeguaensis*	*Dentoglobigerina altispira*	*Dentoglobigerina baroemoenensis*	*Dentoglobigerina galavisi*	*Dentoglobigerina globularis*	*Globigerina ciperoensis*	*Globigerina praebulloides*	*Globigerinella praesiphonifera*	*Globigerinoides primordius*	*Globigerinoides trilobus*	*Globoquadrina binaiensis*	*Globoquadrina dehiscens*	*Globoquadrina praedehiscens*	*Globoquadrina prasaepis*	*Globoquadrina sellii*	*Globoquadrina tapuriensis*	*Globoquadrina tripartita*	*Globoquadrina venezuelana*	*Globorotaloides* sp.	*Globorotaloides suteri*	*Paragloborotalia continuosa*	*Paragloborotalia kugleri*	*Paragloborotalia mayeri*	*Paragloborotalia nana*	*Paragloborotalia opima opima*	*Paragloborotalia pseudokugleri*	*Paragloborotalia siakensis*	*Subbotina angiporoides*	*Subbotina euapertura*	*Subbotina gortanii*	*Subbotina praeturritilina*	*Subbotina utilisindex*	*Tenuitella clemenciae*	*Tenuitella gemma*	*Tenuitellinata angustiumbilicata*	*Turborotalia ampliapertura*	Comments
199-1218A-																																													
1H-CC, 5–15	8.16	Not zoned		B																																									
2H-CC, 9–14	17.95			B																																									
3H-CC, 22–27	27.76			B																																									
4H-6, 134–136	36.04			B																																									
4H-CC, 18–23	37.03			B																																									
5H-6, 7–9	44.27			B																																									
5H-CC, 19–24	46.35		P	R																									R		R				P*										
6H-5, 141–143	53.61			B																																									
6H-6, 94–96	54.64			B																																									
6H-7, 39–41	55.09	M2/3	P	R	R																				P*	R		R																	
6H-CC, 0–5	55.32		P	R			R																			R			R		R														
7H-1, 110–115	56.80		M	C	P*					F	F		F						R		F		F					R			R				F										
7H-2, 110–115	58.30		M	C	R					F	F		R				R				F				F	A		R			A				A								P*		
7H-3, 110–115	59.80		M	C	R						R					P*					F		F			A		R	R		A														
7H-4, 110–115	61.30		P	T																											R														
7H-5, 110–115	62.80			B																																									
7H-6, 110–115	64.30		P	F	R		R			P*											F		F			A		R			F				R										
7H-CC, 19–24	65.70		P	F	R		R																			R					R														
8H-2, 110–114	67.80	M1b	M	C	R		R			P*						R	P*		R	R	F		R			A		P*	R	R	A				P*								R		
8H-3, 110–114	69.30		P	F																P*	F					F			R		F							P*							
8H-4, 110–114	70.80		P	R	F															R	F					F					F														
8H-5, 110–114	72.30		M	F	F						R				R	P*				R	F		R			F		P*	P*	R	A			R	P*								P*		
8H-6, 60–62	73.30	M1a	M	C	R														P*		F		F			A				F	A			R	F								F		
8H-CC, 14–19	74.13		M	F		F	F																P*			F			F	F	F			R											
9H-5, 110–112	81.80		P	R			R																			R					R														
9H-CC, 14–19	84.68		P	R		R	R																			P*			R	R				R											
10H-1, 74–75	84.94		M	F																										R	R														
10H-1, 130–132	85.50		M	F		R																						R	R	R	R														
10H-2, 120–122	86.90			B																																									
10H-3, 120–122	88.40			B																																									
10H-CC, 13–18	93.86			B																																									
11H-1, 2–7	93.72		P	T		P*	P*																			R		P*																	
11H-2, 10–15	95.30		P	T		P*																																							
11H-3, 10–15	96.80		P	T																						P*																			
11H-4, 58–63	98.78		P	T		R	P*																					P*																	
11H-5, 38–43	100.08		P	F		R	R																		R	R		R			R			R									R		
11H-6, 38–43	101.58		P	F	R	R																	R			R		R			R														

Table T4 (continued).

Core, section, interval (cm)	Depth (mbsf)	Zone/ Subzone	Preservation	Group abundance	*Catapsydrax dissimilis ciperoensis*	*Catapsydrax dissimilis*	*Catapsydrax unicavus*	*Chiloguembelina cubensis*	*Dentoglobigerina yeguaensis*	*Dentoglobigerina altispira*	*Dentoglobigerina baroemoenensis*	*Dentoglobigerina galavisi*	*Dentoglobigerina globularis*	*Globigerina ciperoensis*	*Globigerina praebulloides*	*Globigerinella praesiphonifera*	*Globigerinoides primordius*	*Globigerinoides trilobus*	*Globoquadrina binaiensis*	*Globoquadrina dehiscens*	*Globoquadrina praedehiscens*	*Globoquadrina prasaepis*	*Globoquadrina sellii*	*Globoquadrina tapuriensis*	*Globoquadrina tripartita*	*Globoquadrina venezuelana*	*Globorotaloides* sp.	*Globorotaloides suteri*	*Paragloborotalia continuosa*	*Paragloborotalia kugleri*	*Paragloborotalia mayeri*	*Paragloborotalia nana*	*Paragloborotalia opima opima*	*Paragloborotalia pseudokugleri*	*Paragloborotalia siakensis*	*Subbotina angiporoides*	*Subbotina euapertura*	*Subbotina gortanii*	*Subbotina praeturritilina*	*Subbotina utilisindex*	*Tenuitella clemenciae*	*Tenuitella gemma*	*Tenuitellinata angustiumbilicata*	*Turborotalia ampliapertura*	Comments
11H-CC, 19–24	103.72			B																																									
12H-1, 142–147	104.62		P	F	F																					R		F			R												P*		
12H-2, 118–122	105.88		M	F		A	R						F											P*				A			F			R				P*					F		
12H-4, 59–64	108.29		P	R		F	P*																			P*		R																	
12H-5, 120–125	110.40	P22	M	C	R	R			R					R	R										R	R		R			R														
12H-6, 129–134	111.99		P	F	R	F	R																		R			R																	
12H-7, 37–42	112.57		P	T	R	F																			R			R																	
12H-CC, 0–5	112.81		P	T	R	F																			R			R																	
13H-1, 9–11	112.79		P	T	P*	P*																						P*																	
13H-2, 103–105	115.23			B																																									
13H-3, 122–124	116.92			B																																									
13H-4, 122–124	118.42			B																																									
13H-5, 122–124	119.92			B																																									
13H-6, 120–122	121.40		P	T																																									
13H-7, 60–62	122.30		P	F	F	F									P*									R	P*			F				F													
13H-CC, 22–27	122.76		P	R		F																						F																	
14H-1, 27–32	122.47		P	R	R	R																		P*		P*		R			P*	P*													
14H-2, 32–37	124.02		M	F		A																				P*	P*				F	F											P*		
14H-3, 31–36	125.51		P	F	F																			R			P*	F			R														
14H-4, 31–36	127.01		M	F	A				R															F	F		P*	F			F	F											F		
14H-5, 32–37	128.52		M	F	A	F																				R		F			F		R												
14H-6, 32–37	130.02		M	C	R																			F	F			F			F		F												
14H-7, 32–37	131.52		M	F	F	F																		R		F		R				R	R												
14H-CC, 0–10	131.67		M	F		F																						F			F	F	F										F		
15H-1, 50–52	132.20		M	C	R	R			R													R		P*		P*		R			F	F	F				R		R		R		R		
15H-3, 50–52	135.20		M	C	F	F																R		F				F			R	F	F				R		R		P*		R		
15H-5, 50–52	138.20	P21b	M	C	A	F																			R	R		R				F	A				F				R		R		
15H-7, 50–52	141.20		M	C	A				F													F	P*	F	F	R		R			R	P*	D				F	P*					P*		
15H-CC, 19–24	141.82		M	F		F			R															R								R	R				F								
16H-1, 117–122	142.37		G	C	A	F			F													F		F	F		R	R			R		F				R				R		P*		
16H-3, 118–123	145.38		M	C	R	R			F													F		F	F			R					A				F						F		
16H-5, 118–123	148.38		P	F		R																											A				F						P*		
16H-7, 39–44	150.59		G	C	A	R			F													R	R	F	F								A					R			R	R	R		
16H-CC, 0–3	150.80		M	C		R		R	R													R		R				R									R				R		R		
17H-1, 117–121	151.87		M	C	F	R	F	R	F													F					R	R					A				R				R		R		
17H-3, 117–122	154.87																																												
17H-5, 117–122	157.87		M	C	F			R														F						R			P*		A				F				R		R		
17H-7, 60–65	160.32	P20/21a																																											
17H-CC, 20–25	160.79		M	F		F			F													F		F	P*						P*	F	F					P*				P*			
18H-1, 98–103	161.18																																												

Table T4 (continued).

Core, section, interval (cm)	Depth (mbsf)	Zone/ Subzone	Preservation	Group abundance	*Catapsydrax dissimilis ciperoensis*	*Catapsydrax dissimilis*	*Catapsydrax unicavus*	*Chiloguembelina cubensis*	*Dentoglobigerina yeguaensis*	*Dentoglobigerina altispira*	*Dentoglobigerina baroemoenensis*	*Dentoglobigerina galavisi*	*Dentoglobigerina globularis*	*Globigerina ciperoensis*	*Globigerina praebulloides*	*Globigerinella praesiphonifera*	*Globigerinoides primordius*	*Globigerinoides trilobus*	*Globoquadrina binaiensis*	*Globoquadrina dehiscens*	*Globoquadrina praedehiscens*	*Globoquadrina prasaepis*	*Globoquadrina sellii*	*Globoquadrina tapuriensis*	*Globoquadrina tripartita*	*Globoquadrina venezuelana*	*Globorotaloides* sp.	*Globorotaloides suteri*	*Paragloborotalia continuosa*	*Paragloborotalia kugleri*	*Paragloborotalia mayeri*	*Paragloborotalia nana*	*Paragloborotalia opima opima*	*Paragloborotalia pseudokugleri*	*Paragloborotalia siakensis*	*Subbotina angiporoides*	*Subbotina euapertura*	*Subbotina gortanii*	*Subbotina praeturritilina*	*Subbotina utilisindex*	*Tenuitella clemenciae*	*Tenuitella gemma*	*Tenuitellinata angustiumbilicata*	*Turborotalia ampliapertura*	Comments
18H-2, 98–103	162.68			B																																									
18H-3, 98–103	164.18		P	F		R	R		F																			F					F				R			R	R				
18H-4, 98–103	165.68		P	R			F																										A				R								
18H-5, 98–103	167.10		M	C	R	R	R		F													F						F					A				F				R		R	R	
18H-6, 98–103	168.60			B																																									
18H-7, 18–23	169.30		P	F			F															F											A											P*	
18H-CC, 12–17	169.66		P	F		F																		R		F		F				F					R							R	
19H-1, 100–105	170.70		P	R			P*																														P*								
19H-2, 100–105	172.20		P	R			P*																														P*								
19H-3, 100–105	173.70		P	R			R																										P*												Reworked *P. opima*
19H-4, 100–105	175.20		P	F	R	P*	R																		P*			P*				R					R								
19H-5, 100–105	176.70			B																																									
19H-6, 100–105	178.20			B																																									
19H-7, 39–44	179.09			B																																									
19H-CC, 22–27	179.78		P	R		F																						F										P*			R				
20H-1, 100–104	180.20		P	R		P*	P*																									P*												P*	
20H-2, 100–104	181.70		P	T		P*	P*																					P*																	
20H-3, 50–56	182.70	P19/18	P	R		P*																																							
20H-4, 60–65	184.30		P	R		R																						R																	
20H-5, 130–135	186.50		P	R	R	R																			R			R				R											R		
20H-6, 100–105	187.70		P	R		R																			R			R				R													
20H-CC, 0–5	188.47		P	R		R																		R																R	R				
21X-CC, 0–3	188.70		P	R																					R							R													
22X-1, 40–45	196.30		P	R		F						R										R											F*			F				F	R				
22X-2, 28–32	197.68		P	R	F	F						R										R		R	F								F*							R		R		R	
22X-3, 80–85	199.70		P	R		R						R																																R	
22X-4, 128–133	201.68		P	R		R																						R																	
22X-5, 76–81	202.66		P	R		R						R										R			R	R																			
22X-6, 7–12	202.97			B																																									
22X-CC, 10–15	203.58		P	R		R																										R					R			R				R	
23X-1, 49–51	205.99			B																																									
23X-2, 106–108	208.06		P	R			R	P*														R			R							F				R				R				F	
23X-3, 115–117	209.65		P	R									P*									R		R	R							R								P*					
23X-4, 45–47	210.45		P	R		F																			P*			P*								P*								P*	
23X-5, 22–24	211.72			B																																									
23X-6, 14–16	213.14		P	R								R																								R				R					
23X-CC, 37–42	215.34		P	R		F																		R								F	F*											R	
24X-1, 18–20	215.28			B																																									
24X-2, 11–14	216.29			B																																									

Table T4 (continued).

Core, section, interval (cm)	Depth (mbsf)	Zone/ Subzone	Preservation	Group abundance	*Catapsydrax dissimilis ciperoensis*	*Catapsydrax dissimilis*	*Catapsydrax unicavus*	*Chiloguembelina cubensis*	*Dentoglobigerina yeguaensis*	*Dentoglobigerina altispira*	*Dentoglobigerina baroemoenensis*	*Dentoglobigerina galavisi*	*Dentoglobigerina globularis*	*Globigerina ciperoensis*	*Globigerina praebulloides*	*Globigerinella praesiphonifera*	*Globigerinoides primordius*	*Globigerinoides trilobus*	*Globoquadrina binaiensis*	*Globoquadrina dehiscens*	*Globoquadrina praedehiscens*	*Globoquadrina prasaepis*	*Globoquadrina sellii*	*Globoquadrina tapuriensis*	*Globoquadrina tripartita*	*Globoquadrina venezuelana*	*Globorotaloides* sp.	*Globorotaloides suteri*	*Paragloborotalia continuosa*	*Paragloborotalia kugleri*	*Paragloborotalia mayeri*	*Paragloborotalia nana*	*Paragloborotalia opima opima*	*Paragloborotalia pseudokugleri*	*Paragloborotalia siakensis*	*Subbotina angiporoides*	*Subbotina euapertura*	*Subbotina gortanii*	*Subbotina praeturritilina*	*Subbotina utilisindex*	*Tenuitella clemenciae*	*Tenuitella gemma*	*Tenuitellinata angustiumbilicata*	*Turborotalia ampliapertura*	Comments
24X-2, 37–39	216.55			B																																									
24X-2, 83–85	217.01			B																																									
24X-3, 131–133	219.01			B																																									
24X-4, 18–20	219.38			B																																									
24X-4, 109–111	220.29			B																																									
24X-4, 127–129	220.47			B																																									
24X-5, 73–75	221.43			B																																									
24X-5, 85–87	221.55			B																																									
24X-5, 143–145	222.13			B																																									
24X-6, 96–98	223.16			B																																									
24X-7, 37–39	224.07			B																																									
24X-CC, 27–32	224.87			B																																									
199-1218B-																																													
9H-3, 63–65	74.03		M	C				P*													R		F			F				A	F												F		
9H-4, 63–65	75.53	M1b	M	C												F		R		F	R					F			R	F	F										R		R		
9H-5, 63–65	77.03		M	F	R																		R	R	R	F			R		R			R											
9H-6, 63–65	78.53		P																																										
9H-7, 63–65	80.01	M1a	P	F										R							R					R			R		R														
10H-3, 125–127	84.15		M	R	R																R	F			P*	R			R		R			P*	R							P*			
10H-4, 125–127	85.65		M	F	A																				R			R	F	A					A						R				
10H-5, 125–127	87.15		P	R	R																R			R	R	R															R				
10H-6, 125–127	88.65		P	R	R																				R			R																	
10H-7, 39–41	89.24	P22		B																																									
11H-2, 120–122	92.10			B																																									
11H-3, 41–43	92.81			B																																									
11H-4, 41–43	94.31			B																																									

Notes: Preservation: G = good, M = moderate, P = poor. Group abundance: A = abundant, C = common, F = few, R = rare, T = trace (a single specimen was found), B = barren, F* = the presence of specimens referable to *Paragloborotalia opima opima* with a much earlier first occurrence than typical for this species at other sites, P* = the presence of one or two individuals in a given sample.

Table T5. Distribution of middle Eocene planktonic foraminifers, Site 1218.

Core, section, interval (cm)	Depth (mbsf)	Zone	Preservation	Group abundance	*Acarinina bullbrooki*	*Acarinina collactea*	*Acarinina praetopilensis*	*Acarinina punctocarinata*	*Acarinina rohri*	*Clavigerinella akersi*	*Clavigerinella columbiana*	*Clavigerinella eocanica*	*Clavigerinella jarvisi*	*Catapsydrax unicavus*	*Globorotaloides* sp.	*H.* cf. *bolivaraina bolivaraina*	*Muricoglobigerina senni*	*Paragloborotalia wilsoni*	*Paragloborotalia nana*	*Parasubbotina* cf. *linaperta*	*Parasubbotina griffinae*	*Subbotina* cf. *eocaena*
199-1218A-																						
24X-CC, 27–32	224.87	Not zoned		B																		
25X-CC, 21–26	234.26			B																		
26X-2, 63–67	236.43	P11/P12		B																		
26X-3, 100–104	238.3		P	T									R									
26X-5, 25–29	240.55		P	T									P									
26X-6, 120–123	243		P	R				F					F			F	R		F	R		
26X-CC, 30–35	244.12			B																		
27X-5, 20–24	249.6			B																		
27X-CC, 27–32	250.38			B																		
28X-1, 98–100	254.48		M	R	F			F	F				F	R		F	R	R	F	F	F	
28X-2, 98–100	255.98		P	R		R	R		R	R			F			F	R		F		R	
28X-3, 98–100	257.48		P	R	R	R			R		R		F			F	R	R	R	R	F	
28X-4, 104–106	259.04		P	R								R				R			R			
28X-5, 55–57	260.05		P	R		R						R				R			R	R		
28X-6, 85–87	261.85			B																		
28X-CC, 15–19	262.94		P	R	R			F	F			R	R		R	R	R		F	R		
29X-1, 102–105	264.12		P	R		P						R				F			F			
29X-2, 123–127	265.83		P	R	R				R			R		P		F			F	F	F	P
29X-3, 102–106	267.12		P	R		P						R		P		R	R		R		R	
29X-CC, 33–38	268.87		P	R									R				P		R		R	
30X-CC, 20–26	274.23		P	R									P								R	

Notes: Preservation: B = barren, P = poor, M = moderate. Group abundance: F = few, R = rare, T = trace, P = present, B = barren (see Table T4, p. 92).

Table T6. Planktonic foraminifer datum levels, Site 1218.

Marker species	Age (Ma)	Core, section, interval (cm)		Depth (mbsf)		Depth (mcd)	
		Top	Bottom	Midpoint	±	Midpoint	±
		199-1218A-	199-1218A-				
T *Catapsydrax dissimilis ciperoensis*	17.3 [17.5]	6H-6, 94–96	6H-7, 39–41	54.87	0.23	61.71	0.23
T *Paragloborotalia kugleri*	21.5 [21.0]	8H-1, 110–112	8H-2, 110–114	67.05	0.75	75.01	0.75
B *Globoquadrina dehiscens*	23.2	8H-6, 60–62	8H-CC	73.72	0.42	81.68	0.42
B *Paragloborotalia kugleri*	23.8 [22.9]	10H-1, 130–132	10H-2, 74–75	85.97	0.47	97.87	0.47
B *Paragloborotalia pseudokugleri*	[24.6]	12H-2, 118–122	12H-4, 59–64	107.09	1.21	121.56	1.21
T *Paragloborotalia opima opima*	27.1	14H-4, 31–33	14H-5, 32–35	127.77	0.76	143.19	0.76
B *Globorotalia mayeri*	—	16H-1, 117–122	16H-3, 118–122	143.88	1.51	161.72	1.51
B *Globoquadrina tapuriensis*	—	16H-CC	17H-1, 117–121	151.34	0.54	169.21	0.57
T Common *Chiloguembelina cubensis*	28.5 [27.0]	16H-7, 39–44	16H-CC	150.70	0.11	168.54	0.11
T *Turborotalia ampliapertura*	30.3 [29.3]	18H-4, 98–100	18H-5, 98–100	166.39	0.71	186.95	0.71
B *Paragloborotalia opima opima*	30.6 [29.6]	18H-6, 98–100	18H-CC	169.13	0.53	189.69	0.53
		199-1218B-	199-1218B-				
B *Globoquadrina dehiscens*	23.2	9H-4, 63–65	9H-5, 63–65	76.28	0.75	84.62	0.75

Notes: T = top or highest occurrence, B = bottom or first occurrence. Ages are those of Berggren et al. (1995); ages in square brackets are those of Shackleton et al. (1999). Several well defined datums without calibrations to the magnetostratigraphic time scale are also included. This table is also available in **ASCII.**

Table T7. Distribution of benthic foraminifers, Hole 1218A. (Continued on next page.)

Core, section, interval (cm)	Depth (mbsf)	Preservation	Group abundance	Bathymetry	*Abyssamina quadrata*	*Ammodiscus* sp.	*Anomalinoides capitatus*	*Anomalinoides pseudogrosserugosus*	*Anomalinoides semicribratus*	*Anomalinoides spissiformis*	*Bathysiphon* spp.	*Buliminella* cf. *carseyae*	*Cibicidoides eocaenus*	*Cibicidoides grimsdalei*	*Cibicidoides havanensis*	*Cibicidoides praemundulus*	*Cibicidoides* cf. *subspiratus*	*Cribrostomoides* spp.	*Dentalina*/*Nodosaria* spp.	*Eggerella* spp.	*Epistominella exigua*	*Gaudryina laevigata*	*Globocassidulina globosa*	*Globocassidulina* spp.	*Glomospira* sp.	*Gyroidinoides girardanus*	*Gyroidinoides lamarckianus*	*Gyroidinoides neosoldanii*	*Gyroidinoides* spp.	*Heronallenia* sp.	*Karreriella chapapotensis*	*Karreriella subglabra*	*Laticarinina pauperata*	*Lenticulina* spp.	*Martinottiella communis*	*Nodosarella rotundata*	*Nuttallides truempyi*	*Nuttallides umbonifera*	*Oridorsalis umbonatus*	*Osangularia mexicana*	*Pleurostomella* spp.	*Pullenia bulloides*	*Pullenia osloensis*	*Pullenia subcarinata*
199-1218A-																																												
1H-CC, 5–15	8.16		B																																									
2H-CC, 9–14	17.95		B																																									
3H-CC, 22–27	27.76		B																																									
4H-CC, 18–23	37.03		B																																									
5H-CC, 19–24	46.35	VG	F	LB–UA							F			F						R				F					R			R				R		A	A		F	F		R
6H-CC, 0–5	55.32	VG	F	LB–UA					R											R					R		R	R											R		F	R	F	R
7H-CC, 19–24	65.70	VG	F	LB–UA							F			R	R				R					R					F							R		F	A		A			R
8H-CC, 14–19	74.13	VG	F	LB–UA										R						R	F						R			R									F		F		F	R
9H-CC, 14–19	84.68	VG	F	LB–UA											R				R		F			F				F					R		R	R		R	A		F		F	R
10H-CC, 13–18	93.86	VG	R	LB–UA							R			R	R	F				R			F	F	R			F		R					R	R			F		F	R		F
11H-CC, 19–24	103.72	VG	R	LB–UA				F			R			F	F				R	R				A	R			F				R	R					R	R		F			F
12H-CC, 0–5	112.81	VG	R	LB–UA				R		R		R		F										A				F				R							R					R
13H-CC, 22–27	122.76	VG	F	LB–UA					R	R				R	R			R	F	R							F											R	F		F			F
14H-CC, 0–10	131.67	VG	F	LB–UA					R	R			R	R					F						F		R	F				R			R			R	F		F			F
15H-CC, 19–24	141.82	VG	F	LB–UA				F	F	R				R										F		F	R				R							R	F		R		R	
16H-CC, 0–3	150.80	VG	F	LB–UA					F		R	F		F	F				R	R				R		F						R							F					R
17H-CC, 20–25	160.79	VG	F	LB–UA										R		A			A	R				R			F			R									R		F			F
18H-CC, 12–17	169.66	VG	F	LB–UA		R			R			R	R	R		A								R		F				R									F		F			
19H-CC, 22–27	179.78	VG	F	LB–UA					R				F				A			F			A	F							R								F		A			
20H-CC, 0–5	188.47	VG	F	LB–UA						R		R	R	F			F						A				R					R							A			R		
21X-CC, 0–3	188.70	VG	R	LB–UA									R	F		A								F		F			F			R							F			R		
22X-CC, 10–15	203.58	VG	R	LB–UA						F				F			A									R	R												R		F			F
23X-CC, 37–42	215.34	VG	F	LB–UA						F							R							F		F												R	A		R	F		
24X-CC, 27–32	224.87	P	R	LB–UA									F			F																							F					
25X-CC, 21–26	234.26	P	R	LB–UA										A																									F					
26X-CC, 30–35	244.12	P	R	LB–UA										F					F																				F					
27X-CC, 27–32	250.38	P	R	LB–UA									F																										F	F				
28X-CC, 15–19	262.94	VG	C	LB–UA			F		R	F				F	F	F													F					R			A		F					
29X-CC, 33–38	268.87	M	F	LB–UA						F			F	A																							A		F	F	F			
30X-CC, 20–26	274.23	P	F	LB–UA	R				R	F			F	A	R	F			F			R	R	R					F								F		R	R	F			

Notes: Preservation: VG = very good, M = moderate, P = poor. Group abundance: A = abundant, F = few, R = rare. Bathymetry: LB–UA = lower bathyal to upper abyssal.

Table T7 (continued).

Core, section, interval (cm)	Depth (mbsf)	Preservation	Group abundance	Bathymetry	*Pyrulina* spp.	*Recurvoides* sp.	*Rhizammina* sp.	*Siphonodosaria abyssorum*	*Spiroplectammina spectabilis*	*Stilostomella lepidula*	*Stilostomella rugosa*	*Stilostomella subspinosa*	*Subreophax* sp.	Unidentified benthic forams	Unilocular species	*Uvigerina* spp.	*Vulvulina spinosa*
199-1218A-																	
1H-CC, 5–15	8.16		B														
2H-CC, 9–14	17.95		B														
3H-CC, 22–27	27.76		B														
4H-CC, 18–23	37.03		B														
5H-CC, 19–24	46.35	VG	F	LB–UA				R	R			R	R	R	F		
6H-CC, 0–5	55.32	VG	F	LB–UA	R			R		F		F		R	R		
7H-CC, 19–24	65.70	VG	F	LB–UA				F				F		R	F		R
8H-CC, 14–19	74.13	VG	F	LB–UA								F		R			
9H-CC, 14–19	84.68	VG	F	LB–UA				R		F		F		R	F		
10H-CC, 13–18	93.86	VG	R	LB–UA			R		R			F		R	R		R
11H-CC, 19–24	103.72	VG	R	LB–UA				F	R			F		R	R		
12H-CC, 0–5	112.81	VG	R	LB–UA				F	R			F		R	F		R
13H-CC, 22–27	122.76	VG	F	LB–UA				F	R	R		F		R	R		
14H-CC, 0–10	131.67	VG	F	LB–UA				F	R			F		R			R
15H-CC, 19–24	141.82	VG	F	LB–UA		R		R			R	F		R	R		
16H-CC, 0–3	150.80	VG	F	LB–UA				R	R					R	R		R
17H-CC, 20–25	160.79	VG	F	LB–UA				F		F				R	R		
18H-CC, 12–17	169.66	VG	F	LB–UA					R			F		R	F		
19H-CC, 22–27	179.78	VG	F	LB–UA				F	R			F		R	R		R
20H-CC, 0–5	188.47	VG	F	LB–UA								R		R	R		R
21X-CC, 0–3	188.70	VG	R	LB–UA					R	F				R			R
22X-CC, 10–15	203.58	VG	R	LB–UA	R			F						R			R
23X-CC, 37–42	215.34	VG	F	LB–UA				F						R			
24X-CC, 27–32	224.87	P	R	LB–UA				F						R			
25X-CC, 21–26	234.26	P	R	LB–UA				F						R			
26X-CC, 30–35	244.12	P	R	LB–UA				F						R			
27X-CC, 27–32	250.38	P	R	LB–UA				F						R			
28X-CC, 15–19	262.94	VG	C	LB–UA					R					R	R		R
29X-CC, 33–38	268.87	M	F	LB–UA				R						R	R		
30X-CC, 20–26	274.23	P	F	LB–UA						F	R			R	R	R	R

Table T8. Distribution of radiolarian datum levels, Site 1218.

Marker species/ Zonal boundaries	Age (Ma)	Hole, core, section interval (cm)		Depth (mbsf)		Depth (mcd)	
		Top	Bottom	Midpoint	±	Midpoint	±
		199-	199-				
T *Stylatractus universus*	0.41	1218A-1H-2, 45	1218A-1H-3, 46	2.71	0.76	2.71	0.76
B *Collosphaera tuberosa*	0.61	1218A-1H-3, 46	1218A-1H-4, 45	4.21	0.75	4.21	0.75
T *Calocycletta caepa*	6.20	1218A-3H-5, 46	1218A-3H-6, 46	24.91	0.75	27.25	0.75
T *Stichocorys johnsoni*	6.60	1218A-3H-5, 46	1218A-3H-6, 46	24.91	0.75	27.25	0.75
Lithopera neotera → *L. bacca*	8.80	1218A-4H-2, 45	1218A-4H-5, 45	31.40	2.25	35.82	2.25
T *Carpocanopsis cristata*	10.60	1218A-4H-3, 45	1218A-4H-4, 45	31.40	0.75	35.82	0.75
RN7/6	8.77	1218A-4H-3, 45	1218A-4H-5, 47	32.15	1.50	36.57	1.50
T *Stichocorys wolffii*	8.80	1218A-4H-4, 45	1218A-4H-5, 45	32.90	0.75	37.32	0.75
T *Cyrtocapsella cornuta*	12.10	1218A-4H-4, 45	1218A-4H-5, 45	32.90	0.75	37.32	0.75
T *Cyrtocapsella tetrapera*	12.10	1218A-4H-5, 45	1218A-4H-6, 45	34.40	0.75	38.82	0.75
T *Dorcadospyris alata*	13.60	1218A-4H-6, 45	1218A-4H-7, 45	35.90	0.75	40.32	0.75
RN6/5	11.95	1218B-5H-3, 22	1218A-4H-CC	36.33	0.71	41.37	0.09
T *Calocycletta costata*	15.00	1218A-4H-CC	1218A-5H-1, 45	37.09	0.06	41.70	0.25
T *Carpocanopsis bramlettei*	14.70	1218A-5H-3, 45	1218A-5H-4, 47	40.90	0.75	45.70	0.75
RN5/4	15.70	1218A-5H-4, 45	1218A-5H-5, 47	42.41	0.76	47.21	0.76
RN4/3	17.00	1218A-6H-1, 45	1218A-6H-2, 45	47.40	0.75	54.24	0.75
RN3/2	17.90	1218A-6H-7, 45	1218A-6H-CC	55.24	0.09	62.08	0.09
RN2/1	20.53	1218A-7H-6, 46	1218A-7H-7, 46	64.41	0.75	72.47	0.75
RN1/RP22	23.62	1218A-9H-5, 74	1218B-10H-2, 72	81.77	0.33	92.30	0.60
RP22/21	24.60	1218A-11H-3, 44	1218A-11H-4, 44	97.89	0.75	111.29	0.75
RP21/20	28.80	1218A-18H-6, 46	1218A-18H-CC	168.87	0.79	189.43	0.79
RP20/19	32.80	1218A-23X-CC	1218C-17X-4, 58	215.40	0.06	239.23	0.65
RP19/18	34.90	1218A-24X-CC	1218A-25X-1, 24	224.91	0.04	250.58	0.63
RP18/17	36.40	1218A-25X-1, 24	1218A-25X-2, 82	225.98	1.04	252.25	1.04
RP17/16	37.70	1218A-26X-1, 46	1218A-26X-2, 45	235.51	0.75	261.58	0.75
RP16/15	38.80	1218A-27X-1, 45	1218A-27X-2, 45	245.10	0.75	271.23	0.75

Notes: T = top, B = bottom. This table is also available in **ASCII**. [**N1**]

Table T9. Composite depth of identified geomagnetic reversals, Site 1218.

Chron/ Subchron	Depth (mcd)	Age* (Ma)
T C3n.1n	18.99	4.180
B C3n.1n	19.49	4.290
T C3n.2n	20.30	4.680
B C3n.2n	20.50	4.620
T C3n.3n	20.80	4.800
B C3n.3n	20.96	4.890
T C3n.4n	21.21	4.980
B C3n.4n	21.67	5.230
T C3An.1n	23.48	5.875
B C3An.1n	24.24	6.122
T C3An.2n	24.65	6.256
B C3An.2n	25.70	6.555
T C4n	30.70	7.406
B C4n	31.82	8.027
T C4An	32.32	8.631
B C4An	32.93	8.945
T C4Ar.1n	33.28	7.406
B C4Ar.1n	33.53	7.533
T C5n	33.94	9.639
B C5n	36.54	10.839
T C5r.2n	37.84	11.343
B C5r.2n	38.12	11.428
T C5An.1n	38.97	11.841
B C5An.1n	39.37	11.988
T C5An.2n	39.70	12.096
B C5An.2n	40.18	12.320
T C5Ar.1n	41.23	12.605
B C5Ar.1n	41.35	12.637
T C5Ar.2n	41.64	12.705
B C5Ar.2n	41.76	12.752
T C5AAn	42.24	12.929
B C5AAn	42.81	13.083
T C5ABn	43.25	13.252
B C5ABn	43.94	13.466
T C5ACn	44.26	13.666
B C5ACn	44.99	14.053
T C5ADn	45.11	14.159
B C5ADn	46.04	14.607
T C5Bn.1n	46.48	14.800
B C5Bn.1n	46.67	14.888
T C5Bn.2n	47.01	15.034
B C5Bn.2n	47.41	15.155
T C5Cn.1n	51.21	16.014
B C5Cn.1n	52.02	16.293
T C5Cn.2n	52.22	16.327
B C5Cn.2n	52.55	16.488
T C5Cn.3n	52.91	16.556
B C5Cn.3n	53.31	16.726
T C5Dn	55.21	17.277
B C5Dn	55.94	17.615
T C5En	57.39	18.281
B C5En	58.93	18.781
T C6n	59.74	19.048
B C6n	66.93	20.131
T C6An.1n	69.23	20.518
B C6An.1n	70.29	20.725
T C6An.2n	71.38	20.996
B C6An.2n	73.16	21.320
T C6AAn	75.83	21.768
B C6AAn	78.10	21.859
T C6AAr.2n	83.91	22.459
B C6AAr.2n	84.31	22.493
T C6Bn.1n	85.05	22.588
B C6Bn.1n	86.30	22.750
T C6Bn.2n	86.74	22.804
B C6Bn.2n	89.73	23.069
T C6Cn.2n	95.07	23.677
B C6Cn.2n	96.44	23.800
T C6Cn.3n	98.78	23.999
B C6Cn.3n	100.04	24.118
T C7n	108.04	24.730
T C8n	115.27	25.823
B C8n	131.43	25.951
T C9n	137.27	27.027
B C9n	151.66	27.972
T C10n	157.72	28.283
B C10n	164.24	28.512
T C11n	178.33	29.401
B C11n	191.06	29.662
T C12n	200.50	30.479
B C12n	203.77	30.939

Notes: * = Cande and Kent (1995). T = top, B = bottom. This table is also available in ASCII.

Table T10. Core disturbance, Site 1218.

Core, section, interval (cm)	Depth (mbsf) Top	Bottom	Comments
199-1218A-			
1H-1, 0–20	0.00	0.20	Flow-in
2H-1, 0–5	8.20	8.25	Flow-in
2H-1, 126–130	9.46	9.50	Void
2H-3, 26–30	11.46	11.50	Flow-in
3H-1, 0–8	17.70	17.78	Drilling debris
3H-CC, 6–20	27.60	27.74	
4H-4, 140–150	33.10	33.20	
4H-CC, 0–22	36.85	37.07	
5H-1, 0–9	36.70	36.79	Flow-in
5H-1, 26–29	36.96	36.99	Void
5H-3, 145–150	41.15	41.20	
6H-1, 23–25	46.43	46.45	Void
6H-2, 102–103	48.72	48.73	
6H-3, 145–150	50.65	50.70	
7H-1, 0–20	55.70	55.90	Soupy
8H-1, 0–106	65.20	66.26	Soupy
13H-1, 0–1	112.70	112.71	Flow-in
14H-1, 0–9	122.20	122.29	Drilling debris
14H-1, 9–14	122.29	122.34	Flow-in
16H-1, 0–10	141.20	141.30	Flow-in
17H-1, 0–76	150.70	151.46	Flow-in
17H-1, 76–83	151.46	151.53	Void
17H-7, 83–84	160.55	160.56	
19H-1, 0–43	169.70	170.13	
20H-1, 0–17	179.20	179.37	
20H-1, 45–50	179.65	179.70	Splitting disturbance
26X-1, 1–6	234.31	234.36	Chert
26X-2, 74–75	236.54	236.55	Chert
27X-1, 0–4	243.90	243.94	
27X-1, 20–29	244.10	244.19	Chert
27X-1, 34–41	244.24	244.31	Chert
27X-CC, 0–4	250.11	250.15	Downhole debris
27X-CC, 14–24	250.25	250.35	Downhole debris
28X-1, 0–23	253.50	253.73	Chert
28X-2, 80–84	255.80	255.84	Chert
29X-3, 32–34	266.42	266.44	Chert
29X-4, 4–20	267.64	267.80	Chert
29X-CC, 16–20	268.70	268.74	Chert
199-1218B-			
3H-2, 43–52	15.33	15.42	Void
5H-1, 24–35	32.64	32.75	Soupy
5H-1, 47–80	32.87	33.20	Soupy
7H-1, 0–33	51.40	51.73	Soupy
8H-1, 0–40	60.90	61.30	Flow-in
8H-4, 57–60	65.97	66.00	Void
9H-1, 0–31	70.40	70.71	Flow-in
10H-3, 43–44	83.33	83.34	Void
10H-3, 109–113	83.99	84.03	Void
11H-1, 0–17	89.40	89.57	Flow-in
12H-1, 146–150	100.36	100.40	Disturbed
12H-CC, 20–32	108.89	109.01	Disturbed
13H-1, 0–2	108.40	108.42	Flow-in
15H-1, 0–38	127.40	127.78	Soupy
18H-1, 0–1	155.90	155.91	Downhole debris
18H-7, 14–53	165.04	165.43	Splitting disturbance?
19X-1, 0–2	165.40	165.42	Flow-in
19X-1, 144–150	166.84	166.90	Void
20X-1, 0–4	175.10	175.14	Downhole debris
20X-1, 11–20	175.21	175.30	Flow-in
22X-3, 130–133	198.70	198.73	Void
23X-3, 20–40	207.30	207.50	Chert
26X-1, 0–10	228.30	228.40	Downhole debris
27X-1, 0–10	237.90	238.00	Downhole debris
27X-3, 91–101	241.81	241.91	Chert/porcellanite
27X-3, 138–150	242.28	242.40	Fragmented
27X-4, 130–150	243.70	243.90	Fragmented
28X-1, 0–8	247.50	247.58	Fragmented/downhole debris
28X-1, 34–39	247.84	247.89	Slurry
28X-1, 52–59	248.02	248.09	Fragmented
28X-1, 128–137	248.78	248.87	Fragmented/slurry
28X-2, 25–50	249.25	249.50	Fragmented
28X-2, 60–72	249.60	249.72	Fragmented
28X-2, 136–150	250.36	250.50	Slurry/fragmented
28X-3, 77–102	251.27	251.52	Slurry/fragmented
28X-4, 0–18	251.50	251.68	Slurry/fragmented
28X-CC, 0–5	252.43	252.48	Slurry/chert
28X-CC, 15–23	252.58	252.66	Slurry
29X-1, 96–105	258.16	258.25	Chert
29X-2, 106–113	259.76	259.83	Chert
29X-3, 39–44	260.59	260.64	Chert
29X-3, 94–102	261.14	261.22	Chert
199-1218C-			
1H-1, 0–20	55.00	55.20	Soupy
1H-1, 33–36	55.33	55.36	Soupy
5H-1, 0–2	93.00	93.02	Flow-in
6H-1, 0–25	102.50	102.75	Soupy
6H-7, 0–83	111.30	112.13	Crushed line
6H-CC, 0–10	112.14	112.24	Crushed line
8H-1, 78–81	122.28	122.31	Void
9H-1, 0–15	131.00	131.15	Flow-in
9H-1, 33–34	131.33	131.34	Crack
10H-1, 0–6	144.50	144.56	
10H-4, 76–81	149.76	149.81	
10H-6, 47–49	152.47	152.49	Void
10H-7, 0–3	153.50	153.53	
10H-7, 26–28	153.76	153.78	Void
10H-7, 44–62	153.94	154.12	
10H-CC, 0–14	154.12	154.23	
11H-1, 0–4	154.00	154.04	Flow-in
12X-1, 0–11	163.50	163.61	Flow-in
12X-1, 141–150	164.91	165.00	Void
13X-1, 0–10	172.00	172.10	
13X-1, 84–96	172.84	172.96	Soupy
13X-1, 112–113	173.12	173.13	Crack
13X-5, 146–150	179.46	179.50	Splitting disturbance
17X-4, 33–34	215.23	215.24	Chert
19X-1, 0–5	232.60	232.65	Chert
19X-5, 77–80	239.37	239.40	Chert
19X-5, 110–113	239.70	239.73	Chert
19X-5, 137–145	239.97	240.05	Chert

Notes: Data from these intervals were removed from the GRA bulk density, MS, color reflectance, natural gamma, and *P*-wave velocity data sets. This table is also available in **ASCII.** [N1]

Table T11. Composite depths, Site 1218.

Core	Length (m)	Depth (mbsf)	Offset (m)	Depth (mcd)
199-1218A-				
1H	8.2	0.0	0.00	0.00
2H	9.5	8.2	0.78	8.98
3H	9.5	17.7	2.34	20.04
4H	9.5	27.2	4.42	31.62
5H	9.5	36.7	4.80	41.50
6H	9.5	46.2	6.84	53.04
7H	9.5	55.7	8.06	63.76
8H	9.5	65.2	7.96	73.16
9H	9.5	74.7	10.26	84.96
10H	9.5	84.2	11.90	96.10
11H	9.5	93.7	13.40	107.10
12H	9.5	103.2	14.47	117.67
13H	9.5	112.7	14.91	127.61
14H	9.5	122.2	15.42	137.62
15H	9.5	131.7	16.22	147.92
16H	9.5	141.2	17.84	159.04
17H	9.5	150.7	17.90	168.60
18H	9.5	160.2	20.56	180.76
19H	9.5	169.7	20.38	190.08
20H	9.5	179.2	22.28	201.48
22X	9.6	195.9	22.30	218.20
23X	9.6	205.5	23.24	228.74
24X	9.6	215.1	25.08	240.18
25X	9.6	224.7	26.27	250.97
26X	9.6	234.3	26.07	260.37
27X	9.6	243.9	26.13	270.03
28X	9.6	253.5	23.93	277.43
29X	7.6	263.1	24.23	287.33
30X	6.1	270.7	24.23	294.93
199-1218B-				
1H	3.9	0.0	0.00	0.00
2H	9.5	3.9	1.16	5.06
3H	9.5	13.4	3.82	17.22
4H	9.5	22.9	5.18	28.08
5H	9.5	32.4	5.66	38.06
6H	9.5	41.9	7.66	49.56
7H	9.5	51.4	7.29	58.69
8H	9.5	60.9	8.39	69.29
9H	9.5	70.4	8.34	78.74
10H	9.5	79.9	10.80	90.70
11H	9.5	89.4	13.38	102.78
12H	9.5	98.9	15.24	114.14
13H	9.5	108.4	15.49	123.89
14H	9.5	117.9	16.46	134.36
15H	9.5	127.4	17.82	145.22
16H	9.5	136.9	19.02	155.92
17H	9.5	146.4	19.78	166.18
18H	9.5	155.9	20.12	176.02
19X	9.7	165.4	19.04	184.44
20X	9.7	175.1	20.70	195.80
21X	9.6	184.8	22.52	207.32
22X	9.7	194.4	23.02	217.42
23X	9.6	204.1	23.78	227.88
24X	9.6	213.7	26.46	240.16
25X	5.0	223.3	28.13	251.43
26X	9.6	228.3	27.61	255.91
27X	9.6	237.9	29.13	267.03
28X	9.7	247.5	30.53	278.03
29X	6.3	257.2	30.63	287.83
199-1218C-				
1H	9.5	55.0	8.04	63.04
2H	9.5	64.5	9.36	73.86
3H	9.5	74.0	9.78	83.78
4H	9.5	83.5	11.58	95.08
5H	9.5	93.0	12.82	105.82
6H	9.5	102.5	15.58	118.08
7H	9.5	112.0	14.09	126.09
8H	9.5	121.5	14.47	135.97
9H	9.5	131.0	15.90	146.90
10H	9.5	144.5	17.84	162.34
11H	9.5	154.0	18.62	172.62
12X	8.5	163.5	19.78	183.28
13X	9.6	172.0	19.76	191.76
14X	9.6	181.6	19.81	201.41
15X	9.6	191.2	21.92	213.12
16X	9.6	200.8	23.90	224.70
17X	9.6	210.4	23.46	233.86
18X	9.6	223.0	24.42	247.42
19X	9.6	232.6	24.93	257.53
20X	5.0	242.2	27.45	269.65
21X	9.6	247.2	27.57	274.77

Note: This table is also available in **ASCII**. [**N1**]

Table T12. Splice tie points, Site 1218.

Hole, core, section, interval (cm)	Depth (mbsf)	Depth (mcd)		Hole, core, section, interval (cm)	Depth (mbsf)	Depth (mcd)
199-				199-		
1218A-1H-5, 54	6.54	6.54	Tie to	1218B-2H-1, 148	5.38	6.54
1218B-2H-5, 40	10.30	11.46	Tie to	1218A-2H-2, 97	10.68	11.46
1218A-2H-7, 6	17.26	18.04	Tie to	1218B-3H-1, 82	14.22	18.04
1218B-3H-5, 12	19.52	23.34	Tie to	1218A-3H-3, 30	21.00	23.34
1218A-3H-6, 132	26.52	28.86	Tie to	1218B-4H-1, 78	23.68	28.86
1218B-4H-4, 120	28.60	33.78	Tie to	1218A-4H-2, 66	29.36	33.78
1218A-4H-6, 132	36.02	40.44	Tie to	1218B-5H-2, 88	34.78	40.44
1218B-5H-5, 44	38.84	44.50	Tie to	1218A-5H-2, 150	39.70	44.50
1218A-5H-7, 20	45.90	50.70	Tie to	1218B-6H-1, 113	43.04	50.70
1218B-6H-4, 60	47.00	54.66	Tie to	1218A-6H-2, 12	47.82	54.66
1218A-6H-6, 88	54.58	61.42	Tie to	1218B-7H-2, 128	54.13	61.42
1218B-7H-5, 56	57.91	65.20	Tie to	1218A-7H-1, 144	57.14	65.20
1218A-7H-6, 8	63.28	71.34	Tie to	1218B-8H-2, 54.5	62.95	71.34
1218B-8H-5, 76	67.66	76.05	Tie to	1218A-8H-2, 138.5	68.09	76.05
1218A-8H-5, 112	72.32	80.28	Tie to	1218B-9H-2, 3	71.94	80.28
1218B-9H-6, 118	79.08	87.42	Tie to	1218A-9H-2, 96	77.16	87.42
1218A-9H-6, 112	83.32	93.58	Tie to	1218B-10H-2, 138	82.78	93.58
1218B-10H-6, 126	88.66	99.46	Tie to	1218A-10H-3, 36	87.56	99.46
1218A-10H-6, 92	92.62	104.52	Tie to	1218B-11H-2, 24	91.14	104.52
1218B-11H-6, 144	98.34	111.72	Tie to	1218A-11H-4, 12	98.32	111.72
1218A-11H-6, 136	102.56	115.96	Tie to	1218B-12H-2, 32	100.72	115.96
1218B-12H-5, 144	106.34	121.58	Tie to	1218A-12H-3, 90.5	107.11	121.58
1218A-12H-5, 112	110.32	124.79	Tie to	1218B-13H-1, 90	109.30	124.79
1218B-13H-6, 44	116.34	131.83	Tie to	1218A-13H-3, 122	116.92	131.83
1218A-13H-6, 44	120.64	135.55	Tie to	1218B-14H-1, 118.5	119.09	135.55
1218B-14H-4, 66	123.06	139.52	Tie to	1218A-14H-2, 36	124.10	139.52
1218A-14H-6, 104	130.74	146.16	Tie to	1218B-15H-1, 94	128.34	146.16
1218B-15H-4, 40	132.30	150.12	Tie to	1218A-15H-2, 69	133.90	150.12
1218A-15H-7, 48	141.18	157.40	Tie to	1218B-16H-1, 148	138.38	157.40
1218B-16H-6, 40	144.30	163.32	Tie to	1218A-16H-3, 128	145.48	163.32
1218A-16H-6, 64	149.34	167.18	Tie to	1218B-17H-1, 99	147.40	167.18
1218B-17H-6, 46	154.36	174.14	Tie to	1218C-11H-2, 0	155.52	174.14
1218C-11H-5, 58	160.58	179.20	Tie to	1218B-18H-3, 18	159.08	179.20
1218B-18H-5, 118	163.08	183.20	Tie to	1218A-18H-2, 94	162.64	183.20
1218A-18H-5, 8	166.20	186.76	Tie to	1218C-12X-3, 48	166.98	186.76
1218C-12X-6, 28	171.28	191.06	Tie to	1218A-19H-1, 98	170.68	191.06
1218A-19H-6, 76	177.96	198.34	Tie to	1218B-20X-2, 103	177.64	198.34
1218B-20X-5, 120	182.30	203.00	Tie to	1218A-20H-1, 152	180.72	203.00
1218A-20H-6, 92	187.62	209.90	Tie to	1218B-21X-2, 108	187.38	209.90
1218B-21X-6, 66	192.96	215.48	Tie to	1218C-15X-2, 85	193.56	215.48
1218C-15X-4, 76	196.46	218.38	Tie to	1218B-22X-1, 96	195.36	218.38
1218B-22X-7, 20	203.23	226.25	Tie to	1218C-16X-2, 4.5	202.35	226.25
1218C-16X-5, 6	206.86	230.76	Tie to	1218A-23X-2, 52	207.52	230.76
1218A-23X-5, 92	212.42	235.66	Tie to	1218C-17X-2, 30	212.20	235.66
1218C-17X-6, 12	217.72	241.18	Tie to	1218B-24X-1, 101	214.72	241.18
1218B-24X-6, 94	222.14	248.60	Tie to	1218C-18X-1, 118	224.18	248.60
1218C-18X-7, 32	231.89	256.31	Tie to	1218B-26X-1, 40	228.70	256.31
1218B-26X-5, 96	234.76	262.37	Tie to	1218A-26X-2, 50	236.30	262.37
1218A-26X-6, 6	241.86	267.93	Tie to	1218B-27X-1, 90	238.80	267.93
1218B-27X-6, 132	246.72	275.85	Tie to	1218C-21X-1, 108	248.28	275.85
1218C-21X-3, 106	251.26	278.83	Tie to	1218A-28X-1, 139	254.90	278.83
1218A-28X-7, 74	262.74	286.67	Append to	1218A-29X-1, 0	263.10	287.33
1218A-29X-4, 88	268.48	292.71	Append to	1218A-30X-1, 0	270.70	294.93
1218A-30X-2, 140	273.60	297.83				

Note: This table is also available in ASCII.

Table T13. Paleomagnetic events, Site 1218.

Chron/Subchron	Age (Ma)	Depth (mcd)
T C3n.1n	4.180	18.99
B C3n.1n	4.290	19.49
T C3n.2n	4.480	20.30
B C3n.2n	4.620	20.50
T C3n.3n	4.800	20.80
B C3n.3n	4.890	20.96
T C3n.4n	4.980	21.21
B C3n.4n	5.230	21.67
T C3An.1n	5.875	23.48
B C3An.1n	6.122	24.24
T C3An.2n	6.256	24.65
B C3An.2n	6.555	25.70
T C4n	7.135	30.70
B C4n	8.027	31.82
T C4An	8.631	32.32
B C4An	8.945	32.93
T C4Ar.1n	9.142	33.28
B C4Ar.1n	9.218	33.53
T C5n	9.639	33.94
B C5n	10.839	36.54
T C5r.2n	11.343	37.84
B C5r.2n	11.428	38.12
T C5An.1n	11.841	38.97
B C5An.1n	11.988	39.37
T C5An.2n	12.096	39.70
B C5An.2n	12.320	40.18
T C5Ar.1n	12.605	41.23
B C5Ar.1n	12.637	41.35
T C5Ar.2n	12.705	41.64
B C5Ar.2n	12.752	41.76
T C5AAn	12.929	42.24
B C5AAn	13.083	42.81
T C5ABn	13.252	43.25
B C5ABn	13.466	43.94
T C5ADn	14.159	45.11
B C5ADn	14.607	46.04
T C5Bn.2n	15.034	47.01
B C5Bn.2n	15.155	47.41
T C5Cn.2n	16.327	52.22
B C5Cn.2n	16.488	52.55
T C5Cn.3n	16.556	52.91
B C5Cn.3n	16.726	53.31
T C5Dn	17.277	55.21
B C5Dn	17.615	55.94
T C5En	18.281	57.39
B C5En	18.781	58.93
T C6n	19.048	59.74
B C6n	20.131	66.93
T C6An.1n	20.518	69.23
B C6An.1n	20.725	70.29
T C6An.2n	20.996	71.38
B C6An.2n	21.320	73.16
T C6AAn	21.768	75.83
B C6AAn	21.859	78.10
T C6AAr.2n	22.459	83.91
B C6AAr.2n	22.493	84.31
T C6Bn.1n	22.588	85.05
B C6Bn.1n	22.750	86.30
T C6Bn.2n	22.804	86.74
B C6Bn.2n	23.069	89.73
T C6Cn.2n	23.677	95.07
B C6Cn.2n	23.800	96.44
T C6Cn.3n	23.999	98.78
B C6Cn.3n	24.118	100.04
T C7n	25.496	108.04
T C8n	25.823	115.27
B C8n	26.554	131.43
T C9n	27.027	137.27
T C9n	27.972	151.66
T C10n	28.283	157.72
B C10n	28.745	164.24
T C11n	29.401	178.33
B C11n	30.098	191.06
B C12	30.939	203.77

Notes: T = top, B = bottom. This table is also available in **ASCII.**

Table T14. Nannofossil, foraminifer, and radiolarian events, Site 1218.

Marker species/ Zonal boundaries	Age (Ma)	Depth (mcd)	± (m)
Nannofossil events:			
B *Catinaster coalitus*	10.80	40.77	0.06
B *Discoaster kugleri*	11.60	40.12	0.16
T *Cyclicargolithus floridanus*	13.20	47.51	0.19
T *Sphenolithus heteromorphus*	13.60	50.46	0.16
T *Discoaster deflandrei* acme	16.10	50.46	0.16
B *Sphenolithus disbelemnos*	22.70	90.02	0.25
T *Sphenolithus delphix*	23.00	97.50	0.09
B *Sphenolithus delphix*	23.20	98.27	0.54
T *Sphenolithus ciperoensis*	24.10	109.82	0.71
T *Sphenolithus distentus*	26.50	131.18	0.56
B *Sphenolithus ciperoensis*	28.10	144.38	0.75
B *Sphenolithus distentus*	30.40	190.09	0.60
T *Reticulofenestra umbilicus* ≥14 µm	31.70	220.40	0.38
T *Ericsonia formosa*	32.90	231.68	0.16
T *Discoaster saipanensis*	34.00	244.97	0.06
T *Discoaster barbadiensis*	34.20	246.21	0.15
T *Chiasmolithus grandis*	37.10	260.16	0.07
B *Dictyococcites bisectus*	40.00	266.81	0.32
T *Chiasmolithus solitus*	40.40	276.24	0.85
T *Nannotetrina spp.*	42.30	297.33	0.31
Foraminifer events:			
T *Catapsydrax dissimilis ciperoensis*	17.50	61.71	0.11
T *Paragloboratalia kugleri*	21.00	73.76	0.75
B *Paraglobora taliakugleri*	22.90	98.05	0.15
B *Globoquadrina dehiscens*	23.20	81.68	0.21
B *Globoquadrina dehiscens*	23.20	84.62	0.38
B *Paragloboratalia pseudokugleri*	24.60	121.56	0.61
T *Paragloboratalia opima opima*	27.10	143.19	0.38
T Common *Chiloguembelina cubensis*	27.00	168.54	0.05
T *Turborotalia ampliapertura*	29.30	186.95	0.36
B *Paragloboratalia opima opima*	29.60	189.69	0.27
Radiolarian events:			
T *Sylatractus universus*	0.41	2.71	0.38
B *Collosphaera tuberosa*	0.61	4.21	0.38
T *Calocycletta caepa*	6.20	27.25	0.38
T *Stichocorys johnsoni*	6.60	27.25	0.38
Lithopera neotera→*Lithopera bacca*	8.80	35.82	1.13
T *Carpocanpsis cristata*	10.60	35.82	0.38
RN7/6	8.77	36.57	0.75
T *Stichocorys wolffii*	8.80	37.32	0.38
T *Cytocapsella cornuta*	12.10	37.32	0.38
T *Cytocapsella tetrapera*	12.10	38.82	0.38
T *Dorcadospyris alata*	13.60	40.32	0.38
RN6/5	11.95	41.37	0.05
T *Calocycletta costata*	15.00	41.70	0.13
T *Carpocanopsis bramlettei*	14.70	45.70	0.38
RN5/4	15.70	47.21	0.38
RN4/3	17.00	54.24	0.75
RN3/2	17.90	62.08	0.05
RN2/1	20.53	72.47	0.38
RN1/RP22	23.62	92.30	0.30
RP22/21	24.60	111.29	0.38
RP21/20	28.80	189.43	0.40
RP20/19	32.80	238.77	0.10
RP19/18	34.90	250.58	0.32
RP18/17	36.40	252.25	0.52
RP17/16	37.70	261.58	0.38
RP16/15	38.80	271.23	0.38

Note: This table is also available in **ASCII**. [**N1**]

Table T15. Depths, ages, rates, and fluxes of sediments, Hole 1218A. (See table notes. Continued on next two pages.)

Core, section, interval (cm)	Depth (mbsf)	Depth shift to mcd (m)	Depth (mcd)	Age (Ma)	LSR (m/m.y.)	DBD (g/cm^3)	MAR (mg/cm^2/k.y.)
199-1218A-							
1H-1, 76	0.75	0.00	0.75	0.169	4.44	0.33	145
1H-2, 76	2.25	0.00	2.25	0.507	4.44	0.29	130
1H-3, 76	3.75	0.00	3.75	0.845	4.44	0.32	143
1H-4, 82	5.31	0.00	5.31	1.197	4.44	0.31	136
1H-5, 76	6.75	0.00	6.75	1.521	4.44	0.29	127
1H-6, 28	7.77	0.00	7.77	1.751	4.44	0.34	149
2H-1, 76	8.95	0.78	9.73	2.193	4.44	0.33	146
2H-2, 76	10.45	0.78	11.23	2.531	4.44	0.37	163
2H-3, 76	11.95	0.78	12.73	2.869	4.44	0.37	164
2H-4, 76	13.45	0.78	14.23	3.207	4.44	0.40	179
2H-5, 76	14.95	0.78	15.73	3.545	4.44	0.44	193
2H-6, 76	16.45	0.78	17.23	3.883	4.44	0.41	182
2H-7, 31	17.51	0.78	18.29	4.122	4.44	0.41	184
3H-1, 76	18.45	2.34	20.79	4.728	2.69	0.40	106
3H-2, 76	19.95	2.34	22.29	5.286	2.69	0.43	116
3H-3, 76	21.45	2.34	23.79	5.844	2.69	0.34	90
3H-4, 76	22.95	2.34	25.29	6.402	2.69	0.37	99
3H-5, 76	24.45	2.34	26.79	6.961	2.69	0.37	98
3H-6, 76	25.95	2.34	28.29	7.000	2.63	0.36	95
3H-7, 38	27.07	2.34	29.41	7.070	2.63	0.34	89
4H-1, 76	27.95	4.42	32.37	8.650	2.63	0.34	90
4H-2, 76	29.45	4.42	33.87	9.220	2.63	0.37	98
4H-3, 76	30.95	4.42	35.37	9.790	2.63	0.42	110
4H-4, 76	32.45	4.42	36.87	10.360	2.63	0.28	74
4H-5, 76	33.95	4.42	38.37	10.929	2.63	0.28	75
4H-6, 76	35.45	4.42	39.87	11.499	2.63	0.29	76
4H-7, 30	36.49	4.42	40.91	11.894	2.63	0.27	70
5H-1, 76	37.45	4.80	42.25	12.403	2.63	0.28	73
5H-2, 76	38.95	4.80	43.75	12.973	2.63	0.25	66
5H-3, 76	40.45	4.80	45.25	13.543	2.63	0.30	78
5H-4, 76	41.95	4.80	46.75	14.113	2.63	0.28	73
5H-5, 76	43.45	4.80	48.25	14.683	2.63	0.40	104
5H-6, 76	44.95	4.80	49.75	15.253	2.63	0.34	91
5H-7, 20	45.89	4.80	50.69	15.610	2.63	0.29	77
6H-1, 76	46.95	6.84	53.79	16.788	2.63	0.29	76
6H-2, 76	48.45	6.84	55.29	17.357	2.63	0.27	72
6H-3, 76	49.95	6.84	56.79	17.927	2.63	0.26	68
6H-4, 76	51.45	6.84	58.29	18.497	2.63	0.25	66
6H-5, 76	52.95	6.84	59.79	19.056	5.92	0.28	165
6H-6, 76	54.19	6.84	61.03	19.266	5.92	0.29	172
6H-7, 29	54.98	6.84	61.82	19.400	5.92	0.61	362
7H-1, 76	56.45	8.06	64.51	19.854	5.92	0.82	487
7H-2, 76	57.95	8.06	66.01	20.108	5.92	0.90	534
7H-3, 76	59.45	8.06	67.51	20.362	5.92	0.72	427
7H-4, 76	60.95	8.06	69.01	20.615	5.92	0.39	228
7H-5, 76	62.45	8.06	70.51	20.869	5.92	0.62	365
7H-6, 76	63.95	8.06	72.01	21.122	5.92	0.63	371
7H-7, 61	65.30	8.06	73.36	21.350	5.92	0.93	553
8H-1, 142	66.61	7.96	74.57	21.555	5.92	0.38	222
8H-2, 76	67.45	7.96	75.41	21.697	5.92	0.89	526
8H-3, 76	68.95	7.96	76.91	21.893	8.64	0.96	833
8H-4, 82	70.51	7.96	78.47	22.074	8.64	0.67	582
8H-5, 76	71.95	7.96	79.91	22.240	8.64	0.97	840
8H-6, 83	73.52	7.96	81.48	22.422	8.64	0.89	766
9H-3, 76	78.45	10.26	88.71	23.259	8.64	0.93	804
9H-6, 76	82.95	10.26	93.21	23.780	8.64	0.67	576
10H-3, 76	87.95	11.90	99.85	24.548	8.64	0.84	729
10H-4, 76	89.45	11.90	101.35	24.722	8.64	0.81	701
10H-5, 76	90.95	11.90	102.85	24.895	8.64	0.82	704
10H-6, 76	92.45	11.90	104.35	25.069	8.64	0.54	464
10H-7, 33	93.52	11.90	105.42	25.193	8.64	0.53	460
11H-1, 76	94.45	13.40	107.85	25.474	8.64	0.74	643
11H-2, 76	95.95	13.40	109.35	25.568	18.11	0.86	1563
11H-3, 76	97.45	13.40	110.85	25.651	18.11	0.87	1581
11H-4, 76	98.95	13.40	112.35	25.734	18.11	0.83	1503
11H-5, 76	100.45	13.40	113.85	25.817	18.11	0.86	1563

Table T15 (continued).

Core, section, interval (cm)	Depth (mbsf)	Depth shift to mcd (m)	Depth (mcd)	Age (Ma)	LSR (m/m.y.)	DBD (g/cm^3)	MAR ($mg/cm^2/k.y.$)
11H-6, 76	101.95	13.40	115.35	25.900	18.11	0.84	1518
11H-7, 56	103.25	13.40	116.65	25.971	18.11	0.92	1659
12H-1, 76	103.95	14.47	118.42	26.069	18.11	0.80	1440
12H-2, 76	105.45	14.47	119.92	26.152	18.11	0.88	1587
12H-3, 76	106.95	14.47	121.42	26.235	18.11	0.88	1601
12H-4, 106	108.75	14.47	123.22	26.334	18.11	0.67	1221
12H-5, 106	110.25	14.47	124.72	26.417	18.11	0.96	1742
12H-6, 76	111.45	14.47	125.92	26.483	18.11	0.82	1485
12H-7, 31	112.50	14.47	126.97	26.541	18.11	0.99	1798
13H-1, 80	113.49	14.91	128.40	26.620	18.11	0.74	1333
13H-2, 76	114.95	14.91	129.86	26.701	18.11	0.88	1585
13H-3, 76	116.45	14.91	131.36	26.784	18.11	0.79	1424
13H-4, 76	117.95	14.91	132.86	26.866	18.11	0.87	1579
13H-5, 76	119.45	14.91	134.36	26.949	18.11	0.82	1478
13H-6, 76	120.95	14.91	135.86	27.032	18.11	0.89	1608
13H-7, 46	122.15	14.91	137.06	27.098	18.11	0.93	1686
14H-1, 76	122.95	15.42	138.37	27.171	18.11	0.87	1579
14H-2, 76	124.45	15.42	139.87	27.254	18.11	0.96	1740
14H-3, 76	125.95	15.42	141.37	27.336	18.11	0.99	1789
14H-4, 76	127.45	15.42	142.87	27.419	18.11	0.96	1737
14H-5, 76	128.95	15.42	144.37	27.502	18.11	1.02	1842
14H-6, 76	130.45	15.42	145.87	27.585	18.11	1.03	1867
14H-7, 21	131.40	15.42	146.82	27.637	18.11	0.99	1784
15H-1, 76	132.45	16.22	148.67	27.739	18.11	1.05	1896
15H-2, 76	133.95	16.22	150.17	27.822	18.11	1.05	1905
15H-3, 76	135.45	16.22	151.67	27.905	18.11	1.07	1945
15H-4, 76	136.95	16.22	153.17	27.988	18.11	1.00	1811
15H-5, 73	138.42	16.22	154.64	28.069	18.11	1.01	1827
15H-6, 76	139.95	16.22	156.17	28.154	18.11	1.03	1858
15H-7, 38	141.07	16.22	157.29	28.215	18.11	1.04	1876
16H-1, 76	141.95	17.84	159.79	28.353	18.11	1.06	1918
16H-2, 76	143.45	17.84	161.29	28.436	18.11	1.04	1891
16H-3, 76	144.95	17.84	162.79	28.519	18.11	1.05	1898
16H-4, 76	146.45	17.84	164.29	28.602	18.11	1.08	1951
16H-5, 76	147.95	17.84	165.79	28.685	18.11	1.07	1940
16H-6, 84	149.51	17.84	167.35	28.771	18.11	1.11	2001
16H-7, 32	150.51	17.84	168.35	28.826	18.11	1.06	1920
17H-1, 96	151.65	17.90	169.55	28.892	18.11	1.01	1829
17H-2, 80	152.99	17.90	170.89	28.966	18.11	0.95	1728
17H-3, 76	154.45	17.90	172.35	29.047	18.11	0.96	1740
17H-4, 76	155.95	17.90	173.85	29.130	18.11	1.01	1820
17H-5, 76	157.45	17.90	175.35	29.213	18.11	1.04	1887
17H-6, 76	158.96	17.90	176.86	29.296	18.11	1.09	1978
17H-7, 41	160.12	17.90	178.02	29.360	18.11	1.09	1967
18H-1, 76	160.95	20.56	181.51	29.553	18.11	1.04	1887
18H-2, 76	162.45	20.56	183.01	29.635	18.11	1.08	1956
18H-3, 76	163.95	20.56	184.51	29.718	18.11	0.96	1737
18H-4, 76	165.45	20.56	186.01	29.801	18.11	0.96	1733
18H-5, 76	166.87	20.56	187.43	29.880	18.11	1.03	1869
18H-6, 106	168.67	20.56	189.23	29.979	18.11	1.04	1887
19H-1, 76	170.45	20.38	190.83	30.067	18.11	0.98	1768
19H-2, 75	171.95	20.38	192.33	30.150	18.11	1.11	2016
19H-3, 75	173.45	20.38	193.83	30.233	18.11	1.10	1989
19H-4, 81	175.00	20.38	195.38	30.319	18.11	1.05	1903
19H-5, 78	176.45	20.38	196.83	30.399	18.11	1.08	1951
19H-6, 76	177.95	20.38	198.33	30.481	18.11	1.06	1913
19H-7, 68	179.37	20.38	199.75	30.560	18.11	1.09	1965
20H-1, 80	179.98	22.28	202.26	30.698	18.11	0.85	1547
20H-2, 76	181.45	22.28	203.73	30.780	18.11	0.93	1686
20H-3, 76	182.95	22.28	205.23	30.862	18.11	0.87	1574
20H-4, 76	184.45	22.28	206.73	30.945	18.11	0.97	1757
20H-5, 76	185.95	22.28	208.23	31.028	18.11	1.00	1817
20H-6, 76	187.45	22.28	209.73	31.111	18.11	1.02	1847
22X-1, 86	196.76	22.30	219.06	31.626	18.11	1.04	1891
22X-2, 79	198.19	22.30	220.49	31.709	10.32	1.02	1049
22X-3, 69	199.58	22.30	221.88	31.843	10.32	0.88	906
22X-4, 93	201.32	22.30	223.62	32.012	10.32	0.88	907
22X-6, 32	203.21	22.30	225.51	32.195	10.32	0.89	920

Table T15 (continued).

Core, section, interval (cm)	Depth (mbsf)	Depth shift to mcd (m)	Depth (mcd)	Age (Ma)	LSR (m/m.y.)	DBD (g/cm^3)	MAR ($mg/cm^2/k.y.$)
23X-1, 127	206.76	23.24	230.00	32.630	10.32	0.85	873
23X-4, 49	210.48	23.24	233.72	32.990	10.32	0.96	987
23X-6, 25	213.25	23.24	236.49	33.259	10.32	1.06	1098
24X-1, 81	215.90	25.08	240.98	33.693	10.32	0.73	753
24X-3, 36	218.04	25.08	243.12	33.901	10.32	0.46	471
24X-6, 74	222.93	25.08	248.01	34.572	4.84	0.49	239
25X-2, 134	227.53	26.27	253.80	35.767	4.84	0.70	340
25X-4, 61	229.80	26.27	256.07	36.236	4.84	0.54	262
25X-6, 28	232.47	26.27	258.74	36.787	4.84	0.87	423
26X-1, 86	235.15	26.07	261.22	37.299	4.84	0.49	238
26X-3, 75	238.04	26.07	264.11	37.896	4.84	1.04	505
26X-6, 70	242.49	26.07	268.56	38.814	4.84	0.95	458
27X-2, 14	245.53	26.13	271.66	39.454	4.84	0.60	290
27X-3, 135	248.24	26.13	274.37	40.014	4.84	0.52	252
28X-2, 63	255.62	23.93	279.55	40.698	11.10	0.80	884
28X-4, 67	258.66	23.93	282.59	40.972	11.10	0.96	1066
28X-6, 43	261.42	23.93	285.35	41.221	11.10	0.97	1077
29X-2, 76	265.35	24.23	289.58	41.602	11.10	0.97	1079
29X-4, 49	268.08	24.23	292.31	41.848	11.10	1.53	1694
30X-1, 76	271.45	24.23	295.68	42.151	11.10	1.42	1574
30X-3, 6	273.75	24.23	297.98	42.359	11.10	1.35	1497

Notes: LSR = linear sedimentation rate, DBD = dry bulk density, MAR = mass accumulation rate. This table is also available in **ASCII.**

Table T16. Interstitial water data, Hole 1218A.

Core, section, interval (cm)	Depth (mbsf)	pH	Alkalinity (mM)	Salinity	Cl (mM)	Na (mM)	K (mM)	Ca (mM)	Mg (mM)	SO_4 (mM)	NH_4 (µM)	H_4SiO_4 (µM)	Sr (µM)	Li (µM)	Mn (µM)	Ba (µM)	B (µM)
199-1218A-																	
1H-4, 145–150	5.95	7.27	2.80	35.0	555	476	12.4	10.7	53.8	30.1	10.5	548	88	27	31.0	0.32	492
2H-3, 145–150	12.65	7.20	3.18	35.0	558	482	12.7	11.4	53.7	31.8	11.5	601	90	26	38.0	0.19	531
3H-3, 145–150	22.15	7.20	3.30	36.0	561	487	12.4	10.8	52.7	31.1	11.2	643	88	26	21.0	0.21	525
4H-3, 145–150	31.65	7.27	3.63	35.0	561	479	12.1	11.7	53.2	28.4	10.8	676	93	25	6.8	0.21	525
5H-3, 145–150	41.15	7.27	3.54	35.0	562	482	12.0	11.5	52.8	28.4	14.5	646	95	26	1.3	0.22	499
6H-3, 145–150	50.65	7.26	3.62	35.0	563	483	11.5	11.6	53.2	28.9	11.5	623	98	25	0.9	0.26	476
10H-3, 145–150	88.65	7.15	3.48	36.0	561	477	11.5	12.4	52.7	27.4	4.4	746	108	24	3.2	0.22	467
13H-3, 145–150	117.15	7.10	3.89	35.0	562	480	11.2	11.9	52.8	27.7	10.4	811	108	23	7.7	0.48	485
15H-3, 145–150	136.15	7.13	3.75	35.0	561	478	11.4	13.8	50.2	26.3	10.0	876	111	24	5.3	0.31	480
18H-3, 145–150	164.65	7.14	3.85	35.0	562	482	11.1	14.1	49.9	27.5	11.0	931	117	24	3.3	0.27	474
22X-3, 145–150	200.35	7.17	3.80	35.0	561	478	11.0	14.7	49.5	26.5	11.9	1108	119	24	3.3	0.35	475
25X-3, 145–150	229.15	7.16	3.65	35.0	558	481	10.7	15.0	49.3	29.3	12.8	1116	119	24	1.7	0.34	502
28X-3, 145–150	257.95	7.23	3.41	35.0	561	477	10.5	16.0	50.2	28.2	9.7	1098	116	25	2.0	1.16	466
30X-2, 145–150	273.65	7.32	2.26	34.0	548	468	9.8	13.9	49.2	27.1	12.0	626	92	33	1.7	0.41	528

Note: This table is also available in **ASCII.**

Table T17. Bulk sediment data, Hole 1218A. (See table notes. Continued on next two pages.)

Core, section, interval (cm)	Depth (mbsf)	Si (wt%)	Al (wt%)	Ti (wt%)	Fe (wt%)	Mn (wt%)	Ca (wt%)	Mg (wt%)	P (wt%)	Sr (ppm)	Ba (ppm)
199-1218A-											
1H-1, 74–75	0.74	24.29	6.75	0.31	3.97	0.04	0.38	1.61	0.05	235.25	5,524.78
1H-2, 73–74	2.23	23.97	6.91	0.33	3.51	0.11	0.50	1.97	0.09	266.99	6,360.32
1H-3, 74–75	3.74	23.34	6.05	0.28	3.92	0.29	0.32	1.70	0.13	201.18	5,009.31
1H-4, 80–81	5.30	20.74	5.61	0.28	4.24	0.14	0.36	1.45	0.08	216.72	4,864.79
1H-5, 74–75	6.74	21.58	6.17	0.27	4.39	0.11	0.42	1.84	0.14	196.80	4,562.24
2H-1, 74–75	8.94	22.70	6.62	0.29	3.95	0.06	0.37	1.95	0.19	250.18	6,732.96
2H-2, 74–75	10.44	24.24	7.06	0.33	4.07	0.06	0.63	2.14	0.13	252.63	6,363.76
2H-3, 74–75	11.94	21.94	5.55	0.30	4.16	0.42	0.72	1.65	0.22	219.63	6,263.18
2H-4, 74–75	13.44	21.49	6.10	0.28	4.56	0.54	0.71	1.90	0.22	256.55	5,987.46
2H-5, 74–75	14.94	22.41	6.35	0.30	4.28	1.03	1.02	1.93	0.19	270.72	6,265.24
2H-6, 74–75	16.44	22.60	6.57	0.31	3.85	0.88	0.77	1.96	0.22	251.65	6,761.53
3H-1, 74–75	18.44	23.63	6.47	0.31	4.04	0.82	1.01	2.23	0.25	294.40	7,255.54
3H-2, 74–75	19.94	20.37	5.07	0.28	4.11	0.88	0.74	1.62	0.20	311.24	8,909.35
3H-3, 74–75	21.44	23.58	6.27	0.29	3.77	0.63	1.37	2.18	0.31	340.98	9,039.87
3H-4, 74–75	22.94	23.24	5.82	0.29	3.58	0.93	1.10	1.94	0.33	289.78	7,622.67
3H-5, 74–75	24.44	22.76	6.24	0.26	3.44	1.23	0.99	2.17	0.19	356.30	9,321.02
3H-6, 74–75	25.94	25.94	5.60	0.25	3.35	0.66	0.85	1.91	0.18	293.69	8,199.70
3H-7, 36–37	27.06	25.76	5.01	0.27	4.51	0.64	0.81	1.79	0.17	420.87	16,109.29
4H-1, 74–75	27.94	26.75	4.21	0.22	5.11	0.65	0.68	1.51	0.16	322.05	11,099.33
4H-2, 74–75	29.44	23.42	5.58	0.27	4.26	1.18	1.12	2.08	0.32	292.89	7,267.68
4H-3, 74–75	30.94	23.91	5.72	0.28	4.15	1.27	1.12	1.98	0.36	284.45	5,612.17
4H-4, 74–75	32.44	23.53	5.36	0.22	3.34	1.09	1.35	1.99	0.32	293.02	7,258.26
4H-5, 74–75	33.94	23.94	5.11	0.23	4.52	1.05	1.36	1.92	0.42	301.13	7,878.58
4H-6, 74–75	35.44	20.49	4.87	0.15	4.94	0.80	3.89	1.60	0.33	328.09	8,300.08
4H-7, 28–29	36.48	24.37	4.35	0.22	6.06	1.03	2.14	2.10	0.37	346.22	7,173.33
5H-1, 73–74	37.43	22.06	4.71	0.20	6.29	1.05	1.58	2.02	0.36	284.15	6,011.44
5H-2, 73–74	38.93	21.07	5.13	0.24	6.28	1.33	4.16	2.15	0.32	461.21	5,744.34
5H-3, 73–74	40.43	22.19	5.35	0.24	3.65	1.19	1.37	2.42	0.34	323.76	6,344.83
5H-4, 73–74	41.93	23.33	4.50	0.21	3.97	1.13	1.24	2.09	0.32	330.86	6,865.63
5H-5, 73–74	43.43	16.32	3.05	0.13	4.68	0.62	14.51	1.45	0.17	806.36	4,614.45
5H-6, 73–74	44.93	17.46	3.15	0.15	4.37	0.64	14.69	1.53	0.16	957.06	4,929.26
5H-7, 17–18	45.87	19.23	3.16	0.14	4.24	0.76	9.80	1.72	0.23	698.23	5,878.70
6H-1, 73–74	46.93	25.86	4.47	0.21	5.27	0.73	1.03	1.83	0.20	298.70	7,673.87
6H-2, 73–74	48.43	25.92	4.32	0.17	5.68	0.69	1.02	1.65	0.21	286.27	7,698.04
6H-3, 73–74	49.93	24.59	4.52	0.18	4.98	0.84	1.06	1.97	0.25	331.42	7,958.52
6H-4, 73–74	51.43	22.60	3.61	0.15	4.29	0.99	0.75	2.14	0.19	450.63	13,264.21
6H-5, 73–74	52.93	22.91	3.35	0.15	1.38	0.86	6.10	1.97	0.22	617.80	9,642.63
6H-6, 48–49	54.18	18.35	2.87	0.12	0.66	0.73	10.42	1.65	0.22	732.65	8,391.59
6H-7, 26–27	54.96	6.96	0.95	0.05	0.41	0.27	29.66	0.64	0.08	1,633.31	3,949.27
7H-1, 74–75	56.44	3.63	0.45	0.02	0.87	0.13	34.23	0.37	0.04	1,628.71	1,341.17
7H-2, 74–75	57.94	2.27	0.30	0.02	3.01	0.08	36.66*	0.28	0.05	1,541.90	899.36
7H-3, 74–75	59.44	5.88	0.75	0.04	1.29	0.17	32.27	0.46	0.04	1,474.37	2,377.49
7H-4, 74–75	60.94	14.54	3.00	0.15	1.26	0.47	19.64	1.15	0.17	1,080.58	4,326.52
7H-5, 74–75	62.44	6.58	0.99	0.05	0.35	0.23	31.66	0.61	0.05	1,442.61	3,560.55
7H-6, 74–75	63.94	6.51	0.79	0.03	3.01	0.24	30.49	0.58	0.08	1,689.31	2,916.80
7H-7, 59–60	65.29	2.00	0.27	0.02	0.52	0.07	35.58	0.25	0.01	1,588.56	999.20
8H-1, 140–141	66.60	13.19	1.72	0.08	0.32	0.59	21.54	1.19	0.15	1,222.80	7,145.01
8H-2, 74–75	67.44	2.49	0.32	0.02	1.12	0.10	35.48	0.33	0.05	1,677.40	1,270.43
8H-3, 74–75	68.94	1.88	0.17	0.02	0.32	0.06	35.80	0.25	0.03	1,351.21	713.95
8H-4, 79–80	70.49	5.89	0.63	0.03	0.58	0.20	31.26	0.50	0.06	1,463.34	3,104.56
8H-5, 74–75	71.94	1.66	0.23	0.01	0.48	0.06	36.72*	0.26	0.04	1,650.42	424.03
8H-6, 81–82	73.51	2.76	0.47	0.00	1.62	0.15	32.30	0.33	0.04	1,640.42	1,617.08
9H-3, 74–75	78.44	3.09	0.29	0.02	0.61	0.10	40.10*	0.32	0.04	1,791.53	1,151.43
9H-6, 74–75	82.94	7.27	0.94	0.05	0.77	0.31	30.08	0.66	0.11	1,685.98	3,261.94
10H-3, 74–75	87.94	3.25	0.41	0.03	2.11	0.10	33.97	0.34	0.03	1,576.47	1,362.94
10H-5, 74–75	90.94	3.80	0.52	0.03	0.96	0.13	34.65	0.38	0.04	1,801.80	2,092.43
10H-7, 31–32	93.51	12.01	1.37	0.06	0.77	0.37	24.75	0.88	0.10	1,414.65	5,769.52
11H-1, 74–75	94.44	5.52	0.57	0.03	0.76	0.18	32.30	0.45	0.04	1,761.23	2,209.06
11H-2, 74–75	95.94	5.18	0.53	0.03	1.01	0.17	35.51	0.40	0.05	1,746.41	1,998.81
11H-3, 74–75	97.44	4.00	0.49	0.03	0.76	0.17	34.31	0.37	0.05	1,757.68	1,963.26
11H-4, 74–75	98.94	4.74	0.48	0.03	0.80	0.20	32.75	0.47	0.06	1,691.86	2,783.36
11H-5, 74–75	100.44	4.07	0.41	0.03	0.57	0.17	32.94	0.39	0.07	1,582.75	1,993.93
11H-6, 74–75	101.94	4.67	0.53	0.04	0.77	0.17	32.18	0.40	0.08	1,864.94	2,594.17
11H-7, 53–54	103.23	3.22	0.33	0.02	0.66	0.11	34.82	0.30	0.04	1,682.55	1,527.90
12H-1, 74–75	103.94	3.83	0.50	0.03	0.50	0.17	34.36	0.40	0.03	1,739.36	2,320.30
12H-2, 74–75	105.44	3.15	0.45	0.00	0.98	0.14	39.86*	0.40	0.03	2,127.42	1,581.36
12H-3, 73–74	106.93	2.90	0.43	0.00	0.68	0.11	29.36	0.32	0.03	1,773.23	1,616.16

Table T17 (continued).

Core, section, interval (cm)	Depth (mbsf)	Si (wt%)	Al (wt%)	Ti (wt%)	Fe (wt%)	Mn (wt%)	Ca (wt%)	Mg (wt%)	P (wt%)	Sr (ppm)	Ba (ppm)
12H-4, 74–75	108.44	5.68	0.66	0.03	0.66	0.15	31.39	0.47	0.06	1,675.17	2,800.40
12H-5, 74–75	109.94	4.11	0.40	0.03	1.19	0.15	28.30	0.37	0.05	1,514.25	1,984.17
12H-6, 74–75	111.44	4.77	0.41	0.03	0.76	0.12	32.45	0.37	0.06	1,486.35	2,263.29
13H-1, 78–79	113.48	6.26	0.80	0.04	1.00	0.20	31.07	0.55	0.07	1,694.67	2,196.47
13H-2, 74–75	114.94	4.66	0.51	0.03	0.70	0.13	34.08	0.39	0.05	1,777.98	1,658.82
13H-3, 74–75	116.44	5.57	0.65	0.03	0.82	0.18	32.25	0.48	0.05	1,727.89	2,288.32
13H-4, 74–75	117.94	4.48	0.47	0.03	0.65	0.13	33.34	0.37	0.06	1,786.42	2,114.90
13H-5, 74–75	119.44	5.94	0.59	0.03	0.58	0.15	32.99	0.42	0.05	1,733.34	2,527.19
13H-6, 74–75	120.94	4.90	0.57	0.03	0.62	0.10	33.91	0.35	0.02	1,741.88	2,011.68
13H-7, 44–45	122.14	3.61	0.44	0.02	0.37	0.09	35.33	0.32	0.04	1,917.72	1,545.76
14H-1, 74–75	122.94	3.93	0.49	0.04	0.35	0.09	38.58*	0.34	0.05	1,721.23	1,810.03
14H-2, 74–75	124.44	3.18	0.42	0.00	0.56	0.11	33.09	0.28	0.04	1,742.91	1,484.05
14H-3, 74–75	125.94	2.72	0.30	0.02	0.36	0.10	35.85	0.25	0.03	1,683.26	1,235.02
14H-4, 74–75	127.44	3.10	0.45	0.02	0.33	0.10	36.80*	0.31	0.02	1,898.77	1,629.81
14H-5, 74–75	128.94	1.87	0.27	0.02	0.26	0.09	36.27*	0.23	0.04	1,768.09	957.99
14H-6, 74–75	130.44	1.80	0.31	0.02	0.28	0.09	36.32*	0.23	0.03	1,893.81	1,032.91
15H-1, 74–75	132.44	2.39	0.33	0.00	0.18	0.11	35.13	0.26	0.05	1,604.36	1,098.72
15H-2, 74–75	133.94	1.74	0.21	0.02	0.52	0.10	39.92*	0.23	0.04	1,482.00	1,087.84
15H-3, 74–75	135.44	1.73	0.33	0.00	0.37	0.11	37.21*	0.24	0.03	1,624.54	937.30
15H-4, 74–75	136.94	2.82	0.50	0.00	0.40	0.11	36.39*	0.31	0.06	1,719.94	1,477.38
15H-5, 75–76	138.45	2.32	0.42	0.00	0.35	0.10	34.56	0.27	0.03	1,790.37	1,630.79
15H-6, 73–74	139.93	2.45	0.33	0.02	0.27	0.09	36.28*	0.26	0.03	1,706.72	1,642.47
15H-7, 35–36	141.05	2.11	0.40	0.00	0.32	0.10	35.05	0.26	0.04	1,760.18	999.29
16H-1, 74–75	141.94	1.40	0.23	0.01	0.46	0.08	36.91*	0.22	0.02	1,878.00	914.31
16H-2, 74–75	143.44	1.85	0.37	0.00	0.27	0.10	36.71*	0.26	0.03	1,728.50	1,205.68
16H-3, 74–75	144.94	2.53	0.51	0.00	0.29	0.08	34.85	0.28	0.05	1,789.84	1,655.19
16H-4, 74–75	146.44	1.90	0.40	0.00	0.23	0.10	36.23*	0.25	0.03	1,674.81	1,136.20
16H-5, 74–75	147.94	1.98	0.41	0.00	0.46	0.09	35.19	0.25	0.04	1,786.54	1,358.95
16H-6, 81–82	149.51	1.23	0.23	0.02	0.37	0.11	36.83*	0.20	0.04	1,460.22	713.18
16H-7, 30–31	150.50	2.50	0.41	0.04	0.55	0.09	36.68*	0.25	0.07	1,800.24	1,660.99
17H-1, 97–98	151.67	1.98	0.35	0.03	0.56	0.09	31.95	0.24	0.04	1,731.29	1,465.52
17H-2, 81–82	153.01	3.51	0.47	0.04	0.40	0.08	35.57	0.29	0.04	1,733.17	1,532.69
17H-3, 77–78	154.47	3.09	0.43	0.04	0.28	0.07	31.40	0.30	0.04	1,669.78	1,489.18
17H-4, 77–78	155.97	2.76	0.32	0.02	0.32	0.08	36.20*	0.25	0.04	1,652.55	1,309.74
17H-5, 78–79	157.48	2.87	0.40	0.00	0.27	0.08	35.28	0.25	0.04	1,719.87	1,362.11
17H-6, 78–78	158.99	1.49	0.28	0.03	0.36	0.08	37.13*	0.22	0.02	1,715.67	1,105.37
17H-7, 43–44	160.15	2.06	0.33	0.00	0.36	0.09	34.68	0.23	0.05	1,624.25	1,261.63
18H-1, 73–74	160.93	2.22	0.32	0.00	0.60	0.09	34.29	0.26	0.04	1,600.80	1,168.32
18H-2, 74–75	162.44	1.88	0.31	0.03	0.52	0.09	43.24*	0.23	0.02	1,564.73	1,243.39
18H-3, 74–75	163.94	4.09	0.50	0.04	0.51	0.07	34.95	0.30	0.03	1,607.97	1,901.19
18H-4, 73–74	165.43	3.52	0.49	0.00	0.51	0.08	33.53	0.32	0.05	1,662.35	1,753.84
18H-5, 74–75	166.86	2.71	0.38	0.04	0.30	0.08	36.09*	0.28	0.05	1,582.92	1,498.72
18H-6, 104–105	168.66	2.38	0.26	0.02	0.27	0.08	36.27*	0.28	0.02	1,529.80	1,082.72
19H-1, 73–74	170.43	2.16	0.28	0.02	0.31	0.08	36.66*	0.22	0.01	1,585.03	1,245.48
19H-2, 73–74	171.93	1.67	0.23	0.02	0.58	0.09	38.01*	0.22	0.02	1,555.12	907.31
19H-3, 73–74	173.43	1.62	0.23	0.02	0.48	0.08	37.41*	0.22	0.02	1,584.35	896.74
19H-4, 78–79	174.98	2.13	0.38	0.03	0.32	0.07	39.42*	0.35	0.02	1,750.27	963.96
19H-5, 73–74	176.43	2.18	0.35	0.03	0.41	0.08	34.75	0.27	0.04	,680.20	1,413.33
19H-6, 74–75	177.94	1.92	0.31	BDL	1.12	0.09	37.02*	0.27	0.04	1,712.04	1,208.30
19H-7, 66–67	179.36	1.74	0.30	0.03	0.80	0.08	41.58*	0.26	0.02	1,697.83	1,156.92
20H-1, 76–77	179.96	4.83	0.77	0.02	1.15	0.13	33.16	0.48	0.07	1,805.84	2,214.95
20H-2, 74–75	181.44	4.01	0.47	0.04	0.74	0.14	37.89*	0.38	0.06	1,699.72	1,841.65
20H-3, 74–75	182.94	6.41	0.73	0.04	0.62	0.17	34.33	0.49	0.07	1,793.71	3,346.96
20H-4, 74–75	184.44	4.38	0.45	0.04	0.58	0.16	29.99	0.35	0.04	1,573.50	1,603.11
20H-5, 74–75	185.94	4.14	0.39	0.04	0.65	0.12	41.38*	0.31	0.04	1,593.26	1,624.49
20H-6, 74–75	187.44	4.51	0.33	0.02	0.58	0.12	34.67	0.31	0.03	1,615.80	1,444.99
22X-1, 83–85	196.73	4.91	0.38	0.02	1.00	0.13	33.95	0.32	0.04	1,592.78	1,426.62
22X-2, 78–79	198.18	4.85	0.40	0.02	0.82	0.16	34.00	0.30	0.03	1,515.55	1,429.93
22X-3, 60–61	199.50	10.11	0.61	0.04	0.86	0.20	30.96	0.45	0.06	1,381.43	2,626.75
22X-4, 90–91	201.30	10.24	0.55	0.04	0.78	0.15	27.02	0.39	0.02	1,338.05	1,998.96
22X-6, 28–29	203.18	8.85	0.49	0.03	0.82	0.16	29.98	0.42	0.04	1,408.12	1,976.87
23X-1, 41–42	205.91	9.50	0.38	0.03	0.85	0.14	28.89	0.38	0.03	1,380.20	1,658.40
23X-4, 50–51	210.50	7.18	0.41	0.02	2.08	0.18	31.94	0.38	0.03	1,389.92	1,146.75
23X-6, 23–24	213.23	3.84	0.50	0.04	4.75	0.21	38.23*	0.41	0.04	1,684.68	1,504.62
24X-1, 79–80	215.89	11.03	1.15	0.05	5.74	0.46	24.26	0.79	0.07	1,263.82	3,771.36
24X-3, 33–34	218.03	26.79	2.11	0.11	5.98	0.93	0.59	1.62	0.25	288.72	8,719.71
24X-6, 71–72	222.91	23.89	1.88	0.09	4.49	1.24	5.25	1.83	0.27	509.95	8,962.19
25X-2, 133–135	227.53	26.55	1.62	0.07	2.70	1.21	7.55	1.83	0.22	549.52	9,199.35
25X-4, 60–62	229.80	27.62	1.37	0.07	5.99	0.88	7.45	1.52	0.26	527.88	8,858.53

Table T17 (continued).

Core, section, interval (cm)	Depth (mbsf)	Si (wt%)	Al (wt%)	Ti (wt%)	Fe (wt%)	Mn (wt%)	Ca (wt%)	Mg (wt%)	P (wt%)	Sr (ppm)	Ba (ppm)
25X-6, 28–30	232.48	17.95	1.03	0.05	1.84	0.51	19.70	1.04	0.11	862.88	6,005.51
26X-1, 84–87	235.14	27.09	2.04	0.09	1.28	1.14	4.29	2.05	0.35	437.11	9,645.18
26X-2, 74–77	236.54	11.36	0.59	0.03	2.80	0.46	26.25	0.70	0.08	1,104.05	4,158.38
26X-3, 74–77	238.04	9.83	0.44	0.03	1.41	0.28	29.91	0.53	0.05	1,171.74	3,064.46
26X-4, 73–75	239.53	15.15	0.76	0.04	1.99	0.61	23.02	1.01	0.12	916.03	5,309.75
26X-5, 74–76	241.04	10.65	0.43	0.02	2.95	0.33	23.63	0.57	0.05	831.48	2,475.96
26X-6, 69–72	242.49	15.27	0.60	0.04	2.53	0.41	23.33	0.85	0.07	911.38	4,012.57
26X-7, 45–47	243.75	27.61	0.82	0.05	3.08	0.67	11.25	1.15	0.18	550.80	7,051.64
27X-1, 74–76	244.64	31.50	0.58	0.03	2.17	0.33	6.04	0.98	0.08	359.27	6,352.51
27X-2, 74–76	246.14	29.78	0.61	0.03	2.30	0.70	7.41	1.10	0.13	418.20	6,201.11
27X-3, 74–76	247.64	31.56	0.60	0.04	2.12	0.45	0.07	0.95	0.09	158.63	5,333.62
27X-4, 74–76	249.14	34.53	0.60	0.03	0.68	0.42	0.03	0.96	0.08	211.61	7,747.01
27X-5, 50–52	249.90	37.15	0.48	0.03	0.47	0.41	0.05	0.91	0.07	178.77	5,973.41
28X-1, 74–75	254.24	15.92	0.29	0.02	0.82	0.03	24.66	0.48	0.03	860.88	3,183.00
28X-2, 74–75	255.74	16.84	0.18	0.02	0.63	0.02	23.53	0.38	0.02	751.39	2,502.03
28X-3, 74–75	257.24	11.69	0.29	0.02	0.60	0.03	27.25	0.50	0.05	1,032.49	3,063.17
28X-4, 74–75	258.74	7.85	0.27	0.02	0.59	0.03	31.42	0.43	0.05	1,256.08	3,440.83
28X-5, 74–75	260.24	14.22	0.53	0.03	0.67	0.04	25.41	0.44	0.06	899.79	2,706.72
28X-6, 74–75	261.74	8.62	0.24	0.02	0.52	0.04	29.16	0.45	0.05	1,102.56	2,760.91
28X-7, 74–75	262.74	9.78	0.28	0.02	1.41	0.04	29.79	0.50	0.06	1,104.58	2,818.56
29X-1, 74–76	263.84	8.50	0.21	0.02	0.55	0.04	30.59	0.46	0.05	1,137.21	2,138.17
29X-2, 73–75	265.33	12.73	0.43	0.03	1.05	0.03	26.63	1.00	0.10	1,049.87	4,336.48
29X-3, 74–76	266.84	6.93	0.23	0.02	1.34	0.45	31.68	0.72	0.05	1,104.86	2,897.07
29X-4, 50–52	268.10	4.64	0.38	0.02	2.14	0.13	33.71	1.84	0.09	1,173.72	3,699.28
30X-1, 74–74	271.44	5.63	0.48	0.03	1.32	0.17	31.21	2.31	0.10	1,155.29	3,423.78
30X-3, 5–7	273.75	5.35	0.81	0.06	0.00	0.29	27.31	4.59	0.20	942.47	7,239.54
30X-CC, 20–26	274.23	3.86	0.61	0.05	0.00	0.16	30.91	3.48	0.24	901.42	783.23

Notes: * = Ca values higher than 35.9 wt% are out of the range of the standards (see **“Geochemistry,”** p. 20, in the “Explanatory Notes” chapter). This table is also available in **ASCII**. [**N1**]

Table T18. $CaCO_3$ and C_{org} data, Site 1218. (**See table notes.** Continued on next page.)

Core, section, interval (cm)	Depth (mbsf)	$CaCO_3$ (wt%)	Organic C (wt%)	$CaCO_3$ (wt%)*
199-1218A-				
1H-1, 74–75	0.74	0.11		–0.98
1H-2, 73–74	2.23			–0.69
1H-3, 74–75	3.74	0.09	0.13	–1.13
1H-4, 80–81	5.30			–1.05
1H-5, 74–75	6.74	0.10		–0.88
2H-1, 74–75	8.94			–1.00
2H-2, 74–75	10.44	0.08		–0.33
2H-3, 74–75	11.94			–0.10
2H-4, 74–75	13.44	0.13	0.11	–0.13
2H-5, 74–75	14.94			0.66
2H-6, 74–75	16.44	0.14		0.03
3H-1, 74–75	18.44			0.63
3H-2, 74–75	19.94	0.16		–0.03
3H-3, 74–75	21.44			1.55
3H-4, 74–75	22.94	0.18	0.10	0.87
3H-5, 74–75	24.44			0.59
3H-6, 74–75	25.94	0.15		0.22
3H-7, 36–37	27.06			0.13
4H-1, 74–75	27.94			–0.22
4H-2, 74–75	29.44	0.22		0.92
4H-3, 74–75	30.94			0.93
4H-4, 74–75	32.44	0.23	0.07	1.47
4H-5, 74–75	33.94			1.49
4H-6, 74–75	35.44	4.94		7.93
4H-7, 28–29	36.48			3.47
5H-1, 73–74	37.43			2.05
5H-2, 73–74	38.93	5.46		8.61
5H-3, 73–74	40.43			1.53
5H-4, 73–74	41.93	0.23	0.05	1.20
5H-5, 73–74	43.43			34.97
5H-6, 73–74	44.93	29.20		35.43
5H-7, 17–18	45.87			22.97
6H-1, 73–74	46.93			0.67
6H-2, 73–74	48.43	0.30		0.63
6H-3, 73–74	49.93			0.73
6H-4, 73–74	51.43	0.33	0.03	–0.08
6H-5, 73–74	52.93			13.57
6H-6, 48–49	54.18	19.18		24.53
6H-7, 26–27	54.96			73.56
7H-1, 74–75	56.44			85.20
7H-2, 74–75	57.94	88.90		91.38†
7H-3, 74–75	59.44			80.21
7H-4, 74–75	60.94	40.39	0.19	48.04
7H-5, 74–75	62.44			78.64
7H-6, 74–75	63.94	71.31		75.65
7H-7, 59–60	65.29			88.62
8H-1, 140–141	66.60			52.87
8H-2, 74–75	67.44	87.84		88.39
8H-3, 74–75	68.94			89.20
8H-4, 79–80	70.49	73.86	0.18	77.62
8H-5, 74–75	71.94			91.53†
8H-6, 81–82	73.51	86.07		80.28
9H-3, 74–75	78.44	88.35	0.10	100.12†
9H-6, 74–75	82.94	70.06		74.62
10H-3, 74–75	87.94	85.45		84.54
10H-5, 74–75	90.94	83.70	0.21	86.25
10H-7, 31–32	93.51	54.40		61.06
11H-1, 74–75	94.44			80.28
11H-2, 74–75	95.94	79.55		88.45
11H-3, 74–75	97.44			85.40
11H-4, 74–75	98.94	78.61	0.09	81.42
11H-5, 74–75	100.44			81.92
11H-6, 74–75	101.94	80.96		79.97
11H-7, 53–54	103.23			86.69
12H-1, 74–75	103.94			85.53
12H-2, 74–75	105.44	86.92		99.52†
12H-3, 73–74	106.93			72.81
12H-4, 74–75	108.44	76.79	0.14	77.94
12H-5, 74–75	109.94			70.12
12H-6, 74–75	111.44	80.46		80.67
13H-1, 78–79	113.48			77.14
13H-2, 74–75	114.94	80.82		84.80
13H-3, 74–75	116.44			80.15
13H-4, 74–75	117.94	82.19	1.10	82.94
13H-5, 74–75	119.44			82.05
13H-6, 74–75	120.94	82.02		84.37
13H-7, 44–45	122.14			88.00
14H-1, 74–75	122.94			96.25†
14H-2, 74–75	124.44	86.53		82.29
14H-3, 74–75	125.94			89.33
14H-4, 74–75	127.44	86.34	0.25	91.73†
14H-5, 74–75	128.94			90.38†
14H-6, 74–75	130.44	91.11		90.51†
15H-1, 74–75	132.44			87.50
15H-2, 74–75	133.94	84.70		99.67†
15H-3, 74–75	135.44			92.79†
15H-4, 74–75	136.94	87.06	0.17	90.69†
15H-5, 75–76	138.45			86.03
15H-6, 73–74	139.93	89.52		90.42†
15H-7, 35–36	141.05			87.29
16H-1, 74–75	141.94			92.01†
16H-2, 74–75	143.44	90.37		91.52†
16H-3, 74–75	144.94			86.77
16H-4, 74–75	146.44	90.23	0.28	90.30†
16H-5, 74–75	147.94			87.64
16H-6, 81–82	149.51	93.18		91.81†
16H-7, 30–31	150.50			91.43†
17H-1, 97–98	151.67			79.40
17H-2, 81–82	153.01	86.00		88.60
17H-3, 77–78	154.47			77.99
17H-4, 77–78	155.97	88.87	0.10	90.20†
17H-5, 78–79	157.48			87.88
17H-6, 78–78	158.99	92.47		92.58†
17H-7, 43–44	160.15			86.34
18H-1, 73–74	160.93			85.35
18H-2, 74–75	162.44	90.94		108.11†
18H-3, 74–75	163.94			87.03
18H-4, 73–74	165.43	86.16	0.13	83.41
18H-5, 74–75	166.86			89.93
18H-6, 104–105	168.66	89.19		90.38†
19H-1, 73–74	170.43			91.37†
19H-2, 73–74	171.93	92.65		94.81†
19H-3, 73–74	173.43			93.30†
19H-4, 78–79	174.98	90.32	0.16	98.40†
19H-5, 73–74	176.43			86.53
19H-6, 74–75	177.94	90.78		92.29†
19H-7, 66–67	179.36			103.91†
20H-1, 76–77	179.96			82.46
20H-2, 74–75	181.44	84.53		94.51†
20H-3, 74–75	182.94			85.44
20H-4, 74–75	184.44	83.38	0.17	74.40
20H-5, 74–75	185.94			103.39†
20H-6, 74–75	187.44	83.95		86.32
22X-1, 83–85	196.73			84.48
22X-2, 78–79	198.18	83.06		84.62
22X-3, 60–61	199.50			76.88
22X-4, 90–91	201.30	69.47	0.05	66.86
22X-6, 28–29	203.18	71.18		74.38
23X-1, 41–42	205.91	70.82		71.60
23X-4, 50–51	210.50	77.35	–0.02	79.37
23X-6, 23–24	213.23	84.50		95.37†
24X-1, 79–80	215.89	55.04		59.83
24X-3, 33–34	218.03	0.90	–0.05	–0.41
24X-6, 71–72	222.91	9.82		11.45
25X-2, 133–135	227.53	13.65		17.31
25X-4, 60–62	229.80	14.48	0.02	17.05
25X-6, 20–30	232.48	43.00		48.24

Table T18 (continued).

Core, section, interval (cm)	Depth (mbsf)	$CaCO_3$ (wt%)	Organic C (wt%)	$CaCO_3$ (wt%)*
26X-1, 84–87	235.14			8.99
26X-2, 74–77	236.54	61.81		
26X-3, 74–77	238.04			74.22
26X-4, 73–75	239.53	49.59	0.26	
26X-5, 74–76	241.04			
26X-6, 69–72	242.49	51.44		57.46
26X-7, 45–47	243.75			
27X-1, 74–76	244.64	12.26		
27X-2, 74–76	246.14			16.95
27X-3, 74–76	247.64	0.63	–0.04	–1.74
27X-4, 74–76	249.14			
27X-5, 50–52	249.90	0.69		
28X-1, 74–75	254.24			
28X-2, 74–75	255.74	54.32		57.96
28X-3, 74–75	257.24			
28X-4, 74–75	258.74			78.06
28X-5, 74–75	260.24			
28X-6, 74–75	261.74	70.95		72.29
28X-7, 74–75	262.74			
29X-1, 74–76	263.84	74.98		
29X-2, 73–75	265.33			65.86
29X-3, 74–76	266.84	79.28	0.12	
29X-4, 50–52	268.10			83.89
30X-1, 74–74	271.44	76.67		77.53
30X-3, 5–7	273.75	76.28	0.25	67.61
30X-CC, 20–26	274.23	83.62		

Notes: * = calculated from Ca (wt%). Calculated $CaCO_3$ (wt%) values are not provided when Ca or weight percent salinity data is unavailable. † = $CaCO_3$ values higher than 90 wt% are calculated from Ca values out of the range of the standards (see **"Geochemistry,"** p. 20, in the "Explanatory Notes" chapter). This table is also available in **ASCII**. [**N1**]

Table T19. Moisture and density measurements, Hole 1218A. (See table note. Continued on next page.)

Core, section, interval (cm)	Depth (mbsf)	Water content (%)	Density (g/cm^3)			Porosity (%)
			Wet bulk	Dry bulk	Grain	
199-1218A-						
1H-1, 75–77	0.75	73.1	1.22	0.33	2.52	87.0
1H-2, 75–77	2.25	75.7	1.20	0.29	2.60	88.8
1H-3, 75–77	3.75	73.5	1.22	0.32	2.63	87.7
1H-4, 81–83	5.31	74.7	1.21	0.31	2.63	88.4
1H-5, 75–77	6.75	76.1	1.20	0.29	2.57	88.9
1H-6, 27–29	7.77	72.7	1.23	0.34	2.57	86.9
2H-1, 75–77	8.95	73.0	1.22	0.33	2.45	86.6
2H-2, 75–77	10.45	70.5	1.25	0.37	2.59	85.8
2H-3, 75–77	11.95	70.1	1.23	0.37	2.38	84.5
2H-4, 75–77	13.45	67.4	1.24	0.40	2.17	81.4
2H-5, 75–77	14.95	66.3	1.30	0.44	2.71	83.9
2H-6, 75–77	16.45	66.9	1.24	0.41	2.18	81.1
2H-7, 31–33	17.51	67.0	1.26	0.41	2.34	82.3
3H-1, 75–77	18.45	68.4	1.25	0.40	2.41	83.6
3H-2, 75–77	19.95	66.4	1.28	0.43	2.57	83.2
3H-3, 75–77	21.45	72.6	1.23	0.34	2.57	86.9
3H-4, 75–77	22.95	70.4	1.24	0.37	2.54	85.5
3H-5, 75–77	24.45	70.7	1.25	0.37	2.69	86.4
3H-6, 75–77	25.95	71.0	1.24	0.36	2.63	86.3
3H-7, 37–39	27.07	72.5	1.23	0.34	2.58	86.9
4H-1, 75–77	27.95	72.2	1.23	0.34	2.54	86.5
4H-2, 75–77	29.45	70.2	1.25	0.37	2.66	86.0
4H-3, 75–77	30.95	67.6	1.29	0.42	2.82	85.2
4H-4, 75–77	32.45	76.5	1.20	0.28	2.78	89.8
4H-5, 75–77	33.95	76.2	1.19	0.28	2.54	88.8
4H-6, 75–77	35.45	76.0	1.20	0.29	2.60	88.9
4H-7, 29–31	36.49	77.6	1.19	0.27	2.61	89.9
5H-1, 75–77	37.45	76.8	1.19	0.28	2.55	89.2
5H-2, 75–77	38.95	78.9	1.18	0.25	2.67	90.7
5H-3, 75–77	40.45	75.5	1.21	0.30	2.73	89.1
5H-4, 75–77	41.95	76.8	1.20	0.28	2.79	90.0
5H-5, 75–77	43.45	68.7	1.27	0.40	2.68	85.2
5H-6, 75–77	44.95	72.3	1.24	0.34	2.77	87.6
5H-7, 19–21	45.89	75.8	1.21	0.29	2.72	89.3
6H-1, 75–77	46.95	76.0	1.20	0.29	2.60	88.9
6H-2, 75–77	48.45	77.1	1.19	0.27	2.55	89.3
6H-3, 75–77	49.95	78.1	1.19	0.26	2.72	90.5
6H-4, 75–77	51.45	78.9	1.18	0.25	2.64	90.6
6H-5, 75–77	52.95	76.6	1.19	0.28	2.59	89.2
6H-6, 49–51	54.19	75.9	1.21	0.29	2.78	89.5
6H-7, 28–30	54.98	56.5	1.41	0.61	2.72	77.5
7H-1, 75–77	56.45	46.4	1.54	0.82	2.70	69.5
7H-2, 75–77	57.95	43.1	1.59	0.90	2.71	66.8
7H-3, 75–77	59.45	51.0	1.47	0.72	2.70	73.3
7H-4, 75–77	60.95	69.6	1.27	0.39	2.79	86.2
7H-5, 75–77	62.45	55.9	1.40	0.62	2.62	76.4
7H-6, 75–77	63.95	55.6	1.41	0.63	2.68	76.6
7H-7, 60–62	65.30	41.7	1.60	0.93	2.69	65.3
8H-1, 141–143	66.61	70.0	1.25	0.38	2.62	85.7
8H-2, 75–77	67.45	43.6	1.58	0.89	2.70	67.1
8H-3, 75–77	68.95	40.6	1.62	0.96	2.71	64.4
8H-4, 81–83	70.51	53.0	1.43	0.67	2.61	74.2
8H-5, 75–77	71.95	40.5	1.63	0.97	2.74	64.5
8H-6, 82–84	73.52	43.8	1.58	0.89	2.74	67.6
9H-3, 75–77	78.45	42.0	1.60	0.93	2.71	65.7
9H-6, 75–77	82.95	53.5	1.44	0.67	2.68	75.1
10H-3, 75–77	87.95	45.2	1.54	0.84	2.63	67.9
10H-4, 75–77	89.45	47.3	1.54	0.81	2.80	71.0
10H-5, 75–77	90.95	46.7	1.53	0.82	2.70	69.8
10H-6, 75–77	92.45	60.3	1.35	0.54	2.66	79.8
10H-7, 32–34	93.52	60.5	1.35	0.53	2.61	79.6
11H-1, 75–77	94.45	49.9	1.49	0.74	2.70	72.4
11H-2, 75–77	95.95	44.7	1.56	0.86	2.70	68.0
11H-3, 75–77	97.45	44.2	1.56	0.87	2.68	67.4
11H-4, 75–77	98.95	46.2	1.54	0.83	2.73	69.5
11H-5, 75–77	100.45	44.4	1.55	0.86	2.64	67.4
11H-6, 75–77	101.95	45.6	1.54	0.84	2.66	68.5
11H-7, 55–57	103.25	42.6	1.60	0.92	2.73	66.4
12H-1, 75–77	103.95	47.5	1.52	0.80	2.68	70.3
12H-2, 75–77	105.45	44.2	1.57	0.88	2.72	67.8
12H-3, 75–77	106.95	43.8	1.57	0.88	2.70	67.2
12H-4, 105–107	108.75	53.1	1.44	0.67	2.66	74.6
12H-5, 105–107	110.25	40.4	1.61	0.96	2.65	63.7
12H-6, 75–77	111.45	46.6	1.54	0.82	2.73	70.0
12H-7, 30–32	112.50	39.6	1.64	0.99	2.72	63.5
13H-1, 79–81	113.49	50.2	1.48	0.74	2.69	72.6
13H-2, 75–77	114.95	44.3	1.57	0.88	2.73	67.9
13H-3, 75–77	116.45	48.3	1.52	0.79	2.79	71.8
13H-4, 75–77	117.95	44.3	1.56	0.87	2.69	67.6
13H-5, 75–77	119.45	46.9	1.54	0.82	2.76	70.4
13H-6, 75–77	120.95	43.8	1.58	0.89	2.75	67.7
13H-7, 45–46	122.15	42.1	1.61	0.93	2.74	66.0
14H-1, 75–77	122.95	44.3	1.56	0.87	2.69	67.6
14H-2, 75–77	124.45	40.9	1.63	0.96	2.73	64.8
14H-3, 75–77	125.95	39.7	1.64	0.99	2.70	63.4
14H-4, 75–77	127.45	40.7	1.62	0.96	2.68	64.2
14H-5, 75–77	128.95	38.6	1.66	1.02	2.71	62.5
14H-6, 75–77	130.45	38.1	1.66	1.03	2.70	61.8
14H-7, 20–22	131.40	40.2	1.65	0.99	2.80	64.8
15H-1, 75–77	132.45	37.5	1.68	1.05	2.71	61.3
15H-2, 75–77	133.95	37.6	1.69	1.05	2.77	61.9
15H-3, 75–77	135.45	36.8	1.70	1.07	2.75	60.9
15H-4, 75–77	136.95	39.3	1.65	1.00	2.71	63.1
15H-5, 72–74	138.42	38.9	1.65	1.01	2.70	62.6
15H-6, 75–77	139.95	38.3	1.66	1.03	2.72	62.3
15H-7, 37–39	141.07	38.1	1.68	1.04	2.76	62.4
16H-1, 75–77	141.95	37.2	1.69	1.06	2.73	61.2
16H-2, 75–77	143.45	37.9	1.68	1.04	2.75	62.1
16H-3, 75–77	144.95	37.7	1.68	1.05	2.76	62.0
16H-4, 75–77	146.45	36.5	1.70	1.08	2.73	60.5
16H-5, 75–77	147.95	36.6	1.69	1.07	2.70	60.3
16H-6, 81–83	149.51	35.6	1.72	1.11	2.74	59.6
16H-7, 31–33	150.51	37.1	1.68	1.06	2.72	61.0
17H-1, 95–97	151.65	39.1	1.66	1.01	2.75	63.3
17H-2, 79–81	152.99	41.0	1.62	0.95	2.71	64.8
17H-3, 75–77	154.45	40.9	1.63	0.96	2.74	64.9
17H-4, 75–77	155.95	38.9	1.64	1.01	2.67	62.4
17H-5, 75–77	157.45	37.7	1.67	1.04	2.70	61.5
17H-6, 75–77	158.96	35.9	1.70	1.09	2.71	59.7
17H-7, 40–42	160.12	36.2	1.70	1.09	2.72	60.1
18H-1, 75–77	160.95	37.6	1.67	1.04	2.70	61.4
18H-2, 75–77	162.45	36.3	1.69	1.08	2.70	60.0
18H-3, 75–77	163.95	40.7	1.62	0.96	2.69	64.3
18H-4, 75–77	165.45	41.0	1.62	0.96	2.72	64.8
18H-5, 75–77	166.87	38.3	1.67	1.03	2.76	62.6
18H-6, 105–107	168.67	37.6	1.67	1.04	2.70	61.4
19H-1, 75–77	170.45	40.0	1.63	0.98	2.68	63.6
19H-2, 75–77	171.95	35.2	1.72	1.11	2.71	59.0
19H-3, 75–77	173.45	35.6	1.71	1.10	2.70	59.3
19H-4, 80–82	175.00	37.3	1.68	1.05	2.69	61.0
19H-5, 75–77	176.45	36.2	1.69	1.08	2.67	59.7
19H-6, 75–77	177.95	37.1	1.68	1.06	2.70	60.8
19H-7, 67–69	179.37	36.2	1.70	1.09	2.72	60.1
20H-1, 78–80	179.98	45.0	1.55	0.85	2.68	68.2
20H-2, 75–77	181.45	41.8	1.60	0.93	2.68	65.2
20H-3, 75–77	182.95	44.3	1.56	0.87	2.68	67.5
20H-4, 75–77	184.45	40.3	1.63	0.97	2.70	64.0
20H-5, 75–77	185.95	38.9	1.64	1.00	2.67	62.4
20H-6, 75–77	187.45	38.1	1.65	1.02	2.64	61.4
22X-1, 85–87	196.76	37.8	1.68	1.04	2.74	61.9
22X-2, 78–80	198.18	38.8	1.66	1.02	2.74	63.0
22X-3, 68–70	199.58	43.7	1.56	0.88	2.62	66.4
22X-4, 92–94	201.32	44.0	1.57	0.88	2.70	67.5
22X-6, 31–33	203.21	43.3	1.57	0.89	2.65	66.3
23X-1, 126–128	206.76	44.7	1.53	0.85	2.55	66.8

Table T19 (continued).

Core, section, interval (cm)	Depth (mbsf)	Water content (%)	Density (g/cm^3) Wet bulk	Dry bulk	Grain	Porosity (%)
23X-4, 48–50	210.48	40.6	1.61	0.96	2.65	63.9
23X-6, 24–26	213.25	36.8	1.68	1.06	2.69	60.4
24X-1, 80–82	215.90	50.6	1.48	0.73	2.68	72.9
24X-3, 34–36	218.04	64.3	1.28	0.46	2.29	80.1
24X-6, 73–75	222.93	62.4	1.31	0.49	2.43	79.7
25X-2, 133–135	227.53	50.9	1.43	0.70	2.40	70.8
25X-4, 60–62	229.80	59.4	1.33	0.54	2.35	77.0
25X-6, 27–29	232.47	45.0	1.59	0.87	2.89	69.8
26X-1, 85–87	235.15	62.8	1.32	0.49	2.60	81.1
26X-3, 74–76	238.04	37.3	1.66	1.04	2.65	60.6
26X-6, 69–71	242.49	40.8	1.60	0.95	2.62	63.8
27X-2, 13–15	245.53	55.7	1.35	0.60	2.26	73.6
27X-3, 134–136	248.24	59.9	1.30	0.52	2.15	75.8
28X-2, 62–62	255.62	46.3	1.48	0.80	2.42	67.1
28X-4, 66–68	258.66	40.0	1.60	0.96	2.56	62.4
28X-6, 42–44	261.42	39.8	1.61	0.97	2.60	62.7
29X-2, 75–77	265.35	39.3	1.60	0.97	2.51	61.3
29X-4, 48–50	268.08	22.7	1.97	1.53	2.71	43.7
30X-1, 75–77	271.45	25.7	1.91	1.42	2.73	48.0
30X-3, 5–7	273.75	28.1	1.88	1.35	2.78	51.5

Note: This table is also available in **ASCII**. [**N1**]

Table T20. LAS-based mineralogy, Hole 1218A. (**See table note.** Continued on next two pages.)

Core, section, interval (cm)	Depth (mbsf)	Calcite (model wt%)	Opal (model wt%)	Smectite (model wt%)	Illite (model wt%)
199-1218A-					
1H-1, 75–77	0.76	9.0	30.0	10.1	51.0
1H-1, 125–127	1.26	16.3	29.3	9.7	44.7
1H-2, 23–25	1.74	18.7	26.3	7.2	47.7
1H-2, 75–77	2.26	21.1	26.0	14.2	38.7
1H-3, 23–25	3.24	30.8	10.3	4.4	54.5
1H-3, 75–77	3.76	19.3	19.7	14.6	46.4
1H-4, 23–25	4.74	10.7	22.1	25.5	41.7
1H-4, 81–83	5.32	6.1	27.5	34.0	32.4
1H-5, 23–25	6.24	0.0	30.8	57.3	11.9
1H-5, 75–77	6.76	0.0	26.8	49.9	23.4
1H-6, 23–25	7.74	0.0	26.9	73.1	0.0
1H-6, 27–29	7.78	0.0	15.5	62.6	21.9
2H-1, 75–77	8.96	0.0	30.8	68.9	0.3
2H-1, 125–127	9.46	0.0	12.8	87.2	0.0
2H-2, 25–27	9.96	0.0	31.3	68.7	0.0
2H-2, 75–77	10.46	0.0	27.7	61.7	10.6
2H-3, 25–27	11.46	0.0	18.4	81.6	0.0
2H-3, 75–77	11.96	0.0	10.4	89.6	0.0
2H-4, 25–27	12.96	0.0	25.7	74.3	0.0
2H-4, 75–77	13.46	0.0	4.9	95.1	0.0
2H-5, 25–27	14.46	0.0	8.2	91.8	0.0
2H-5, 75–77	14.96	7.4	0.0	92.6	0.0
2H-6, 25–27	15.96	0.0	2.0	98.0	0.0
2H-6, 75–77	16.46	7.2	0.0	92.8	0.0
2H-6, 23–25	17.44	0.0	7.5	92.5	0.0
2H-7, 31–33	17.52	4.2	0.0	95.8	0.0
3H-1, 75–77	18.46	7.6	0.0	92.4	0.0
3H-1, 125–127	18.96	0.0	8.6	91.4	0.0
3H-2, 23–25	19.44	0.0	12.4	87.6	0.0
3H-2, 75–77	19.96	24.4	0.0	75.6	0.0
3H-3, 23–25	20.94	0.0	0.2	99.8	0.0
3H-3, 75–77	21.46	13.4	0.4	86.2	0.0
3H-4, 23–25	22.44	0.0	18.6	81.4	0.0
3H-4, 75–77	22.96	23.8	0.0	72.1	4.1
3H-5, 23–25	23.94	20.6	4.7	74.7	0.0
3H-5, 75–77	24.46	32.6	0.0	58.1	9.3
3H-6, 23–25	25.44	42.7	0.0	27.6	29.7
3H-6, 75–77	25.96	41.9	0.0	43.3	14.8
3H-7, 23–25	26.94	43.0	0.0	31.0	26.0
3H-7, 37–39	27.08	42.6	4.8	45.7	6.9
4H-1, 75–77	27.96	47.6	1.8	28.9	21.7
4H-1, 125–127	28.46	50.4	0.0	21.9	27.7
4H-2, 23–25	28.94	45.6	0.0	21.0	33.4
4H-2, 75–77	29.46	28.0	0.0	65.2	6.8
4H-3, 23–25	30.44	11.5	0.0	88.5	0.0
4H-3, 75–77	30.96	16.1	0.0	83.9	0.0
4H-4, 23–25	31.94	13.0	0.0	87.0	0.0
4H-4, 75–77	32.46	33.3	0.0	51.3	15.4
4H-5, 23–25	33.44	46.0	0.0	25.0	29.0
4H-5, 75–77	33.96	39.0	0.0	34.6	26.4
4H-6, 23–25	34.94	46.1	0.0	23.1	30.7
4H-6, 75–77	35.46	53.3	0.0	32.1	14.6
4H-7, 29–31	36.50	46.4	0.0	40.5	13.1
4H-7, 56–58	36.75	52.3	0.0	24.7	23.1
5H-1, 75–77	37.46	34.6	0.0	52.9	12.5
5H-1, 124–126	37.95	41.8	0.0	38.5	19.7
5H-2, 23–25	38.44	42.3	0.0	31.0	26.7
5H-2, 75–77	38.96	34.0	0.0	59.4	6.6
5H-3, 23–25	39.94	18.4	0.0	81.6	0.0
5H-3, 75–77	40.46	30.4	0.0	57.4	12.2
5H-4, 23–25	41.44	32.4	0.0	46.9	20.7
5H-4, 75–77	41.96	33.9	0.0	45.5	20.7
5H-5, 23–25	42.94	64.6	0.0	10.0	25.4
5H-5, 75–77	43.46	76.8	3.4	17.0	2.7
5H-6, 23–25	44.44	67.9	8.4	0.0	23.6
5H-6, 75–77	44.96	65.0	5.6	9.7	19.8
5H-7, 19–21	45.90	53.3	0.0	43.6	3.1
5H-7, 40–42	46.11	84.5	0.0	0.0	15.5
6H-1, 75–77	46.96	36.8	10.7	18.1	34.4
6H-1, 125–127	47.46	34.8	19.5	10.5	35.2
6H-2, 23–25	47.94	36.4	18.6	15.2	29.8
6H-2, 75–77	48.46	34.2	20.2	24.1	21.5
6H-3, 23–25	49.44	39.3	3.4	20.1	37.2
6H-3, 75–77	49.96	31.3	4.5	46.7	17.5
6H-4, 23–25	50.94	38.0	10.0	23.0	29.1
6H-4, 75–77	51.46	36.3	8.2	44.7	10.9
6H-5, 23–25	52.44	44.9	10.1	19.2	25.8
6H-5, 75–77	52.96	47.9	3.8	46.0	2.4
6H-6, 23–25	53.94	61.3	6.0	26.5	6.2
6H-6, 49–51	54.20	60.7	2.9	34.9	1.5
6H-7, 28–30	54.99	81.1	0.0	18.9	0.0
6H-7, 56–58	55.27	92.6	0.0	7.4	0.0
7H-1, 75–77	56.46	76.7	0.0	23.3	0.0
7H-1, 126–128	56.97	81.2	0.0	18.8	0.0
7H-2, 24–26	57.45	88.3	0.0	11.7	0.1
7H-2, 75–77	57.96	78.0	0.0	22.0	0.0
7H-3, 24–26	58.95	86.2	0.0	12.1	1.7
7H-3, 75–77	59.46	85.4	0.0	14.6	0.0
7H-4, 24–26	60.45	89.2	0.0	3.3	7.5
7H-4, 75–77	60.96	79.3	0.0	17.6	3.1
7H-5, 24–26	61.95	92.1	0.0	2.8	5.2
7H-5, 75–77	62.46	84.7	0.0	15.3	0.0
7H-6, 24–26	63.45	85.3	2.8	8.4	3.5
7H-6, 75–77	63.96	81.8	0.0	18.2	0.0
7H-7, 24–26	64.95	86.7	0.0	13.3	0.0
7H-7, 60–62	65.31	78.2	0.0	21.8	0.0
8H-1, 125–127	66.46	91.4	0.0	8.6	0.0
8H-1, 141–143	66.62	67.0	0.6	32.4	0.0
8H-2, 23–25	66.94	87.9	0.0	12.1	0.0
8H-2, 75–77	67.46	77.2	0.0	22.8	0.0
8H-3, 23–25	68.44	80.9	0.0	19.1	0.0
8H-3, 75–77	68.96	77.7	0.0	22.3	0.0
8H-4, 23–25	69.94	85.0	0.0	15.0	0.0
8H-4, 81–83	70.52	85.0	0.0	15.0	0.0
8H-5, 23–25	71.44	80.6	0.0	19.4	0.0
8H-5, 75–77	71.96	78.7	0.0	21.3	0.0
8H-6, 23–25	72.94	84.6	0.0	15.4	0.0
8H-6, 82–84	73.53	76.7	0.0	23.3	0.0
9H-3, 75–77	78.46	77.7	0.0	22.3	0.0
9H-6, 75–77	82.96	85.3	0.0	14.7	0.0
10H-3, 75–77	87.96	79.0	0.0	21.0	0.0
10H-4, 75–77	89.46	93.4	0.0	6.6	0.0
10H-5, 75–77	90.96	82.6	0.0	17.4	0.0
10H-6, 75–77	92.46	90.7	0.0	5.6	3.6
10H-7, 32–34	93.53	85.5	0.9	13.6	0.0
11H-1, 23–25	93.94	96.2	0.0	0.0	3.8
11H-1, 75–77	94.46	92.8	0.0	7.2	0.0
11H-2, 23–25	95.44	94.6	0.0	1.6	3.8
11H-2, 75–77	95.96	87.2	0.0	12.8	0.0
11H-3, 23–25	96.94	91.7	0.0	8.3	0.0
11H-3, 75–77	97.46	92.9	0.0	7.1	0.0
11H-4, 23–25	98.44	96.1	0.0	0.0	3.9
11H-4, 75–77	98.96	87.5	0.0	12.5	0.0
11H-5, 23–25	99.94	87.0	0.0	0.0	13.0
11H-5, 75–77	100.46	90.5	0.0	9.5	0.0
11H-6, 23–25	101.44	97.6	0.0	1.6	0.8
11H-6, 75–77	101.96	88.8	0.0	11.2	0.0
11H-7, 23–25	102.94	95.7	0.0	4.3	0.0
11H-7, 55–57	103.26	80.4	0.0	19.6	0.0
12H-1, 23–25	103.44	94.2	0.0	5.8	0.0
12H-1, 75–77	103.96	82.6	0.0	17.4	0.0
12H-2, 23–25	104.94	75.0	0.0	25.0	0.0
12H-2, 75–77	105.46	73.1	0.0	26.9	0.0
12H-3, 23–25	106.44	84.6	0.0	15.4	0.0
12H-3, 75–77	106.96	72.4	0.0	27.6	0.0

Table T20 (continued).

Core, section, interval (cm)	Depth (mbsf)	Calcite (model wt%)	Opal (model wt%)	Smectite (model wt%)	Illite (model wt%)
12H-4, 23–25	107.94	85.2	4.1	10.7	0.0
12H-4, 105–107	108.76	64.5	11.6	23.9	0.0
12H-5, 23–25	109.44	97.2	2.8	0.0	0.0
12H-5, 105–107	110.26	72.3	0.0	27.7	0.0
12H-6, 23–25	110.94	92.2	0.9	6.9	0.0
12H-6, 75–77	111.46	77.0	5.8	17.3	0.0
12H-7, 23–25	112.44	92.4	0.0	7.6	0.0
12H-7, 30–32	112.51	77.7	2.1	20.2	0.0
13H-1, 22–24	112.93	81.5	6.2	12.2	0.0
13H-1, 79–81	113.50	86.2	0.0	13.8	0.0
13H-2, 23–25	114.44	91.5	0.0	8.5	0.0
13H-2, 75–77	114.96	72.8	0.0	27.2	0.0
13H-3, 23–25	115.94	92.3	0.0	7.7	0.0
13H-3, 75–77	116.46	80.6	0.0	19.4	0.0
13H-4, 23–25	117.44	78.1	0.0	21.9	0.0
13H-4, 75–77	117.96	76.9	0.7	22.4	0.0
13H-5, 23–25	118.94	86.4	6.3	7.3	0.0
13H-5, 75–77	119.46	69.4	5.2	25.4	0.0
13H-6, 23–25	120.44	84.0	5.8	10.2	0.0
13H-6, 75–77	120.96	75.6	3.7	20.7	0.0
13H-7, 23–25	121.94	80.9	0.0	19.1	0.0
13H-7, 45–47	122.16	80.2	0.7	19.1	0.0
14H-1, 23–25	122.44	81.3	4.4	14.3	0.0
14H-1, 75–77	122.96	74.5	3.6	21.9	0.0
14H-2, 23–25	123.94	76.7	0.0	23.3	0.0
14H-2, 75–77	124.46	75.1	0.0	24.9	0.0
14H-3, 23–25	125.44	73.6	0.0	26.4	0.0
14H-3, 75–77	125.96	73.9	0.0	26.1	0.0
14H-4, 23–25	126.94	76.9	0.0	23.1	0.0
14H-4, 75–77	127.46	67.7	0.0	32.3	0.0
14H-5, 23–25	128.44	79.4	0.0	20.6	0.0
14H-5, 75–77	128.96	71.5	0.0	28.5	0.0
14H-6, 23–25	129.94	72.7	0.0	27.3	0.0
14H-6, 75–77	130.46	73.5	0.0	26.5	0.0
14H-7, 20–22	131.41	72.8	0.0	27.2	0.0
14H-7, 23–25	131.44	77.1	0.0	22.9	0.0
15H-1, 23–25	131.94	78.8	0.0	21.2	0.0
15H-1, 75–77	132.46	68.7	0.0	31.3	0.0
15H-2, 23–25	133.44	83.6	0.0	16.4	0.0
15H-2, 75–77	133.96	68.9	0.0	31.1	0.0
15H-3, 23–25	134.94	82.5	2.2	15.3	0.0
15H-3, 75–77	135.46	70.6	0.0	29.4	0.0
15H-4, 23–25	136.44	85.1	0.5	14.4	0.0
15H-4, 75–77	136.96	60.8	0.0	39.2	0.0
15H-5, 23–25	137.94	79.4	0.0	20.6	0.0
15H-5, 72–74	138.43	65.4	0.0	34.6	0.0
15H-6, 23–25	139.44	80.7	0.0	19.3	0.0
15H-6, 75–77	139.96	68.7	0.0	31.3	0.0
15H-7, 23–25	140.94	80.8	0.0	19.2	0.0
15H-7, 37–39	141.08	68.2	0.0	31.8	0.0
16H-1, 23–25	141.44	83.1	0.0	16.9	0.0
16H-1, 75–77	141.96	67.4	0.0	32.6	0.0
16H-2, 23–25	142.94	79.9	0.0	20.1	0.0
16H-2, 75–77	143.46	63.8	0.0	36.2	0.0
16H-3, 23–25	144.44	76.5	0.0	23.5	0.0
16H-3, 75–77	144.96	63.1	0.0	36.9	0.0
16H-4, 23–25	145.94	82.0	0.0	18.0	0.0
16H-4, 75–77	146.46	71.5	0.0	28.5	0.0
16H-5, 23–25	147.44	77.2	0.0	22.8	0.0
16H-5, 75–77	147.96	60.3	1.7	37.9	0.0
16H-6, 23–25	148.94	72.7	0.0	27.3	0.0
16H-6, 81–83	149.52	71.3	0.0	28.7	0.0
16H-7, 23–25	150.44	76.7	0.0	23.3	0.0
16H-7, 31–33	150.52	73.8	0.0	26.2	0.0
17H-1, 95–97	151.66	71.6	0.0	28.4	0.0
17H-1, 125–127	151.96	73.3	0.0	26.7	0.0
17H-2, 23–25	152.44	75.1	0.0	24.9	0.0
17H-2, 79–81	153.00	73.9	3.1	23.0	0.0
17H-3, 23–25	153.94	78.4	7.2	14.4	0.0
17H-3, 75–77	154.46	76.3	0.0	23.7	0.0
17H-4, 23–25	155.44	80.9	7.7	11.4	0.0
17H-4, 75–77	155.96	72.4	0.0	27.6	0.0
17H-5, 23–25	156.94	75.7	8.2	16.0	0.0
17H-5, 75–77	157.46	66.0	0.0	34.0	0.0
17H-6, 23–25	158.45	78.8	0.0	21.2	0.0
17H-6, 75–77	158.97	64.1	0.0	35.9	0.0
17H-7, 25–27	159.98	81.0	0.0	19.0	0.0
17H-7, 40–42	160.13	69.1	0.0	30.9	0.0
18H-1, 23–25	160.44	74.0	0.0	26.0	0.0
18H-1, 75–77	160.96	65.8	0.0	34.2	0.0
18H-2, 23–25	161.94	76.6	0.0	23.4	0.0
18H-2, 75–77	162.46	72.1	0.0	27.9	0.0
18H-3, 23–25	163.44	79.7	5.1	15.2	0.0
18H-3, 75–77	163.96	71.1	5.4	23.5	0.0
18H-4, 23–25	164.94	81.7	5.2	13.1	0.0
18H-4, 75–77	165.46	73.0	1.5	25.5	0.0
18H-5, 23–25	166.36	84.0	1.8	14.1	0.0
18H-5, 75–77	166.88	71.1	0.0	28.9	0.0
18H-6, 54–56	168.17	80.4	0.9	18.6	0.0
18H-6, 105–107	168.68	71.5	0.0	28.5	0.0
18H-7, 24–26	169.37	79.2	0.0	20.8	0.0
19H-1, 75–77	170.46	75.1	0.0	24.9	0.0
19H-1, 127–129	170.98	82.4	0.0	17.6	0.0
19H-2, 23–25	171.44	82.0	0.0	18.0	0.0
19H-2, 75–77	171.96	73.4	0.0	26.6	0.0
19H-3, 23–25	172.94	78.0	0.0	22.0	0.0
19H-3, 75–77	173.46	68.8	0.0	31.2	0.0
19H-4, 23–25	174.44	78.1	0.0	21.9	0.0
19H-4, 80–82	175.01	68.1	0.0	31.9	0.0
19H-5, 23–25	175.94	83.1	0.6	16.4	0.0
19H-5, 75–77	176.46	72.7	0.0	27.3	0.0
19H-6, 23–25	177.44	82.7	0.4	16.9	0.0
19H-6, 75–77	177.96	73.4	0.0	26.6	0.0
19H-7, 23–25	178.94	80.2	0.0	19.8	0.0
19H-7, 67–69	179.38	70.7	0.0	29.3	0.0
20H-1, 23–25	179.44	79.4	4.2	16.4	0.0
20H-1, 78–80	179.99	80.6	3.4	16.0	0.0
20H-2, 23–25	180.94	77.8	8.9	13.3	0.0
20H-2, 75–77	181.46	73.2	0.0	26.8	0.0
20H-3, 23–25	182.44	81.9	6.1	12.0	0.0
20H-3, 75–77	182.96	81.6	4.1	14.3	0.0
20H-4, 23–25	183.94	98.6	1.4	0.0	0.0
20H-4, 75–77	184.46	83.8	0.0	16.2	0.0
20H-5, 23–25	185.44	83.0	0.0	17.0	0.0
20H-5, 75–77	185.96	81.3	0.0	18.7	0.0
20H-6, 23–25	186.94	84.1	1.4	14.5	0.0
20H-6, 75–77	187.46	85.2	0.0	14.8	0.0
22X-1, 23–25	196.14	85.8	0.0	14.2	0.0
22X-1, 85–87	196.76	85.3	0.0	14.7	0.0
22X-2, 23–25	197.64	69.3	13.1	17.6	0.0
22X-2, 78–80	198.19	79.2	1.1	19.7	0.0
22X-3, 23–25	199.14	74.6	11.2	14.2	0.0
22X-3, 68–70	199.59	74.3	10.4	15.3	0.0
22X-4, 23–25	200.64	98.8	1.2	0.0	0.0
22X-4, 92–94	201.33	69.4	17.3	13.4	0.0
22X-5, 23–25	202.14	66.5	17.1	16.4	0.0
22X-6, 24–26	203.15	75.4	11.6	13.1	0.0
22X-6, 31–33	203.22	65.8	13.6	20.6	0.0
23X-1, 126–128	206.77	63.5	23.1	13.4	0.0
23X-4, 48–50	210.49	83.9	5.0	11.0	0.0
23X-6, 24–26	213.25	89.2	0.0	10.8	0.0
24X-1, 80–82	215.91	82.4	0.0	0.0	17.6
24X-3, 34–36	218.05	57.5	0.0	0.0	42.5
24X-6, 73–75	222.94	70.0	0.0	0.6	29.4
25X-2, 133–135	227.54	69.8	0.0	6.5	23.7
25X-4, 60–62	229.81	70.0	0.0	4.6	25.4

Table T20 (continued).

Core, section, interval (cm)	Depth (mbsf)	Calcite (model wt%)	Opal (model wt%)	Smectite (model wt%)	Illite (model wt%)
25X-6, 27–29	232.48	87.8	0.0	0.0	12.2
26X-1, 21–23	234.52	75.4	0.0	20.4	4.2
26X-1, 85–87	235.16	59.9	0.0	18.4	21.8
26X-2, 24–26	236.05	78.0	0.0	9.6	12.4
26X-3, 23–25	237.54	65.2	0.0	30.3	4.5
26X-3, 74–76	238.05	86.6	0.0	13.4	0.0
26X-4, 23–25	239.04	92.6	0.0	7.4	0.0
26X-5, 23–25	240.54	88.2	0.0	11.8	0.0
26X-6, 23–25	242.04	74.5	12.9	12.6	0.0
26X-6, 69–71	242.50	90.5	4.1	5.4	0.0
27X-1, 30–32	244.21	31.7	37.7	30.6	0.0
27X-2, 13–15	245.54	31.1	38.3	30.6	0.0
27X-2, 66–69	246.07	29.5	35.1	35.5	0.0
27X-3, 23–25	247.14	0.0	56.3	43.7	0.0
27X-3, 134–136	248.25	3.3	56.9	39.8	0.0
27X-4, 28–30	248.69	5.3	60.4	34.3	0.0
27X-5, 24–26	249.65	25.9	49.0	25.1	0.0
28X-1, 24–26	253.75	48.1	38.5	13.4	0.0
28X-2, 24–26	255.25	52.2	23.4	24.4	0.0
28X-2, 62–64	255.63	43.7	39.8	16.5	0.0
28X-3, 24–26	256.75	60.2	22.0	17.7	0.0
28X-4, 24–26	258.25	49.9	31.4	18.7	0.0
28X-4, 66–68	258.67	55.2	22.4	22.5	0.0
28X-5, 24–26	259.75	50.7	24.2	25.1	0.0
28X-6, 24–26	261.25	51.1	27.2	21.7	0.0
28X-6, 42–44	261.43	54.2	22.6	23.1	0.0
28X-7, 24–26	262.25	59.8	15.2	25.0	0.0
29X-1, 29–31	263.40	57.8	22.2	20.0	0.0
29X-2, 27–29	264.88	40.6	31.1	28.3	0.0
29X-2, 75–77	265.36	41.7	26.2	32.0	0.0
29X-4, 8–10	267.68	55.3	0.0	44.7	0.0
29X-4, 48–50	268.08	57.8	0.0	42.2	0.0
30X-1, 20–22	270.91	57.8	0.0	42.2	0.0
30X-1, 75–77	271.46	57.0	0.0	43.0	0.0
30X-2, 108–110	273.29	64.5	0.0	35.5	0.0
30X-3, 5–7	273.76	55.0	0.0	45.0	0.0

Note: This table is also available in ASCII. [N1]

Table T21. Split-core velocity measurements, Hole 1218A. (See table notes. Continued on next page.)

Core, section, interval (cm)	Depth (mbsf)	Velocity (m/s)			Anisotropy (%)
		z*	y*	x†	
199-1218A-					
1H-1, 76	0.76	1491	1481		–0.6
1H-2, 76	2.26	1490	1506		1.0
1H-3, 76	3.76	1492	1477		–1.0
1H-4, 82	5.32	1492	1512		1.3
1H-5, 76	6.76	1493	1512		1.2
1H-6, 28	7.78	1490	1509		1.2
2H-1, 76	8.96	1490	1507		1.1
2H-2, 76	10.46	1487	1504		1.1
2H-3, 76	11.96	1488	1508		1.3
2H-4, 76	13.46	1487	1504		1.1
2H-5, 76	14.96	1487	1504		1.2
2H-6, 76	16.46	1490	1504		1.0
2H-7, 31	17.51	1489	1503		0.9
3H-1, 76	18.46	1493	1508		1.0
3H-2, 76	19.96	1488	1506		1.2
3H-3, 76	21.46	1497	1513		1.1
3H-4, 76	22.96	1495	1519		1.6
3H-5, 76	24.46	1499	1519		1.4
3H-6, 76	25.96	1501	1521		1.3
3H-7, 38	27.08	1500	1523		1.5
4H-1, 76	27.96	1505	1502		–0.2
4H-2, 76	29.46	1500	1519		1.3
4H-3, 76	30.96	1496	1522		1.7
4H-4, 76	32.46	1506	1529		1.5
4H-5, 76	33.96	1505	1531		1.7
4H-6, 76	35.46			1540	
4H-7, 30	36.50			1535	
5H-1, 76	37.46			1522	
5H-2, 76	38.96			1543	
5H-3, 76	40.46			1555	
5H-4, 76	41.96			1529	
5H-5, 76	43.46			1508	
5H-6, 76	44.96			1524	
5H-7, 20	45.90			1529	
6H-1, 76	46.96			1536	
6H-2, 76	48.46			1529	
6H-3, 76	49.96			1538	
6H-4, 76	51.46			1538	
6H-5, 76	52.96			1536	
6H-6, 50	54.20			1529	
6H-7, 29	54.99			1512	
7H-1, 76	56.46			1517	
7H-2, 76	57.96			1522	
7H-3, 76	59.46			1520	
7H-4, 76	60.96			1521	
7H-5, 76	62.46			1522	
7H-6, 76	63.96			1520	
7H-7, 61	65.31			1529	
8H-1, 142	66.62			1529	
8H-2, 76	67.46			1524	
8H-3, 76	68.96			1533	
8H-4, 82	70.52			1523	
8H-5, 76	71.96			1531	
8H-6, 83	73.53			1530	
9H-1, 99	75.69			1523	
9H-2, 76	76.96			1529	
9H-3, 76	78.46			1542	
9H-4, 66	79.86			1530	
9H-5, 71	81.41			1528	
9H-6, 76	82.96			1502	
9H-7, 58	84.28			1526	
10H-1, 76	84.96			1526	
10H-2, 61	86.31			1526	
10H-3, 76	87.96			1528	
10H-4, 76	89.46			1514	
10H-5, 76	90.96			1509	
10H-6, 76	92.46			1512	
10H-7, 33	93.53			1529	
11H-1, 76	94.46			1526	
11H-2, 76	95.96			1532	
11H-3, 76	97.46			1529	
11H-4, 76	98.96			1526	
11H-5, 76	100.46			1528	
11H-6, 76	101.96			1535	
11H-7, 56	103.26			1526	
12H-1, 76	103.96			1529	
12H-2, 76	105.46			1544	
12H-3, 76	106.96			1542	
12H-4, 106	108.76			1521	
12H-5, 106	110.26			1553	
12H-6, 76	111.46			1548	
12H-7, 31	112.51			1549	
13H-1, 80	113.50			1522	
13H-2, 76	114.96			1534	
13H-3, 76	116.46			1529	
13H-4, 76	117.96			1522	
13H-5, 76	119.46			1521	
13H-6, 76	120.96			1526	
13H-7, 46	122.16			1534	
14H-1, 76	122.96			1539	
14H-2, 76	124.46			1529	
14H-3, 76	125.96			1534	
14H-4, 76	127.46			1530	
14H-5, 76	128.96			1523	
14H-6, 76	130.46			1533	
14H-7, 21	131.41			1529	
15H-1, 76	132.46			1542	
15H-2, 76	133.96			1544	
15H-3, 76	135.46			1566	
15H-4, 76	136.96			1524	
15H-5, 73	138.43			1534	
15H-6, 76	139.96			1529	
15H-7, 38	141.08			1533	
16H-1, 76	141.96			1535	
16H-2, 76	143.46			1531	
16H-3, 76	144.96			1533	
16H-4, 76	146.46			1543	
16H-5, 76	147.96			1539	
16H-6, 84	149.54			1546	
16H-7, 32	150.52			1543	
17H-1, 96	151.66			1542	
17H-2, 80	153.00			1558	
17H-3, 76	154.46			1532	
17H-4, 76	155.96			1536	
17H-5, 76	157.46			1544	
17H-6, 76	158.97			1534	
17H-7, 41	160.13			1543	
18H-1, 76	160.96			1541	
18H-2, 76	162.46			1541	
18H-3, 76	163.96			1534	
18H-4, 76	165.46			1535	
18H-5, 76	166.88			1535	
18H-6, 106	168.68			1543	
19H-1, 76	170.46			1542	
19H-2, 75	171.95			1574	
19H-3, 75	173.45			1559	
19H-4, 81	175.01			1556	
19H-5, 78	176.48			1542	
19H-6, 76	177.96			1531	
19H-7, 68	179.38			1538	
20H-1, 80	180.00			1529	
20H-2, 76	181.46			1535	
20H-3, 76	182.96			1525	
20H-4, 76	184.46			1528	
20H-5, 76	185.96			1535	
20H-6, 76	187.46			1539	
22X-1, 86	196.76	1542	1551		0.6

Table T21 (continued).

Core, section, interval (cm)	Depth (mbsf)	Velocity (m/s)			Anisotropy (%)
		z*	y*	x†	
22X-2, 79	198.19	1522	1535		0.8
22X-3, 69	199.59	1524	1527		0.2
22X-4, 93	201.33	1524	1551		1.7
22X-6, 32	203.22	1535	1562		1.7
23X-1, 127	206.77	1529	1556		1.7
23X-4, 49	210.49	1525	1532		0.4
23X-6, 25	213.25	1549	1549		0.0
24X-1, 81	215.91	1509	1536		1.8
24X-3, 36	218.06	1584	1602		1.1
24X-6, 74	222.94	1538	1554		1.0
25X-2, 134	227.54	1537	1551		0.9
25X-4, 61	229.81	1553	1576		1.5
25X-6, 28	232.48	1544	1569		1.6
26X-1, 86	235.16	1559	1586		1.7
26X-3, 75	238.05	1561	1590		1.9
26X-6, 70	242.50	1575	1590		1.0
27X-2, 14	245.54	1555	1583		1.8
27X-3, 135	248.25	1573	1598		1.5
28X-2, 63	255.63	1545	1563		1.1
28X-4, 67	258.67	1578	1587		0.6
28X-6, 43	261.43	1594	1589		–0.3
29X-2, 76	265.36	1570	1575		0.3
29X-4, 49	268.09	1687	1716		1.7
30X-1, 76	271.46	1641	1667		1.6
30X-3, 6	273.76	1586	1628		2.6

Notes: * = determined by insertion probe, † = determined by contact probe. This table is also available in **ASCII.**

Table T22. Thermal conductivity, Holes 1218A and 1218B.

Core, section, interval (cm)	Depth (mbsf)	Thermal conductivity (W/[m·K])
199-1218A-		
1H-3, 76	3.76	0.72
2H-3, 76	11.96	0.72
4H-3, 76	30.96	0.73
5H-3, 76	40.46	0.71
6H-3, 76	49.96	0.71
7H-3, 76	59.46	0.97
8H-3, 76	68.96	1.15
9H-3, 76	78.46	1.14
10H-3, 76	87.96	1.07
11H-3, 76	97.46	1.08
12H-3, 76	106.96	1.07
13H-3, 76	116.46	1.02
14H-3, 76	125.96	1.15
15H-3, 76	135.46	1.18
16H-3, 76	144.96	1.19
17H-3, 76	154.46	1.13
18H-3, 76	163.96	1.13
19H-3, 76	173.46	1.22
199-1218B-		
1H-3, 40	3.40	0.71
2H-3, 76	7.66	0.74
3H-3, 76	17.16	0.75
4H-3, 76	26.66	0.73
5H-3, 76	36.16	0.71
6H-3, 76	45.66	0.73
7H-3, 76	55.11	0.94
8H-3, 76	64.66	1.06
9H-3, 76	74.16	1.12
10H-3, 64	83.54	0.82
11H-3, 76	93.16	1.01
12H-3, 76	102.66	1.04
13H-3, 76	112.16	1.06
14H-3, 76	121.66	1.09
15H-3, 76	131.16	1.09
16H-3, 76	140.66	1.22
17H-3, 76	150.16	1.18
18H-3, 76	159.66	1.18
19X-3, 76	169.16	1.17

Note: This table is also available in **ASCII**.

Table T23. In situ temperature, Holes 1218B and 1218C.

Hole, core	Depth (mbsf)	In situ temperature* (°)
199-		
	0.00	1.78
1218B-7H	60.90	6.22
1218C-3H	83.50	7.74
1218B-10H	89.40	6.93
1218C-5H	102.50	8.90
1218B-12H	108.40	9.00
1218C-7H	121.50	9.95

Notes: * = seafloor temperature is the average of the determinations accompanying the six cores. This table is also available in **ASCII.**

Table T24. Logging operations, Hole 1218A.

Date (Nov 2001)	Local time (hr)	Operations
16	1130	Hole preparation complete, rig up wireline
	1700	Run into hole with triple combo (MGT, HNGS, APS, HLDT, DITE, TAP)
	2210	Uplog with triple combo at 900 ft/hr from total depth (279 mbsf)
	2250	Going down for a second pass
	2330	Uplog with triple combo at 900 ft/hr from total depth (279 mbsf)
17	0010	Going down for an MGT pass
	0050	Uplog with MGT at 700 ft/hr from total depth (247 mbsf)
	0140	Pull tools out of hole and rigdown
	0630	Rig up FMS-sonic
	0740	Run into hole with FMS-sonic (NGT, DSI, GPIT, FMS)
	1230	Uplog with FMS-sonic at 900 ft/hr from total depth (281.2 mbsf)
	1310	Going down for a second pass
	1400	Uplog with FMS-sonic at 900 ft/hr from total depth (280 mbsf)
	1445	Pipe withdrawal and extra 20 m uplogging
	1455	Pull tools out of hole and rig down
	1900	End of logging operations

Notes: Drillers total depth = 5098 mbsf, water depth = 4817 m, initial end of pipe = 80.0 mbsf, final end of pipe = 60.0 mbsf. MGT = multisensor gamma ray tool, HNGS = hostile environment natural gamma ray sonde, APS = accelerator porosity sonde, DITE = dual induction tool, TAP = high-temperature acceleration pressure tool, FMS = Formation MicroScanner, NGT = natural gamma ray tool, DSI = dipole sonic induction tool, GPIT = general purpose inclinometry tool.

CHAPTER NOTE

N1. 13 December 2002—After the CD-ROM version of this volume was published, errors were noted in the ASCII versions of Tables T3, T8, T10, T11, T14, T17, T18, T19, and T20. This version contains the corrected ASCII files.

*Dates reflect file corrections or revisions.